

An investigation of medial prefrontal cortex –
hippocampal circuit function in a mouse model of
familial Alzheimer's disease

Submitted by

Erica Sarrag Brady

to the University of Exeter as a thesis for the degree of
Doctor of Philosophy in Medical Studies
in September 2021

This thesis is available for Library use on the understanding that it is copyright material and that no quotation from the thesis may be published without proper acknowledgement.

I certify that all material in this thesis which is not my own work has been identified and that any material that has previously been submitted and approved for the award of a degree by this or any other University has been acknowledged.

Signature:

A rectangular box containing a handwritten signature in black ink. The signature is cursive and appears to read 'Erica Sarrag Brady'.

Abstract

The communication between the medial prefrontal cortex (mPFC) and hippocampus is crucial for spatial memory, decision making and the long-term consolidation of our memories during sleep. This communication is mediated *via* the temporal coupling of key neuronal oscillations. Alzheimer's disease (AD) is a progressive neurodegenerative disorder which affects the electrical activity of the brain, causing disrupted neuronal oscillations and a decline in episodic, spatial and working memory. In the preclinical stages of the disease, sleep disruptions are common and are accompanied by impairments to several of the oscillations responsible for long-term memory consolidation in the mPFC-hippocampal circuit. However, less is known about how the functional interactions of the different neuronal oscillations in this circuit are affected. Additionally, impairments to the oscillations involved in spatial memory and decision making in the mPFC-hippocampal circuit are known to occur in first-generation mouse models of amyloidopathy, yet have been scarcely studied in second-generation models. Therefore, using *in vivo* electrophysiology, the oscillatory activity of this circuit was studied during sleep and exploratory behaviour in the second-generation APP^{NL-G-F} mouse model of amyloidopathy, to investigate potential dysfunctions.

The neuronal oscillations in the mPFC-hippocampal circuit were studied during natural sleep. In these experiments, impairments to local oscillations in the mPFC and CA1 region of the hippocampus were identified, yet long-range coordination of oscillations between brain regions was unaffected. Additionally, the oscillations recorded in CA1 during spatial memory showed local disruptions. Finally, impairments to the function of inhibitory neurons have been proposed to underlie changes to the oscillatory dynamics of neuronal circuit activity in AD. Therefore, immunohistochemical analysis of interneuron protein markers was performed to complement electrophysiological analyses of mPFC and CA1 circuit function. Collectively, these experiments further our understanding of how the mPFC-hippocampal circuit is affected in AD and provide a basis to study the underlying circuit disruptions.

Table of contents

TITLE PAGE	1
ABSTRACT.....	2
TABLE OF CONTENTS	3
ACKNOWLEDGMENTS	7
LIST OF FIGURES	8
LIST OF TABLES	12
LIST OF ABBREVIATIONS.....	13
1 INTRODUCTION.....	17
1.1 WHAT ARE NEURONAL OSCILLATIONS AND WHAT IS THEIR PURPOSE?	18
1.1.1 <i>The field potential</i>	18
1.1.2 <i>Oscillations</i>	18
1.2 SLEEP	19
1.2.1 <i>Sleep stages and sleep state switching</i>	19
1.2.2 <i>NREM Sleep</i>	20
1.2.2.1 Generation of the slow wave oscillation	22
1.2.2.2 Generation of spindles.....	28
1.2.2.3 Generation of sharp-wave ripples	31
1.2.2.4 The mPFC-hippocampal circuit and its role within systems consolidation	34
1.2.2.5 Alternate theories to systems consolidation	39
1.2.3 <i>REM sleep</i>	39
1.3 AWAKE OSCILLATIONS	40
1.3.1 <i>Theta oscillation generation and function</i>	40
1.3.2 <i>Gamma oscillation generation and function</i>	42
1.3.3 <i>Theta-gamma coupling</i>	43
1.4 ALZHEIMER'S DISEASE.....	46
1.4.1 <i>Introduction to Alzheimer's disease</i>	46
1.4.2 <i>APP processing and the amyloid hypothesis</i>	47
1.4.3 <i>Aberrant neuronal network activity in Alzheimer's disease</i>	50
1.4.3.1 Evidence for neuronal hyperexcitability in AD.....	50
1.4.3.2 Disrupted neuronal oscillations in AD.....	53
1.4.4 <i>Are sleep disturbances a cause or consequence of Alzheimer's disease?</i>	55
1.4.5 <i>The APP^{NL-G-F} mouse model</i>	57
1.5 HYPOTHESES AND AIMS	60
2 METHODS	62
2.1 ANIMALS.....	63
2.1.1 <i>Ethics</i>	63
2.1.2 <i>Housing</i>	63
2.1.3 <i>APP^{NL-G-F} mice</i>	63
2.1.4 <i>APP^{NL-G-F} x SST-Cre and APP^{NL-G-F} x PV-Cre mice</i>	64
2.1.5 <i>Emx1-Cre mice</i>	64
2.2 CHRONIC <i>IN VIVO</i> ELECTROPHYSIOLOGY	65
2.2.1 <i>Animals</i>	65
2.2.2 <i>Silicon multielectrode array</i>	65
2.2.3 <i>Surgical implantation of silicon probes</i>	66
2.2.4 <i>Acquisition of neural signals</i>	67
2.2.5 <i>Sleep recordings</i>	68
2.2.6 <i>Open field recordings</i>	68
2.2.7 <i>Novel object location</i>	69
2.2.8 <i>The effects of anaesthesia on the SWO</i>	71
2.2.9 <i>Verification of silicon probe placement</i>	72
2.3 ACUTE <i>IN VIVO</i> ELECTROPHYSIOLOGY	74

2.3.1 <i>Animals</i>	74
2.3.2 <i>Viral injection surgery</i>	74
2.3.3 <i>Silicon microelectrode arrays</i>	75
2.3.4 <i>Acquisition of neural signals</i>	76
2.3.5 <i>Experimental set-up</i>	76
2.3.6 <i>Histological verification of probes</i>	78
2.4 ANALYSIS OF ELECTROPHYSIOLOGICAL DATA	79
2.4.1 <i>Spectral analysis</i>	79
2.4.2 <i>Phase-amplitude coupling</i>	80
2.4.3 <i>Detection of slow wave sleep</i>	82
2.4.4 <i>SWO and delta power analysis</i>	84
2.4.5 <i>Detection of the SWO, spindles and ripples</i>	85
2.4.6 <i>Cross-frequency analysis of sleep oscillations</i>	87
2.4.6.1 <i>UDS-gamma coupling</i>	87
2.4.6.2 <i>UDS-spindle and UDS-ripple coupling</i>	87
2.4.6.3 <i>Spindle-spindle coupling</i>	88
2.4.6.4 <i>Spindle-ripple coupling</i>	88
2.4.6.5 <i>UDS-spindle-ripple coupling</i>	88
2.4.7 <i>Animal position during Open Field behaviour</i>	89
2.4.8 <i>Speed-modulated theta and gamma power</i>	89
2.4.9 <i>Speed modulated theta-gamma coupling</i>	89
2.4.10 <i>Speed modulated theta coherence</i>	90
2.5 IMMUNOHISTOCHEMISTRY.....	90
2.5.1 <i>PV and Aβ_{1-42} staining</i>	90
2.5.2 <i>cFos staining</i>	92
2.6 STATISTICAL ANALYSIS.....	93
2.7 LISTS OF CONSUMABLES AND EQUIPMENT	94

3 | IMMUNOHISTOCHEMICAL ANALYSIS OF PV-EXPRESSING INTERNEURONS AND A β PLAQUES IN THE APP^{NL-G-F} MOUSE MODEL..... 99

3.1 INTRODUCTION	100
3.2 RESULTS	103
3.2.1 <i>Target brain regions</i>	103
3.2.2 <i>Aβ_{1-42} plaque immunoreactivity in the mPFC and CA1 region of the hippocampus</i>	103
3.2.3 <i>PV-expressing interneuron immunoreactivity in the mPFC</i>	109
3.2.4 <i>PV-expressing interneuron immunoreactivity in the CA1 region of the hippocampus</i>	113
3.3 DISCUSSION	116
3.3.1 <i>Summary</i>	116
3.3.2 <i>Aβ_{1-42} deposition in the mPFC and CA1</i>	116
3.3.3 <i>An increase in CA1 PV-expressing interneuron immunoreactivity</i>	117
3.3.4 <i>A decrease in ACC PV-expressing interneuron immunoreactivity</i>	117
3.3.4 <i>Similarities with other mouse models and humans</i>	119
3.3.5 <i>Limitations and future directions</i>	119
3.3.6 <i>Conclusions</i>	120

4 | A CHEMOGENETIC APPROACH FOR TARGETING PV- AND SST-EXPRESSING INTERNEURON POPULATIONS TO AMELIORATE SLOW WAVE OSCILLATION IMPAIRMENTS IN THE APP^{NL-G-F} MOUSE MODEL

4.1 INTRODUCTION	123
4.2 RESULTS	125
4.2.1 <i>Viral transduction of excitatory DREADDs</i>	125
4.2.2 <i>Experimental approach</i>	128
4.2.3 <i>No difference in UDS dynamics between WT and APP mice</i>	129
4.2.4 <i>Differences in UDS dynamics between baseline and saline control conditions</i>	133
4.2.5 <i>Isoflurane produces large variation in UDS dynamics compared with urethane and natural sleep</i>	137
4.3 DISCUSSION	140
4.3.1 <i>Summary</i>	140
4.3.2 <i>UDS dynamics appear to be unaffected in 8-month APP animals</i>	140

4.3.3 <i>Anaesthetics vs natural sleep to study the SWO</i>	141
4.3.3.1 <i>Isoflurane</i>	141
4.3.3.2 <i>Anaesthesia vs natural sleep</i>	142
4.3.4 <i>Conclusions</i>	143
5 INVESTIGATING THE OSCILLATIONS UNDERLYING SYSTEMS CONSOLIDATION IN THE MPFC- HIPPOCAMPAL CIRCUIT DURING NREM SLEEP IN THE APP^{NL-G-F} MOUSE MODEL	144
5.1 <i>INTRODUCTION</i>	145
5.2 <i>RESULTS</i>	147
5.2.1 <i>SWS detection</i>	147
5.2.2 <i>Cortical UDS and delta oscillation power</i>	148
5.2.3 <i>UDS dynamics</i>	150
5.2.4 <i>UDS nested gamma oscillations</i>	152
5.2.5 <i>Cortical and hippocampal spindles</i>	154
5.2.6 <i>UDS nested spindles</i>	159
5.2.7 <i>Spindle – spindle coupling</i>	163
5.2.8 <i>Hippocampal ripples</i>	164
5.2.9 <i>UDS nested ripples</i>	167
5.2.10 <i>Spindle – ripple coupling</i>	169
5.2.11 <i>UDS – spindle – ripple coupling</i>	173
5.2.12 <i>A hippocampus-dependant memory task</i>	174
5.3 <i>DISCUSSION</i>	177
5.3.1 <i>Summary</i>	177
5.3.2 <i>Impaired local oscillations</i>	177
5.3.2.1 <i>The slow wave oscillation</i>	177
5.3.2.2 <i>Gamma oscillations</i>	178
5.3.2.3 <i>Spindles</i>	178
5.3.2.4 <i>Ripples</i>	180
5.3.3 <i>Spared oscillation coupling</i>	182
5.3.4 <i>Relevance to hippocampus-dependant memory</i>	183
5.3.5 <i>Conclusions</i>	184
6 OSCILLATION DYNAMICS IN CA1 AND THE MPFC DURING EXPLORATORY BEHAVIOUR IN THE APP^{NL-G-F} MOUSE MODEL	186
6.1 <i>INTRODUCTION</i>	187
6.2 <i>RESULTS</i>	190
6.2.1 <i>Speed-modulated theta oscillations in CA1 and the mPFC</i>	190
6.2.2 <i>Speed-modulated gamma oscillations in CA1</i>	194
6.2.3 <i>Speed-modulated gamma oscillations in the mPFC</i>	198
6.2.4 <i>Theta-gamma coupling in CA1</i>	202
6.2.5 <i>Theta coherence between CA1 and the mPFC</i>	204
6.2.6 <i>Locomotor activity in the Open Field</i>	206
6.3 <i>DISCUSSION</i>	209
6.3.1 <i>Summary</i>	209
6.3.2 <i>Increased theta power in CA1</i>	209
6.3.3 <i>Mild impairments to theta communication between CA1 and the mPFC during increasing locomotion velocity</i>	211
6.3.4 <i>Gamma oscillation power and frequency in CA1 and the mPFC</i>	212
6.3.5 <i>Gamma oscillation power and frequency with respect to running speed in the mPFC and CA1</i>	213
6.3.6 <i>Theta-gamma coupling in CA1</i>	214
6.3.7 <i>Ambulatory activity in the OF paradigm</i>	215
6.3.9 <i>Conclusions</i>	216
7 FINAL DISCUSSION AND CONCLUSIONS	217
7.1 <i>KEY FINDINGS</i>	218
7.1.1 <i>Original hypotheses</i>	218
7.1.2 <i>Key findings investigating hypothesis 1</i>	218
7.1.3 <i>Key findings investigating hypothesis 2</i>	220

7.1.4 <i>Key findings investigating hypothesis 3</i>	222
7.1.5 <i>Summary of new knowledge about the mPFC-hippocampal circuit in the APP^{NL-G-F} mouse model</i>	223
7.2 LIMITATIONS OF MOUSE MODELS OF ALZHEIMER'S DISEASE	224
7.2.1 <i>Limitations of first-generation mouse models</i>	224
7.2.2 <i>Second-generation mouse models</i>	225
7.3 BROADER IMPACT WITHIN ALZHEIMER'S DISEASE RESEARCH	228
7.4 FUTURE DIRECTIONS	230
7.5 FINAL CONCLUSIONS	231
REFERENCES	232

Acknowledgments

First, I would like to thank my supervisors; Mick Craig and Jon Witton. Throughout my PhD, Mick has been encouraging in not only the experiments intended for my thesis, but for the scientific ideas and extra-curricular pursuits that have happened outwith my PhD research. He has always believed in me and had confidence in my abilities, which has helped me grow as a researcher. Also, I thank him for providing such a great lab to be a part of! I am also grateful to Jon for taking me on as a student last year. His help during the final stages of my PhD was invaluable and he taught me a lot about what is required of a thesis and electrophysiological analysis.

Next, I would like to thank the members of the Craig Lab. I was extremely lucky to be surrounded by such great people and talented scientists. Shivali Kohli was always so willing to help and I learnt a lot from her about behavioural research. Ella Margetts-Smith was a great friend / fellow PhD student and I enjoyed / needed our “mentoring” sessions. Lastly, I want to say how grateful I am to Lilya Andrianova, who was not only a great postdoc, but became one of my best friends at Exeter. She was always happy to help me with my research, both in the discussions we would have and in the practical side of things. She is a great postdoc and teacher and I have learnt a lot from her over the past few years. It was great to have such a great friend both in and out of the lab and I will miss our post-work exploits.

I am also grateful to have such a great family, who have always been so encouraging of everything I do. Their constant support means a lot.

Of course, I could not have completed my PhD without the love and support of my partner, Alastair MacDonald. He is my biggest cheerleader, is always pushing and encouraging me to do the things that I want, was my rock the past 4 years and makes me strive to be a better researcher. He is my best friend and I can't wait to start our adventure in San Francisco.

Finally, I want to express how grateful I am to the animals used in the following experiments, without which this research would not be possible.

List of figures

- Figure 1.2.1** Anatomy of the mouse mPFC and dorsal hippocampus.
- Figure 1.2.2** The cortical slow wave oscillation.
- Figure 1.2.3** Thalamocortical sleep spindle generation.
- Figure 1.2.4** Generation of hippocampal sharp-wave ripples.
- Figure 1.2.5** The mPFC-hippocampal circuit during systems consolidation.
- Figure 1.3.1** Hippocampal theta and gamma oscillations and their coupling.
- Figure 1.4.1** Images of extracellular A β plaques and intracellular NFTs.
- Figure 1.4.2** Pathogenic processing of APP and progressing of AD.
- Figure 1.4.3** A timeline of cognitive and network decline in the APP^{NL-G-F} mouse model.
- Figure 2.2.1** Silicon microelectrode design for chronic *in vivo* electrophysiology.
- Figure 2.2.2** Schematic of a mouse skull with details of the different landmarks for microelectrode and skull screw placement.
- Figure 2.2.3** OF and NOL paradigms.
- Figure 2.2.4** Verification of electrode placement.
- Figure 2.3.1** Viral injection procedure in the mPFC.
- Figure 2.3.2** Size specifications of microelectrode used during acute *in vivo* electrophysiology.
- Figure 2.3.3** A flow diagram describing the experimental methods used to chemogenetically study the effects of PV- and SST-expressing interneuron populations on UDS dynamics.
- Figure 2.3.4** Histological verification of silicon probe placement.
- Figure 2.4.1** Effect of taper parameters on power spectra.
- Figure 2.4.2** Method for measuring the PAC between two oscillations.
- Figure 2.4.3** Method for isolating periods of SWS.
- Figure 2.4.4** Schematics representing sleep oscillation detection methods.
- Figure 2.5.1** Method for detecting A β_{1-42} plaques.
- Figure 3.2.1** Representative images and schematics displaying the defined regions of interest.

- Figure 3.2.2** $A\beta_{1-42}$ deposition increases with age in APP animals in the IL and PL cortices.
- Figure 3.2.3** $A\beta_{1-42}$ deposition increases with age in APP animals in the ACC.
- Figure 3.2.4** $A\beta_{1-42}$ deposition increases with age in APP animals in the CA1 region of the hippocampus.
- Figure 3.2.5** PV-expressing interneuron density does not differ in APP mice compared with WT in IL and PL cortices at all ages.
- Figure 3.2.6** PV-expressing interneuron density does not differ in APP mice compared with WT in the ACC at 3, 6, and 8 months but decreases at 16 months.
- Figure 3.2.7** PV-expressing interneuron density does not differ in APP mice compared with WT in CA1 at 3, 6, and 16 months but increases at 8 months.
- Figure 4.2.1** Strategy for controlling PV and SST interneuron populations in the mPFC of WT and APP mice.
- Figure 4.2.2** Subcutaneous injection of compound 21 successfully activates neurons expressing the hM3D(Gq) excitatory DREADD as seen by the expression of the immediate early gene cFos.
- Figure 4.2.3** Experimental protocol for chemogenetically controlling PV and SST interneuron populations to alter UDS dynamics in WT and APP mice.
- Figure 4.2.4** Baseline UDS dynamics do change in APP animals compared with WT at 8 months under isoflurane anaesthesia.
- Figure 4.2.5** Variation in baseline UDS dynamics is not due to an effect of expressing Cre-recombinase in PV or SST-expressing neurons.
- Figure 4.2.6** No correlation between breathing rate and UDS dynamics is observed.
- Figure 4.2.7** UDS dynamics change between baseline and vehicle treated conditions.

- Figure 4.2.8** UDS dynamics are highly variable under isoflurane anaesthesia.
- Figure 5.2.1** Method for isolating periods of SWS.
- Figure 5.2.2** The power of both UDS and delta oscillations in the mPFC is not altered in APP animals compared with WT controls.
- Figure 5.2.3** UDS dynamics is not altered in APP animals compared with WT controls.
- Figure 5.2.4** No change in UDS-locked gamma power and PAC between genotypes.
- Figure 5.2.5** A statistically significant increase in the amplitude and power of mPFC spindles in APP mice relative to WT.
- Figure 5.2.6** A trending decrease in the amplitude and power of CA1 spindle events and statistically significant decrease in the number of detected of events in APP mice.
- Figure 5.2.7** PV-expressing interneuron immunoreactivity does not change in APP animals within the aTRN.
- Figure 5.2.8** No changes in the coupling of UDS with mPFC spindles.
- Figure 5.2.9** Impaired UDS coupling to CA1 spindles.
- Figure 5.2.10** Unimpaired mPFC to CA1 spindle coupling in APP mice.
- Figure 5.2.11** A statistically significant decrease in the power of ripple events but a trending increase in ripple occurrence in APP mice.
- Figure 5.2.12** A larger proportion of UDS are coupled to ripples without mPFC spindles in APP mice.
- Figure 5.2.13** A larger proportion of ripples occur without mPFC spindles in APP mice.
- Figure 5.2.14** A larger proportion of ripples occur without CA1 spindles in APP mice.
- Figure 5.2.15** No change in the frequency of the three cardinal oscillations occurring together.
- Figure 5.2.16** Greater exploration in APP mice during NOL task.
- Figure 6.2.1** Speed-modulated theta power and frequency in CA1.
- Figure 6.2.2** Speed-modulated theta power and frequency in the mPFC.
- Figure 6.2.3** Speed-modulated low gamma power and frequency in CA1.
- Figure 6.2.4** Speed-modulated high gamma power and frequency in CA1.

- Figure 6.2.5** Speed-modulated low gamma power and frequency in the mPFC.
- Figure 6.2.6** Speed-modulated high gamma power and frequency in the mPFC.
- Figure 6.2.7** Theta-gamma PAC is comparable between APP and WT animals in CA1.
- Figure 6.2.8** Speed-modulated theta coherence between CA1 and the mPFC.
- Figure 6.2.9** Locomotor activity of WT and APP animals in an OF arena.
- Figure 7.1.1** Summary of results: mPFC-hippocampal circuit during SWS.
- Figure 7.1.2** Summary of results: mPFC-hippocampal circuit during exploratory behaviour.

List of tables

Table 2.1.1	Genotype shorthand notation.
Table 2.7.1	List of antibodies used in the present study.
Table 2.7.2	List of viral vectors used in the present study.
Table 2.7.3	List of reagents used in the present study.
Table 2.7.4	List of mice strains used in the present study.
Table 2.7.5	List of the silicon microelectrodes used in the present study.
Table 2.7.6	List of the hardware used in the present study.
Table 2.7.7	List of the software used in the present study.
Table 2.7.8	List of other essential consumables used in the present study.

List of abbreviations

ACC	Anterior cingulate cortex
A β	Amyloid- β
AD	Alzheimer's disease
AICD	Amyloid precursor protein-intracellular domain
AMPA	α -amino-3-hydroxy-5-methyl-4-isoxazolepropionic acid
ANOVA	Analysis of variance
APOE	Apolipoprotein E
APP	Amyloid precursor protein
aTRN	Anterior thalamic reticular nucleus
CA1	Cornu ammonis 1
CA2	Cornu ammonis 2
CA3	Cornu ammonis 3
Ca ²⁺	Calcium
cAMP	Cyclic adenosine monophosphate
CNO	Clozapine N-oxide
CSF	Cerebral spinal fluid
CT	Corticothalamic
dB	Decibels
DC	Direct current
DG	Dentate gyrus
dHPC	Dorsal hippocampus
DiD	1,1'-Dioctadecyl-3,3',3'-Tetramethylindodicarbocyanine Perchlorate
DIO	Double floxed inverse orientation
DREADDS	Designer receptors exclusively activated by designer drugs
dSub	Dorsal subiculum
EC	Entorhinal cortex
ECoG	Electrocorticogram
EEG	Electroencephalogram
E-I	Excitatory-inhibitory
EMG	Electromyogram
EOAD	Early-onset Alzheimer's disease
FAD	Familial Alzheimer's disease

fEPSP	Field excitatory post-synaptic potential
FFT	Fast-fourier transform
fMRI	Functional magnetic resonance imaging
GABA	Gamma aminobutyric acid
GENUS	Gamma entrainment using sensory stimulation
HCN	Hyperpolarisation-activated cation-nonselective
HFO	High frequency oscillation
HPC	Hippocampus
IEG	Immediate early genes
IHC	Immunohistochemistry
IIR	Infinite impulse response
ING	Interneuron network gamma
IPSPs	Inhibitory post-synaptic potentials
ISF	Interstitial fluid
IQR	Inter-quartile ranges
K ⁺	Potassium
KI	Knock-in
IL	Infralimbic cortex
LED	Light-emitting diodes
LFP	Local field potential
LOAD	Late-onset Alzheimer's disease
LTD	Long-term depression
LTM	Long-term memory
LTP	Long-term potentiation
MCI	Mild cognitive impairment
mEC	Medial entorhinal cortex
mEPSP	Miniature excitatory post-synaptic potential
MD	Mediodorsal
mGluR	Metabotropic glutamate receptors
MI	Modulation index
mIPSC	Miniature inhibitory post-synaptic current
mPFC	Medial prefrontal cortex
MS-DBB	Medial septum-diagonal band of Broca
MUA	Multi-unit activity
MVL	Mean vector length

Na ⁺	Sodium
NFT	Neurofibrillary tangles
NMDA	N-methyl-D-aspartate
NOL	Novel object location
NREM	Non-rapid eye movement sleep
NRe	Nucleus reuniens
NPY	Neuropeptide-Y
OF	Open field
OLM	<i>Oriens-lacunosum moleculare</i>
PAC	Phase-amplitude coupling
PB	Phosphate buffer
PBS	Phosphate buffered saline
PBS-T	PBS with 0.3% Triton X-100
PC	Pyramidal cells
PFA	Paraformaldehyde
PGO	Ponto-geniculo-occipital waves
PING	Pyramidal-interneuron network gamma
PL	Prelimbic cortex
PSEN1	Presenilin 1
PSEN2	Presenilin 2
PV	Parvalbumin
REM	Rapid eye movement sleep
ROI	Region of interest
sAPP β	Soluble amyloid precursor protein β
SCn	Suprachiasmatic nucleus
SD	Standard deviation
SEM	Standard error of the mean
SHY	Synaptic homeostasis hypothesis
SPW	Sharp-wave
SST	Somatostatin
STDP	Spike-time-dependant-plasticity
STM	Short-term memory
Str.LM	<i>Stratum lacunosum-moleculare</i>
Str.O	<i>Stratum oriens</i>
Str.P	<i>Stratum pyramidale</i>

Str.R	<i>Stratum radiatum</i>
SWA	Slow wave activity
SWO	Slow wave oscillation
SWR	Sharp-wave ripples
SWS	Slow wave sleep
TA	Temporoammonic
Tau	Hyperphosphorylated microtubule-associate protein tau
TC	Thalamocortical
tDCS	Transcranial direct current stimulation
TREM2	Triggering receptor expressed on myeloid cells 2
TRN	Thalamic reticular nucleus
TTX	Tetrodotoxin
UDS	Up and Down states
V	Volts
WT	Wild-type

1 | Introduction

The communication between the hippocampus and medial prefrontal cortex (mPFC) is pivotal for spatial memory, decision making and the long-term consolidation of our memories during sleep (Jin & Maren, 2015; Sigurdsson & Duvarci, 2015). In this thesis, disruptions to the neuronal oscillations that underlie the cognitive function of this circuit are investigated in a second-generation mouse model of familial Alzheimer's disease (AD). The following introduction will discuss how the different oscillations within this circuit are generated, their functional role, evidence for the circuit's disruption in AD, with particular emphasis on the role that interneurons play, all culminating in the proposed hypotheses for this research.

1.1 | What are neuronal oscillations and what is their purpose?

1.1.1 | The field potential

Neurons use electrical signals to transfer and store information throughout the brain. At any given point in the brain's extracellular space, the cumulative ongoing electrical activity of the surrounding neurons summates to create an electrical potential, measured in Volts (V) (Buzsáki, Anastassiou & Koch, 2012). This field potential can be recorded extracellularly at varying levels of invasiveness; from the scalp using an electroencephalogram (EEG) first described by Hans Berger in 1929 (Buzsáki & Draguhn, 2004), to the cortical surface using the subdural electrocorticogram (ECoG) and intracerebrally, referred to as the local field potential (LFP) (Buzsáki, Anastassiou & Koch, 2012). For decades, scientists have been able to measure extracellular changes in voltage with sub-millisecond precision to record the activity of large populations of neurons and relate it to ongoing cognitive tasks.

1.1.2 | Oscillations

In brain regions such as the cortex and hippocampus (which are the primary focus of this thesis), neurons can be crudely split into one of two groups; excitatory glutamatergic pyramidal cells (PC) that act to excite other neurons and cause them to fire action potentials and GABAergic (gamma aminobutyric acid) inhibitory interneurons, which act to suppress this firing, and silence neurons. The activity of interneurons shapes the firing of PCs, with this interplay of excitation and inhibition creating waves of electrical activity called neuronal oscillations.

Oscillations are grouped into frequency bands, somewhat arbitrarily, ranging from 0.5-500 Hz, with different bands having different roles within cognition (Buzsáki & Draguhn, 2004). Interneurons form a large heterogeneous population that differ in their morphology, intrinsic firing properties, protein expression and the different PC compartments they target. The complexity of interneurons is what helps generate the different frequencies bands (Pelkey *et al.*, 2017).

The coordinated network synchrony produced by neuronal oscillations is thought to facilitate the transfer of information through connected brain regions and provide precise temporal windows for binding neuronal assemblies for information encoding, processing, storage and retrieval (Buzsáki & Draguhn, 2004). Oscillations have been shown to be important in myriad cognitive tasks and for memory related processes such as spike-time-dependant-plasticity (STDP), that is a process involved in the strengthening and weakening of synapses through the precise timing of a neuron's inputs and outputs (Caporale & Dan, 2008; Igarashi, 2015).

1.2 | Sleep

1.2.1 | Sleep stages and sleep state switching

Sleep is a behaviourally conserved process throughout the animal kingdom. As humans, we spend a large proportion of our lives sleeping, with poor sleep associated with impaired cognitive process as well as both obesity and cardiovascular problems (Weber & Dan, 2016). The typical human sleep cycle lasts around 90 minutes and dynamically switches between two distinct states; Non-Rapid Eye Movement (NREM) and Rapid Eye Movement (REM) sleep. These stages can be identified using an EEG to record the changing cortical oscillations, an electromyogram (EMG) to measure skeletal muscle tone and polysomnography that combines these measures along with breathing and heart rate, blood oxygen levels and eye movements (Weber & Dan, 2016; Adamantidis, Gutierrez Herrera & Gent, 2019).

The sleep cycle begins with NREM sleep, which can be further classified into 3 different stages of increasing sleep depth. Stage 1 is the shortest of the stages and occurs as one starts to fall asleep; low amplitude mixed frequency oscillations

are present and some humans can experience myoclonic jerks. In stage 2, sleep begins to deepen and both K-complexes, which are large surface negative deflections in the LFP and spindle oscillations (11-15 Hz) are evident. In stage 3 these oscillations are replaced with high amplitude, low frequency oscillations; the slow wave oscillation (SWO) (0.5-1.25 Hz) and delta oscillations (1.25-4 Hz) with intermittent spindle activity, also known as slow wave sleep (SWS) (Saper *et al.*, 2010; Krishnan *et al.*, 2016; Adamantidis & Lüthi, 2019). The duration of NREM sleep reduces across sleep cycles as well as throughout a human's lifetime. Finally, the sleep cycle finishes with REM sleep, which is distinguishable by the presence of low amplitude, higher frequency oscillations such as theta (5-12 Hz) and gamma (30-120 Hz) as well as ponto-geniculo-occipital (PGO) waves and reduced skeletal muscle tone. The duration of REM sleep increases across sleep cycles and this is when dreams are predominantly experienced (Saper *et al.*, 2010; Adamantidis, Gutierrez Herrera & Gent, 2019). The switching between these different states is under the control of several different circuits involving the basal forebrain, hypothalamus and areas in the brainstem and their cholinergic, monoaminergic, GABAergic and glutamatergic projections (Krishnan *et al.*, 2016; Weber & Dan, 2016; Weber *et al.*, 2018). There are additionally hormonal, circadian and astrocytic components to sleep state switching (Saper *et al.*, 2010; Weber & Dan, 2016; Poskanzer & Yuste, 2016), however this is outside the scope of this thesis.

1.2.2 | NREM Sleep

Memory consists of three processes; encoding, consolidation and retrieval. Strong evidence points towards sleep in being integral to the consolidation process, as evidenced by both the enhancement of sleep improving memory (Plihal & Born, 1997) and sleep disruptions having the converse effect (Nilsson *et al.*, 2005; Heuer, Kohlisch & Klein, 2005). Sleep supports the consolidation of both declarative and procedural memory systems that can be distinguished based on their reliance on the temporal lobe (e.g. hippocampus, perirhinal and entorhinal cortices). Declarative memory includes episodic memory involving the spatial context (where, what, when information) and semantic memory for facts and objects, both of which require the hippocampus. Procedural memories are distributed across multiple regions such as motor and sensory cortices and the

cerebellum for the learning of motor and cognitive skills, for example. Both forms of memory can initially interact during encoding but greater attention has been given to studying declarative memory (Stickgold, 2005; Diekelmann & Born, 2010; Rasch & Born, 2013).

Declarative memories are subject to the widely accepted two-stage memory hypothesis. This hypothesis posits that a memory is initially encoded quickly within hippocampal neural networks and is labile to forgetting and disruption before being slowly integrated within cortical structures for long-term storage through what is called systems consolidation (Diekelmann & Born, 2010; Rasch & Born, 2013). The hippocampus and the mPFC are two brain regions that have been extensively studied in systems consolidation, due to their role in declarative memory encoding and higher-order executive functions, respectively. The mPFC can be split into 3 sub-regions based on its afferents and efferents; the anterior cingulate cortex (ACC), prefrontal cortex (PL) and infralimbic cortex (IL) (Van De Werd *et al.*, 2010; Riga *et al.*, 2014) (**Figure 1.2.1 A–C**). The hippocampus proper can also be sub-divided into the regions dentate gyrus (DG), *cornu ammonis* (CA)3, CA2, and CA1 (**Figure 1.2.1 A, B, D**). Systems consolidation is achieved through the temporal coupling of the 3 cardinal oscillations found within mPFC-hippocampal network; the slow wave oscillation (SWO), spindles and hippocampal sharp-wave ripples (SWR) (Maingret *et al.*, 2016a). This is a multifaceted process for which I will begin by first describing the generation of these different oscillations in this circuit, then their functional interactions, evidence for their role in consolidation and will finish by discussing alternative consolidation theories.

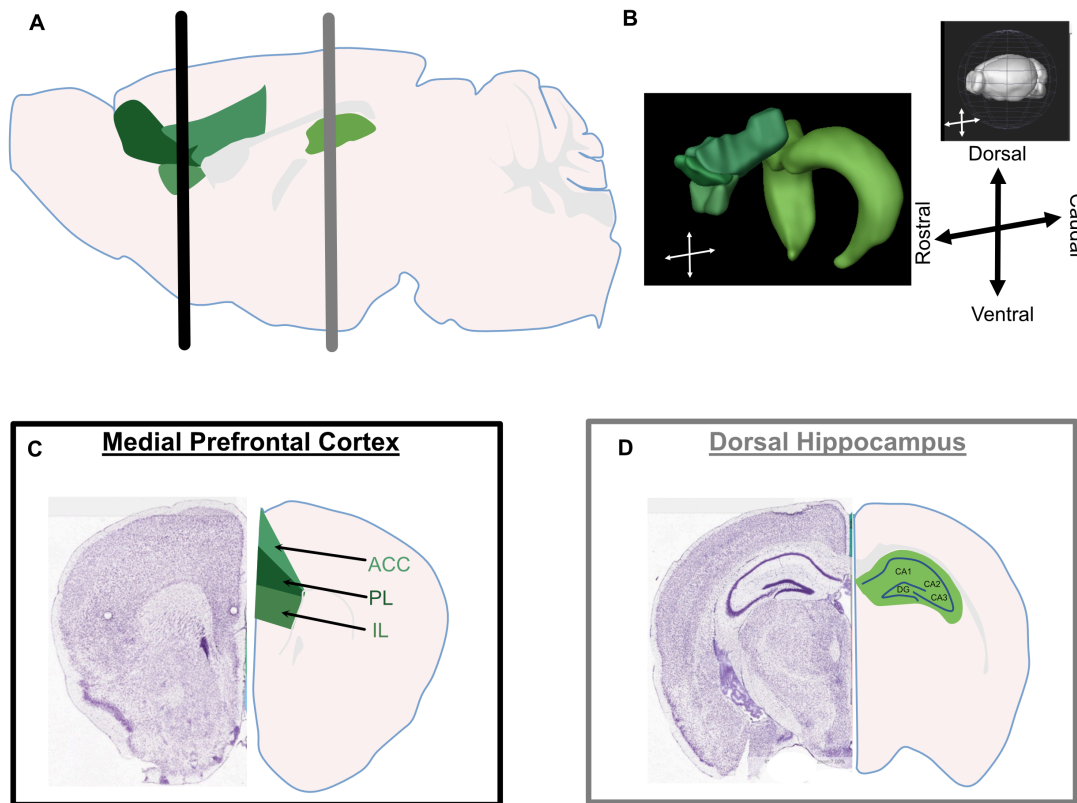


Figure 1.2.1 | Anatomy of the mouse mPFC and dorsal hippocampus. The sub-regions of the mPFC and dorsal hippocampus have been identically colour-coded (shades of green) in each panel. **A** Drawing of a sagittal section of a mouse brain. Sub-regions of the mPFC (rostral) and dorsal hippocampus (caudal) are shaded. The black horizontal line represents the coronal section in panel **C**, the grey line represents panel **D**. **B** 3D image of the mPFC sub-regions and dorsal hippocampus. Top right shows the orientation of the brain in the 3D images. Arrows further highlight orientation. **C** Nissl stain of a coronal brain section (left) with the positions of the mPFC sub-regions highlighted and annotated (right). **D** Nissl stain of a coronal brain section (left) with the dorsal hippocampus and its sub-regions highlighted and annotated (right). 2D images and drawings of the brain adapted from Allen Brain Atlas website (<https://mouse.brain-map.org/>). 3D image taken from the Brain Explorer 2 (<https://mouse.brain-map.org/static/brainexplorer>).

1.2.2.1 | Generation of the slow wave oscillation

Following on from the work of Hans Berger, William Grey Walter was the first to identify delta oscillations using an EEG, with an initial frequency range of 1-4 Hz

(Grey Walter & Wyllie, 1936). Since then, the delta band has widened (0.5-4 Hz) to encompass the thalamocortical SWO (~1 Hz), characterised by Steriade and colleagues in a series of articles in 1993 (Steriade, Nunez & Amzica, 1993a, 1993b; Steriade *et al.*, 1993). There are discrepancies in the literature over the definition of delta oscillations; some speak of broadband delta (0.5-4 Hz) as being one oscillation (Sirota *et al.*, 2003; Maingret *et al.*, 2016a; Varela & Wilson, 2020), however it is important to differentiate delta (1.25-4 Hz) from the SWO (0.5-1.25 Hz) as they both have separate mechanisms of generation (Amzica & Steriade, 1998) and potentially different roles within memory consolidation (Kim, Gulati & Ganguly, 2019). Both can be viewed within the LFP during NREM sleep, but it is the SWO that has shown greater significance within memory consolidation and the mPFC-hippocampal circuit (Diekelmann & Born, 2010).

Using intracellular recordings in anaesthetised cats, Steriade *et al* identified neurons in the cortex that slowly oscillated between being highly depolarised (with action potentials) and long-lasting hyperpolarisations. This pattern was also reflected in the simultaneously-recorded ECoG, with the depolarising, action potential firing phase of these oscillating neurons matching up with negative deflections in the field potential (surface EEG positive) and the long-lasting hyperpolarisations matching with positive deflections (surface EEG negative), now named Up and Down states (UDS), respectively (Steriade, Nunez & Amzica, 1993a) (**Figure 1.2.2 A**). The SWO has since been identified in humans, non-human primates, ferrets and rodents (Neske *et al.*, 2016) and travels as a highly coherent wave across the cortex, moving in an anterior to posterior direction (Ts'o, Gilbert & Wiesel, 1986; Volgushev *et al.*, 2006). It can be generated and studied *ex vivo* (Sanchez-Vives & McCormick, 2000; Timofeev *et al.*, 2000) and *in vivo* under several different types of anaesthesia (Chauvette *et al.*, 2011; Busche *et al.*, 2015; Torao-Angosto *et al.*, 2021) as well in natural sleep (Mölle *et al.*, 2004; Mukovski *et al.*, 2007), with slight differences seen to its frequency and rhythmicity depending on the method used (Chauvette *et al.*, 2011; David *et al.*, 2013; Torao-Angosto *et al.*, 2021).

There are several different mechanisms thought to initiate the Up states of the SWO; through persistently active pacemaker-like neurons, the summation of miniature excitatory post-synaptic potentials (mEPSPs) and through thalamic

input (David *et al.*, 2013; Neske *et al.*, 2016). Multiple lines of evidence point to cortical layer 5 PCs in being instrumental in these processes (Steriade & Amzica, 1996; Chauvette, Volgushev & Timofeev, 2010; Beltramo *et al.*, 2013). However, the contribution of the thalamus has previously been a source of debate. Indeed, thalamocortical (TC) and thalamic reticular nucleus (TRN) neurons also exhibit Up and Down states, with TC neurons exhibiting burst firing prior to the onset of the SWO in the cortex (Steriade *et al.*, 1993; Contreras & Steriade, 1995). Both optogenetic (David *et al.*, 2013; Gent *et al.*, 2018) and electrical (Rigas & Castro-Alamancos, 2007) stimulation of TC neurons can elicit the cortical SWO and the involvement of the thalamus can help explain the strong coherence of the SWO across distant cortical regions (Gent *et al.*, 2018). However, the cortical SWO has shown to be maintained in experiments in which the cortex has been deafferented from the thalamus, prompting debate as to the necessity of the thalamus in generating the SWO (Steriade *et al.*, 1993; Timofeev *et al.*, 2000). On the other hand, in these experiments a significant time lag exists between deafferentation and experimentation, allowing time for compensatory mechanisms to occur. In fact, more recent work found that a more acute deafferentation in similar experiments reduced the frequency of the cortical SWO, impaired SWO coherence across the cortex and in some experiments abolished the SWO altogether (Lemieux *et al.*, 2014). Reverse microdialysis of the Na⁺ channel blocker tetrodotoxin (TTX) into TC cells *in vivo* has additionally been shown to reduce the occurrence of the SWO and affect the duration of both UDS (David *et al.*, 2013). It is therefore clear that the thalamus plays an important role in SWO generation and coordination (Gent *et al.*, 2018).

Additionally, a prominent feature of the SWO is the presence of fast gamma oscillations (30-120 Hz) nested with the SWO Up states (Steriade *et al.*, 1996; Valderrama *et al.*, 2012) (**Figure 1.2.2 B**). Cross-frequency coupling such as this, with the phase of the slower oscillation modulating the amplitude of the faster oscillation, named phase-amplitude coupling (PAC), is important for the integration of information across different spatial and temporal scales (Canolty & Knight, 2010). Gamma oscillations are important for information processing and encoding during awake cognitive tasks (see **section 1.3.2**) (Colgin & Moser, 2010). A theory put forward by Destexhe and colleagues is that Up states are “fragments of wakefulness”, and play a role within memory consolidation during

NREM sleep (Destexhe *et al.*, 2007). Indeed, there are multiple similarities between the SWO Up states and the neuronal patterns of activation, including the presence of gamma oscillations, seen during awake states (Destexhe *et al.*, 2007). It is therefore possible that Up states provide brief time windows in which neurons are kept in a depolarised state conducive to information processing and memory consolidation.

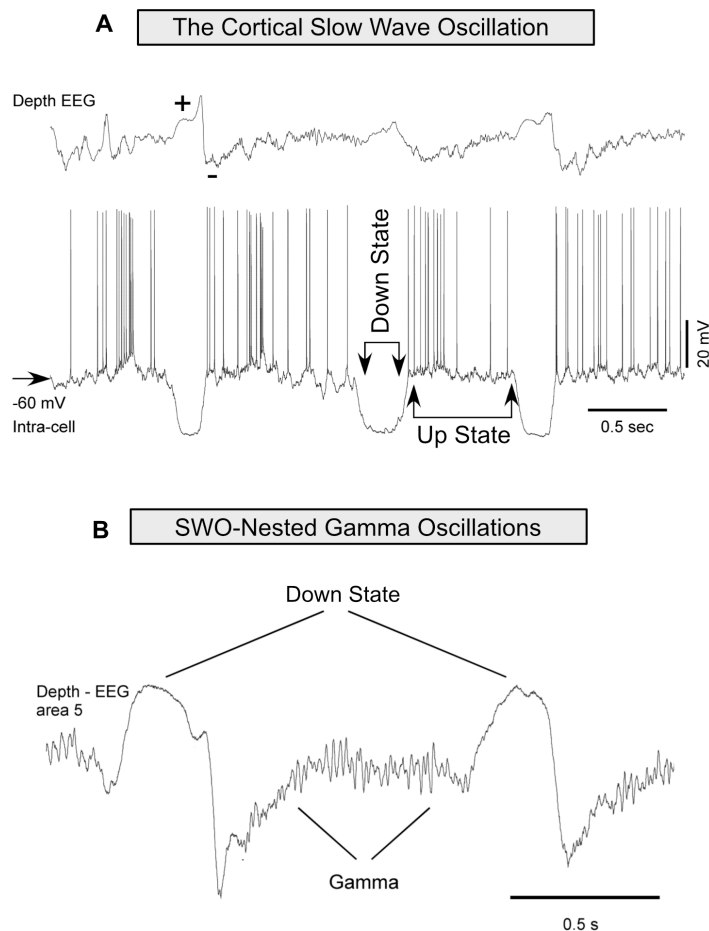


Figure 1.2.2 | The cortical slow wave oscillation. A Example of the SWO as it appears in a depth EEG (top) and a corresponding intracellular recording of a pyramidal cell exhibiting Up and Down states (bottom). **B** Example of a gamma oscillation nested within a cortical SWO Up state. Figure adapted from (Timofeev *et al.*, 2012).

The importance of interneurons within the SWO should also be stated. Interneurons are extremely diverse and can be split based on their morphology, firing patterns, embryonic origin and by the expression of different neuropeptides and Ca^{2+} -binding proteins (Pelkey *et al.*, 2017). Fast-spiking parvalbumin (PV)-

expressing basket cells have shown to play an important role in the maintenance of Up states due to their ability to balance the rapid firing of excitatory neurons (Haider *et al.*, 2006). They target the cell soma and mediate inhibition through the fast-acting GABA_A receptors, that are important in Up state maintenance (Mann, Kohl & Paulsen, 2009; Sanchez-Vives *et al.*, 2010; Pelkey *et al.*, 2017). Not only this, but these cells are well documented in creating gamma oscillations (Mann, Radcliffe & Paulsen, 2005), which are nested within SWO Up states (Steriade *et al.*, 1996; Valderrama *et al.*, 2012).

Additionally, both somatostatin (SST) and neuropeptide-Y (NPY)-expressing interneurons are thought to be involved in the initiation of Down states. Both groups of neurons target the apical dendrites of layer 5 PCs that terminate within layer 1 (Pelkey *et al.*, 2017; Funk *et al.*, 2017). Evidence for layer 5 being involved in the initiation of Up states (Steriade & Amzica, 1996; Beltramo *et al.*, 2013) therefore places these cells in an optimum position for terminating Up states. These interneurons are additionally known to mediate inhibition through a second class of inhibitory receptor; the metabotropic GABA_B receptor (Craig MT, 2014; Urban-Ciecko, Fanselow & Barth, 2015) which has shown to be important in initiating Down states (Mann, Kohl & Paulsen, 2009; Craig *et al.*, 2013). Indeed, layer 1 stimulation within the medial entorhinal cortex can initiate Down states (Mann, Kohl & Paulsen, 2009), a result that was recently discovered to be due to TC projections synapsing onto cortical layer 1 neurogliaform cells (Hay *et al.*, 2021), with both effects blocked by the antagonism of GABA_B receptors. Furthermore, SST-expressing interneurons have been shown to increase their firing and Ca²⁺ signals towards the end of Up states (Fanselow & Connors, 2010; Niethard *et al.*, 2018), with chemogenetic activation of these interneurons enhancing slow wave activity (Funk *et al.*, 2017). NPY itself acts as a neuromodulator, enhancing both inhibitory currents arriving at the post-synaptic membrane, and decreasing excitatory currents (Bacci, Huguenard & Prince, 2002). Despite the large amount of evidence for role that interneurons play in initiating Down states, this view is not widely accepted. Some believe that Down states occur solely due to intrinsic mechanisms and the activation of activity-dependant hyperpolarising currents (Neske *et al.*, 2016). However, Up-to-Down state transitions are extremely synchronous events across the cortex; NPY and SST-expressing interneurons are connected *via* gap junctions (Simon *et al.*,

2005; Volgushev *et al.*, 2006; Fanselow, Richardson & Connors, 2008; Chen *et al.*, 2012), which allows widespread network hyperpolarisation, something intrinsic mechanisms alone could not achieve.

The SWO has additionally been found in hippocampal region CA1 and nests hippocampal spindles and ripples within Up states similar to the cortex (Staresina *et al.*, 2015; Maingret *et al.*, 2016a), as well as displaying PC and interneuron phase-locked firing (Wolansky *et al.*, 2006; Hahn, Sakmann & Mehta, 2006; Isomura *et al.*, 2006). However, unlike cortical PCs, CA1 PCs do not display bimodal membrane potential fluctuations representing UDS (Isomura *et al.*, 2006), a feature that is hypothesised to be due to the lack of PC recurrent excitation in CA1 compared with the cortex (Tukker *et al.*, 2020). The hippocampal SWO and cell spiking occurs at a time lag to the cortical SWO and is believed to be generated through medial entorhinal cortex (mEC) input (Hahn, Sakmann & Mehta, 2006; Wolansky *et al.*, 2006; Isomura *et al.*, 2006; Sirota *et al.*, 2003). Indeed, strong excitatory current sinks can be found within *stratum lacunosum-moleculare* (*Str.LM*) (Wolansky *et al.*, 2006; Isomura *et al.*, 2006), the termination site of mEC layer 3 input *via* the temporoammonic (TA) pathway, with CA1 cell spiking more strongly correlated with the mEC SWO than other cortical regions (Hahn *et al.*, 2012). Additionally, gamma oscillations occurring in *Str.LM* that are generated through the same pathway are also phase locked to hippocampal SWO Up states (Isomura *et al.*, 2006), with similar GABA_A receptor mediation inhibition needed for SWO generation (Xu *et al.*, 2016). The purpose of the hippocampal SWO is not fully understood but is perhaps a way of grouping together cortical and hippocampal neural activity for systems consolidation (see **section 1.2.2.4**).

Finally, the SWO can also be seen within the striatum and cerebellum and is influenced by cholinergic, noradrenergic and serotonergic projections originating from brainstem nuclei (Steriade, Amzica & Nuñez, 1993; Roš *et al.*, 2009; Eschenko *et al.*, 2012; Neske *et al.*, 2016). However, these phenomena are outside the scope of this thesis and so are not discussed further, but are reviewed in (Neske *et al.*, 2016).

1.2.2.2 | Generation of spindles

Sleep spindles, also known as sigma oscillations, are waxing - waning oscillations (11-15 Hz) that typically last between 0.5-2 seconds and are found in both stage 2 and 3 of NREM sleep (Lüthi, 2014) (**Figure 1.2.3 A**). In humans, two distinct spindle events have been identified; slow spindles (~12 Hz) that can be found in more frontal cortices and faster spindles (~14 Hz), found in parietal cortices (Möller *et al.*, 2011; Rasch & Born, 2013). Regardless of type, they are both generated through thalamocortical networks comprising interneurons of the TRN, excitatory TC projections of the thalamic nuclei and reciprocal excitatory corticothalamic (CT) projections. During some of the first recordings of TC cells, inhibitory post-synaptic potentials (IPSPs) were found that occurred in phase with spindles (Rasch & Born, 2013; Contreras & Steriade, 1996) and were later attributed to inputs from the interneurons of the TRN (Fuentelba & Steriade, 2005) (**Figure 1.2.3 B**). The TRN forms a thin envelope around the thalamic nuclei and contains non-overlapping populations of PV- and SST-expressing interneurons that differ both in projection patterns to the different thalamic nuclei across the rostral-caudal extent, and in functional role (Clemente-Perez *et al.*, 2017a; Vantomme *et al.*, 2019). In fact, the IPSPs arriving at TC cells during spindles cease when lesioned from the TRN, indicating that this structure is crucial to spindle generation (Steriade *et al.*, 1985).

During spindle activity, PV-expressing interneurons burst-discharge through the action of T-type Ca^{2+} channels (Clemente-Perez *et al.*, 2017a); channels that are de-inactivated at slightly hyperpolarised membrane potentials. These hyperpolarised membrane potentials are achieved, in part, by the reduced cholinergic tone onto TRN interneurons that occurs during NREM sleep (Saper *et al.*, 2010). Importantly, this hyperpolarisation and subsequent burst-discharging occurs through CT projections to the dendrites of TRN PV-expressing interneurons and is mediated through the fast-acting α -amino-3-hydroxy-5-methyl-4-isoxazolepropionic acid (AMPA) receptors (Fuentelba & Steriade, 2005; Gardner, Hughes & Jones, 2013). Hyperpolarisation through an excitatory pathway is thought to be achieved by second messenger systems that activate GABA_B receptors and inwardly rectifying K^+ channels (Fuentelba, Timofeev & Steriade, 2004). PV-expressing interneurons are therefore pivotal in

the generation of spindles, further shown by optogenetic activation of these cells being sufficient to induce spindle activity (Clemente-Perez *et al.*, 2017a; Latchoumane *et al.*, 2017). The firing of PV-interneurons then propagates along the TRN *via* connexin-36 gap junctions (Cruikshank *et al.*, 2005) which in turn inhibit the TC cells of the thalamic nuclei through both synaptic GABA_A and extra-synaptic GABA_B receptors (Beenhakker & Huguenard, 2009). The burst-firing of the TRN interneurons is sustained through the excitatory, T-type Ca²⁺ channel mediated rebound burst-discharging of TC cells back to TRN interneurons and through the activation of Ca²⁺-dependant small-conductance type 2 K⁺ channels that hyperpolarise the neuron (Lüthi, 2014) (**Figure 1.2.3 C**).

The rebound burst-firing of TC cells also sends excitatory volleys to both interneurons and PCs of the deep layers of prefrontal and sensory cortices that quickly propagate to the superficial layers (Peyrache *et al.*, 2011). This entrainment of larger cortical cell populations likely creates the waxing part of the spindle (Lüthi, 2014). Finally, spindles are terminated through several different synaptic and intrinsic mechanisms. Asynchronous CT firing onto TRN interneurons has shown to be important in terminating the rhythmic burst-discharges (Bonjean *et al.*, 2011; Gardner, Hughes & Jones, 2013) as well as lateral inhibition from neighbouring interneurons (Beenhakker & Huguenard, 2009). Additionally, the increased Ca²⁺ entry in TC cells during burst-discharging activates Ca²⁺-sensitive adenylate cyclases, leading to the synthesis of cyclic adenosine monophosphate (cAMP) which in turn activates hyperpolarisation-activated cation-nonselective (HCN) channels, depolarising the neuron to a point where IPSP-induced burst firing is ceased (Lüthi & McCormick, 1999). This cessation of the reciprocal input back to the TRN along with Ca²⁺ sequestration and the recruitment of Na⁺-dependant-K⁺ channels in TRN interneurons helps terminate the spindle event (Coulon, Budde & Pape, 2012).

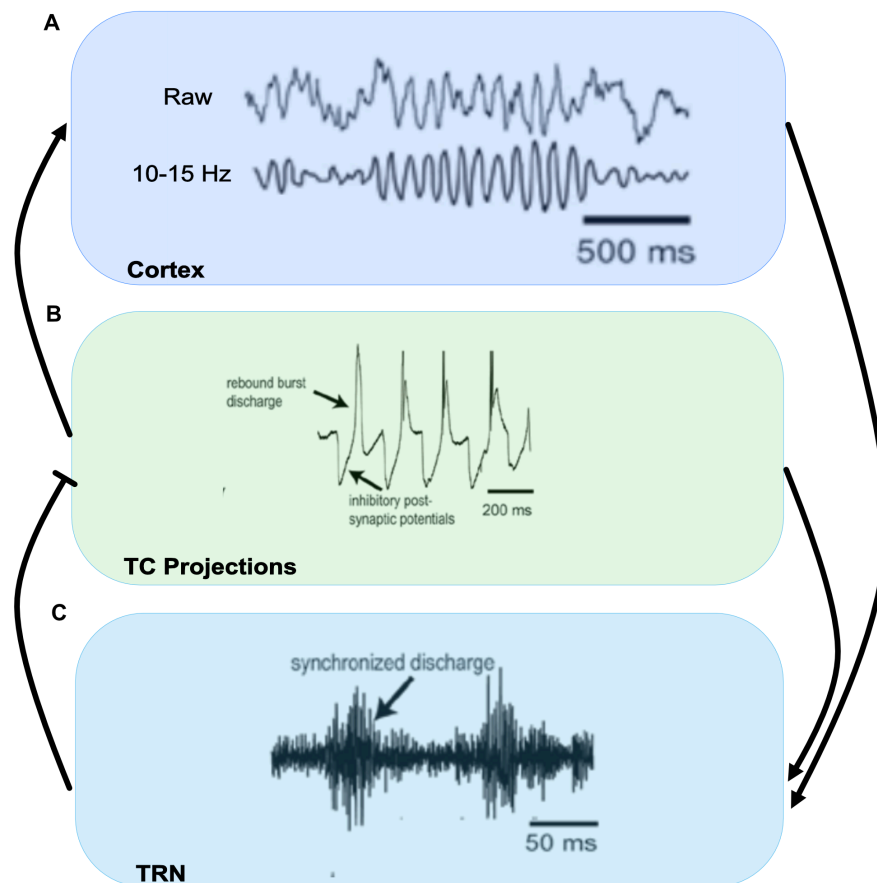


Figure 1.2.3 | Thalamocortical sleep spindle generation. **A** Examples of raw and filtered traces showing a cortical spindle event. **B** IPSP-mediate rebound burst-discharges of a TC neuron during spindle activity. The generated excitatory volleys are then sent to PCs and interneurons in the cortex, denoted by the black arrow going from **B** to **A**. **C** Burst-discharging of TRN interneurons during spindle activity. TRN burst-discharging in turn inhibits TC neurons, causing the IPSP-mediate rebound burst-discharges, denoted by the black bar going from **C** to **B**. TRN burst-discharging is, in part, initiated and terminated through CT input, denoted by the black arrow going from **A** to **C**, and is sustained, in part, through TC projections, denoted by the black arrow going from **B** to **C**. Figure adapted from (Lüthi, 2014).

Although less characterised than neocortical spindles, spindle events can also be identified in the CA1 subfield of the hippocampus during NREM sleep in both humans (Staresina *et al.*, 2015; Ngo, Fell & Staresina, 2020) and rodents (Sullivan *et al.*, 2014; Latchoumane *et al.*, 2017). Hippocampal spindles are thought to be created by similar mechanisms to neocortical spindles, as the optogenetic stimulation of TRN PV-expressing interneurons can elicit spindles in

both regions (Latchoumane *et al.*, 2017). However, it is unclear how spindles reach the hippocampus. Strong current sinks are seen within CA1 *Str.LM* during spindle activity (Sullivan *et al.*, 2014), implicating two possible pathways; thalamic nucleus reuniens (NRe) input to *Str.LM* or *via* the mEC. I believe that a stronger case can be made for mEC input. Hippocampal spindles show strong coherence with those found in the mEC (Sullivan *et al.*, 2014) and, similar to neocortical spindles, are found nested within the hippocampal SWO (Staresina *et al.*, 2015), which, as discussed previously, reaches the hippocampus through the mEC. Additionally, the NRe has shown to synapse onto neurogliaform interneurons located in *Str.LM* (Chittajallu *et al.*, 2017), potentially negating the possibility of creating the strong excitatory current sinks located in *Str.LM* that are associated with spindles. What is not clear is how the mEC receives this information to send to the hippocampus. It is possible that the mEC receives information through NRe input, as this brain region has been shown to be critical in mPFC – hippocampal communication (Contreras *et al.*, 1996; Dolleman-Van Der Weel *et al.*, 2019).

1.2.2.3 | Generation of sharp-wave ripples

Sharp-waves (SPW) and associated ripples (SWR) can be seen in the hippocampus during NREM sleep, immobility and consummatory behaviours such as eating and drinking (Buzsáki, Lai-Wo S. & Vanderwolf, 1983; Buzsáki, 1986), and are known to play an important role in memory consolidation (Sawangjit *et al.*, 2018) (see **section 1.2.2.4**). They have been identified in humans, non-human primates and rodents, both *ex vivo* and *in vivo* and there is evidence for them also occurring within the wider hippocampal formation (Adamantidis, Gutierrez Herrera & Gent, 2019). SPWs are irregularly occurring events that are created through the synchronous bursting of CA3 PCs synapsing onto the apical dendrites of CA1 PCs through the Schaffer collateral pathway (Ylinen *et al.*, 1995; Csicsvari *et al.*, 2000) (**Figure 1.2.4 A**). This therefore creates large amplitude, negative deflections (40-100 ms duration) viewed in the LFP of *stratum radiatum* (*Str.R*) (sink) and upwards deflections in *stratum pyramidale* (*Str.P*) (source) (Ylinen *et al.*, 1995). These SPWs are associated with, but do not always cooccur with ripple oscillations (130-250 Hz) in *Str.P* (Buzsaki *et al.*, 1992; Buzsáki, 2015) (**Figure 1.2.4 B**).

Ripples are one of the most synchronous oscillatory events in the brain and require a delicate balance between excitation and inhibition, mediated through the firing of CA1 PCs and PV-expressing basket cells (Ylinen *et al.*, 1995; Klausberger *et al.*, 2003; Schlingloff *et al.*, 2014). *Oriens-lacunosum moleculare* (OLM) and axo-axonic interneurons have additionally shown to fire prior to ripples onset but are not necessary for ripple generation (Klausberger *et al.*, 2003; Pangalos *et al.*, 2013). CA1 PCs fire first in the trough of the ripple cycle (Buzsáki *et al.*, 1992; Ylinen *et al.*, 1995; Schlingloff *et al.*, 2014; Stark *et al.*, 2014) and basket cells follow (Schlingloff *et al.*, 2014; Stark *et al.*, 2014). Very few PCs are required for the generation of ripples (Stark *et al.*, 2014) and they fire in a similar sequence seen during initial encoding of experience (Nádasy *et al.*, 1999; Foster & Wilson, 2006; Diba & Buzsáki, 2007), giving these oscillations their proposed role in “replaying” information for sequential long-term consolidation (see **section 1.2.2.4**).

PCs have been described as a “precondition” and basket cells as “necessary condition” for ripple generation (Stark *et al.*, 2014). Indeed, optogenetic depolarisation of PCs in CA1 is enough to initiate ripple events that can be blocked by either increasing inhibitory tone onto the PCs (Stark *et al.*, 2014) or through chemogenetic hyperpolarisation of the neuron (Ognjanovski *et al.*, 2017). While the optogenetic inhibition of CA1 PV-expressing basket cells has no effect upon ripple occurrence (Gan *et al.*, 2017; Xia *et al.*, 2017). However, CA1 PV-expressing basket cells are highly phase-locked to the ripple oscillation (Klausberger *et al.*, 2003; Gan *et al.*, 2017) with their optogenetic inhibition impairing the spike-timing of both basket cells and PCs to the ripple as well as disrupting ripple dynamics (Gan *et al.*, 2017; Ognjanovski *et al.*, 2017). Basket cells are reciprocally connected (Fukuda & Kosaka, 2000) and it is this interneuron-interneuron interaction that is thought to be the pacemaker of the oscillation (Stark *et al.*, 2014; Schlingloff *et al.*, 2014).

CA1 SWRs are generated through excitatory CA3 input (Ylinen *et al.*, 1995; Csicsvari *et al.*, 2000; Nakashiba *et al.*, 2009). Excitatory drive from CA3 to CA1 during SWRs occurs through the recruitment of only a few CA3 PCs. It is these neurons that are thought to participate in routing information from CA3 to CA1 during SWRs (Buzsáki, 1986; Csicsvari *et al.*, 2000; Ylinen *et al.*, 1995) for

sequential dissemination to cortical structures for long-term storage (see **section 1.2.2.4**) (**Figure 1.2.4 A**). They are selectively ‘chosen’ through the action of basket cells (Schlingloff *et al.*, 2014); at the start of a SPW, CA3 PCs show a brief hyperpolarising current followed by a strong excitatory rebound (Ellender *et al.*, 2010). Additionally, in contrast to CA1, ripples can be generated in CA3 through optogenetic activation of PV-expressing interneurons (Schlingloff *et al.*, 2014). What initiates CA3 SWR activity is still unknown, but given their strong temporal communication with the cortical SWO (Mölle *et al.*, 2006) and that the SWO can also be detected in the hippocampus (Wolansky *et al.*, 2006), a case can be made for a cortical influence.

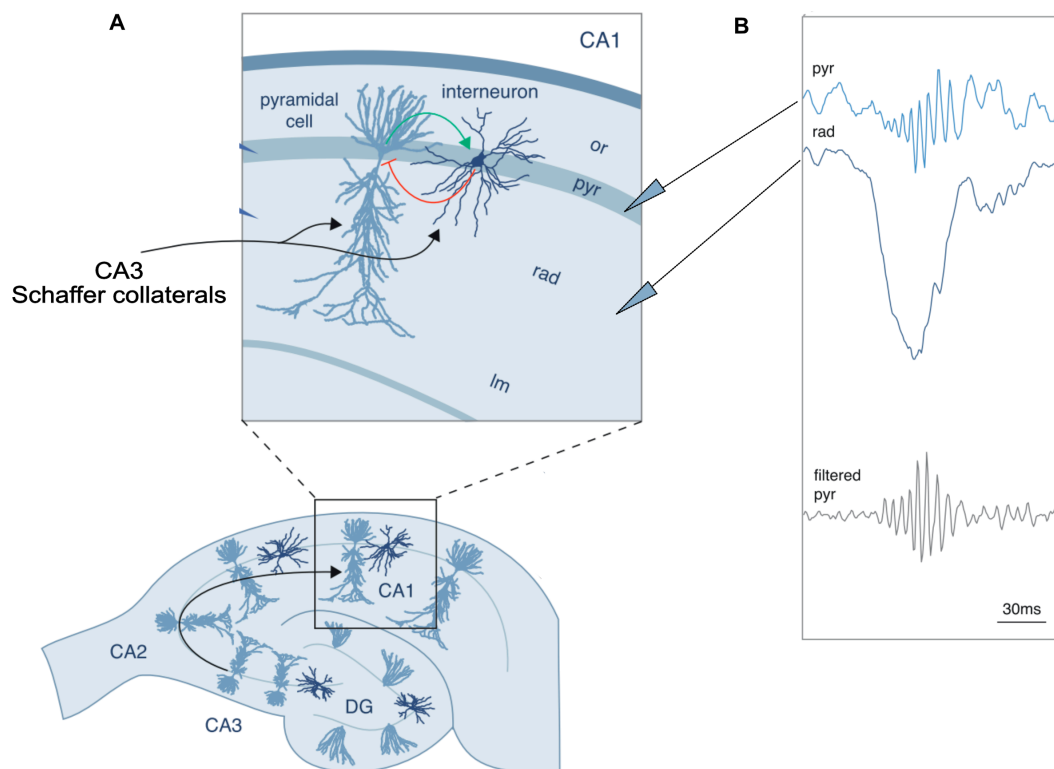


Figure 1.2.4 | Generation of hippocampal sharp-wave ripples. **A** The image below depicts the anatomy of the hippocampus, with the arrow highlighting the Schaffer collateral pathway. The expanded image above more specifically illustrates the excitatory projections of Schaffer collateral efferents synapsing onto the dendrites of CA1 PCs and interneurons. **B** These excitatory inputs generate a sharp-wave, viewed in *Str.R*, and an associated ripple oscillation, viewed in *Str.P*. Figure adapted from (Girardeau & Zugaro, 2011).

1.2.2.4 | The mPFC-hippocampal circuit and its role within systems consolidation

During NREM sleep the SWO, spindles and SWRs within the mPFC-hippocampal circuit have been shown to be important for systems consolidation, both individually and through their temporal communication. Evidence from both humans and rodents show that declarative memory tasks such as word-pair and odour-reward learning enhance slow wave activity (SWA) by increasing the size and duration of the SWO UDS (Möller *et al.*, 2009) and well as the coherence of the SWO across cortical regions (Möller *et al.*, 2004). Indeed, potentiating the SWO using transcranial direct current stimulation (tDCS) can enhance SWA and improve performance in declarative memory tasks in both humans (Marshall *et al.*, 2006; Westerberg *et al.*, 2015) and rodents (Binder *et al.*, 2014). The SWO can achieve this memory-enhancing effect both alone and through the coupling of faster oscillations. Stimulating TC neurons at the neuronal firing frequency of the SWO can induce long-term potentiation (LTP) within post-synaptic neurons (Chauvette, Seigneur & Timofeev, 2012), with gamma oscillations nested within SWO Up states being able to induce plasticity-related changes (Igarashi, 2015). Additionally, the SWO provides a temporal framework for the nesting of spindles and ripples within its Up states (Möller *et al.*, 2006) (**Figure 1.2.5 B**). Moreover, during post-encoding sleep and tDCS-induced SWA, the power and nesting of both spindles and SWRs increases (Möller *et al.*, 2009), indicating the importance of cardinal oscillator coupling for systems consolidation.

Both the power and number of spindles increase during post-encoding sleep of declarative memory tasks in humans and rodents, with a positive linear relationship existing between the number of spindle events and memory performance (Möller *et al.*, 2004; Marshall *et al.*, 2006; Möller *et al.*, 2009). In stage 3 NREM sleep, spindles are found nested within the beginning of SWO Up states (Contreras & Steriade, 1996; Möller *et al.*, 2002, 2006) (**Figure 1.2.5 A-B**). Both spindles and Up states are initiated by similar TC feedback loops (Peyrache *et al.*, 2011; David *et al.*, 2013; Gent *et al.*, 2018), perhaps explaining the precise timing of spindles at the start of Up states. In fact, the optogenetic activation of TRN PV-expressing interneurons at spindle frequency can generate both cortical spindles and Up states (Latchoumane *et al.*, 2017). TC cells receive strong

inhibitory currents from the TRN that cause them to fire rebound-burst spikes and generate Up states (Steriade *et al.*, 1993; Contreras & Steriade, 1995) and spindles (Peyrache *et al.*, 2011). A necessary requirement for the generation of spindles and TRN-mediated inhibition is CT input (Fuentealba & Steriade, 2005; Gardner, Hughes & Jones, 2013). It can therefore be postulated that shortly after Up states are initiated, the returned excitatory CT volleys to the TRN acts as a signal for the initiation of spindles.

Spindles reach the mPFC through mediodorsal (MD) thalamic input (Delevich *et al.*, 2015; Varela & Wilson, 2020) (**Figure 1.2.5 C**). Fast-spiking PV-expressing interneurons and PCs in the mPFC increase their firing rates during spindles, which are phase-locked to the spindle oscillation (Hartwich, Pollak & Klausberger, 2009; Peyrache *et al.*, 2011), with PC firing rate found to induce LTP (Rosanova & Ulrich, 2005). Additionally, it is thought that TC input during spindles selectively 'picks' which neurons are to be involved in systems consolidation (Ribeiro *et al.*, 2007). PCs increase their intracellular Ca^{2+} during spindle activity that is thought to prime the neuron for plasticity related changes (Niethard *et al.*, 2018), with PV-expressing interneurons targeting the soma to preserve Ca^{2+} levels within the dendrites, ready for information to be transmitted from the hippocampus during SWRs (Sjöström *et al.*, 2008; Delevich *et al.*, 2015).

SWRs occur shortly after spindles and are found nested in the SWO just before the Up-Down transition (Mölle *et al.*, 2006) (**Figure 1.2.5 A-B**). Ripples are thought to "replay our experiences", as evidenced by studies that found that the order of neuronal spiking of place cells repeats itself during a ripple event (Wilson M, 1994; Nádasdy *et al.*, 1999; Foster & Wilson, 2006; Diba & Buzsáki, 2007). Indeed, blocking the generation of ripples impairs both hippocampal (Girardeau *et al.*, 2009) and non-hippocampal memories (Sawangjit *et al.*, 2018). This "replay" of prior encoded information is transmitted to the mPFC, most likely through dorsal subiculum (Nitzan *et al.*, 2020), with multi-unit activity (MUA) within all 3 sub-regions of the mPFC time-locking to the hippocampal ripple event (Wierzynski *et al.*, 2009a; Dong, Wang & Ikemoto, 2016). During ripples, these excitatory projections synapse on to the dendrites of PCs that have been primed with increased intracellular Ca^{2+} during spindles and this is where plasticity related changes occur (Sjöström *et al.*, 2008). High frequency oscillations such

as ripples are the optimum frequency for inducing LTP of synapses and the inhibitory currents that shape the firing of PCs make ripples conducive for spike-time dependant plasticity (Buzsáki, Haas & Anderson, 1987; King *et al.*, 1999). It is this coupling between spindles and ripples that is thought to be the driver of systems consolidation (Siapas & Wilson, 1998; Clemens *et al.*, 2007; Xia *et al.*, 2017) with an increase in spindle-ripple coupling being observed during post-learning sleep of hippocampal-dependant memory tasks (Mölle *et al.*, 2009). It is then after the ripple event that the SWO Down state occurs and the cycle repeats itself (Mölle *et al.*, 2006) (**Figure 1.2.5 B**).

An open question is how the hippocampus initiates SWRs that are time-locked to both the cortical SWO and spindles. One theory is that spindles play a role in this signalling process (Latchoumane *et al.*, 2017). Indeed, coupling between mPFC and hippocampal spindles is found to occur during SWRs, with spindles in the mPFC occurring first and ripples being nested with the hippocampal spindle troughs (Latchoumane *et al.*, 2017; Ngo, Fell & Staresina, 2020). Additionally, optogenetic activation of PV-expressing interneurons within the TRN at spindle frequency can create hippocampal spindle-ripple coupling, providing strong evidence for the role of spindles in this signalling process (Latchoumane *et al.*, 2017). However, as discussed in **section 1.2.2.2**, strong excitatory current sinks seen in CA1 *Str.LM* during spindles (Sullivan *et al.*, 2014) indicate direct mEC input (**Figure 1.2.5 C**). SWRs are generated though the Schaffer-collateral pathway, therefore mEC input generating spindles bypasses this circuit, negating the possibility that CA1 spindles initiate ripples. Whether spindles are also seen in CA3 however remains to be seen.

A second theory is that the SWO initiates SWRs. Similar to the cortical SWO, the CA1 SWO nests spindles and ripples within its Up states (Ngo, Fell & Staresina, 2020). As discussed in **section 1.2.2.1**, the SWO most likely reaches CA1 through the mEC, as evidenced by the strong excitatory current sinks within *Str.LM* (Isomura *et al.*, 2006). Similar to spindles, this bypasses the Schaffer-collateral pathway. However, PCs within the DG and CA3 exhibit time-locked firing to the cortical SWO (Hahn, Sakmann & Mehta, 2007) and receive mEC input through the perforant pathway, suggesting that it is the SWO that modulates hippocampal activity and provides this precise temporal framework to facilitate

systems consolidation. This is further backed-up by a computational study that found mEC input to CA3 during the SWO generated CA1 SWRs (Taxidis *et al.*, 2013). Evidence for the TRN optogenetically-evoked hippocampal spindle-ripple complexes can potentially be explained by thalamic NRe input to mEC (Dolleman-van der Weel, Lopes da Silva & Witter, 2017; Hauer, Pagliardini & Dickson, 2019) generating Up states similar to the mPFC, although this has not been directly tested (Latchoumane *et al.*, 2017) (**Figure 1.2.5 C**). The role of hippocampal spindles therefore still remains unknown. One yet untested hypothesis is that they play a similar role to cortical spindles in synaptic plasticity.

Taken together, a circuit is created that begins with thalamic induction of mPFC Up states, recurrent CT excitatory feedback initiating spindles, propagation of the SWO through the NRe to the mEC (Dolleman-van der Weel, Lopes da Silva & Witter, 2017; Hauer, Pagliardini & Dickson, 2019; Varela & Wilson, 2020) and on to CA3, initiating SWRs within CA1 and the “replay” of experience-induced neuronal activity, with information being sent to the mPFC for long-term consolidation before a Down state occurs (**Figure 1.2.5 A-C**).

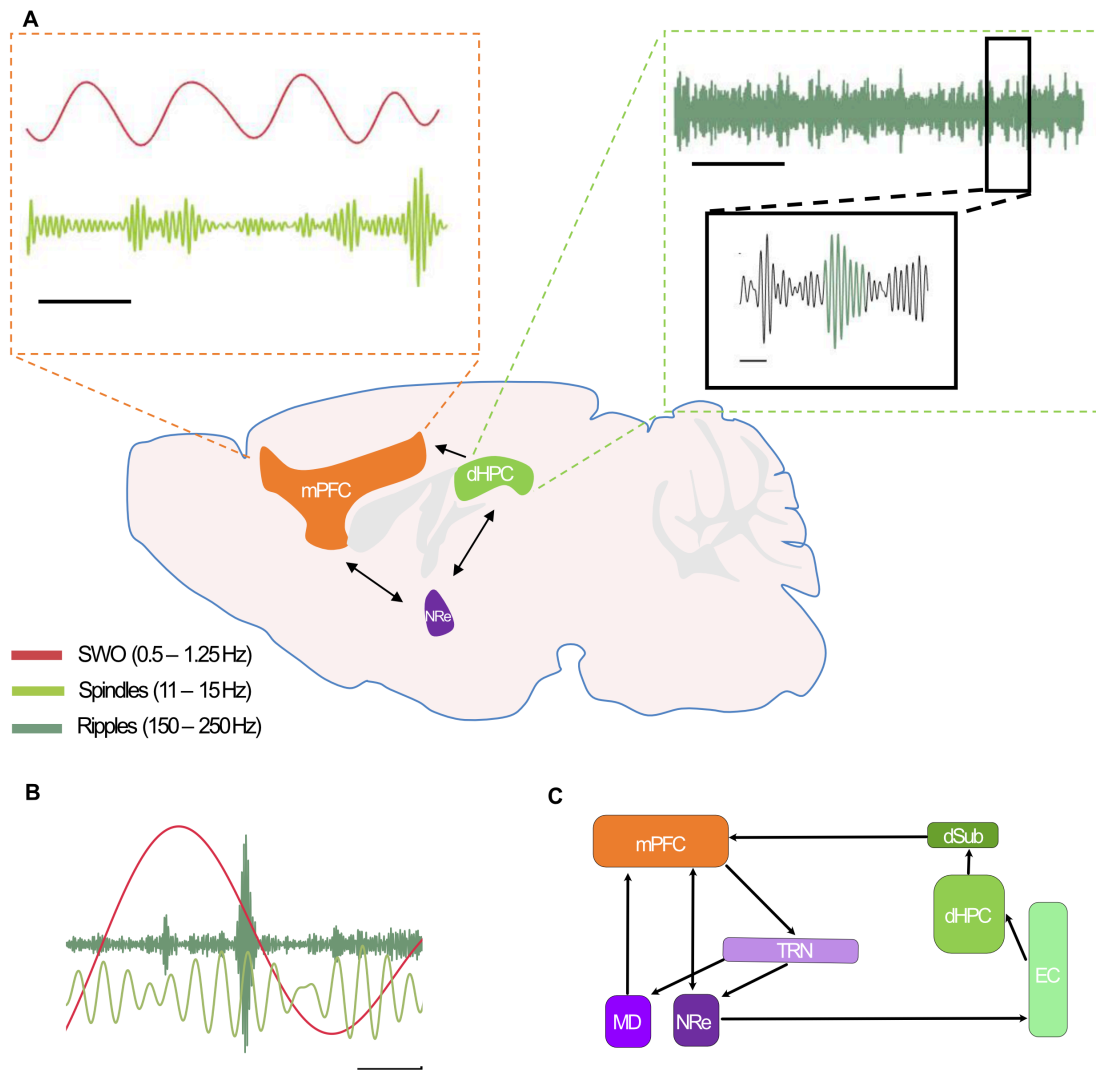


Figure 1.2.5 | The mPFC-hippocampal circuit during systems consolidation. **A** Overview of the circuit during systems consolidation. The SWO in the mPFC nests cortical spindles and hippocampal SWRs. Brain regions thought to communicate through the NRe. Scale bar: 1 s. **B** An example of all 3 cardinal oscillations and their temporal coupling during systems consolidation. Scale bar: 400 ms. **C** Schematic depicts the circuitry underlying systems consolidation as it currently stands in the literature, that is described in this chapter. Arrows point in the direction of information flow. Note, the schematic is not a full representation of the anatomical connections of this circuit, as some regions are interconnected, but highlights the direction of the flow of information during systems consolidation. Drawing of the brain is traced from an image found on the Allen Brain Atlas website (<https://mouse.brain-map.org/>). Example oscillations are taken from experiments conducted in **sections 4 and 5**. mPFC = medial prefrontal cortex, MD = mediodorsal

thalamus, NRe = nucleus reuniens, TRN = thalamic reticular nucleus, dHPC = dorsal hippocampus, dSub = dorsal subiculum, EC = entorhinal cortex.

1.2.2.5 | Alternate theories to systems consolidation

An opposing view to systems consolidation is one in which the SWO actively downscaling synapses rather than potentiates them, called the synaptic homeostasis hypothesis (SHY) (Tononi & Cirelli, 2006; Diekelmann & Born, 2010). This hypothesis proposes that synapses that are weakly potentiated during encoding are actively downscaled, whereas strongly potentiated synapses are spared, increasing the signal:noise ratio (Tononi & Cirelli, 2006; Rasch & Born, 2013). Indeed, the frequency of the SWO (1 Hz) favours long-term depression (LTD) (Kemp & Bashir, 2001). However, stimulating thalamocortical networks at the neuronal firing frequency found during the SWO induces LTP (Chauvette, Seigneur & Timofeev, 2012) and the presence of both spindles and ripples also supports synaptic potentiation (Buzsáki, Haas & Anderson, 1987; King *et al.*, 1999; Rosanova & Ulrich, 2005). Additionally, the SHY hypothesis doesn't account for the sleep associated increase in plasticity related immediate early genes (IEG) (Seibt *et al.*, 2012). However, although there is greater evidence for systems consolidation over synaptic downscaling, the two may not be mutually exclusive (Tononi & Cirelli, 2006; González-Rueda *et al.*, 2018).

1.2.3 | REM sleep

REM sleep follows NREM and is identified by the presence of rapid eye movements, skeletal muscle atonia, both theta (5-12 Hz) and gamma (30-120 Hz) oscillations in thalamocortical, hippocampal and amygdalar circuits as well as PGO waves arising from the brainstem (Diekelmann & Born, 2010; Rasch & Born, 2013). Like NREM sleep, there is evidence for REM sleep playing a role in the consolidation of both declarative (Boyce *et al.*, 2016) and procedural memories (Rasch & Born, 2013). Whereas NREM sleep has been identified as important for the reorganisation of memories within cortical networks and systems consolidation, REM sleep appears to have a sequential role in synaptic consolidation and the strengthening of newly formed synapses (Diekelmann & Born, 2010). During REM sleep, synapses associated with prior learning are pruned and maintained (Li *et al.*, 2017) and there is an upregulation of plasticity-

related IEGs (Ribeiro *et al.*, 2002, 2007; Seibt *et al.*, 2012) that is dependent on the increase cholinergic tone found during REM sleep (Teber *et al.*, 2004; Diekelmann & Born, 2010). Furthermore, a link has also been found between the amplitude of cortical sleep spindles during NREM sleep and the expression of IEGs during REM sleep, suggesting that spindles prime the relevant synapses involved in systems consolidation for subsequent synaptic consolidation (Ribeiro *et al.*, 2007). Collectively, this points towards complementary roles of NREM and REM sleep in memory consolidation.

1.3 | Awake oscillations

1.3.1 | Theta oscillation generation and function

The hippocampus plays crucial roles in episodic memory and spatial navigation and integrates spatial and non-spatial information arising from multiple brain regions (Drieu & Zugaro, 2019). In the rodent hippocampus, the theta oscillation dominates during both awake behaviour and REM sleep and spans a range of frequencies from 4-12 Hz (Buzsáki, 2002) (**Figure 1.3.1 B, C**). In humans, however, an identical theta oscillation has not been found, instead delta (1-4 Hz) and alpha (8-12 Hz) oscillations are present that are more transient, with the latter encompassing the higher bounds of rodent theta (Buzsáki, Logothetis & Singer, 2013; Lever *et al.*, 2014). Two different forms of rodent hippocampal theta exist; type I that is atropine-resistant (resistant to muscarinic acetylcholine receptor antagonists) and found during locomotion and type II, that is atropine-sensitive and more prominent during immobility and under different types of anaesthesia (Buzsáki, 2002).

The medial septum-diagonal band of Broca (MS-DBB) and its cholinergic, glutamatergic and GABAergic projections are crucial in theta generation, with lesions to this area impairing theta (Buzsáki, 2002) as well as spatial navigation (Brioni *et al.*, 1990). Cholinergic inputs synapsing on *Str.LM* of CA1 have a modulatory role in theta generation, as their optogenetic activation can increase theta power but exert no effect upon frequency (Vandecasteele *et al.*, 2014). Instead, it is inhibition from MS-DBB GABAergic projections synapsing onto CA1 interneurons that generates the theta oscillation (Freund & Antal, 1988; Simon *et al.*, 2006; Hangya *et al.*, 2009). Several different interneuron subtypes have been

shown to fire preferentially at different phases of the theta cycle; SST-expressing OLM cells and PV-expressing axo-axonic and basket cells (Klausberger *et al.*, 2003). Indeed, the optogenetic inactivation of PV-expressing interneurons can prevent the creation of theta and conversely their activation generates theta, with PC firing closely following (Amilhon *et al.*, 2015). The glutamatergic projections play a role in locomotion velocity, and the increase in CA1 theta power and frequency that accompanies increased locomotion velocity (McFarland, Teitelbaum & Hedges, 1975; Fuhrmann *et al.*, 2015). Additionally, multiple CA1 theta rhythm generators have been identified that also receive input from the MS-DBB, such as mEC and CA3, that preferentially couple to CA1 theta during memory encoding and retrieval, respectively (Buzsáki, 2002; Zhang *et al.*, 2019; López-Madrona *et al.*, 2020).

One of the roles of theta is to bind anatomically-connected brain regions for information processing and transfer, achieved by its slow frequency facilitating long conduction delays (Colgin & Moser, 2010). This coupling is behaviour-dependant, for example, coupling between the hippocampus and mEC facilitates episodic and spatial memory (Colgin & Moser, 2010) whereas hippocampal coupling to the amygdala is important for emotional memory (Seidenbecher *et al.*, 2003). Theta coherence between CA1 and the mPFC has also been shown to be important for the integration of spatial information with executive decision making (Jones & Wilson, 2005), with theta coherence increasing when mice reach a choice point in a Y-maze task (Liu *et al.*, 2018). This coherence is led by the hippocampus, with mPFC unit spiking phase-locked to the hippocampal theta oscillation, signalling a transfer of spatial information from the hippocampus to the mPFC for executive control (Jones & Wilson, 2005; Liu *et al.*, 2018). Theta coherence and spike phase-locking between these regions is reduced when animals make an error in these choice trials (Jones & Wilson, 2005), further demonstrating their role in spatial working memory. Finally, another function of the theta oscillation is to help bind neuronal firing into distinct cell assemblies, providing temporal windows for STDP and segregating information to prevent interference (Buzsáki, 2002). This is, in part, aided by a second oscillation: gamma.

1.3.2 | Gamma oscillation generation and function

Gamma oscillations group the firing of neurons into distinct cell assemblies with temporal precision, for the encoding and retrieval of information (Colgin & Moser, 2010; Buzsaki & Wang, 2012). Gamma oscillations are thought to be important in working memory (Lisman, 2010) and can be found throughout the cortex and hippocampal formation (Chrobak & Buzsáki, 1998; Sirota *et al.*, 2008; Colgin & Moser, 2010). Three different gamma oscillation frequency bands exist; slow (30-50 Hz), mid (50-90 Hz) and high/epsilon (90-150 Hz) (Tort *et al.*, 2008; Belluscio *et al.*, 2012), with the latter also named a high frequency oscillation (HFO) (Tort *et al.*, 2013). Within hippocampal region CA1, the frequency bands are created through different gamma oscillation generators, although an intrinsic CA1 gamma oscillation has been identified *ex vivo* (Craig & McBain, 2015). Slow gamma displays strong excitatory current sinks within *Str.R*, the termination site of the Schaffer-collateral pathway, and is highly coherent with CA3 slow gamma, whereas mid gamma is generated through mEC layer 3 input synapsing onto *Str.LM* via the TA pathway, with mid gamma being highly coherent between these regions (Colgin *et al.*, 2009; Colgin & Moser, 2010) (**Figure 1.3.1 A-C**). Both oscillations are thought to have different functions; slow gamma is thought to play a role in memory retrieval whereas mid gamma is important in memory encoding (Colgin *et al.*, 2009). HFO can be found both within the cortex and hippocampus, with strong excitatory current sinks found in the superficial *stratum oriens* (*Str.O*) layer of CA1. A lot less is known about these oscillations but it is thought that they too play a role in memory processing (Tort *et al.*, 2008, 2013).

There are two different models of gamma oscillation generation; through the reciprocal activation of interneurons (interneuron network gamma, or ING model) or through connected interneurons and PCs (pyramidal-interneuron network gamma, or PING model)(Whittington *et al.*, 2000). In the first model, PC firing is temporally-modulated by interneurons without playing a role in synchronisation and in the second, the activation of interneurons by PCs causes feedback inhibition, recruiting and inhibiting neurons into ensembles (Mann, Radcliffe & Paulsen, 2005). In both models, PV-expressing interneurons are crucial for gamma generation and pace the activity of PCs (Mann, Radcliffe & Paulsen, 2005; Sohal *et al.*, 2009b). The spiking of perisomatic-targeting interneurons is

phase-locked to the gamma oscillation, such as fast-spiking basket cells and axo-axonic cells (Hájos *et al.*, 2004; Mann, Radcliffe & Paulsen, 2005; Hájos & Paulsen, 2009; Craig & McBain, 2015) and to a lesser extent, SST-expressing, dendritic targeting interneurons such as OLM cells (Hájos *et al.*, 2004; Mann, Radcliffe & Paulsen, 2005). Recently, it was found that the optogenetic inhibition of SST-expressing interneurons could reduce the power of the slow gamma oscillation *ex vivo*, with their optogenetic activation being able to induce gamma (Antonoudiou *et al.*, 2020).

1.3.3 | Theta-gamma coupling

Phase-amplitude coupling (PAC) is the most well studied mode of cross-frequency coupling in which the phase of a slower oscillation modulates the amplitude of a faster oscillation (Canolty & Knight, 2010). Theta-gamma PAC has been identified across the hippocampal formation and neocortex in both rodents and humans and is a phenomenon that binds the firing of neurons across spatial and temporal scales for information transfer and processing (Lisman & Jensen, 2013). While theta oscillations route information flow and bind neuronal ensembles, the frequency of gamma oscillations, particularly mid gamma, makes them ideally suited for encoding information and STDP (Igarashi, 2015).

Multiple synaptic pathways converge onto hippocampal CA1, such as the mEC and CA3 that generate both theta (Buzsáki, 2002) as well as mid and low gamma oscillations (Scheffer-Teixeira *et al.*, 2012), respectively (**Figure 1.3.1 A**). Different gamma oscillations couple to different phases of the theta cycle and contribute to different aspects of cognition (Tort *et al.*, 2008; Scheffer-Teixeira *et al.*, 2012; Amemiya & Redish, 2018; Lopes-dos-Santos *et al.*, 2018) (**Figure 1.3.1 A-D**). Recently, this discovery was updated; not only do CA3 and the mEC create different frequencies of gamma oscillation, but also different theta frameworks that couple preferentially to their respective gamma oscillation (Zhang *et al.*, 2019). Gamma oscillations were additionally shown to precede the onset of PAC, with higher PAC corresponding to stronger theta coupling between regions, suggesting it is the local gamma oscillations that initiate theta coherence between regions, for routing information flow (López-Madróna *et al.*, 2020). These different frameworks allow information to be segregated, preventing interference, while

also providing a mechanism of integration; different theta frameworks couple together during behavioural tasks that require the combination of past experiences (CA3) with current spatial information (mEC) (Zhang *et al.*, 2019; López-Madróna *et al.*, 2020) (**Figure 1.3.1 D**).

Theta-gamma coupling has shown to be a marker of cognitive performance; the strength of coupling within the hippocampus predicts the success of spatial memory retrieval in a radial-arm water maze (Shirvalkar, Rapp & Shapiro, 2010) as well as the success of discriminating reward and non-reward in a context-dependant task (Tort *et al.*, 2009). Interestingly, in this task the strength of theta coupling to low gamma within CA3 increased across consecutive training days (Tort *et al.*, 2009). In humans, cortical theta-gamma coupling occurred while memorising random words (Schack *et al.*, 2002) and it is thought that the limited number of gamma cycles within a theta cycle reflects the capacity for short-term memory storage such as this (Lisman, 2010). Additionally, an increase in hippocampal theta-gamma coupling is observed during a correct decision in a T-maze task (Tort *et al.*, 2008), that is attributed to theta coherence between the hippocampus and mPFC, with hippocampal theta additionally modulating mPFC gamma (Sirota *et al.*, 2008; Tamura *et al.*, 2017).

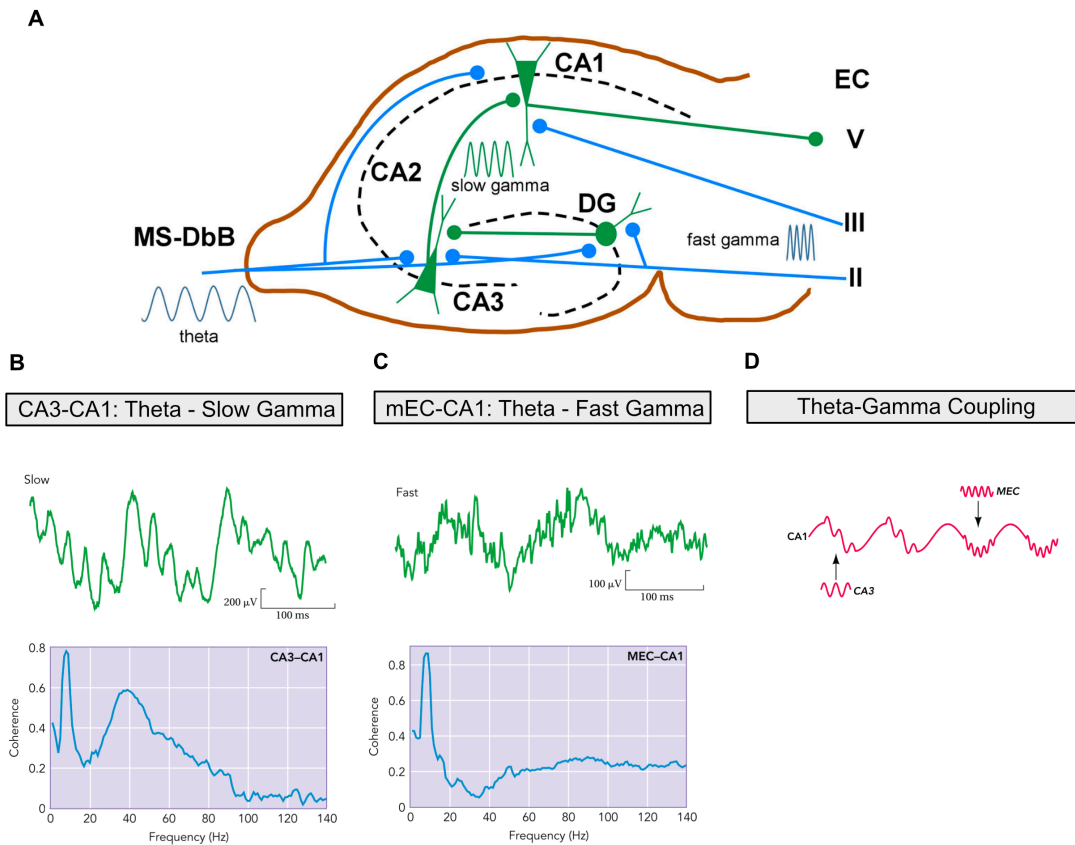


Figure 1.3.1 | Hippocampal theta and gamma oscillations and their coupling. **A** Image depicts theta hippocampal theta-generating inputs arising from the MS-DBB and the different gamma oscillation generators; CA3 (slow) and mEC (fast). **B** Above signal shows a theta oscillation coupled to a slow gamma oscillation. Below is graph showing peak theta and slow gamma coherence between CA3 and CA1. **C** Above signal shows a theta oscillation coupled to a fast gamma oscillation. Below is graph showing peak theta and fast gamma coherence between the mEC and CA1. **D** Drawing is an example of slow and fast gamma oscillations coupling to different phases of the CA1 theta cycle. Figure adapted from (Colgin & Moser, 2010; Nuñez & Buño, 2021).

1.4 | Alzheimer's disease

1.4.1 | Introduction to Alzheimer's disease

Alzheimer's disease (AD) is a progressive neurodegenerative disorder that impairs cognition and memory and is the leading cause of dementia worldwide. In the brains of patients with AD, Alois Alzheimer (1907) first described the presence of extracellular senile plaques and intracellular neurofibrillary tangles (NFTs), made by the aggregation of amyloid- β ($A\beta$) proteins and hyperphosphorylated microtubule-associate protein tau (tau), respectively (Duyckaerts, Delatour & Potier, 2009) (**Figure 1.4.1 A-B**). Since then, the pathology of AD has extended to include astrogliosis, synaptic dystrophy, neuronal loss and changes to the brain's vasculature (De Strooper & Karran, 2016; Long & Holtzman, 2019). The majority of AD cases occur in patients over the age of 65, named late-onset AD (LOAD), with <5% of patients developing the disease before this age; early-onset AD (EOAD). Around 1% of AD cases arise due to an inherited autosomal dominant mutation whereas most patients develop the disease through a variety of different environmental and lifestyle factors. Those with familial AD tend to present symptoms early on, although LOAD also has a genetic component (Long & Holtzman, 2019; De Strooper & Karran, 2016). The familial mutations associated with AD have been harnessed to generate rodent models for the study of the disease (Sasaguri *et al.*, 2017). Most AD research focusses on mutations that either lead to the development of plaques (amyloidopathy) or NFTs (tauopathy), with the research outlined in this thesis focussing on the former. Therefore, I will focus on discussing research that pertains to the pathophysiology of amyloidopathy.

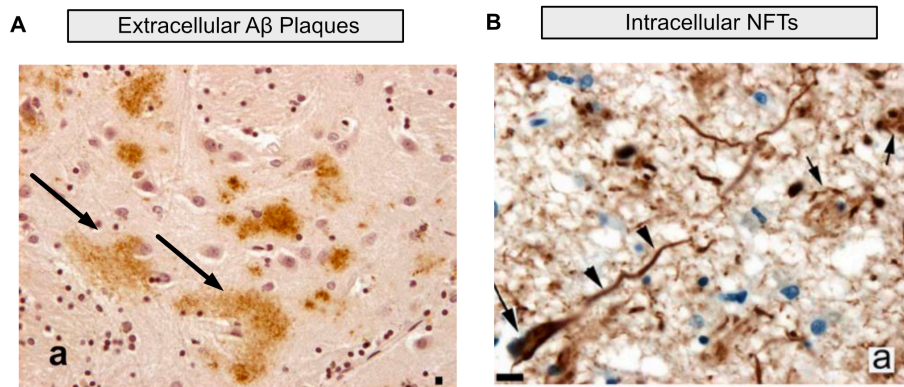


Figure 1.4.1 | Images of extracellular A β plaques and intracellular NFTs. **A** Arrowheads point towards example of diffuse deposits of A β into plaques. **B** Arrowheads point towards examples of intracellular NFTs. Figure adapted from (Duyckaerts, Delatour & Potier, 2009).

1.4.2 | APP processing and the amyloid hypothesis

The amyloid precursor protein (APP) is a transmembrane protein that is thought to be important for development, synapse formation, dendritic sprouting and neuronal migration (Nalivaeva & Turner, 2013). To generate A β , the APP protein is proteolytically cleaved at its β site by the β -secretase, BACE1, and at its γ site by a γ -secretase complex (**Figure 1.4.2 B**). A β fragments are typically between 38 and 43 amino acids long. A greater proportion of A β_{1-42} fragments are generated in AD; these fragments are more hydrophobic, causing the monomers to oligomerise, form fibrils and the characteristic A β plaques (O'Brien & Wong, 2011; Long & Holtzman, 2019). This cleavage of APP also generates the APP-intracellular domain (AICD) and a soluble APP β (sAPP β) fragments, with the former linked to creating AD-like symptoms and disrupting cellular pathways (Kametani & Hasegawa, 2018) (**Figure 1.4.2 A**). Under normal conditions, A β is degraded or removed. However, in AD this process is disrupted, leading to the build up of A β that spreads through the brain in a prion-like fashion (Braak & Braak, 1991; Walker & Jucker, 2015; Grothe *et al.*, 2017).

The original amyloid hypothesis states that it is this initial deposition of A β in the brain that leads to the creation of NFTs and subsequent neuron and synapse loss and cognitive decline (Hardy & Higgins, 1992) (**Figure 1.4.2 C**). This hypothesis

is supported by the effect of AD genetic risk factors; the mutations found on the β and γ cleavage sites on the *APP* gene as well as mutations to presenilins 1 and 2 (*PSEN1*, *PSEN2*) of the γ -secretase complex cause an increase in the deposition of $A\beta$, particularly the $A\beta_{1-42}$ isoform that is more prone to aggregation (Tcw & Goate, 2017; Chévez-Gutiérrez *et al.*, 2012). The presence of a third copy of the *APP* gene, located on the chromosome 21 trisomy found in Down's Syndrome also causes an increase in amyloid deposition and a higher susceptibility to AD (Hof *et al.*, 1995). However, rodent models that express these mutations and develop plaques do not go on to develop tau pathology (Sasaguri *et al.*, 2017). This could be due to rodents not living long enough to develop this next step in the amyloid cascade or because rodents don't possess the human form of the tau protein, which may be necessary for this interaction to take place. Evidence for the latter comes from a study in which AD-derived human pathological tau was injected into the brain in a mouse model of amyloidopathy, which found that the prion-like spreading of tau and the formation of NFTs was dependant on the proximity of $A\beta$ plaques (He *et al.*, 2018). On the contrary, several phase 3 clinical trials that use immunotherapies to target the $A\beta$ plaques are successful in ameliorating amyloid pathology, but fail to stop the development of NFTs and cognitive decline (Long & Holtzman, 2019). Potentially this intervention is occurring too far along in the progression of $A\beta$ pathology, such that intermediary mechanisms have been activated that lead to NFTs. There are multiple lines of evidence from human imaging, animal models and *in vitro* preparations that show that the development of tau pathology is highly dependent on the deposition of $A\beta$, therefore favouring the amyloid hypothesis (Long & Holtzman, 2019). The exact mechanism that is thought to induce NFTs from $A\beta$ is not fully known, but there is evidence for AICD causing axonal deficits, leading to the mis-localisation and aggregation of tau (Kametani & Hasegawa, 2018). The amyloid hypothesis has been debated for many years, but perhaps this theory needs to be re-examined in the wider context of AD, and beyond this simplistic view. Both $A\beta$ plaques and NFTs are found to occur separately during normal ageing, suggesting that these hallmarks of AD are not the sole cause of cognitive decline (Price, 1994; Braak & Del Tredici, 2011). It is in fact a cascade of events, encompassing more than just these pathologies, that creates a tipping

point that switches these perhaps normal features of ageing into a pathological process.

A more recent reevaluation of the amyloid hypothesis has therefore been proposed by Bart de Strooper and Eric Karran, called the “cellular phase of AD” (De Strooper & Karran, 2016), that encompasses the wider AD field. This theory posits that during the “biochemical phase” of AD, there are myriad interactions involving both pathologies and the way they exert stress upon different cell types through membrane receptors and proteins. In the early stages, compensatory mechanisms are in place, such as inflammation that combat this “proteopathic” stress. It is when these mechanisms become chronic and pathological that normal cellular function starts to degrade. This leads to the reduced clearance of A β and tau pathologies and the progression to the “cellular phase” of AD. This phase is characterised by impaired neurovascular coupling, astrogliosis, inflammation and aberrant neuronal activity that create an irreversible tipping point in which there is a breakdown in cellular and network homeostasis, leading to the “clinical phase” of AD, where symptoms of cognitive decline appear.

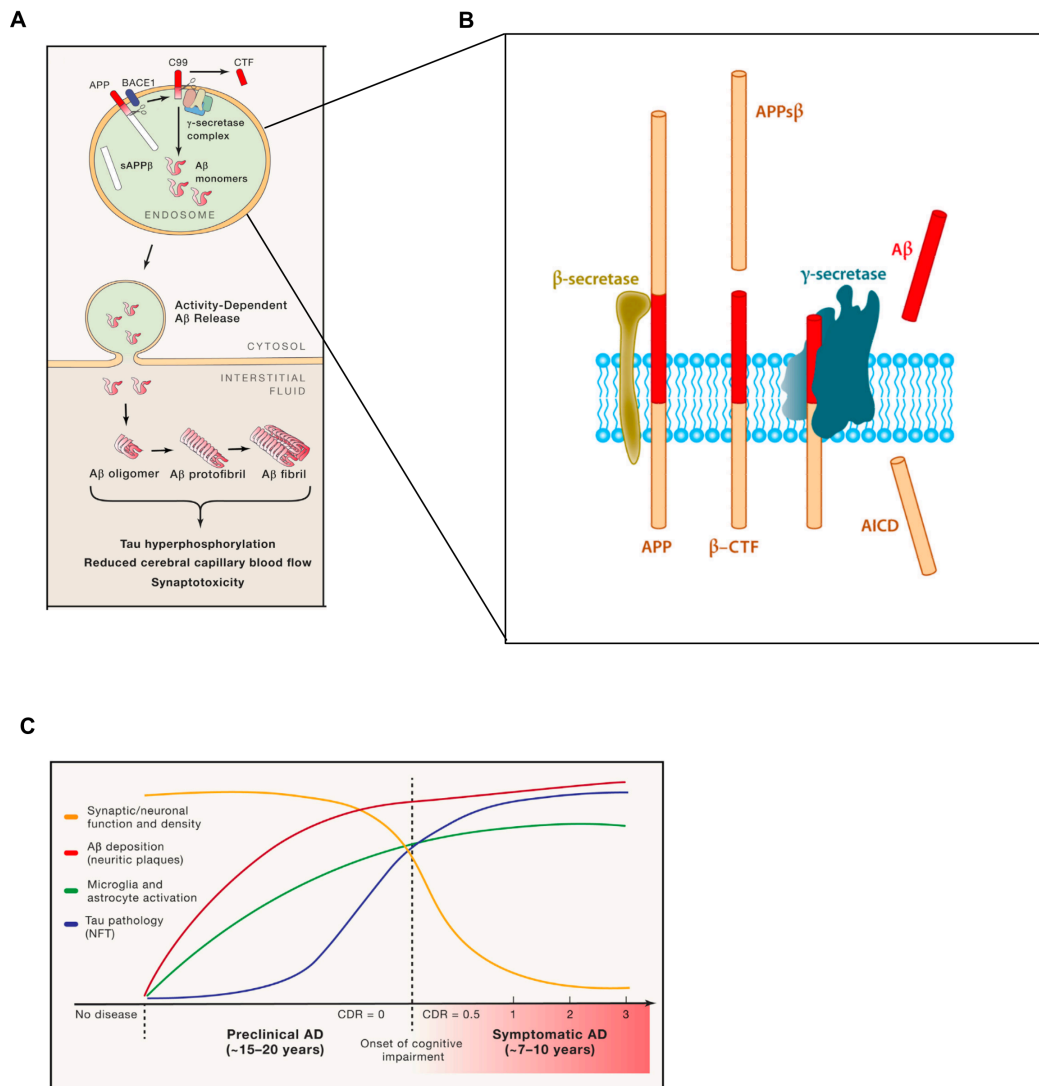


Figure 1.4.2 | Pathogenic processing of APP and progressing of AD. A Picture represents the endosomal processing of the APP into A β and its activity-dependant release from cells, where it oligomerises and forms the phenotypic A β plaques. This causes a cascade of pathological events. **B** A more detailed description of the pathogenic processing of the APP by β - and γ -secretases, generating A β as well as AICD and sAPP β . **C** Progression of the different stages found in AD and how they relate to one another and cognitive decline. Figure adapted from (O'Brien & Wong, 2011; Long & Holtzman, 2019).

1.4.3 | Aberrant neuronal network activity in Alzheimer's disease

1.4.3.1 | Evidence for neuronal hyperexcitability in AD

In the early stages of AD, soluble A β oligomers cause neuronal synapse loss and dysfunction prior to the deposition of plaques, leading to dysfunctional network

activity and ultimately culminating in cognitive decline (Heffter *et al.*, 2019). Increased hippocampal activation and reduced deactivation of the default mode network (DMN), consisting of cortical regions that are activated during quiet introspection and deactivated during attention-demanding tasks, are found in the preclinical stages of AD and in the brains of cognitively-healthy individuals with amyloid deposits (Sperling *et al.*, 2009; Bakker *et al.*, 2012; Palop & Mucke, 2016). This increased activity, measured by functional magnetic resonance imaging (fMRI), correlates with poor cognitive performance and is considered an early biomarker of AD (Bakker *et al.*, 2012; Palop & Mucke, 2016).

Neuronal hyperactivity is also found in mouse models of amyloidopathy (Busche *et al.*, 2008, 2012) and is considered an early pathological event. Hyperactive neurons appear prior to the deposition of plaques (Busche *et al.*, 2012) with studies implicating soluble oligomeric forms of A β being responsible (Busche *et al.*, 2012; Yamamoto *et al.*, 2015). Not only do oligomers cause hyperactivity, but A β is released from synapses in an activity dependant manner; increased neuronal activity leads to the deposition of A β ₁₋₄₂ proteins and the formation of plaques (Yamamoto *et al.*, 2015), with hyperactive neurons found in close proximity to plaques (Busche *et al.*, 2008). Thus, creating a vicious cycle in which A β is both a cause and product of hyperactivity.

Oligomers are thought to mediate their effects through several mechanisms acting on the synapse (Busche *et al.*, 2008). A β has been linked to dendritic spine loss which reduces neuronal capacitance and increases excitability (Hsieh *et al.*, 2006; Shankar *et al.*, 2007). A β also reduces re-uptake of glutamate at the synapse (Zott *et al.*, 2019), increasing neuronal firing. However, the sustained activation of N-methyl-D-aspartate (NMDA) receptors can cause them to desensitise and internalise, with glutamate spill-over also activating peri-synaptic GluN2B-containing NMDA receptors and metabotropic glutamate receptors (mGluRs) (Shankar *et al.*, 2007; Li *et al.*, 2009). There is also evidence for AMPA receptor internalisation (Hsieh *et al.*, 2006), all of which causes LTD and depotentiation of synapses, ultimately leading to spine loss and a further decrease in cell capacitance and increase in neuronal excitability. A β oligomers have also been shown to increase the pre-synaptic release probability of neurons, such that

when stimulated at high-frequencies the plasticity potential of these neurons favours LTD over LTP (Palop & Mucke, 2016). Additionally, A β causes astrocytes to increase their Ca²⁺ transients, leading to the increased release of gliotransmitters such as glutamate and D-serine, both of which can further increase neuronal excitability (Kuchibhotla *et al.*, 2009). Cultured astrocytes have also shown to reduce glutamate re-uptake upon application of A β , furthering exacerbating these effects (Matos *et al.*, 2008).

Neuronal hyperactivity leads to the hypersynchronous firing of neurons and epileptic activity. Convulsive and non-convulsive epileptic seizures and epileptiform activity are found to occur both in the late stages of AD and prior to cognitive decline, potentially serving as a catalyst for AD development (Born, 2015). Indeed, anti-epileptic drugs such as levetiracetam have shown to reduce hippocampal activation and improve memory performance in individuals with mild cognitive impairment (MCI) (Bakker *et al.*, 2012). Epileptic activity is additionally found in mouse models of amyloidopathy (Palop *et al.*, 2007; Verret *et al.*, 2012; Martinez-Losa *et al.*, 2018; Brown *et al.*, 2018; Johnson *et al.*, 2020). In addition to spine loss and aberrant glutamatergic transmission causing hyperactivity, there is also strong evidence for impaired inhibitory neurotransmission producing epileptic discharges. The inhibitory neurotransmitter GABA, GABA_A receptors and protein markers for several different interneuron subtypes are reduced in the brains of patients with AD (Ambrad Giovannetti & Fuhrmann, 2019). Additionally, oligomeric A β can induce epileptiform activity that is rescued upon administration of GABA_A receptor agonists in mice (Busche *et al.*, 2008). A large research focus has been placed upon the action of PV-expressing interneurons in mediating hyperactivity and epileptic discharges. The size of PV interneuron action potentials is greatly reduced in the hAPP-J20 mouse model that has been linked to a reduction in both the mRNA and protein levels of the Nav1.1 voltage-gated Na⁺ channel subunit (Verret *et al.*, 2012). Over-expressing this subunit in this model ameliorates epileptiform activity and can additionally improve memory performance (Verret *et al.*, 2012; Martinez-Losa *et al.*, 2018). Compensatory changes to inhibition have also been observed in the DG; synaptic and interneuron remodelling was found in a model of amyloidopathy that promoted an increase in granule cell miniature inhibitory post-synaptic current (mIPSC)

amplitude (Palop *et al.*, 2007). This effect was dependant on neuronal over-excitation and points towards compensatory remodelling of inhibitory networks.

1.4.3.2 | Disrupted neuronal oscillations in AD

Neuronal oscillations are created by a delicate balance of excitation and inhibition that shapes the firing of neurons to facilitate information processing and transmission. Impaired inhibition causing the hyperexcitability of neurons and epileptic discharges can therefore perturb the generation and function of oscillations. Indeed, gamma oscillations in both the cortex and hippocampus have reduced amplitude (Palop *et al.*, 2007; Palop & Mucke, 2016; Martinez-Losa *et al.*, 2018; Etter *et al.*, 2019) and are associated with epileptiform discharges in mouse models of AD, suggesting a mechanistic link between altered inhibition and changes in neuronal oscillations in AD (Verret *et al.*, 2012). PV-expressing interneurons are the main driver of gamma oscillations (Mann, Radcliffe & Paulsen, 2005; Sohal *et al.*, 2009b) and their spike-timing relationship with the gamma cycle is disturbed upon application of soluble A β oligomers (Chung *et al.*, 2020a). These impairments are linked to poor memory, with the optogenetic restoration of the activity of PV-expressing interneurons during working memory tasks improving performance, restoring gamma power and the spike-timing relationship of both PCs and PV-expressing interneurons to the gamma oscillation (Chung *et al.*, 2020a). Additionally, as with epileptic discharges, over-expressing the Nav1.1 subunit in PV-expressing interneurons can restore gamma oscillations and improve declarative memory performance (Verret *et al.*, 2012; Martinez-Losa *et al.*, 2018).

Not only are there impairments to PV-expressing interneurons, but SST-expressing OLM cells have been found to have fewer axon boutons and dendritic spines in an APP/PSEN1 mouse model of amyloidopathy (Schmid *et al.*, 2016b). Optogenetic activation of SST-expressing interneurons can rescue reduced theta power upon application of soluble A β as well as restore the timing of SST-expressing interneuron and PC spiking relative to the theta oscillation (Chung *et al.*, 2020a). Theta-gamma coupling is also impaired in humans with AD (Goodman *et al.*, 2018) and upon application of soluble A β oligomers in mice (Park *et al.*, 2020). Interestingly, optogenetic activation of PV-expressing

interneurons could rescue this coupling whereas activation of SST-expressing interneurons could not (Park *et al.*, 2020). However, this increase in coupling is likely attributed to the increased gamma power associated with PV-expressing interneuron activation.

Impairments are also seen to the 3 cardinal oscillators involved in systems consolidation during NREM sleep. Reduced SWA and the density of spindle events correlate with plaque load in the brains of humans with AD and even precede cognitive decline (Mander *et al.*, 2015a; Kam *et al.*, 2019). The SWO oscillation in particular has been found to have reduced power (Kastanenka *et al.*, 2017), reduced frequency (Castano-Prat *et al.*, 2019) and impaired coherence across cortical regions (Busche *et al.*, 2015) in mouse models of amyloidopathy, all of which can be rescued upon administration of a GABA_A receptor agonist, further implicating disrupted inhibition in the pathophysiology of AD. Additionally, during post-learning sleep in a spatial memory task, the number of SWR events diminished upon administration of soluble A β oligomers, resulting in poor memory performance (Nicole *et al.*, 2016). Similar disruptions to SWRs have been found to occur in first-generation mouse models of amyloidopathy, as a result of impaired PV-expressing interneuron activity (Caccavano *et al.*, 2020). Not only are there disruptions to the oscillations, but fMRI studies in humans show reduced functional connectivity between the hippocampus and mPFC early in the disease progression (Wang *et al.*, 2006). Application of A β oligomers can also reduce the size of the mPFC field excitatory post-synaptic potential (fEPSP) upon hippocampal stimulation *ex vivo*, as well as reduce the number of recruited neurons (Flores-Martínez & Penã-Ortega, 2017). mPFC interneuron dysfunction has also been linked to reduced cholinergic tone, which is a common feature in AD (Zhong *et al.*, 2003).

The SWO, spindles and SWRs individually play an important role in systems consolidation, but it is their temporal coupling that drives the reorganisation of newly acquired hippocampal memories into distributed cortical networks for long-term consolidation (Crunelli & Hughes, 2010a; Maingret *et al.*, 2016a). Only one study to date has investigated the impact of amyloidopathy on this coupling in the mPFC-hippocampal circuit. Using an APP/PSEN1 model, delta coherence between regions was reduced, as was SWR locked-spindle power

(Zhurakovskaya *et al.*, 2019). This research only superficially addressed the full breadth of oscillatory coupling and dynamics that occurs in this circuit. Given the importance of this circuit in systems consolidation and the current evidence for impaired oscillations and long-range communication in AD, it is clear that a more in-depth assessment is needed.

1.4.4 | Are sleep disturbances a cause or consequence of Alzheimer's disease?

As discussed in **section 1.2**, one of the biological functions of sleep is memory consolidation. The duration of NREM sleep increases after learning a declarative memory task, and disruptions of the sleep-wake cycle can perturb memory performance (Rasch & Born, 2013). Not only is sleep important for memory, but it is responsible for the clearance of metabolites from the interstitial fluid (ISF) and into cerebral spinal fluid (CSF) for drainage through the glymphatic system, with the size of the interstitial space increasing during sleep to support this process (Xie *et al.*, 2013). More specifically, sleep has been shown to facilitate the clearance of both A β and tau proteins. Greater levels of A β are found in the ISF during waking periods compared with sleep and sleep deprivation in both humans and mice causes an increase in A β found in the CSF (Kang *et al.*, 2009; Ooms *et al.*, 2014). Furthermore, it is the deprivation of SWS in particular that causes this increase along with an increase in hyperphosphorylated tau protein (Varga *et al.*, 2016; Ju *et al.*, 2017).

Sleep disturbances are extremely common in the preclinical stages of AD (Kabeshita *et al.*, 2017) and are a predictor of cognitive decline (Bubu *et al.*, 2017). AD patients exhibit night-time awakenings, sleep fragmentation and disruptions to the sleep cycle, particularly a reduction in the time spent in SWS (Vitiello *et al.*, 1990; Bubu *et al.*, 2017). Clinical sleep disorders such as insomnia or obstructive sleep apnoea syndrome have additionally been linked to cognitive decline and a reduction in SWS (Cellini, 2017), with several studies identifying links between these sleep disorders and AD prevalence (Klauber *et al.*, 1991; Sindi *et al.*, 2018). What is interesting is that sleep disorders and disturbances are associated with reduced grey matter volume in areas more prone to AD pathology, such as the hippocampus, thalamus and areas of the cortex, and this

is exacerbated in individuals who carry the apolipoprotein E (APOE)- ϵ 4 allele (Alperin *et al.*, 2019; Grau-Rivera *et al.*, 2020); a large risk factor for the development of LOAD (Kim, Basak & Holtzman, 2009). APOE is released by astrocytes and microglia and functions as a ligand that binds lipoproteins such as A β for degradation and clearance. APOE- ϵ 4 binds to A β with less affinity compared with APOE- ϵ 2 and APOE- ϵ 3 and is linked to the increased deposition of A β into plaques and reduced clearance, with APOE- ϵ 4 carriers showing greater levels of A β in the ISF (Wildsmith *et al.*, 2013). The reduced clearance of A β and tau pathologies is proposed to be one of the drivers of the “cellular phase” of AD (De Strooper & Karran, 2016), but the question remains, do sleep disturbances cause this shift, or does the pathological changes occurring in the early stages of AD development cause the sleep disturbances?

It is hypothesised that the link between sleep disturbances and AD is cyclical (Cedernaes *et al.*, 2017; Lloret *et al.*, 2020). Under this framework, sleep disturbances and sleep disorders both cause an increase in AD pathologies by reducing the time spent in SWS and therefore reducing clearance of A β and tau (Ju *et al.*, 2017; Varga *et al.*, 2016); one of the drivers of the “cellular phase” of AD. The increased time spent in wake additionally increases the production of these pathologies as both are released from neurons in an activity-dependant manner, with increased neuronal activity seen during awake states (Spires-Jones & Hyman, 2014). As discussed in **section 1.4.3**, A β causes aberrant network activity and impairs several oscillations involved in memory consolidation. Both A β and tau are inversely correlated with SWA and spindle density (Mander *et al.*, 2015a; Kam *et al.*, 2019) and these impairments made to the sleep circuitry underlying consolidation leads to cognitive decline. The increased pathology due to sleep disturbances can additionally affect brain regions critical in maintaining the sleep/wake cycle. AD-related pathology is found in the suprachiasmatic nucleus (SCN); the brain’s circadian pacemaker, as well as in the brainstem nuclei and basal forebrain, regions responsible for sleep state switching and neuromodulatory control of the sleep cycle, respectively (H. Ferreira-Vieira *et al.*, 2016; Holth, Patel & Holtzman, 2017; Van Erum, Van Dam & De Deyn, 2018). Dysfunction of these regions can in turn lead to sleep disturbances, resulting in the iterative advancement of AD pathology.

1.4.5 | The APP^{NL-G-F} mouse model

The majority of AD cases occur sporadically, yet have an extremely similar pathophysiology to familial AD. Therefore, to better understand AD, multiple mouse models have been generated that harness the mutations found in familial AD to induce similar pathological hallmarks. The mutations used are typically found on the *APP* or *PSEN1* and *PSEN2* genes, that increase the deposition and aggregation of A β ₁₋₄₂ protein fragments, with a variety models created that utilise a combination of different mutations (Sasaguri *et al.*, 2017). First-generation mouse models over-express these mutated genes under the control of several different promoters, in combination with the endogenous murine gene copies (Games *et al.*, 1995; Hsiao *et al.*, 1996). A criticism of this approach for modelling AD is that it leads to several over-expression artefacts, such as the translation of mutated genes in cells that do not typically express APP, interference with intracellular transport, increased deposition of C-terminal fragments such as AICD that are also pathogenic and altered native gene expression (Nilsson, Saito & Saido, 2014; Sasaguri *et al.*, 2017). The use of these models is one hypothesis to explain the translational gap between pharmaceutical interventions that show efficacy in mice, but not in humans.

Second-generation knock-in (KI) mouse models have since been created that overcome these over-expression artefacts, with the aim of bridging this translational gap. The APP^{NL-G-F} KI mouse model, first described in 2014, is one such second-generation model used in the experiments discussed in this thesis (Nilsson, Saito & Saido, 2014; Saito *et al.*, 2014). To generate these mice, the mouse *APP* gene was first humanised by replacing 3 amino acids that differ between humans and mice and 3 mutations associated with familial AD were inserted into its sequence. The gene was then knocked-in to the mouse genome, replacing any endogenous copies of the mouse *APP* gene. The Swedish (KM670/671**NL**) and Beyreuther/Iberian (I716**F**) mutations were inserted that increase APP β -site cleavage and γ -site cleavage at amino acid position 42, respectively, generating a greater proportion of A β ₁₋₄₂ that is more prone to aggregation. The Arctic (E693**G**) mutation was also inserted that speeds up the deposition of A β ₁₋₄₂ protein fragments, with mice homozygous for the mutated

gene displaying A β plaques as early as 2 months old. From 2 months, APP^{NL-G-F} mice show a steady increase in A β protein and plaques in the hippocampus, cortex and subcortical regions and additionally display reactive gliosis and synaptic alterations (Nilsson, Saito & Saido, 2014; Saito *et al.*, 2014). Like first-generation models, second-generation models such as the APP^{NL-G-F} do not develop NFTs. However, it is thought that this makes these mice an effective model for studying the preclinical stages of AD, as plaques precede NFTs, and it is in the preclinical stages of the disease that researchers should be focussing their efforts, before the onset of irreversible cognitive decline (Sasaguri *et al.*, 2017).

Due to its fairly recent generation, very little information is known about this model and similarities between the APP^{NL-G-F} and first-generation models should not be assumed. However, similar to the commonly used hAPP-J20 model of amyloidopathy, APP^{NL-G-F} mice exhibit cortical epileptiform activity at around 6-8 months-old, indicating impaired excitatory-inhibitory (E-I) balance (Johnson *et al.*, 2020). Interestingly, APP^{NL-G-F} mice show impairments in the sleep-wake cycle as early as 6 months, with mice having fewer NREM sleep episodes that reduce in duration around 12 months (Maezono *et al.*, 2020). There is also building evidence for disrupted oscillations within the hippocampus and mEC. Fast gamma oscillations within the mEC show impairments at 5 months (Nakazono *et al.*, 2017) that progress to impaired communication between mEC and CA1 between 7-13 months, disrupting fast gamma input to CA1 and the spatial tuning of both mEC grid cells and CA1 place cells (Jun *et al.*, 2020). This spread of disruption is in-keeping with the progression of amyloid pathology (Grothe *et al.*, 2017). Disruptions to these oscillations would predict corresponding impairments to spatial navigation, for which there is mixed evidence in the literature, particularly regarding the age of onset. Some report spatial memory impairments in the Y-maze as young as 6 months (Nilsson, Saito & Saido, 2014; Saito *et al.*, 2014), that cannot be replicated by others (Whyte *et al.*, 2018), with groups reporting deficits in contextual fear conditioning and the Morris Water Maze from 11 months onwards (Latif-Hernandez *et al.*, 2019; Sakakibara *et al.*, 2019; Maezono *et al.*, 2020) (**Figure 1.4.3**). The differences in the literature and the accuracy of this model in recapitulating AD pathophysiology are discussed and reviewed further in **section 7.2.2**. It is clear however that more research is

needed to understand the network dysfunctions occurring in APP^{NL-G-F} mice, both during awake behaviour and during asleep systems consolidation, not only to validate findings in first-generation models, but to progress our understanding of preclinical amyloidopathy for the development of biomarkers and treatments.

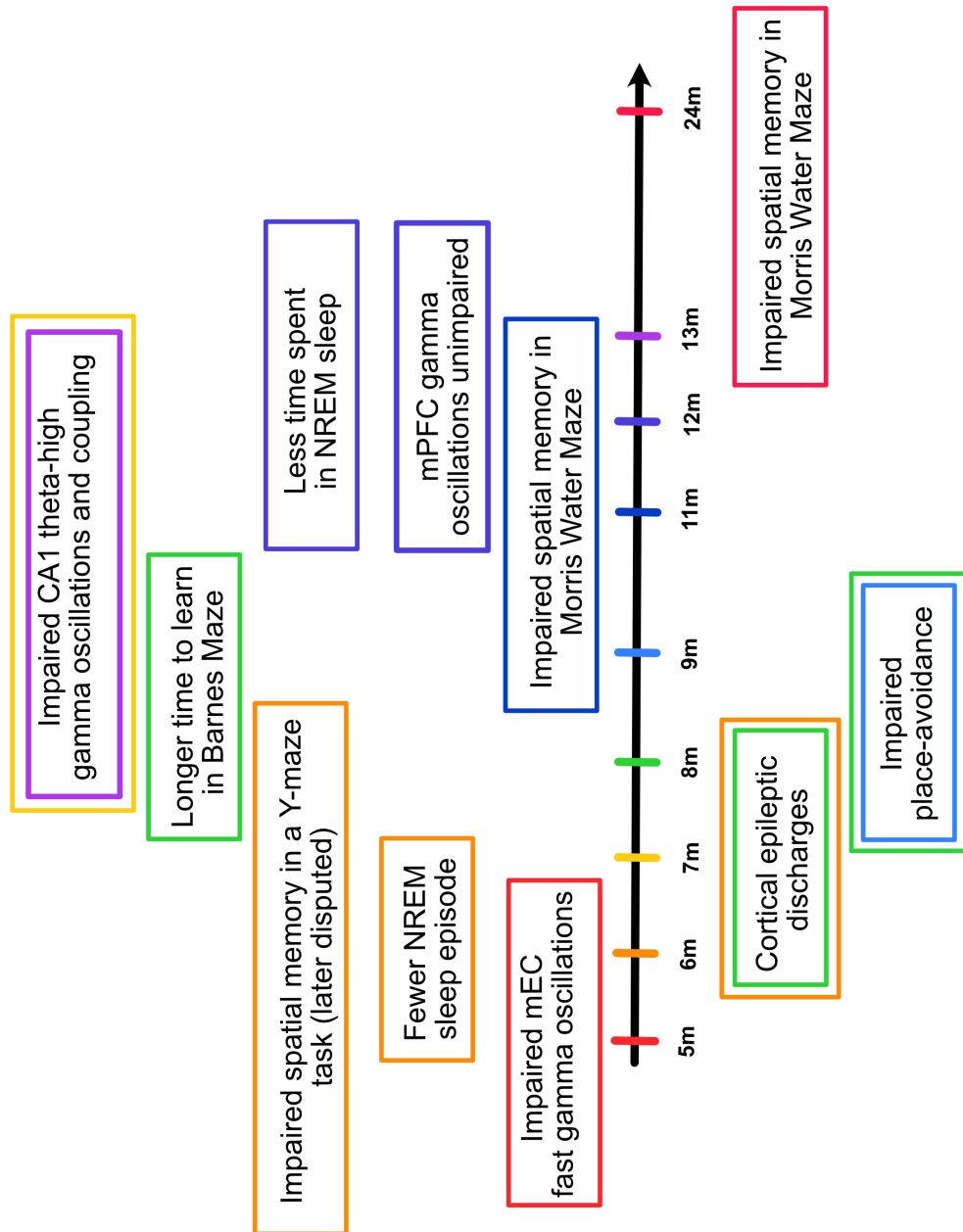


Figure 1.4.3 | A timeline of cognitive and network decline in the APP^{NL-G-F} mouse model. Schematic highlights the current literature conducted using the APP^{NL-G-F} mouse model as it pertains to the research in this thesis. Each age and the matched cognitive/electrophysiological findings are colour coded. Findings with two colours represent the age-span used in the study. 5m:

(Nakazono *et al.*, 2017), 6m: (Nilsson, Saito & Saido, 2014; Saito *et al.*, 2014; Whyte *et al.*, 2018; Maezono *et al.*, 2020), 7-13m: (Jun *et al.*, 2020), 6-8m: (Johnson *et al.*, 2020), 8m: (Sakakibara *et al.*, 2018), 8-9m: (Masuda *et al.*, 2016), 11m: (Latif-Hernandez *et al.*, 2019), 12m: (Pervolaraki *et al.*, 2019; Maezono *et al.*, 2020), 24m: (Sakakibara *et al.*, 2019).

1.5 | Hypotheses and aims

Hypothesis 1: Within the mPFC-hippocampal circuit, the oscillations involved in systems consolidation and their coupling are disrupted in the APP^{NL-G-F} mouse model of familial AD.

It is clear that the oscillations found within the mPFC-hippocampal circuit during NREM sleep are extremely important for systems consolidation. In the preclinical stages of AD, sleep disturbances are extremely common. There is also accumulating evidence from both humans and first-generation mouse models for disruptions to several of the oscillations involved within this circuit and to the interneurons responsible for the generating and modulating them, as well as functional connectivity problems between these regions. Moreover, these deficits appear to be linked to the amyloidopathy phenotype found in AD. However, very little is known about how this circuit is affected as a whole. Therefore, using the APP^{NL-G-F} mouse model, I aim to determine if there are any impairments to the oscillations in the mPFC-hippocampal circuit and their coupling during NREM sleep. Researching this circuit in a next-generation mouse model provides a novel insight into the role A β has in disrupted network activity, without contamination of over-expression artefacts.

Hypothesis 2: The oscillations involved in spatial memory in both the hippocampus and mPFC are disrupted in the APP^{NL-G-F} mouse model, similar to first-generation models of amyloidopathy.

Theta and gamma oscillations and their coupling have been documented to be impaired in both humans and first-generation mouse models of AD. However, there is limited evidence for the same being true in second-generation mouse models. Similarities between first and second-generation mouse models should not be assumed, therefore it is important that prior research is validated in second-generation mice before they can be used to understand the pathological

mechanisms creating this disrupted network activity. I aim to assess any impairments to theta and gamma oscillations in both the mPFC and hippocampus of APP^{NL-G-F} mice as they navigate an open field arena.

Hypothesis 3: The function of PV- and SST-expressing interneurons is perturbed in the APP^{NL-G-F} mouse model, contributing to disrupted SWA.

Interneurons are integral to balancing excitation in the brain, to create oscillations and shape the firing of neurons for spike-time dependant plasticity. Interneurons and inhibition are impaired in both humans and mouse models of AD. Evidence from first-generation mouse models point towards impaired inhibition causing disruptions to gamma, theta and the SWO, with particular emphasis on the PV and SST-expressing interneurons that shape them. Building evidence from the APP^{NL-G-F} mouse model suggests disrupted network activity similar to humans and first-generation models, yet the contribution of interneurons has not been assessed. My first aim is to use immunohistochemistry in this model to identify any changes to the immunoreactivity of PV or SST in the mPFC and hippocampus at various stages of amyloidopathy. Next, using Designer Receptors Exclusively Activated by Designer Drugs (DREADDS), I propose that increasing the function of these interneurons can ameliorate impairments to the SWO in the APP^{NL-G-F} model.

2 | Methods

The experimental methods detailed in this section, as well as the results chapters they correspond to, are set out as follows:

- Animals
- Chronic *in vivo* electrophysiology (see **sections 4, 5, 6**)
- Acute *in vivo* electrophysiology (see **section 4**)
- Analysis of electrophysiological data (see **sections 4, 5, 6**)
- Immunohistochemistry (see **sections 3, 4, 5**)
- Statistical analysis

2.1 | Animals

2.1.1 | Ethics

All animal procedures carried out in this thesis were done in accordance with the UK Animals (Scientific Procedures) Act (ASPA) 1986 and were approved by the University of Exeter Institutional Animal Welfare and Ethical Review Body.

2.1.2 | Housing

All mice were housed under a 12-hour standard light-dark cycle at $22^{\circ}\text{C} \pm 2^{\circ}\text{C}$ and were given access to standard laboratory rodent chow and water *ad libitum*. All experiments were conducted at the lights-on circadian epoch. For experiments involving chronic *in vivo* electrophysiology (see **section 2.2**), mice were group housed before surgical implantation of silicon microelectrodes and singly housed thereafter to prevent cage mates from tampering with the implant. All other mice were group housed.

2.1.3 | APP^{NL-G-F} mice

The second-generation APP^{NL-G-F} KI mouse model of familial amyloidopathy is used for the experiments outlined in this thesis and bred on a C57BL/6J background. To create this model, the *APP* gene is first humanised and the Swedish (NL), Arctic (G) and Beureuther/Iberian (F) mutations associated with familial AD are inserted into its sequence. This mutated gene is then knocked-in to the mouse genome at the *APP* locus, replacing the endogenous form of *APP*. This model was created to avoid putative confounds produced by the overexpression of mutated *APP* genes (Saito *et al.*, 2014)(see **section 1.4.5**). Mice were generously provided by the MRC Harwell Institute and bred in-house

at the University of Exeter. Mice homozygous for the APP^{NL-G-F} gene are used in all experiments as they develop pathology at a faster rate and are more comprehensively characterised compared with heterozygous mice (Saito *et al.*, 2014).

2.1.4 | APP^{NL-G-F} x SST-Cre and APP^{NL-G-F} x PV-Cre mice

In the experiments outlined in **section 4**, APP^{NL-G-F} mice were cross-bred with either SST-Cre or PV-Cre mice, that express Cre recombinase in SST and PV-expressing interneurons, respectively. SST-Cre and PV-Cre mice were originally purchased from Jackson Laboratories and were maintained on a C57BL/6J background. All breeding was done internally at the University of Exeter. Mice were cross-bred to achieve the following genotypes: APP^{WT} x SST-Cre^{Het}, APP^{Hom} x SST-Cre^{Het}, APP^{WT} x PV-Cre^{Het}, APP^{WT} x PV-Cre^{Hom}, APP^{Hom} x PV-Cre^{Het}, APP^{Hom} x PV-Cre^{Hom} (**Table 2.1.1**). Only mice heterozygous for SST-Cre were selected, as homozygous mice display reduced levels of endogenous SST (Viollet *et al.*, 2017) and behaviour abnormalities (unpublished results, The Jackson Laboratory website).

Genotype	Shorthand
PV-Cre ^{Het} x APP ^{WT}	PV ^{WT}
PV-Cre ^{Hom} x APP ^{WT}	
PV-Cre ^{Het} x APP ^{Hom}	PV ^{APP}
PV-Cre ^{Hom} x APP ^{Hom}	
SST-Cre ^{Het} x APP ^{WT}	SST ^{WT}
SST-Cre ^{Het} x APP ^{Hom}	SST ^{APP}

Table 2.1.1 | Genotype shorthand notation. APP^{NL-G-F} mice were cross-bred with either SST-Cre or PV-Cre mice to generate the following genotypes. Genotype shorthand notation is noted next to each genotype.

2.1.5 | Emx1-Cre mice

Emx1-Cre mice were purchased from The Jackson Laboratories and bred at the University of Exeter on a C57BL/6J background. They express Cre-recombinase in excitatory neurons of the neocortex and hippocampus. These animals were only used to generate **Figure 4.2.1** in **section 4.2**.

2.2 | Chronic *in vivo* electrophysiology

2.2.1 | Animals

Both male and female, homozygous APP^{NL-G-F} mice (*female*: N = 3, *male*: N = 2) and wildtype (WT) littermate controls (*female*: N = 2, *male*: N = 3) were used for the following experiments, hereafter named APP and WT animals, respectively. Mice were surgically implanted with silicon microelectrodes at 14 months of age and used for experiments at 16 months of age.

2.2.2 | Silicon multielectrode array

Silicon multielectrode arrays are a widely used tool for studying the electrical activity of neural circuits, with the configurations used in these experiments able to record both the LFP and MUA. 4-channel linear silicon probes (Q-trodes) with 200 μm inter-electrode spacing and a 50 μm electrode diameter were used (model: Q1x4-5mm-200-177-CQ4). These electrodes had an impedance of 0.2-1 $\text{m}\Omega$ and were attached to a CQ4 pinout (**Figure 2.2.1 A-C**).

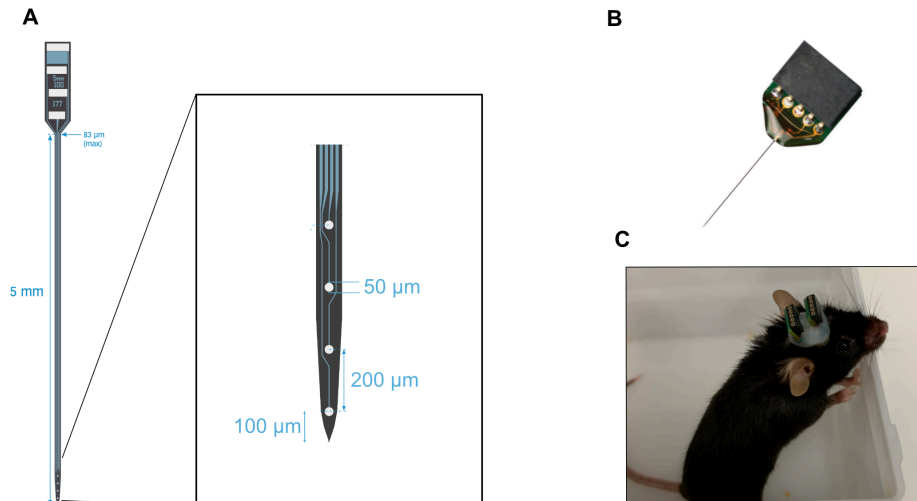


Figure 2.2.1 | Silicon microelectrode design for chronic *in vivo* electrophysiology. **A** Size specification for Q1x4-5mm-200-177 microelectrodes. The white dots on the inset image indicate the electrode positions. **B** Image of the microelectrode. Images taken from <https://www.neuronexus.com/>. **C** Photo taken of a mouse implanted with two microelectrode arrays: one in the mPFC and one in dorsal CA1.

2.2.3 | Surgical implantation of silicon probes

All surgical procedures were conducted using aseptic technique. Mice were first weighed, anaesthesia was induced using 5% isoflurane, their head shaved and then placed in a stereotaxic frame where surgical anaesthesia was maintained using an isoflurane concentration of around 2%. Mice were also given a subcutaneous injection of buprenorphine (0.03 mg/Kg) for analgesia. Throughout surgery, the anaesthesia level was monitored by periodically checking for a pedal reflex (paw pinch) and a breathing rate of between 1-2 breaths per second, with the isoflurane concentration adjusted accordingly. Isoflurane was delivered in a constant flow of oxygen at approximately 1 L/min and eyes were moisturised (Lubrithal) to prevent them from drying out, and covered to protect them from the light. Body temperature was additionally maintained at around 36-37°C using a feedback rectal probe and heat mat.

Iodine was applied to the scalp and a vertical incision was made to expose the skull, which was cleaned and positioned in the skull-flat configuration by ensuring that bregma and lambda were aligned in the horizontal plane. Small craniotomies were made into several of the bone plates with small screws inserted to stabilise the implant. Silver wire was wrapped around the screw placed at the surface of the cerebellum to act as a ground for the probes (**Figure 2.2.2**).

Further craniotomies were made over the mPFC (+1.75 mm anterior and +0.25 mm lateral to bregma) and dorsal CA1 (-2 mm posterior and 1.4 mm lateral to bregma) and the silicon probes were inserted to the required depth (mPFC: 1.7 mm, CA1: 1.5 mm from the surface of the brain) (**Figure 2.2.2**). The silver wire attached to the ground screw over the cerebellum was attached to the ground wires of both probes using conductive silver paint and the full surgical implant was cemented in place and the surrounding skin was sutured around the implant.

Mice were weighed post-operatively to check the weight of the implant, were given a subcutaneous injection of both carprofen (1 mg/Kg) and sterile saline (500 µl) and monitored in a heated recovery chamber for 30-60 minutes or until they had fully regained consciousness. Mice were given a second dose of carprofen (1

mg/Kg) the following morning and were monitored closely throughout the rest of the experiments.

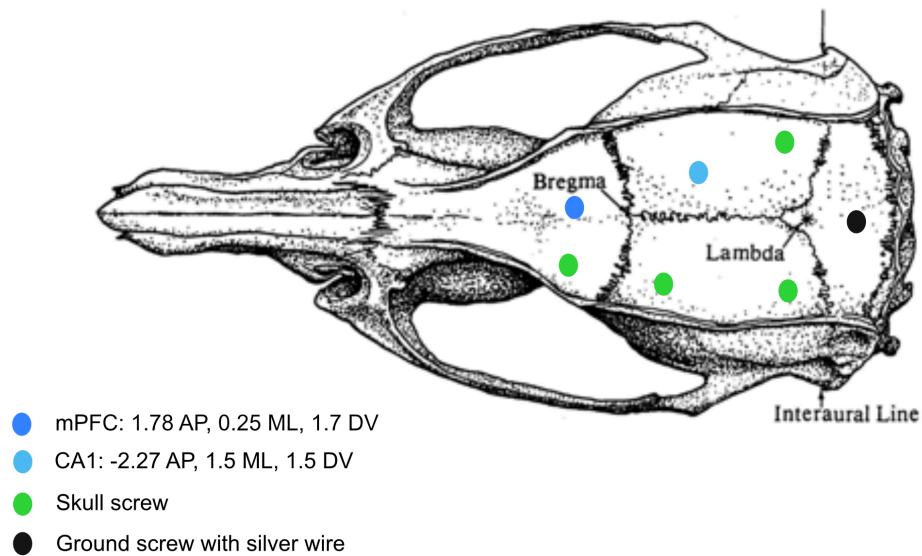


Figure 2.2.2 | Schematic of a mouse skull with details of the different landmarks for microelectrode and skull screw placement. Image of the skull obtained from (Paxinos *et al.*, 1985)

2.2.4 | Acquisition of neural signals

LFPs in both the mPFC and dorsal CA1 were recorded using an OpenEphys recording system. Mice were tethered to two Intan RHD2000 headstage pre-amplifiers that attached to the CQ4 probe pin outs using an OM16 adaptor (NeuroNexus). The headstages were connected using an Intan RHD dual headstage adapter to allow for the simultaneous recording of both brain regions and attached *via* Intan RHD SPI cables to an OpenEphys acquisition board and analogue to digital converter. The weight of the headstages was counterbalanced using a moveable counterweight to allow for as much mobility and comfort as possible. Neural signals were continuously recorded at a sample rate of 30 kHz, bandpass filtered online at 0.1-7932.3 Hz, and were stored for offline analysis.

Mice were habituated to the tether for 15 minutes in their home cage with the lid removed and the quality of the signals was checked prior to the commencement of experiments. All animals were found to acclimatise to the tether and did not show any adverse reactions. 2 mice (WT: N = 1, APP: N = 1) were found to have

poor signal quality in the CA1 probe, potentially due to poor grounding; these signals were excluded from analysis involving CA1 neuronal oscillations.

2.2.5 | Sleep recordings

A Logitech colour webcam was fitted overhead (30 Hz frame rate) and videos of the animals were recorded throughout the duration of the neural signal acquisition. Animals were recorded in their home cage to enable recording of neural signals during sleep. The lid was removed to allow for tethering and mice had access to food but not water, to prevent water damage to the headstage. Cages were placed in a clear Perspex box (40 x 40 x 45 cm) that was covered in white paper to prevent distraction from the rest of the recording room. An overhead light remained on throughout recording (440 lux).

On experimental days, mice were brought into the holding room directly adjacent to the recording room 15 minutes prior to recording (570 lux). During recording they were left tethered for 3 hours with noise disturbance kept to a minimum. On average, 3 mice were recorded per day during lights on with the order of genotype counterbalanced. The experimenter remained in the holding room throughout to monitor the mice.

2.2.6 | Open field recordings

Mice were brought into the holding room adjacent to the recording room 15 minutes before recording. Mice were tethered and placed in an open-topped wooden box (54 x 54 x 51 cm) that was painted white and had black stripes on the floor and on 2 of the walls. On the other walls there was a green square and 2 green triangles (**Figure 2.2.3 A**). Mice were left to explore the open field (OF) for 1 hour. Two light-emitting diodes (LEDs) were attached and grounded to one of the headstages that allowed the animal's position to be tracked using an overhead Logitech webcam and the tracking software Bonsai (Lopes *et al.*, 2015). Tracking data collected from Bonsai were acquired through the OpenEphys recording system at the same time as the neural signals. To allow for the LEDs to be visualised, all lights were switched off apart from an overhead LED light (1 lux). The OF was cleaned with 70% ethanol between recording

sessions and all experiments occurred at the lights-on circadian epoch, with genotype counterbalanced throughout the day.

2.2.7 | Novel object location

Novel object location (NOL) behavioural testing was carried out to study hippocampus-dependant memory (Antunes & Biala, 2012; Denninger, Smith & Kirby, 2018). The experiments were conducted with the help of Dr Shivali Kohli, so that two animals could be recorded at once. Two clear, Perspex boxes (40 x 40 x 45 cm) were placed on the floor, side-by-side, with a white piece of paper in between to block the mice view of each other. Red triangles were taped to the west wall of one box and east wall of the other box, and green rectangles to the north wall to act as local spatial cues, to avoid confusion with idiothetic information (**Figure 2.2.3 B**). Distant spatial cues included a black chair visible through the north wall and a black zero-maze visible through the south wall. Experimenters also stood in the same position throughout. Lamps were placed in each corner of the room with a brightness of 55 lux. Two different objects were used for these experiments; a clear bottle with a blue lid and a Lego tower (**Figure 2.2.3 C**). Previous unpublished experiments carried out by Dr Shivali Kholi found that APP^{NL-G-F} mice do not show a strong preference for either object. Animals were presented two of the same objects which were counterbalanced between genotypes. A mouse of each genotype was recorded at the same time and the box they went into was counterbalanced. In each phase of the experiment, animals were placed in the south-west corner of the box. No neural signals were recorded during these experiments.

Mice were brought into the holding room adjacent to the recording room 15 minutes before recording. On day 1, mice were given 15 minutes to explore the arena and habituate. On day 2, mice were given a further 10 minutes habituation to the arena then placed back in their home cage while the arenas were cleaned and the objects added to the north wall. They were then given 10 minutes to explore the objects with the time spent at each object recorded using stopwatches. An animal was considered exploring an object if it was sniffing around it (Antunes & Biala, 2012). Short-term memory (STM) was then tested (Vogel-Ciernia & Wood, 2014). Mice remained in their home cage for 30 minutes

while the arenas were cleaned and one object was moved to the south wall, with the object chosen counterbalanced between genotypes. Mice were then allowed to explore the objects for 10 minutes. On day 3, the second object was moved to the south wall and mice were allowed to explore for 10 minutes, with this 24-hour period measuring their long-term memory (LTM) (Tagliavante *et al.*, 2009; Vogel-Ciernia & Wood, 2014) (**Figure 2.2.3 D**). The arenas and objects were cleaned with 70% ethanol.

A discrimination index was used to measure the ability of animals to discriminate between novel and familiar stimuli, with an index greater than 0 signifying animals spent more time exploring the novel object.

$$\text{Discrimination index} = \frac{\text{Time at novel object} - \text{Time at familiar object}}{\text{Time at novel object} + \text{Time at familiar object}}$$

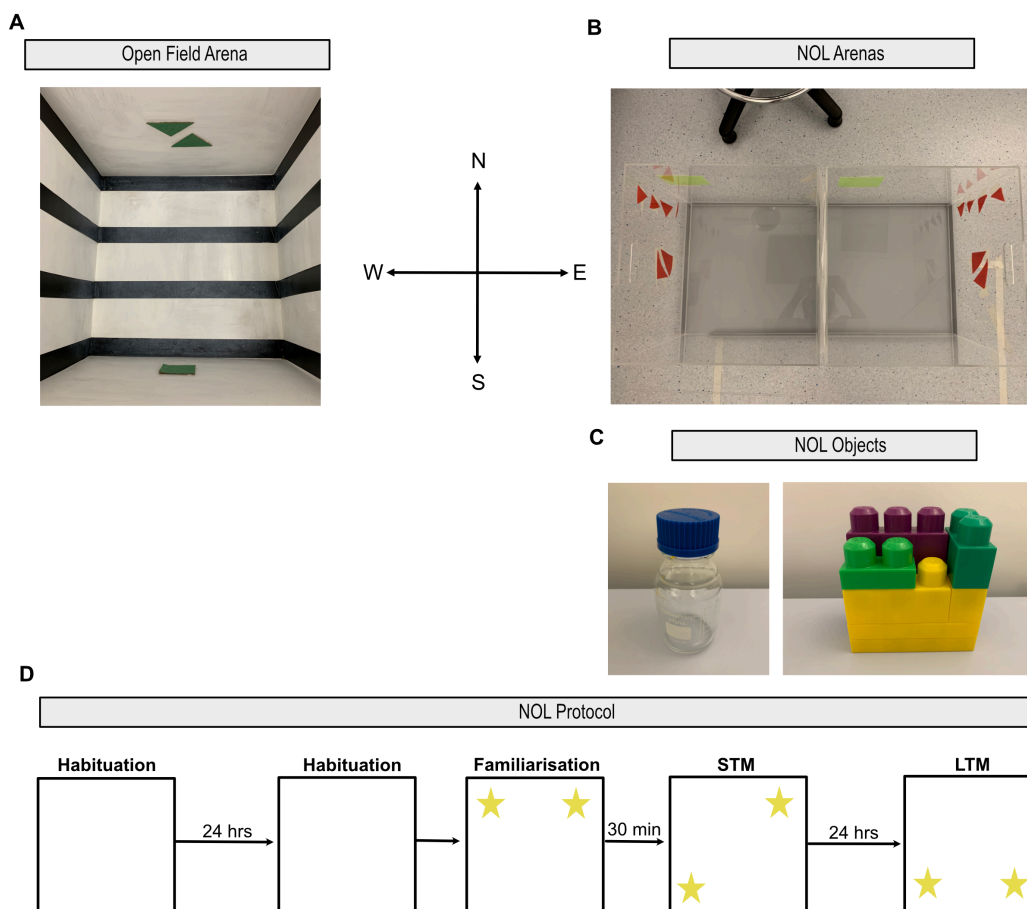


Figure 2.2.3 | OF and NOL paradigms. A Photo taken of the OF arena. **B** Photo taken of both the arenas used for NOL. **C** Photos of the two different

objects used in NOL, the use of which were counterbalanced between genotypes. **D** Schematic of the NOL behavioural protocol.

2.2.8 | The effects of anaesthesia on the SWO

The following method details a non-recovery procedure performed on WT animals. Anaesthesia was induced with 5% isoflurane and mice were mounted onto a stereotaxic frame where anaesthesia was maintained using approximately 2% isoflurane delivered in oxygen at 1 L/min. The anaesthesia level was monitored by periodically checking for a pedal reflex (paw pinch) throughout the recording. Body temperature was additionally maintained at around 36-37°C using a feedback rectal probe and heat mat.

Neural signals were acquired as described in **section 2.2.4**, with the headstages attached to clamps on the stereotaxic frame to support their weight. To reduce unwanted vibration and electrical noise, an air table was turned on, a Faraday cage was placed over the stereotaxic frame and several pieces of equipment were grounded to the OpenEphys acquisition box. A pressure transducer was placed under the animal's thorax and was attached *via* an amplifier to the OpenEphys Acquisition box to monitor the respiration rate.

The isoflurane concentration was gradually lowered by 0.2% every 5 minutes to around 0.7-0.8% and neural activity was recorded for 15 minutes. Animals were brought back up to 1% and given an intraperitoneal injection of urethane (800 mg/Kg). Mice received a second dose of urethane (300 mg/Kg) 10 minutes later, and then a final injection (200 mg/Kg) 10 minutes after that, while gradually being brought down to 0% isoflurane. If needed, mice received a top-up, with the total dose of urethane never exceeding 1500 mg/Kg, as this can be lethal (Maggi & Meli, 1986). Once stable urethane anaesthesia was induced (based on monitoring of the breathing rate and pedal reflex), mice were recorded for 15 minutes. To keep depth of anaesthesia consistent between animals, a breathing rate of roughly 2 Hz was required as well as large amplitude, slow oscillations visible in the LFP. At the end of recordings, mice were deeply anaesthetised using a lethal dose of sodium pentobarbital (350 μ l delivered intraperitoneally) and transcardially perfused as described in **section 2.2.9**.

2.2.9 | Verification of silicon probe placement

Mice were deeply anaesthetised using a lethal injection of sodium pentobarbital (350 μ l delivered intraperitoneally). Once pedal reflexes subsided, the brain was electrolytically lesioned at several electrode sites for histological marking by applying a 70 μ A, 1 s, square wave current a total of 10 times.

Mice were transcardially perfused with 0.1 M phosphate buffer (PB) (21.88 mM $\text{H}_2\text{NaO}_4\text{P}$ and 80.83 mM Na_2HPO_4) and 4% paraformaldehyde (PFA) in 0.1 M PB. Brains were extracted and placed in 4% PFA in 0.1 M PB overnight before being transferred to a 30% sucrose solution in 0.01 M phosphate buffered saline (PBS) for cryoprotection. Using a freezing sledge microtome (Leica SM2010R with Physitemp BFS-5MP temperature controller), frozen brains (-20°C) were sectioned (40 μ m) and every 4th slice through the mPFC and dorsal CA1 was mounted and stained with DAPI. All other sections were used for immunohistochemistry (see **section 2.5**).

Probe position was visualised using brightfield microscopy at 10x objective magnification (Nikon Eclipse 800 microscope with CoolLED, pE-4000 light source) and captured using a SPOT RT monochrome camera and imaging software. mPFC regions were defined based on previous literature (Van De Werd *et al.*, 2010), with electrode positions found in both the ACC and PL cortex (**Figure 2.2.4 A-B**). The electrophysiological data produced from electrodes located in the ACC and PL cortex were compared and did not show a sub-region difference. Hippocampal electrode placement was identified through histology and the changing polarity of SWRs in LFP traces recorded through the layers of CA1 (Buzsaki *et al.*, 1992; Buzsáki, 2015). Only electrodes found in *Str.P* were used for analysis (**Figure 2.2.4 C-D**).

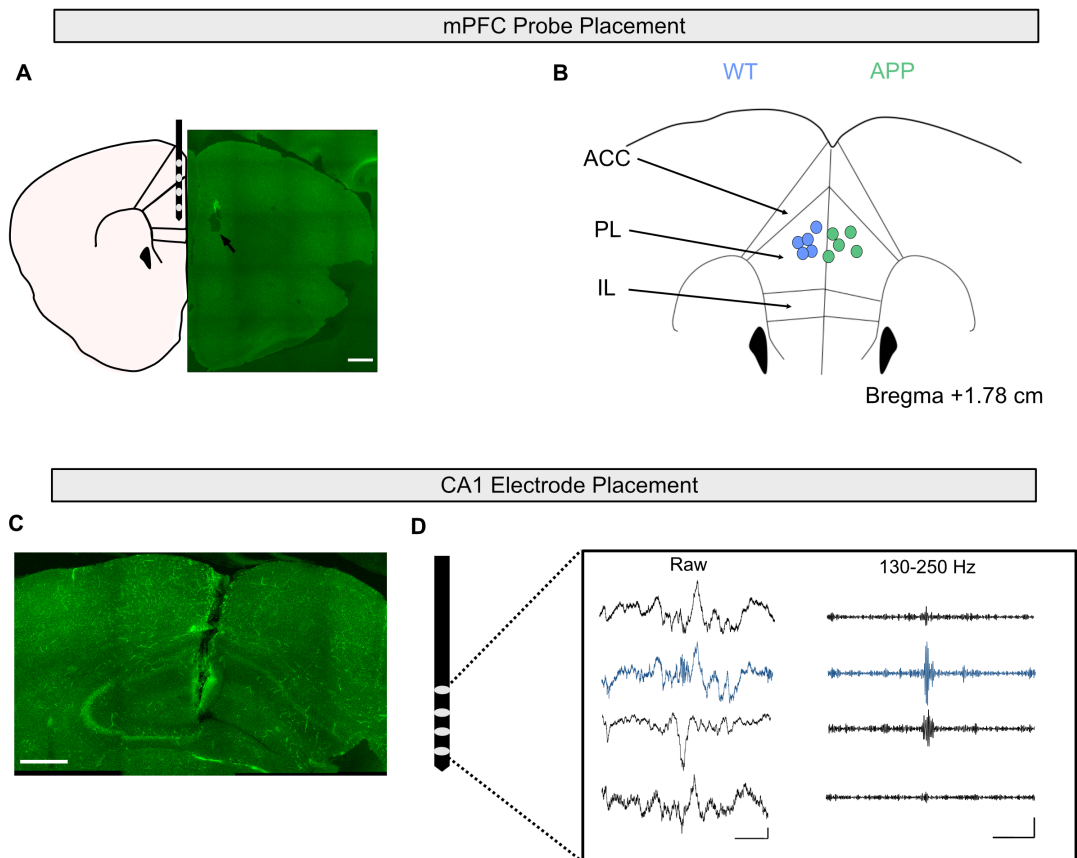


Figure 2.2.4 | Verification of electrode placement. **A** Schematic of mPFC sub-regions with silicon probe placement (left) and an example image of an electrolytic lesion at the bottom electrode site (right) described in **Figure 2.2.2.1**. Black arrow points to the lesion. Scale bar: 500 μm . **B** Schematic summarising the placement of mPFC silicon probes in WT (left, blue) and APP (right, green) animals as verified by histological markings. Dots represent tip of silicon probe. **C** Image showing a tract left by a silicon probe in the CA1 region of the hippocampus. Scale bar: 500 μm . **D** Raw and 130-250 Hz bandpass filtered traces displaying a SWR event. In blue is an electrode located in the *Str.P* layer of CA1. SWR were used to identify the layers of CA1. Scale bars: 200ms, 0.1 mV. Representative images in **A** and **C** were taken on a Leica confocal microscope and are from WT animals that had been immunohistochemically stained with anti-A β_{1-42} as described in **section 2.5.1**.

2.3 | Acute *in vivo* electrophysiology

2.3.1 | Animals

Both male and female SST^{WT} (*female*: N = 5), SST^{APP} (*female*: N = 1), PV^{WT} (*female*: N = 2, *male*: N = 3) and PV^{APP} (*female*: N = 3, *male*: N = 4) mice were used for these experiments (see **Table 2.1.1**). Mice were stereotaxically injected with viral vectors between 5-7 months old and all recordings were carried out at 8 months. A minimum of 2 weeks was given for viral transduction with animals receiving either a vector containing the excitatory Designer Receptor Exclusively Activated by Designer Drug (DREADD) (AAV_{8/2}-hSyn1-DIO-hM3D(Gq)_mCherry) (DIO: double floxed inverse orientation) or mCherry control (AAV_{8/2}-hSyn1-DIO-mCherry) (Roth, 2016) (**Figure 2.3.1 B**).

2.3.2 | Viral injection surgery

All surgical procedures were conducted using aseptic technique. Mice were first weighed, anaesthesia was induced using 5% isoflurane, their head shaved and then placed in a stereotaxic frame where surgical anaesthesia was maintained using an isoflurane concentration of around 2%. Mice were also given a subcutaneous injection of buprenorphine (0.03 mg/Kg) for analgesia. Throughout surgery, the anaesthesia level was monitored by periodically checking for a pedal reflex (paw pinch) and a breathing rate of between 1-2 breaths per second, with the isoflurane concentration adjusted accordingly. Isoflurane was delivered in a constant flow of oxygen and body temperature was additionally maintained at around 36-37°C using a feedback rectal probe and heat mat.

Iodine was applied to the scalp and a vertical incision was made to expose the skull, which was cleaned and flattened with regards to the z-position of bregma and lambda. A craniotomy was made over the mPFC (+1.75 mm anterior and +0.25 mm lateral to bregma) and a Hamilton needle (33 gauge) connected to a syringe and microinjection pump was slowly lowered to the required depth (1.7 mm from the surface of the brain). 500 nl of virus was injected into the tissue at a rate of 100 nl/min and the syringe was left in position for a further 3 minutes. The syringe was slowly extracted by 200 µm, left for 2 minutes, then removed from the brain. The site was cleaned and the skin was sutured (**Figure 2.3.1 A-B**).

Post-operation, mice were given a subcutaneous injection of carprofen (1 mg/Kg) and monitored in a heated recovery chamber for 30-60 minutes or until they had fully regained consciousness. Mice were given a second dose of carprofen (1 mg/Kg) the following morning and were monitored closely throughout the rest of the experiments.

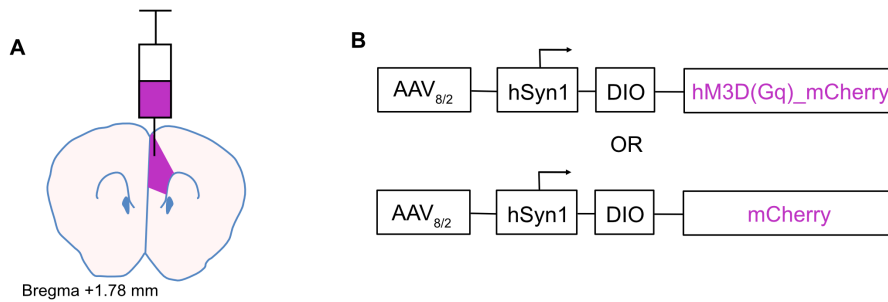


Figure 2.3.1 | Viral injection procedure in the mPFC. **A** Schematic showing unilateral targeting of the viral vector (purple) to the mPFC. **B** Schematic showing the design of the viral vectors that were intracerebrally injected.

2.3.3 | Silicon microelectrode arrays

32-channel silicon microelectrode arrays were used to record the LFPs produced by the mPFC and dorsal CA1. Probes had 4 shanks spaced 400 μm apart, an inter-electrode spacing of 100 μm , 15 μm electrode diameter and a CM32 adapter for attachment to an Intan pre-amplifier (model: A4x8-5mm-100-400-177-CM32). The electrodes had an impedance between 0.3-0.4 $\text{m}\Omega$ (**Figure 2.3.2**).

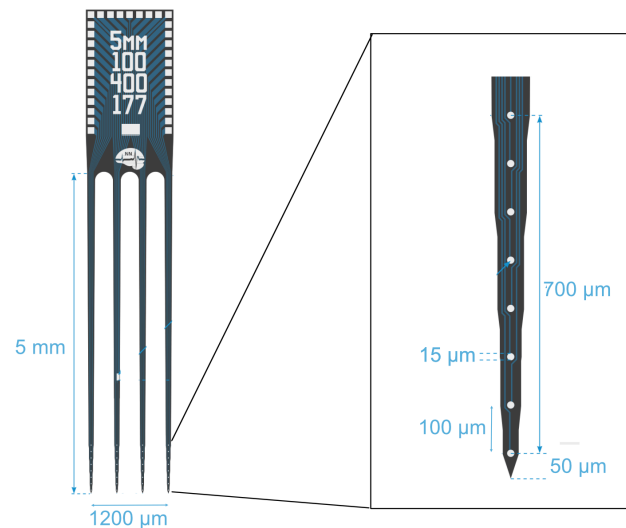


Figure 2.3.2 | Size specifications of microelectrode used during acute *in vivo* electrophysiology. Images taken from <https://www.neuronexus.com/>.

2.3.4 | Acquisition of neural signals

LFPs in both the mPFC and dorsal CA1 were acquired using the parameters described in **section 2.2.4**.

2.3.5 | Experimental set-up

The following method details a non-recovery procedure. Anaesthesia was induced using 5% isoflurane, their heads were shaved and mice were mounted onto a stereotaxic frame where surgical anaesthesia was maintained using approximately 2% isoflurane. Throughout surgery the anaesthesia level was monitored by periodically checking for a pedal reflex (paw pinch). Isoflurane was delivered in a constant flow of oxygen and body temperature was additionally maintained at around 36-37°C using a feedback rectal probe and heat mat.

The scalp was removed to expose the skull and was cleaned and flattened with regards to the z-position of bregma and lambda. Marks in the skull were made over the mPFC (+1.75 mm anterior and +0.25 mm lateral to bregma) and dorsal CA1 (-2 mm posterior and 1.4 mm lateral to bregma) and a craniotomy was carefully drilled and removed surrounding the coordinate. A skull screw that had been soldered to silver wire was inserted over the cerebellum to act as a reference for the probes. The silicon probes were inserted to the required depth (mPFC: 2 mm, CA1: 1.6 mm from the surface of the brain) and were attached to

the reference wire. Care was then taken to reduce any unwanted noise; an air table was turned on, a Faraday cage was placed over the stereotaxic frame and both probes as well as several pieces of equipment were grounded to the OpenEphys acquisition box. A pressure transducer was placed under the animal's thorax that was attached *via* an amplifier to the OpenEphys Acquisition box to monitor the breathing rate (Lockmann *et al.*, 2016).

Mice were given a subcutaneous injection of chlorprothixene hydrochloride (2 mg/Kg, 5 μ l/g), a sedative that is frequently used in conjunction with low concentrations of isoflurane to evoke anaesthesia for neurophysiological recording (Procyk *et al.*, 2015; Hillier *et al.*, 2017). The probes were allowed to settle in the brain for 30 minutes prior to recording. The concentration of isoflurane was gradually lowered by 0.2% every 5 minutes until stable anaesthesia was achieved between 0.4-0.7%. 15 minutes of baseline activity was recorded. The isoflurane concentration was increased to around 1% and mice were given a subcutaneous injection of 0.9% sterile saline (5 μ l/g). After 30 minutes, the concentration of isoflurane was reduced to 0.4-0.7% and a second baseline recording was made for 15 minutes to act as an internal control. To keep the anaesthesia depth consistent between recordings and animals, a breathing rate of roughly 2 Hz was maintained as well as visible large amplitude, slow oscillatory activity in the LFP. Mice were then given a subcutaneous injection of compound 21 (1 mg/Kg, 5 μ l/g) at 1% isoflurane and left for 30 minutes before the isoflurane concentration was reduced to 0.4-0.7% and further 15 minutes were recorded. Mice were given a terminal overdose of sodium pentobarbital (350 μ l delivered intraperitoneally) 2 hours post-injection of compound 21, to allow time for drug efficacy and cFos expression. Mice were then transcardially perfused as described in **section 2.2.9 (Figure 2.3.3)**.

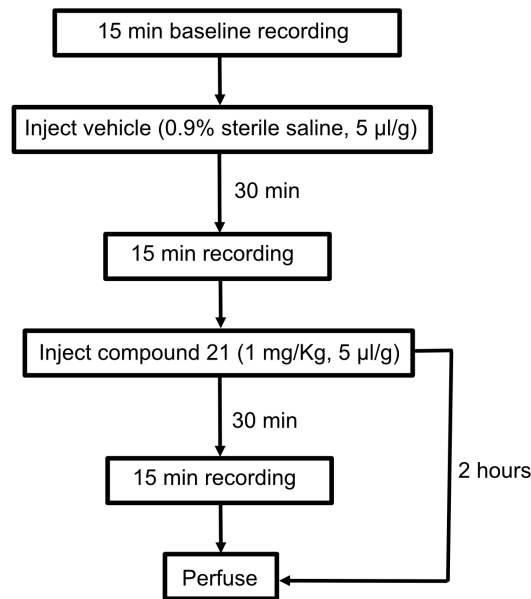


Figure 2.3.3 | A flow diagram describing the experimental methods used to chemogenetically study the effects of PV- and SST-expressing interneuron populations on UDS dynamics.

2.3.6 | Histological verification of probes

Mice were given a terminal overdose of sodium pentobarbital (350 μl delivered intraperitoneally). Prior to insertion into the brain for acute *in vivo* recording, probes were dipped in the fluorescent far-red shifted dye DiD (1,1'-Dioctadecyl-3,3,3',3'-Tetramethylindodicarbocyanine Perchlorate) for histological verification (**Figure 2.3.4 A**). Far-red was chosen to distinguish probe marking from viral expression of fluorescent proteins such as mCherry. All other procedures remained the same as in **section 2.2.9**. Only the silicon probe shanks located in the mPFC were used for analysis and data were compared between electrodes to determine whether there was an effect of mPFC sub-region (**Figure 2.3.4 B**).

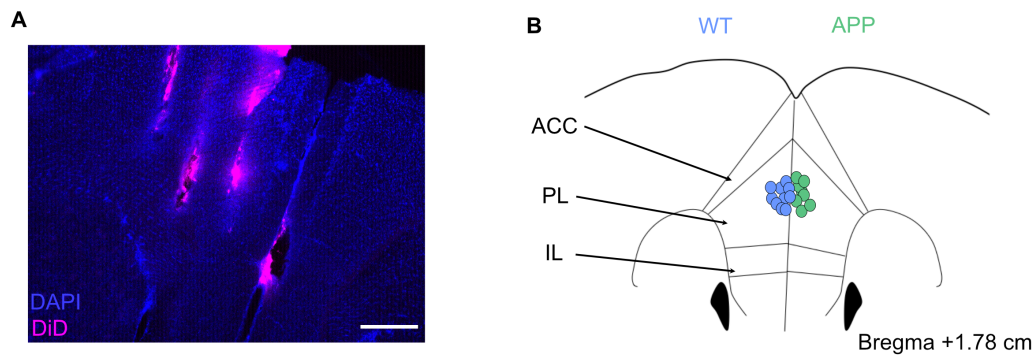


Figure 2.3.4 | Histological verification of silicon probe placement. **A** A representative image of the markings left by the silicon probe described in **Figure 2.3.2**. Scale bar: 200 μm . **B** Schematic summarising the placement of mPFC silicon probes in pooled WT (left, blue) and APP (right, green) animals as verified by histological markings. Dots represent tip of silicon probe.

2.4 | Analysis of electrophysiological data

All electrophysiological data were analysed using custom-made scripts in MATLAB.

2.4.1 | Spectral analysis

Spectral analysis was carried out using the Chronux toolbox, using the function *mtspecgramc* (Bokil *et al.*, 2010). This function allows the power-frequency relationship of a signal to be displayed as a function of time. The signal is divided into discrete time windows and then a Slepian window function is applied prior to performing a Fast-Fourier Transform (FFT), to smooth the signal's tail ends and prevent discontinuities that display as low frequency noise in the spectrum. Multiple window functions were applied to each time window (multitaper spectral analysis) and averaged together to yield a smoother spectral estimate and reduce spectral leakage (Melman & Victor, 2016). The average power spectrum was obtained by averaging the power and frequency components of the signal across time. Where appropriate, the width of the time window used will be stated. In all instances, 3 tapers were used as the average spectra that were produced resulted in the best balance between being smooth while not obscuring smaller changes in power (**Figure 2.4.1**).

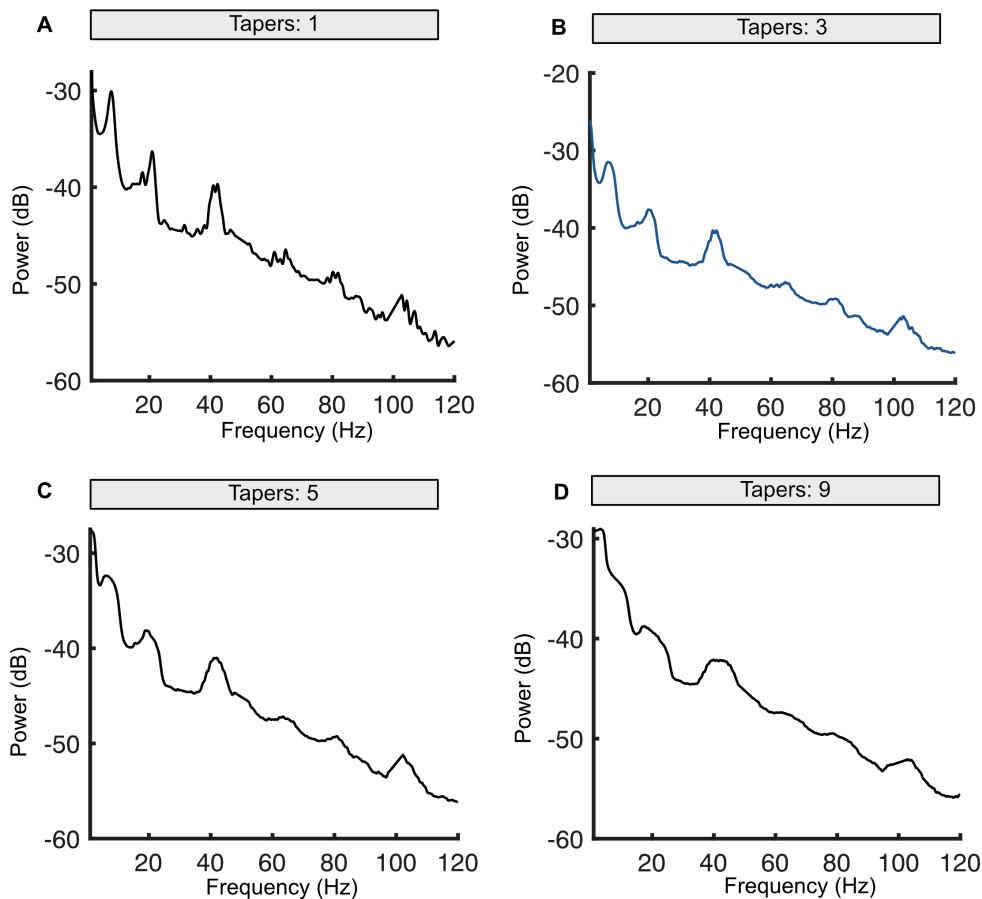


Figure 2.4.1 | Effect of taper parameters on power spectra. Representative power spectra taken from a hippocampal electrode as a mouse explored an open field for 1 hour. The resultant spectra differ depending on the number of tapers used. **A** Tapers: 1 **B** Tapers: 3. **C** Tapers: 5. **D** Tapers: 9. In blue is the number of tapers used throughout analysis.

2.4.2 | Phase-amplitude coupling

Several different phase amplitude (PAC) coupling methods exist and have been compared elsewhere (Hülsemann, Naumann & Rasch, 2019). PAC was analysed following the well-verified method of (Canolty *et al.*, 2006). To calculate this, the signal(s) were first bandpass-filtered for the phase (f_p) and amplitude frequencies (f_a) (4th order IIR Butterworth) (**Figure 2.4.2 A, B**). The Hilbert transform was then applied to both signals to obtain the instantaneous phase values of the slower oscillation ($\theta_{f_p}(t)$) and instantaneous amplitude values of the faster oscillation ($A_{f_a}(t)$), both as a function of time (t) (**Figure 2.4.2 C**). These values were arranged in ascending phase order ($-\pi:\pi$) and were combined to create a composite signal of complex values ($Z_{f_p,f_a}(t)$). Each data point reflecting the

instantaneous amplitude of the faster oscillation at each phase of the slower oscillation, described by the below equation:

$$Z_{fp,fa}(t) = A_{fa}(t) * e^{i\theta_{fp}(t)}$$

These values were averaged to obtain the mean instantaneous amplitude, or mean vector length (MVL), that reflects the coupling strength of the two oscillations (**Figure 2.4.2 D**).

$$MVL = |Z_{fp,fa}(t)_{average}|$$

In order to obtain a standardised MVL, to allow statistical comparison, the composite signal was put through permutation testing (Canolty *et al.*, 2006). First, a set of surrogate composite signals were created by offsetting the instantaneous amplitude ($A_{fa}(t)$) and instantaneous phase ($\theta_{fp}(t)$) by a time lag. In all instances, a set of 100, random, surrogate composite signals were created. The mean (μ) and standard deviation (SD) (σ) of the instantaneous amplitudes of the surrogate composite signals were obtained. These values were used in combination with the original MVL to generate a z-score, with the value generated describing how far away the original MVL fell relative to the average surrogate MVL (μ). This value was called the modulation index (MI).

$$MI = \frac{(MVL - \mu)}{\sigma}$$

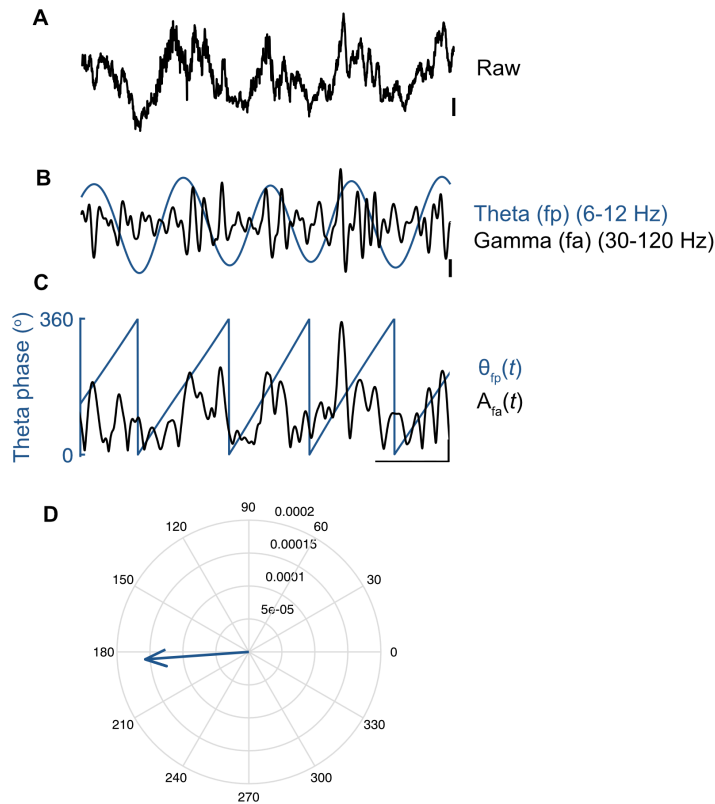


Figure 2.4.2 | Method for measuring the PAC between two oscillations. A Raw LFP taken from an electrode situated in *Str.P*. Scale bar: 100 μ V. **B** Bandpass-filtered traces showing theta (fp) and gamma (fa) oscillations. Scale bar: 50 μ V. **C** Traces display the instantaneous phase of theta ($\theta_{fp}(t)$) and instantaneous amplitude of gamma ($A_{fa}(t)$) over time. Scale bar: 100ms, 30 μ V. **D** Polar plot representing the mean instantaneous amplitude (MVL) of the composite signal ($Z_{fp,fa}(t)$), pointing in the direction of the mean instantaneous phase.

2.4.3 | Detection of slow wave sleep

The three stages of NREM sleep are typically grouped together in mice and named slow wave sleep (SWS) (Latchoumane *et al.*, 2017; Adamantidis, Gutierrez Herrera & Gent, 2019). An average mouse sleep cycle lasts around 20 minutes (90 minutes in humans) and animals were recorded for 3 hours. To isolate SWS periods from non-SWS periods, signals were split into sections defined as either non-SWS (awake, microarousals, REM sleep) or SWS, using an algorithm based on previously published work (Kohto *et al.*, 2008; Witton *et al.*, 2016).

First, using Noldus Ethovision software, video recordings of mice were manually scored offline into 30 second epochs of movement vs non-movement. For an epoch to be defined as non-movement, mice had to be completely stationary for the full 30 seconds. Next, LFP signals were split into 30 second epochs and the power of SWO/delta oscillations (1-4 Hz) and theta oscillations (6-12 Hz) were found using a non-overlapping 2 second window and a theta:delta power ratio was created (**Figure 2.4.3 A**). If the power ratio in a 30 second epoch fell below a threshold (median + 1 SD of the cumulative power ratios from all epochs), signifying greater delta power over theta, and was also accompanied by a lack of movement, the epoch was considered SWS (**Figure 2.4.3 B-C**). If an epoch did not meet this requirement it was considered to be non-SWS; only SWS epochs were used for subsequent analysis. A representative channel from the mPFC was used for detection and the obtained SWS epochs were extracted from all other channels. All large-amplitude artefacts were removed from the signal and adjoining data points were linearly interpolated. The portions of data removed from the signal were kept consistent between channels, to prevent shifts in the time-domain between channels. Automatically-detected epochs of SWS were visually confirmed by ensuring that delta and / or SWOs were present in the filtered LFP (**Figure 2.4.3 D**).

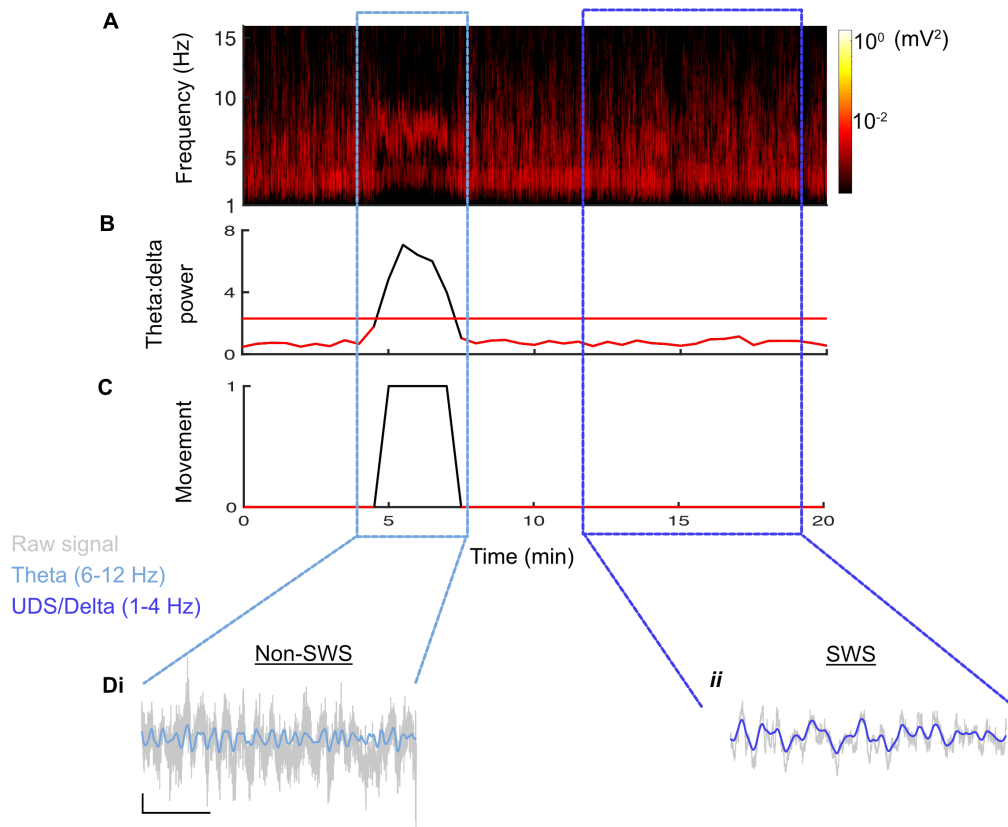


Figure 2.4.3 | Method for isolating periods of SWS. **A** Spectrogram showing power changes over time within the combined UDS and delta band (1-4 Hz) and theta (6-12 Hz) band. **B** Corresponding theta:delta power ratio over time. Horizontal red line shows the threshold for distinguishing periods of non-SWS from SWS (median + 1SD). **C** Corresponding manually-scored movement of the animal over time, taken as a binary measure, with 1 showing movement and 0 showing no movement. **B-C** Portions of the time series highlighted in red signify periods of detected SWS that fell below the theta:delta ratio and when no movement was detected. **D** Example traces of theta oscillations in non-SWS (*i*) and UDS and delta oscillations during SWS (*ii*). Scale bars: 1 s, 200 μV.

2.4.4 | SWO and delta power analysis

Signals were first high-pass filtered (4th order, IIR Butterworth, 0.35 Hz) and detrended to offset the DC shift. Given the low frequency of the SWO (0.5-1.25 Hz), 5 second non-overlapping windows were used that could capture at least 2 cycles of a 0.5 Hz rhythm. Resultant power spectra were normalised to total spectral power to counteract any differences in electrode impedance and then converted into decibels (dB), to facilitate visualisation of power in higher

frequency bands. SWO and delta power were taken as the average power between 0.5-1.25 Hz and 1.25-4 Hz, respectively. Spectra were visually examined to confirm the presence of defined SWO and delta peaks.

2.4.5 | Detection of the SWO, spindles and ripples

To analyse the dynamics of each of the three cardinal oscillations, custom-made detection scripts based on previously described methods were used to isolate and analyse individual oscillation cycles (Möller *et al.*, 2009; Chauvette *et al.*, 2011; Nir *et al.*, 2011; Phillips *et al.*, 2012; David *et al.*, 2013; Staresina *et al.*, 2015; Latchoumane *et al.*, 2017; Niethard *et al.*, 2018; Bartsch *et al.*, 2019). UDS were detected by first low-pass-filtering the raw SWS signal (10th order IIR Butterworth, 1.5 Hz) and all negative to positive zero-crossings were found. Two consecutive negative-positive zero-crossings within 0.25-2 s (0.5-1.25 Hz) of each other and the largest peak and trough between them were used in the next stage of detection. Events were classed as UDS if the peak was greater than the 60th percentile of all detected peaks and the total amplitude (peak-trough) was also greater than the 60th percentile of all detected amplitudes (**Figure 2.4.4 A**).

For the detection of spindle events, the raw SWS signal was first bandpass-filtered (16th order IIR Butterworth, 9-16 Hz), z-scored and peaks were interpolated using cubic spline interpolation. Peaks that crossed a 3.5 SD threshold crossing were found and start and stop times of 1.5 SD either side were taken. Events were then classed as spindles if they were between 0.5 and 2 s long and had an intra-spindle frequency (taken as the number of positive peaks divided by the length of the event) of 11-15 Hz. Events that occurred within 0.25 s of each other were grouped and re-assessed by the same criteria (**Figure 2.4.4 B**).

Ripples were detected with similar methods to spindles; the raw SWS signal was bandpass-filtered (26th order IIR Butterworth, 130-250 Hz), z-scored and peaks interpolated using cubic spline interpolation. Peaks that crossed a 6.5 SD threshold were found and start and stop times were taken as 2 SD. Events were classed as ripples if their duration was between 30-250 ms and had an intra-ripple

frequency of 130-250 Hz. Events that were within 50 ms of each other were grouped and re-assessed for the same criteria (**Figure 2.4.4 C**).

For each oscillation, the duration, amplitude (largest peak – trough), intra-oscillation frequency and incidence of oscillation events was obtained. Additionally, a short-time FFT was computed for individual spindle and ripples events, with data from events located on the same channel averaged together. Spindle power was calculated as the total 11-15 Hz power using a 0.09 s time window (1/11 Hz) with 50% overlap. Ripple power was calculated as the total 130-250 Hz power using a 0.008 s time window (1/130 Hz) with 50% overlap.

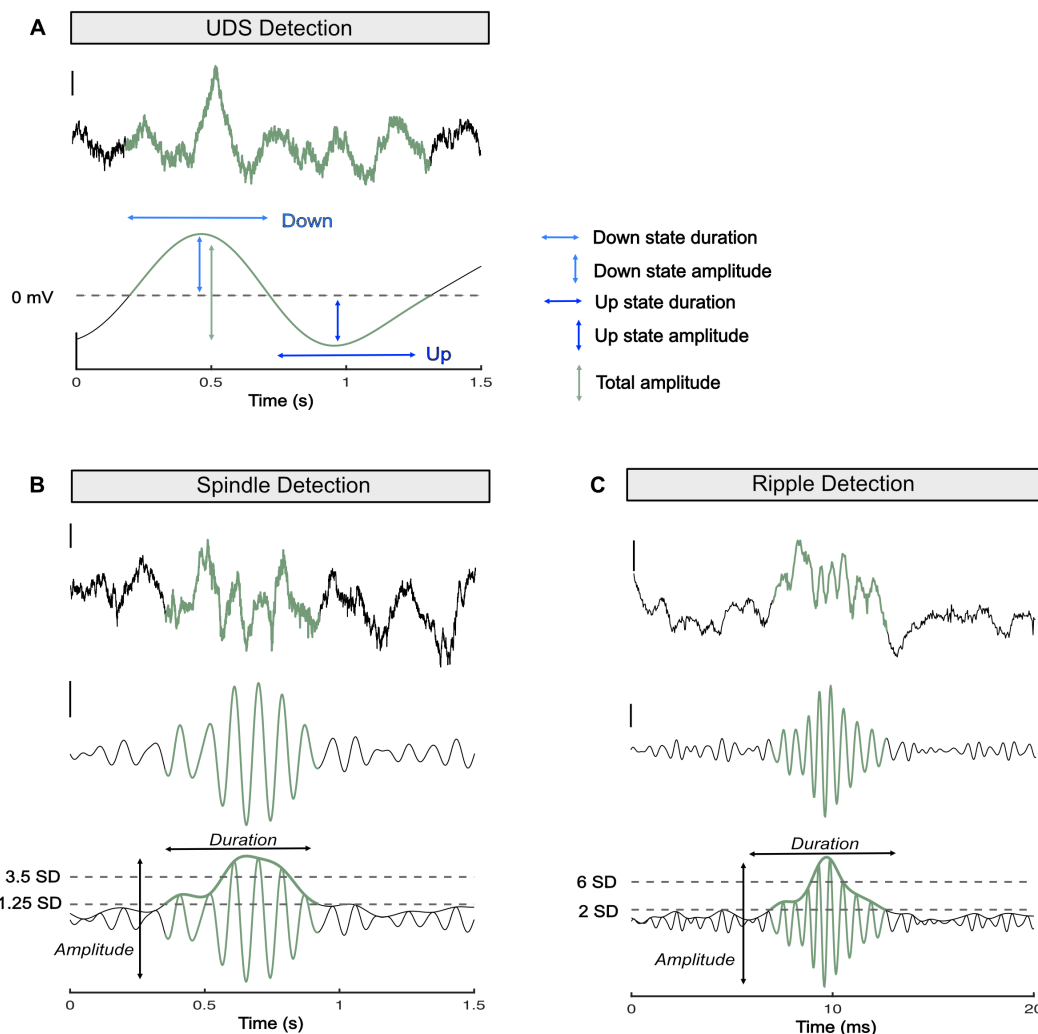


Figure 2.4.4 | Schematics representing sleep oscillation detection methods. A Method for detecting UDS. Raw signal (top) scale bar: 200 μ V, 1.5 Hz low-pass filtered signal (bottom) scale bar: 50 μ V. **B** Method for detecting spindles. Raw Signal (top) scale bar: 200 μ V. 9-16 Hz filtered signal (middle,

bottom) scale bar: 100 μ V. **C** Method for detecting ripples. Raw Signal (top) scale bar: 200 μ V. 130-250 Hz filtered signal (middle, bottom) scale bar: 50 μ V.

2.4.6 | Cross-frequency analysis of sleep oscillations

2.4.6.1 | UDS-gamma coupling

Communication between the cardinal oscillations drives systems consolidation (Diekelmann & Born, 2010; Maingret *et al.*, 2016b), therefore I set out to analyse the degree of coupling between these different oscillations. Gamma oscillations are found nested within SWO Up states (Steriade *et al.*, 1996; Valderrama *et al.*, 2012) and are considered by some to be “fragments of wakefulness” (Destexhe *et al.*, 2007). Given that gamma oscillations are disrupted during awake behaviour in first-generation mouse models of amyloidopathy (Verret *et al.*, 2012; Martinez-Losa *et al.*, 2018) and in the APP^{NL-G-F} mouse model (Jun *et al.*, 2020), it was hypothesised that SWS-nested gamma oscillations would also be disrupted in the APP^{NL-G-F} mouse model. Gamma power that was time-locked to individual UDS was computed using a short-time FFT. A 1 s window with 5% overlap was used and the average power (area under the curve, trapezoid method) was obtained for low gamma (30-60 Hz) and high gamma (60-120 Hz); frequency ranges for each band were chosen based on the peaks visible in the power spectra. Next, analysis windows spanning 2 s on each side of detected Down states were used to analyse the PAC of detected UDS with both low and high gamma oscillations. Electrical noise at 50 Hz and 100 Hz (4th order IIR Butterworth Bandstop, 47-53 Hz and 97-103 Hz, respectively) was removed from the spectra for analysis.

2.4.6.2 | UDS-spindle and UDS-ripple coupling

If the peak of a detected spindle event occurred within 1 s after the peak of a detected Down state, the time-lag between them was calculated and sections of raw signal were cut out that began 2 s before the onset of the Down state and ended 2 s after the peak of the spindle event, to analyse the PAC of the two oscillations. The percentage of UDS that were followed by a spindle was also determined. Similar analysis methods were applied for UDS and ripples, except a 0.5 s period after the ripple peak was used for PAC. When determining the latency between different oscillations, peak times were chosen over onset /

termination times as the peaks could be more robustly and precisely detected, improving the reliability of the detection algorithm. Window sizes used were the minimum duration required to capture both oscillations and conduct successful permutation testing for PAC (see **section 2.4.2**) (Hülsemann, Naumann & Rasch, 2019).

2.4.6.3 | Spindle-spindle coupling

Spindle-spindle coupling between the mPFC and hippocampus was computed using a similar method to that described above. If a hippocampal spindle began within 1 s following the start of a cortical spindle, the latency between the onset times was computed, as was the percentage of cortical spindles coupled to hippocampal spindles. Spindle onset times were chosen instead of oscillation peaks, as spindles within the hippocampus were found to be shorter in duration than in the cortex (see **section 5.2.5**), therefore it was possible they could peak before cortical spindles.

2.4.6.4 | Spindle-ripple coupling

Spindle-ripple coupling was computed for both cortical and hippocampal spindles. If a ripple began within 2 s following the onset of a spindle, the spindle-ripple latency was determined, as was the percentage of spindles occurring with a subsequent ripple and the percentage of ripples occurring with a preceding spindle. Additionally, for hippocampal spindles, a 2 s time window either side of the spindle peak was taken to compute the PAC between spindles and ripples (Ngo, Fell & Staresina, 2020).

2.4.6.5 | UDS-spindle-ripple coupling

Lastly, the coupling of all three cardinal oscillations was investigated, as together they drive systems consolidation (Diekelmann & Born, 2010; Maingret *et al.*, 2016b). Similar methods were used as in **sections 2.4.6.2** and **2.4.6.4**. First, if the peak of a cortical spindle occurred within 1 s following the peak of a Down state, this coupling was used for the next stage of analysis. Next, if a ripple then occurred within 2 s following the beginning of the spindle, it was considered that there was coupling between all three cardinal oscillations. The frequency of these events occurring within a recording (measured in Hz) was used for analysis.

2.4.7 | Animal position during Open Field behaviour

During the OF test, two LEDs were attached to the headstage to track the animal's position during data acquisition (see **section 2.2.6**). Time-points in which the LEDs failed to reach detection levels or occurred out of range of the OF were automatically rejected and adjoining data points linearly interpolated. The animal's position was used to compute the animal's distance travelled (cm) over time as well as instantaneous speed (cm/s).

2.4.8 | Speed-modulated theta and gamma power

The frequency and power of theta and gamma oscillations in the CA1 region of the hippocampus are modulated by running speed (McFarland, Teitelbaum & Hedges, 1975; Ahmed & Mehta, 2012; Fuhrmann *et al.*, 2015). There is also evidence for speed-modulated theta power in the mPFC (Adhikari, Topiwala & Gordon, 2010a). Therefore, the speed-modulated frequency and power of theta and gamma oscillations were analysed in both brain regions. Speed was initially computed in 1 s time-bins ranging from 1-30 cm/s. The LFP was then split into corresponding 1 s time bins and the total power (area under the curve, trapezoid method) was found for theta (6-12 Hz), low gamma (30-60 Hz) and high gamma (60-120 Hz) oscillations, as well as the peak power and frequency of each oscillation. Data within 1 s bins were then averaged together for each speed and a linear regression was computed between each spectral property with speed. For spectral analysis, 1 s time bins with 50% overlap were used and resultant spectra were normalised to total power. Gamma oscillations were defined based on identified peaks in the spectra and electrical noise at 50 Hz and 100 Hz (4th order IIR Butterworth Bandstop, 47-53 Hz and 97-103 Hz, respectively) was removed from the spectra for analysis.

2.4.9 | Speed modulated theta-gamma coupling

PAC between theta and gamma oscillations has also been shown to change with running speed and was analysed similarly to speed modulated power (Sheremet *et al.*, 2019). Speed data and the LFP were binned into 0.5 s time-bins and the PAC (see **section 2.4.2**) between theta and gamma oscillations was computed

for each speed. Linear regression was used to analyse the relationship between the resultant MI and speed.

2.4.10 | Speed modulated theta coherence

Theta coherence between CA1 and the mPFC is important for the integration of spatial information with executive decision making (Jones & Wilson, 2005). Therefore, theta coherence between both regions was determined as a function of running speed. Speed data and the LFP were binned into 1 s time-bins. Coherence was analysed using the Chronux toolbox (Bokil *et al.*, 2010) (*cohgramc* function). To calculate coherence, 3 tapers were used and a 1 s time window with 50% overlap. Data were normalised to total coherence.

2.5 | Immunohistochemistry

All animals were transcardially perfused and brains were removed as described in **section 2.2.9**. Using a freezing sledge microtome (Leica SM2010R with Physitemp BFS-5MP temperature controller), frozen brains (-20°C) were sectioned (40 µm). Sections were cleaned in PBS and stored in either PBS with 0.05% sodium azide at 4°C or in antifreeze (1 L solution: 250 ml glycerol, 300 ml ethylene glycol, 250 ml 0.2 M PB, 200 ml ddH₂O) at -20°C, depending on the time between slicing and staining. All staining was carried out in-well while being agitated.

2.5.1 | PV and Aβ₁₋₄₂ staining

WT and APP animals of both sexes were used for the following immunohistochemical staining. Four different ages were used: 3 months (WT: N = 5 (female), N = 1 (male), APP: N = 4 (female), N = 3 (male)), 6 months (WT: N = 3 (female), N = 3 (male), APP: N = 3 (female), N = 4 (male)), 8 months (WT: N = 5 (female), N = 4 (male), APP: N = 4 (female), N = 7 (male)) and 16 months (WT: N = 2 (female), N = 5 (male), APP: N = 5 (female), N = 3 (male)).

Sections were first washed (3x10 minutes) in PBS with 0.3% Triton X-100 (PBS-T) before being incubated in 100 mM glycine in PBS-T for 15 minutes. Sections were then washed (3x10 minutes) in PBS-T and then left to block in 3% goat serum in PBS-T (blocking solution) for 1 hour. Slices were then incubated in

blocking solution containing a primary antibody (rabbit anti-PV, 1:5000 or rabbit anti-A β ₁₋₄₂, 1:1000) overnight at 4°C. On the second day, sections were washed (3x10 minutes) in PBS-T and then incubated in blocking solution containing biotinylated goat anti-rabbit secondary antibody (1:250) for 1 hour at room temperature. Sections were then washed (3x10 minute) in PBS-T and then incubated in blocking solution containing DyLight 488 Streptavidin (1:250) for 1 hour. Finally, sections were washed (3x10 minutes) in PBS-T, mounted onto glass slides and covered with glass cover slips with mounting medium and DAPI. As negative controls, a separate set of sections were processed identically, except with primary antibody substituted with blocking solution to determine if there was any non-specific binding of the secondary antibody.

All images were taken at 10x magnification on a Leica confocal microscope, with parameters kept consistent between images (e.g. gain, line average). Additionally, for consistency, only the right hemisphere was imaged and quantified and each brain region remained at a similar distance from bregma between animals. Brain regions were defined according to previously published criteria (Van De Werd *et al.*, 2010) and the Allen Brain Atlas (<https://mouse.brain-map.org/>).

All image analysis was carried out in FIJI software (Schindelin *et al.*, 2012). To quantify the number of PV-expressing interneurons, the cell counter plugin was used. All cell counts were normalised to the brain region area. To quantify the area covered by A β ₁₋₄₂-containing plaques, plaques were first manually drawn around and defined as regions of interest (ROI) (**Figure 2.5.1 B**). ROIs were then overlaid onto the original image and used to create a binary mask (**Figure 2.5.1 C-D**). This allowed the area covered by plaques and the average size of plaques to be determined for a given brain region.

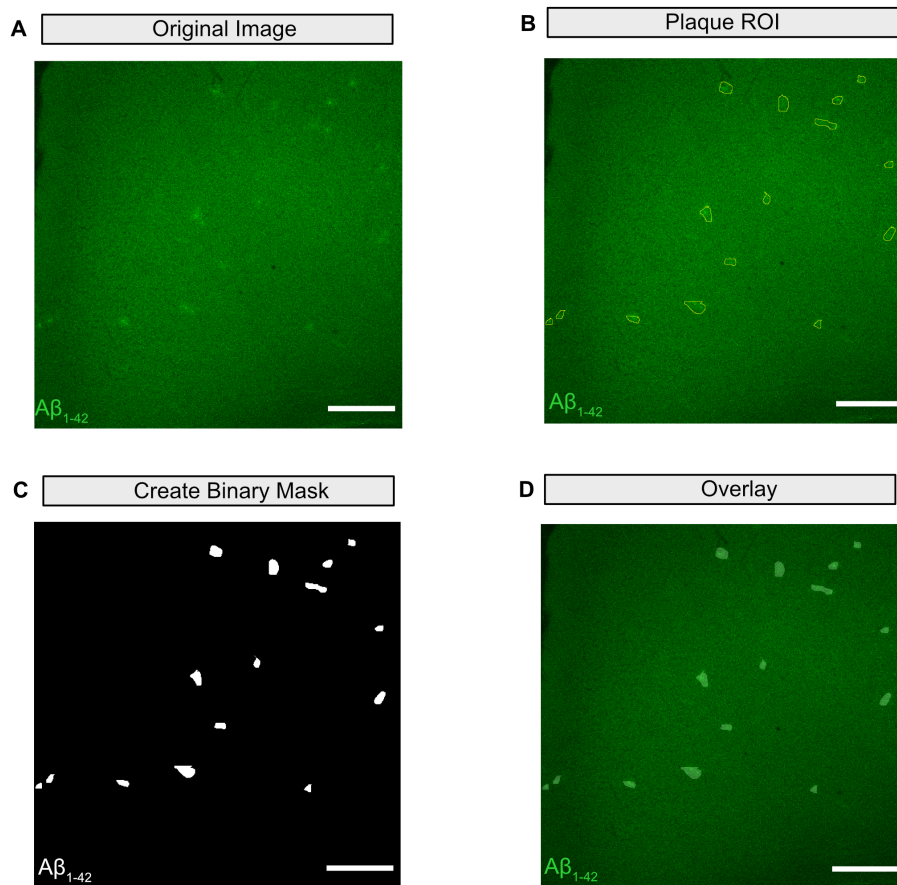


Figure 2.5.1 | Method for detecting $A\beta_{1-42}$ plaques. **A** Original image taken from the ACC of a 3 month APP mouse. **B** Plaques were manually drawn around as ROI. **C** A binary mask was created. **D** Mask was overlaid to help define brain region for analysis. Scale bar: 200 μm .

2.5.2 | cFos staining

The images found in **section 4.2, Figure 4.2.2**, were taken from an Emx1-Cre mouse that had been stereotaxically injected (500 nl, 100 nl/min) with a viral vector to transduce expression of an excitatory DREADD (AAV₈-Ehq-DIO-hM3D(Gq)_mCherry) into the barrel cortex (-0.4 mm posterior, 2.6 mm lateral to bregma, 1.7 mm depth from the surface of the brain). Surgical procedures were identical to those described in **section 2.3.2**. After allowing two weeks to achieve sufficient expression of virally-transduced genes, mice were subcutaneously injected with compound 21 (1 mg/Kg) to activate the excitatory DREADDs, with the aim of later testing for a marker of neural activation; cFos. Mice were euthanised with an overdose of sodium pentobarbital 2 hours after treatment with compound 21, to allow time for DREADD activation and subsequent increases in

cFos expression. Transcardial perfusion and processing of brains for immunohistochemistry (IHC) was carried out as described in **section 2.2.9**.

Immunohistochemical procedures were similar to those described in **section 2.5.1** except the primary antibody, rabbit anti-cFos (1:5000), was used with a conjugated secondary, goat anti-rabbit DyLight 488. Epifluorescence images were taken using a 20x objective on a Nikon Eclipse 800 microscope with a CoolLED light source and captured using a SPOT RT monochrome camera and accompanying imaging software.

2.6 | Statistical analysis

All statistical testing was carried out using GraphPad Prism. The data were first tested for normality using a D'Agostino and Pearson test. When comparing two groups, a Mann-Whitney U-test of comparable ranks was used for non-parametric data and a Student's T-test for parametric data. Welch's correction was used on parametric data that had unequal SD between groups. To compare the ranks of multiple groups, either a non-parametric Friedman's or Kruskal-Wallis test was used, on repeated measures and independent data, respectively. 2-way analysis of variance (ANOVA) was performed when analysing 2 independent variables, with Tukey's *post-hoc* pairwise comparisons used to compare the means between groups. A Spearman's rank-order correlation was employed on non-parametric data to determine the strength and direction of a relationship between two continuous variables. Linear regression was performed on the analysis described in **sections 2.4.8-2.4.10**. To compare correlation coefficients between two groups, r/R^2 values were z-transformed and statistically compared using an online Fisher z-transformation calculator (<https://www.psychometrica.de/correlation.html#fisher>).

All non-parametric results are displayed as box plots showing the median, range and the 25th and 75th inter-quartile ranges (IQR). Where appropriate, all parametric results are displayed as the mean and standard error of the mean (SEM). Descriptive statistics are reported within the figure legends.

2.7 | Lists of consumables and equipment

Antibodies		
Antibody	Source	Identifier
DyLight 488 streptavidin	Vector Laboratories	SA-5488
Rabbit anti-Ab1-42	Cell Signalling Technology	14974
Rabbit anti-cFos	Cell Signalling Technology	2250
Rabbit anti-parvalbumin	Swant	PV27
Goat anti-rabbit biotinylated	Vector Laboratories	BA-1000
Goat anti-rabbit DyLight 488	Vector Laboratories	DI-1488

Table 2.7.1 | List of antibodies used in the present study.

Viral vectors (vg = vector genomes)			
Construct	Titer	Source	Identifier
AAV _{8/2} -hEF1a-DIO- hM3D(Gq)_mCherry	$\geq 1 \times 10^{12}$ vg/ml	ETH Zurich Viral Vector Facility	V98-8
AAV _{8/2} -hSyn1-DIO- hM3D(Gq)_mCherry	$\geq 5.4 \times 10^{12}$ vg/ml	ETH Zurich Viral Vector Facility	V101-8
AAV _{8/2} -hSyn1-DIO- mCherry	$\geq 9 \times 10^{12}$ vg/ml	ETH Zurich Viral Vector Facility	V116-8

Table 2.7.2 | List of viral vectors used in the present study.

Chemicals		
Reagent	Source	Identifier
Bupenorphine	Covetrus	N/A
Carpofen	Covetrus	N/A
Chlorprothexene	Sigma-Aldrich	C1671-1G
Compound 21	HelloBio	HB6124
DiD	Fisher Scientific	11530286

Mounting medium with DAPI	2B Scientific	H-1200-10
Ethanol	Sigma-Aldrich	443611
Ethylene glycol	Sigma-Aldrich	324558
Glycerol	Sigma-Aldrich	G5516
Glycine	Sigma-Aldrich	G8898
Goat serum	2B Scientific	995-08-FA-0.1
Isoflurane	Covetrus	N/A
Paraformaldehyde (PFA)	Sigma-Aldrich	158127
Phosphate buffered saline (PBS)	Sigma-Aldrich	524650
Sodium azide	Sigma-Aldrich	S2002
Sodium chloride	Sigma-Aldrich	S9888
Sodium pentobarbital	Covetrus	N/A
Sodium phosphate monobasic	Sigma-Aldrich	S0751
Sodium phosphate dibasic	Sigma-Aldrich	S9763
Sucrose	Sigma-Aldrich	S0389
Triton X-100	Sigma-Aldrich	X102
Urethane	Sigma-Aldrich	U2500

Table 2.7.3 | List of reagents used in the present study.

Mice		
Strain	Source	Identifier
APP ^{NL-G-F}	MRC Harwell	APP ^{NL-G-F}
SST-Cre	Jackson Laboratories	B6N.Cg-Sst ^{tm2.1(cre)Zjh} /J
PV-Cre	Jackson Laboratories	B6;129P2-Pvalb ^{tm1(cre)Arbr} /J
Emx1-Cre	Jackson Laboratories	B6.129S2-Emx1 ^{tm1(cre)Krij} /J

Table 2.7.4 | List of mice strains used in the present study.

Silicon microelectrodes		
Probe	Source	Identifier
A4x8-5mm-100-400-177-CM32	NeuroNexus Technologies	N/A
Q1x4-5mm-200-177-CQ4	NeuroNexus Technologies	N/A

Table 2.7.5 | List of the silicon microelectrodes used in the present study.

Hardware		
Equipment	Source	Identifier
CoolLED Box	CoolLED	pE-4000
Confocal Microscope	Leica	DMi8
Drill (viral injection)	World Precision Instruments	503598
Drill (chronic and acute <i>in vivo</i> electrophysiology)	RS Components	472-2776
Electrode impedance tester	BAK Electronics Inc.	IMP-2A
Injection Controller	World Precision Instruments	N/A
Injection Syringe	Hamilton	Neuros
Logitech Camera	Logitech	Logitech HD Pro Web Camera C920
Microtome	Leica	SM2010R
Microtome Temperature Controller	Phsitemp	BFS-5MP
Open Ephys Acquisition Board	Open Ephys	N/A
Open Ephys I/O Board	Open Ephys	N/A
Open Field Boxes		
Stereotaxic Frame (acute <i>in vivo</i> electrophysiology)	Stoelting	51730D

Stereotaxic Frame (chronic implantation / viral injection)	David Kopf Instruments	Model 940
Stimulator	Digitimer Ltd.	DS3
SPOT RT Slider Microscope Camera	SPOT	N/A
Upright Microscope	Nikon Eclipse 800	Eclipse 800

Table 2.7.6 | List of the hardware used in the present study.

Software		
Resource	Source	Identifier
Affinity Designer	Affinity	N/A
Bonsai	Bonsai-rx.org	N/A
Ethovision	Noldus	N/A
Fiji	National Institutes for Health (Schindelin <i>et al.</i> , 2012)	N/A
Leica Acquisition Suite	Leica	LASX
MATLAB	Mathworks	R2020b
Open Ephys GUI	Open Ephys	N/A
Prism 9	GraphPad	N/A
Spot Basic Imaging Capture	SPOT	N/A

Table 2.7.7 | List of the software used in the present study.

Other		
Item	Source	Identifier
Cement	Henry Schein Dental	1113427
BA Optima 10 Curing Light	Henry Schein Dental	1118799
Intan Headstage	Intan Technologies	RHD2000
Screws	Antrin Minitature Specialists Inc	NAS721CE80-060P
Silver paint	RS-Components	101-5621

Silver wire	World Precision Instruments	AGT0525
-------------	-----------------------------	---------

Table 2.7.8 | List of other essential consumables used in the present study.

3 | Immunohistochemical analysis of PV-
expressing interneurons and A β plaques in the
APP^{NL-G-F} mouse model

3.1 | Introduction

GABAergic inhibitory interneurons are an extremely diverse group of neurons that modulate neuronal excitability, providing precise temporal windows for information processing and transfer. Interneurons are classified by their morphology, intrinsic firing properties, embryonic origin, the neuronal compartments they target and by the expression of different neuropeptides and Ca²⁺-binding proteins (Pelkey *et al.*, 2017). Parvalbumin (PV) is one such Ca²⁺-binding protein that is expressed by perisomatic-targeting fast-spiking basket cells, chandelier cells/axo-axonic cells and dendrite-targeting bistratified cells (Pelkey *et al.*, 2017). PV-expressing interneurons, particularly fast-spiking basket cells, are implicated in the generation of multiple neuronal oscillations such as the SWO, theta, gamma, spindles, and SWRs, all of which are studied and discussed in this thesis (Mann, Radcliffe & Paulsen, 2005; Sanchez-Vives *et al.*, 2010; Stark *et al.*, 2014; Amilhon *et al.*, 2015; Clemente-Perez *et al.*, 2017a).

One of the pathological hallmarks of AD is the presence of A β plaques, with soluble, oligomeric forms of A β being linked to aberrant neural activity and impaired neuronal oscillations (Busche *et al.*, 2008, 2012, 2015; Chung *et al.*, 2020a). These effects are mediated, in part, through disruptions to inhibitory neurotransmission (see **section 1.4.3**) (Busche *et al.*, 2008; Palop & Mucke, 2016). In particular, a large research focus has been placed upon PV-expressing interneurons, which display both functional and immunohistochemical changes in both humans with AD and mouse models of amyloidopathy (Verret *et al.*, 2012; Sanchez-Mejias *et al.*, 2020; Giesers & Wirths, 2020). PV-expressing interneuron hypofunction in both the hippocampus and cortex has been identified in the hAPP-J20 mouse model that has been linked to epileptic discharges and a reduction in gamma oscillation power (Verret *et al.*, 2012; Martinez-Losa *et al.*, 2018). Additionally, contrary to hypofunction, PV-expressing interneuron hyperexcitability has recently been observed in young APP/PSEN1 mice (Hijazi *et al.*, 2019). Targeting these interneurons to ameliorate their dysfunction rescues impairments to neuronal oscillations as well as improves performance in hippocampus-dependant memory tasks (Verret *et al.*, 2012; Martinez-Losa *et al.*, 2018; Hijazi *et al.*, 2019; Etter *et al.*, 2019; Chung *et al.*, 2020a).

Additionally, changes to PV-expressing interneuron immunoreactivity have also been identified. A loss of PV-expressing interneuron immunoreactivity has been observed in the brains of patients with AD (Arai *et al.*, 1987; Brady & Mufson, 1997; Mikkonen *et al.*, 1999; Sanchez-Mejias *et al.*, 2020), along with a loss of other markers of inhibition such as the neurotransmitter GABA and GABA_A receptors; the primary receptor through which PV-expressing interneurons mediate inhibition (Ambrad Giovannetti & Fuhrmann, 2019). Moreover, this loss has also been identified in several first-generation mouse models of amyloidopathy and has been found to manifest as a loss of the protein PV, as well as a loss of the interneurons themselves (Cattaud *et al.*, 2018; Ali *et al.*, 2019; Giesers & Wirths, 2020). However, a reduction in PV-expressing interneuron immunoreactivity is not consistently observed across models, with an increase being detected in young APP/PSEN1 mice (Hollnagel *et al.*, 2019). Whether these differences are due to the different mutations the models possess or reflect changes in expression as a function of disease progression is unknown.

Changes to the expression of PV-expressing interneurons can have functional consequences for neuronal networks. In the second-generation APP^{NL-G-F} KI mouse model, accumulating evidence suggests the existence of a disrupted E-I balance, consistent with first-generation mouse models of amyloidopathy and humans with AD. In these mice, cortical epileptic discharges are found at around 6-8 months (Johnson *et al.*, 2020), with impairments to fast gamma oscillations occurring in the mEC at 5 months (Nakazono *et al.*, 2017) that progress to the CA1 region of the hippocampus between 7-13 months (Jun *et al.*, 2020). However, nothing is known about how PV-expressing interneurons are affected or their contribution to these changes. Studying the immunohistochemical expression of these interneurons at different points in this disease progression can give insights into the underlying mechanisms of network dysfunction. Therefore, using immunohistochemistry, the anatomical density of PV-expressing interneurons was investigated in the APP^{NL-G-F} mouse model at ages 3, 6, 8 and 16 months. These experiments were conducted in the mPFC and CA1 region of the hippocampus as they are the main focus of this thesis and are both regions affected by AD pathophysiology (Bakker *et al.*, 2012; Palop & Mucke, 2016; Grothe *et al.*, 2017). The deposition of A β ₁₋₄₂-containing plaques was also

assessed in these regions to confirm an age-dependant increase in amyloid pathology (Nilsson, Saito & Saido, 2014; Saito *et al.*, 2014).

3.2 | Results

3.2.1 | Target brain regions

Using immunohistochemistry, the anatomical density of PV-expressing interneurons and A β_{1-42} -containing plaques was assessed in the APP^{NL-G-F} mouse model at ages 3, 6, 8 and 16 months. Analysis was restricted to the mPFC and CA1 region of the hippocampus, with the mPFC further subdivided into the anterior cingulate cortex (ACC), prelimbic (PL) and infralimbic (IL) cortices (Van De Werd *et al.*, 2010). Regions were consistently defined as described in **Figure 3.2.1** and full details of the methods used can be found in **section 2.5**.

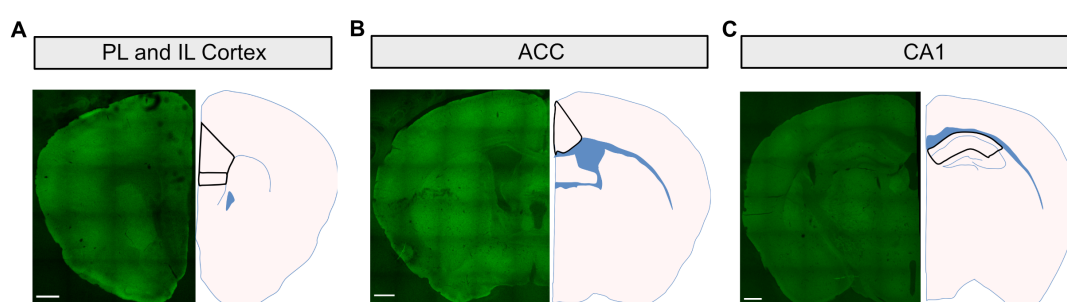


Figure 3.2.1 | Representative images and schematics displaying the defined regions of interest. A Outlined in black is the PL (top) and IL (bottom) cortices. **B** Outlined in black is the ACC. Blue shading in **A** and **B** represents ventricles and white matter tracts. **C** Outlined in black is the CA1 region of the hippocampus. Block blue shading represents white matter tracts, thin shading represents the cell body layers of the hippocampus. Scale bars: 500 μ m.

3.2.2 | A β_{1-42} plaque immunoreactivity in the mPFC and CA1 region of the hippocampus

Pathological processing of the APP protein in AD results in a larger proportion of A β protein fragments that are 42 amino acids long. These fragments are more prone to aggregation and are the main constituent of amyloid plaques (O'Brien & Wong, 2011; Long & Holtzman, 2019). The percentage of cortical and hippocampal surface area covered with A β_{1-42} plaques has previously been reported to increase with age in mice homozygous for the APP^{NL-G-F} gene, with deposition occurring as early as 2 months (Nilsson, Saito & Saido, 2014; Saito *et al.*, 2014). To confirm that this steady increase in deposition occurs within the

mPFC and CA1 region of the hippocampus, regions were immunohistochemically stained for the A β ₁₋₄₂ protein.

A statistically significant increase in the area covered with A β ₁₋₄₂ plaques was found in APP animals compared with WT controls in the IL and PL cortices (**Figure 3.2.2 A-D, E, G**) as well as the ACC (**Figure 3.2.3 A-E**) and CA1 region of the hippocampus (**Figure 3.3.4 A-E**) at ages 6, 8 and 16 months. This result is unsurprising given that WT mice do not typically develop AD pathology. APP mice did not show a statistically significant increase in the area covered by A β ₁₋₄₂ plaques at 3 months in any region, although plaques were visible. Consistent with what is already reported with this animal model, APP animals developed a statistically significant increase in plaque load over time in all mPFC sub-regions and CA1. Additionally, a statistically significant increase in the average size of the plaques with age was found in all regions (**Figures 3.2.2 H, 3.2.3 F, 3.2.4 F**) other than the IL cortex (**Figure 3.2.2 F**), although a trending increase can be seen. Therefore, mice homozygous for the APP^{NL-G-F} gene develop a steady increase in the deposition of A β ₁₋₄₂ in the mPFC and CA1.

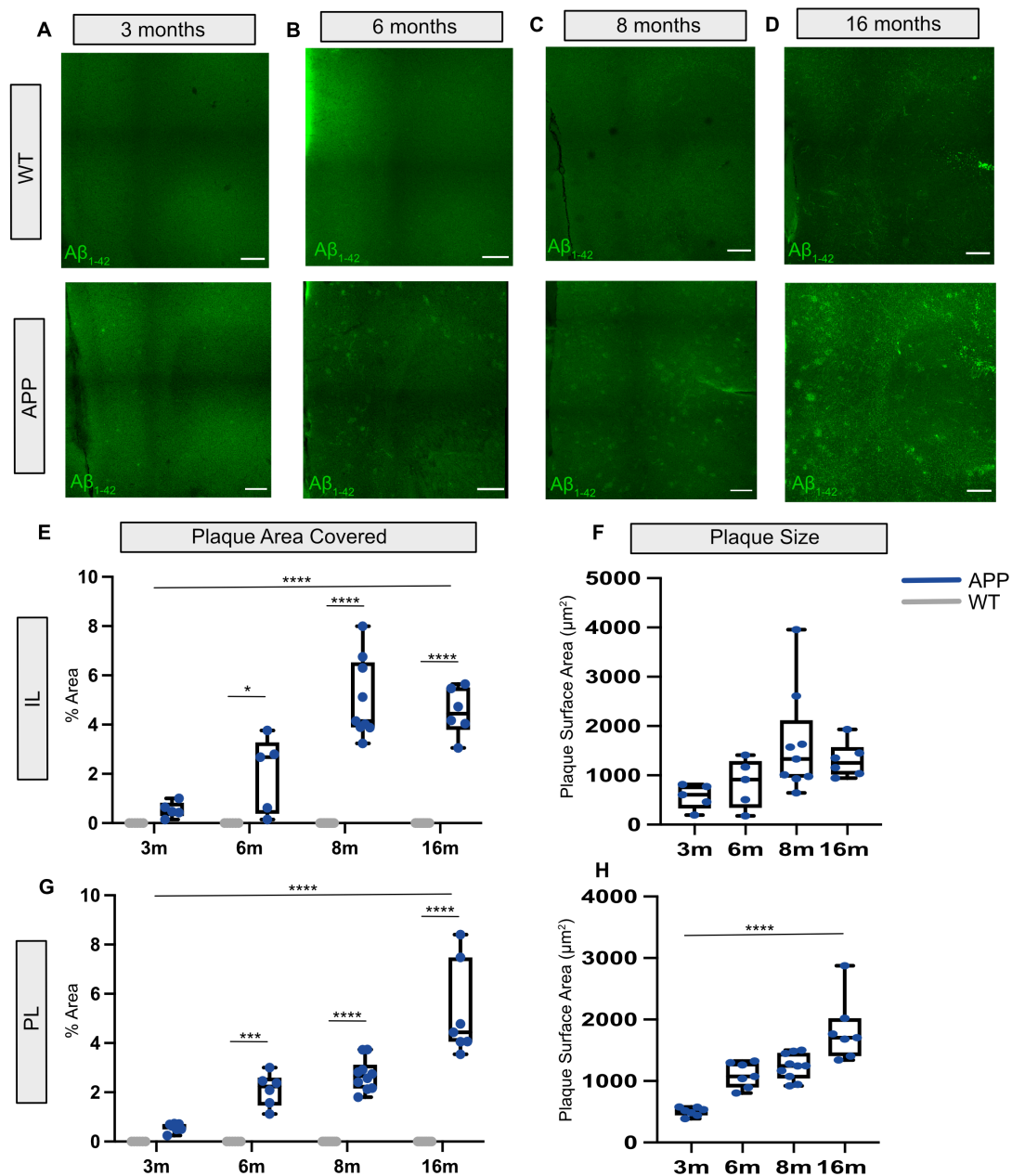


Figure 3.2.2 | Aβ₁₋₄₂ deposition increases with age in APP animals in the IL and PL cortices. **A-D** Representative images of Aβ₁₋₄₂ deposition in IL and PL cortices in WT and APP animals at 3 (**A**), 6 (**B**), 8 (**C**) and 16 months (**D**). Scale bars: 200 μm. **E** A statistically significant main effect of age ($F(3,48) = 20.10, p < 0.0001$, 2-way ANOVA) and genotype ($F(1,48) = 160.9, p < 0.0001$, 2-way ANOVA) was identified when analysing the area covered by Aβ₁₋₄₂ plaques in the IL cortex (**3m** WT: 0 (0-0) vs APP: 0.47 (0.28-0.82), **6m** WT: 0 (0-0) vs APP: 2.68 (0.38-3.76), **8m** WT: 0 (0-0) vs APP: 4.14 (3.89-7.99), **16m** WT: 0 (0-0) vs APP: 4.45 (3.79-5.51) %). Tukey's *post-hoc* pairwise comparisons revealed an increase in APP animals relative to WT at 6m ($p <$

0.05), 8m ($p < 0.0001$) and 16m ($p < 0.0001$). An increase was also identified between certain ages of APP animals (3m vs 8m, 3m vs 16m, 6m vs 8m, 6m vs 16m, all $p < 0.05$). **F** No statistically significant increase in the average plaque size in the IL cortex (3m: 608.2 (328.6-795.2) vs 6m: 912.6 (340.4-1290.0) vs 8m: 1331.0 (953.6-2119.0) vs 16m: 1254.0 (1013.0-1572.0) μm^2 , $F(3,21) = 2.88$, $p = 0.06$, 1-way ANOVA). **G** A statistically significant main effect of genotype ($F(1,53) = 197.8$, $p < 0.0001$, 2-way ANOVA) and age ($F(3,53) = 26.30$, $p < 0.0001$, 2-way ANOVA) was identified when analysing the area covered by $\text{A}\beta_{1-42}$ plaques in the PL cortex (**3m WT**: 0 (0-0)% vs **APP**: 0.64 (0.49-0.71), **6m WT**: 0 (0-0) vs **APP**: 2.24 (1.46-2.60), **8m WT**: 0 (0-0) vs **APP**: 2.66 (2.16-3.12), **16m WT**: 0 (0-0) vs **APP**: 4.43 (4.06-7.48) %). Tukey's *post-hoc* pairwise comparisons revealed an increase in APP animals relative to WT at 6m ($p < 0.001$), 8m ($p < 0.0001$) and 16m ($p < 0.0001$). An increase was also identified between certain ages of APP animals (3m vs 6m, 3m vs 8m, 3m vs 16m, 6m vs 16m, all $p < 0.05$). **H** A statistically significant increase in the average plaque size was found in the PL cortex (3m: 518.9 (442.0-576.3) vs 6m: 1074.0 (893.6-1297.0) vs 8m: 1246.0 (1042.0-1457.0) vs 16m: 1707.0 (1405.0-2023.0) μm^2 , $F(3,27) = 24.74$, $p < 0.0001$, 1-way ANOVA). Tukey's *post-hoc* comparisons revealing increases between certain ages (3m vs 6m, 3m vs 8m, 3m vs 16m, 6m vs 16m, 8m vs 16m, all $p < 0.05$). Box-plots display the median and ranges. Descriptive statistics display the median and IQR. * $p < 0.05$, *** $p < 0.001$, **** $p < 0.0001$.

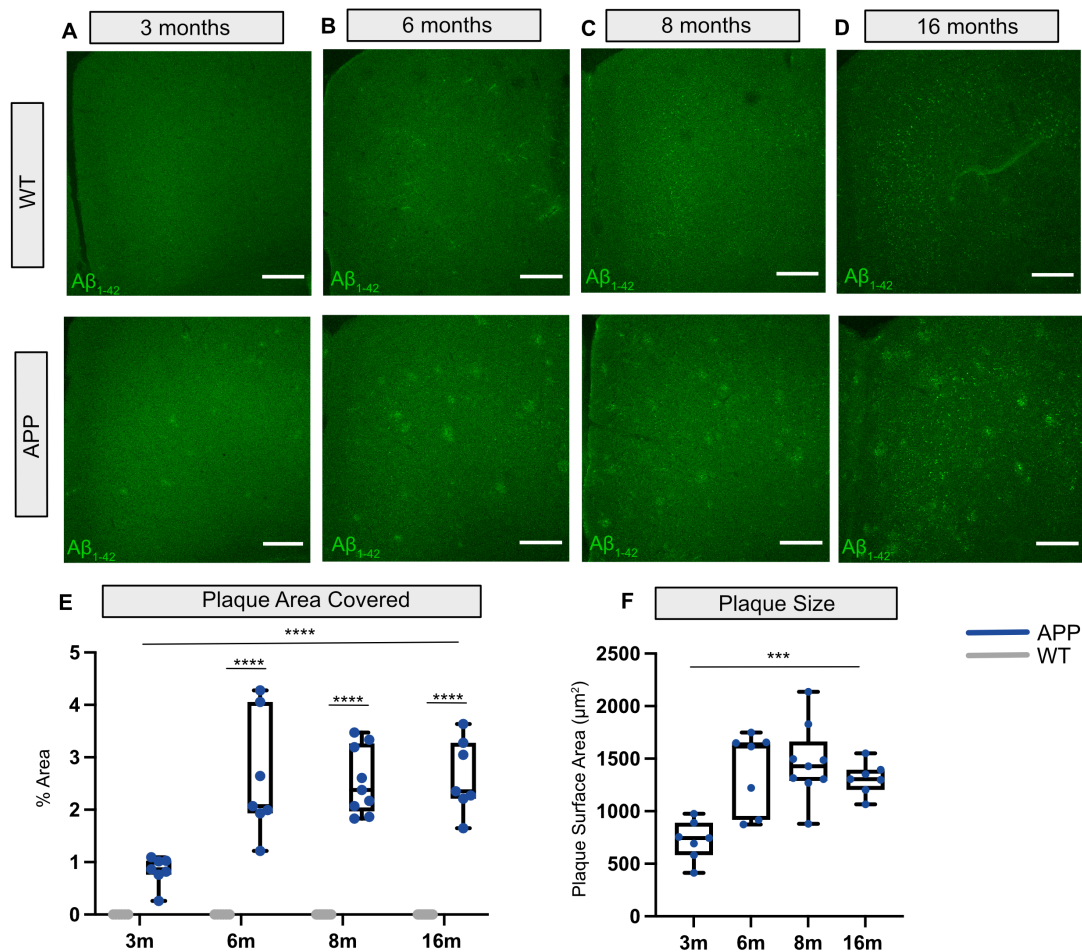


Figure 3.2.3 | $A\beta_{1-42}$ deposition increases with age in APP animals in the ACC. A-D Representative images of $A\beta_{1-42}$ deposition in the ACC cortex in WT and APP animals at 3 (A), 6 (B), 8 (C) and 16 months (D). Scale bars: 200 μm . **E** A statistically significant main effect of age ($F(3,53) = 9.47$, $p < 0.0001$, 2-way ANOVA) and genotype ($F(1,53) = 247.60$, $p < 0.0001$, 2-way ANOVA) was identified when analysing the area covered by $A\beta_{1-42}$ plaques (3m WT: 0 (0-0) vs APP: 0.86 (0.76-1.03), 6m WT: 0 (0-0) vs APP: 2.07 (1.93-4.06), 8m WT: 0 (0-0) vs APP: 4.14 (3.89-7.99), 16m WT: 0 (0-0) vs APP: 2.35 (2.21-3.26) %). Tukey's *post-hoc* pairwise comparisons revealed an increase in APP animals relative to WT at 6m ($p < 0.00001$), 8m ($p < 0.0001$) and 16m ($p < 0.0001$). An increase was also identified between certain ages of APP animals (3m vs 6m, 3m vs 8m, 3m vs 16m, all $p < 0.05$). **F** A statistically significant increase in the average plaque size was found (3m: 745.5 (582.4-890.1) vs 6m: 1615.0 (918.5-1656.0) vs 8m: 1428.0 (1288.0-1663.0) vs 16m: 1306.0 (1203.0-1394.0) μm^2 , $F(3,26) = 9.85$, $p = 0.0002$, 1-way ANOVA). Tukey's *post-hoc* comparisons revealing increases between certain ages (3m vs 6m, 3m vs 8m, 3m vs 16m,

all $p < 0.05$). Box-plots display the median and ranges. Descriptive statistics display the median and IQR. *** $p < 0.001$, **** $p < 0.0001$.

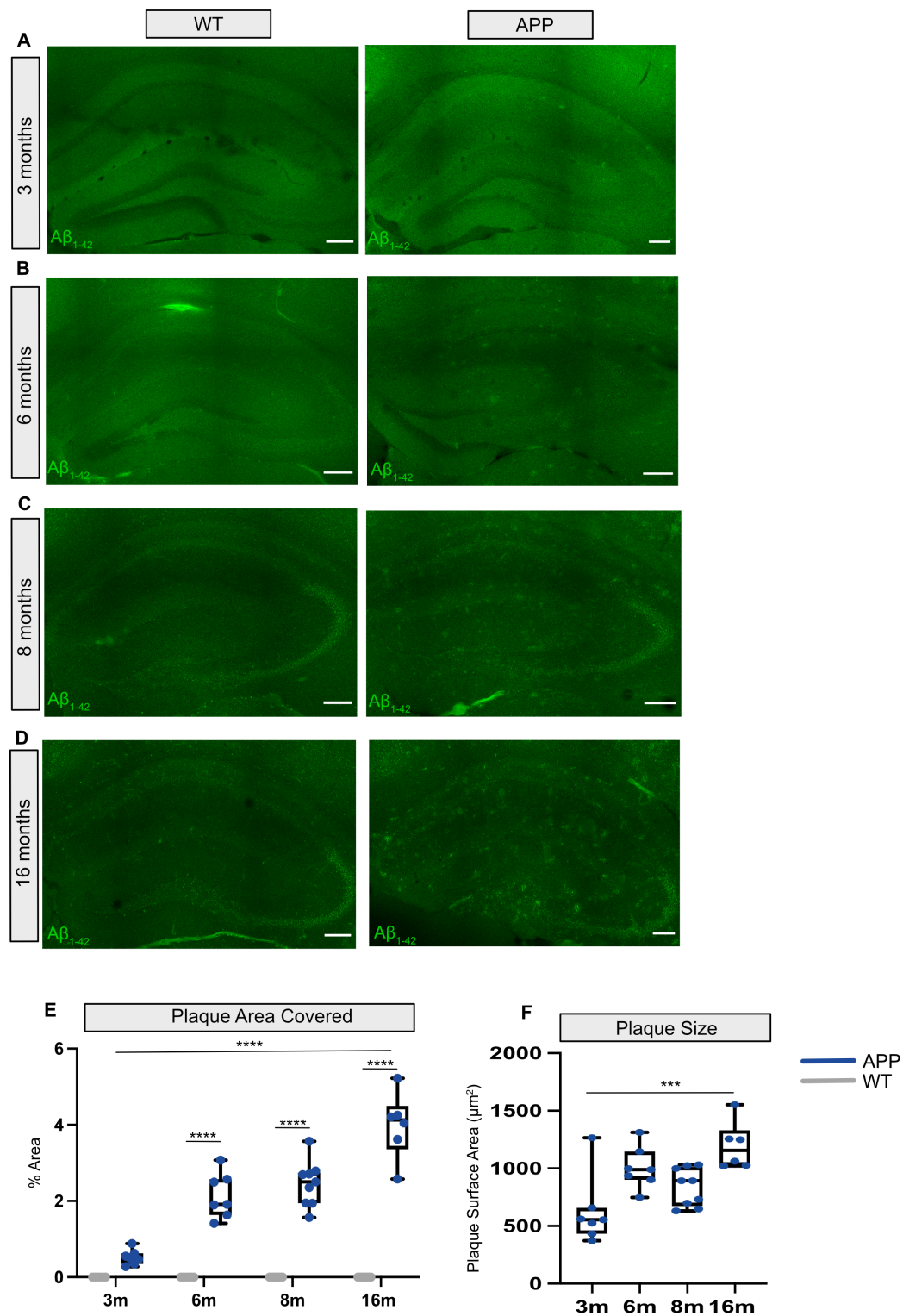


Figure 3.2.4 | $A\beta_{1-42}$ deposition increases with age in APP animals in the CA1 region of the hippocampus. A-D Representative images of $A\beta_{1-42}$

deposition in CA1 in WT and APP animals at 3 **(A)**, 6 **(B)**, 8 **(C)** and 16 months **(D)**. Scale bars: 200 μm . **E** A statistically significant main effect of age ($F(3,52) = 40.22$, $p < 0.0001$, 2-way ANOVA) and genotype ($F(1,52) = 437.20$, $p < 0.0001$, 2-way ANOVA) was identified when analysing the area covered by $\text{A}\beta_{1-42}$ plaques (**3m WT**: 0 (0-0) vs **APP**: 0.50 (0.35-0.63), **6m WT**: 0 (0-0) vs **APP**: 1.91 (1.63-2.57), **8m WT**: 0 (0-0) vs **APP**: 2.50 (1.95-2.75), **16m WT**: 0 (0-0) vs **APP**: 4.12 (3.56-4.50) %). Tukey's *post-hoc* pairwise comparisons revealed an increase in APP animals relative to WT at 6m ($p < 0.00001$), 8m ($p < 0.0001$) and 16m ($p < 0.0001$). An increase was also identified between certain ages of APP animals (3m vs 6m, 3m vs 8m, 3m vs 16m, 6m vs 16m, 8m vs 16m, all $p < 0.05$). **F** A statistically significant increase in the average plaque size was found (**3m**: 554.0 (433.1-657.0) vs **6m**: 989.7 (901.6-1146.0) vs **8m**: 891.7 (672.8-1012.0) vs **16m**: 1156.0 (1024.0-1330.0) μm^2 , $F(3,25) = 8.41$, $p = 0.0005$, 1-way ANOVA). Tukey's *post-hoc* comparisons revealing increases between certain ages (3m vs 6m, 3m vs 16m, 8m vs 16m, all $p < 0.05$). Box-plots display the median and ranges. Descriptive statistics display the median and IQR. *** $p < 0.001$, **** $p < 0.0001$.

3.2.3 | PV-expressing interneuron immunoreactivity in the mPFC

The density of PV-expressing interneuron immunoreactivity was first analysed between WT and APP animals in the IL and PL cortices. No statistically significant difference was found between genotypes for either region at all ages (**Figure 3.2.5 A-F**), nor was there a relationship between PV-expressing interneuron density and $\text{A}\beta_{1-42}$ burden (**Figure 3.2.5 G-H**). Next, the density of PV-expressing interneuron immunoreactivity was assessed in the ACC. No statistically significant difference was found between WT and APP animals at ages 3, 6 and 8 months. However, a statistically significant decrease was found in 16-month-old APP animals compared with age-matched WT controls (**Figure 3.2.6 A-E**). This change in immunoreactivity in APP animals was not found to be correlated with $\text{A}\beta_{1-42}$ burden (**Figure 3.2.6 F**). Therefore, despite the widespread presence of $\text{A}\beta_{1-42}$ plaques, the decrease in PV-expressing interneuron immunoreactivity was confined to the ACC region of the mPFC in 16-month-old APP animals. Additionally, the lack of correlation between $\text{A}\beta_{1-42}$ load and PV-expressing

interneuron immunoreactivity potentially suggests other region-specific influences acting upon PV-expressing interneuron density.

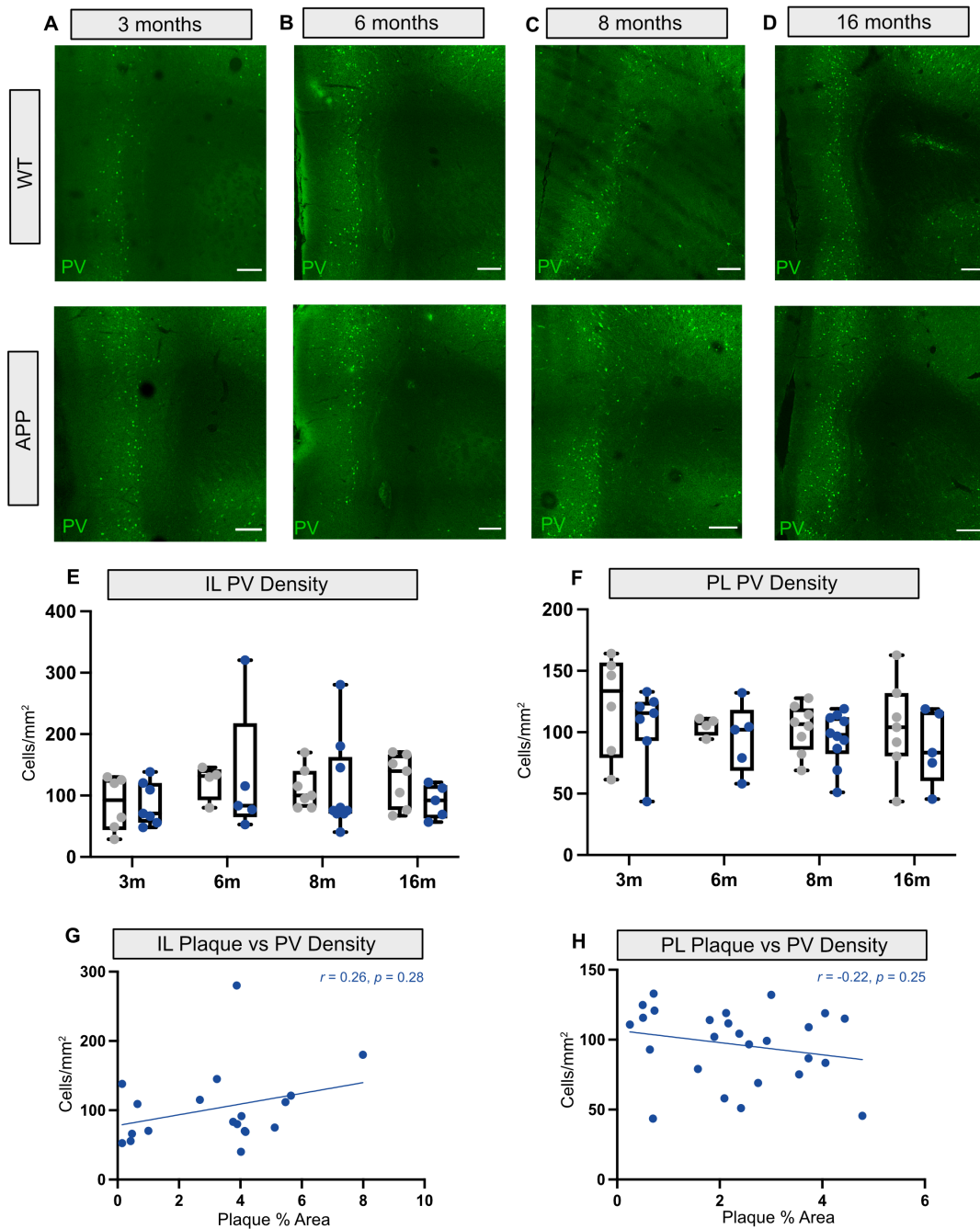


Figure 3.2.5 | PV-expressing interneuron density does not differ in APP mice compared with WT in IL and PL cortices at all ages. A-D Representative images of PV-expressing interneurons in the IL and PL cortices in WT and APP animals at 3 (**A**), 6 (**B**), 8 (**C**) and 16 months of age (**D**). Scale bars: 200 μ m. **E** No statistically significant change in PV-expressing interneuron immunoreactivity in the IL cortex of APP animals (3m WT: 92.34

(43.93-126.8) vs *APP*: 70.35 (55.56-120.30), **6m** *WT*: 132.00 (92.50-142.90) vs *APP*: 83.33 (64.65-217.60), **8m** *WT*: 100.00 (80.00-140.00) vs *APP*: 75.00 (70.00-162.50), **16m** *WT*: 139.90 (76.43-166.70) vs *APP*: 91.67 (62.65-116.50) cells/mm², all $p > 0.05$, 2-way ANOVA). **F** No statistically significant change in PV-expressing interneuron immunoreactivity in the PL cortex of *APP* animals (*WT*: 133.60 (79.07-156.80) vs *APP*: 115.70 (92.88-124.80), **6m** *WT*: 107.20 (97.18-110.50) vs *APP*: 102.00 (68.55-118.20), **8m** *WT*: 106.60 (85.76-119.40) vs *APP*: 97.92 (82.25-112.30), **16m** *WT*: 104.10 (80.39-131.80) vs *APP*: 83.45 (60.33-117.00) cells/mm², all $p > 0.05$, 2-way ANOVA). **G** No statistically significant correlation was found between the area covered by plaques and PV-expressing interneuron immunoreactivity in pooled *APP* animals in the IL ($r = 0.26$, $p = 0.28$, Spearman's correlation) and **H** PL cortex ($r = -0.23$, $p = 0.25$, Spearman's correlation). Box-plots display the median, IQR and ranges. Descriptive statistics display the median and IQR.

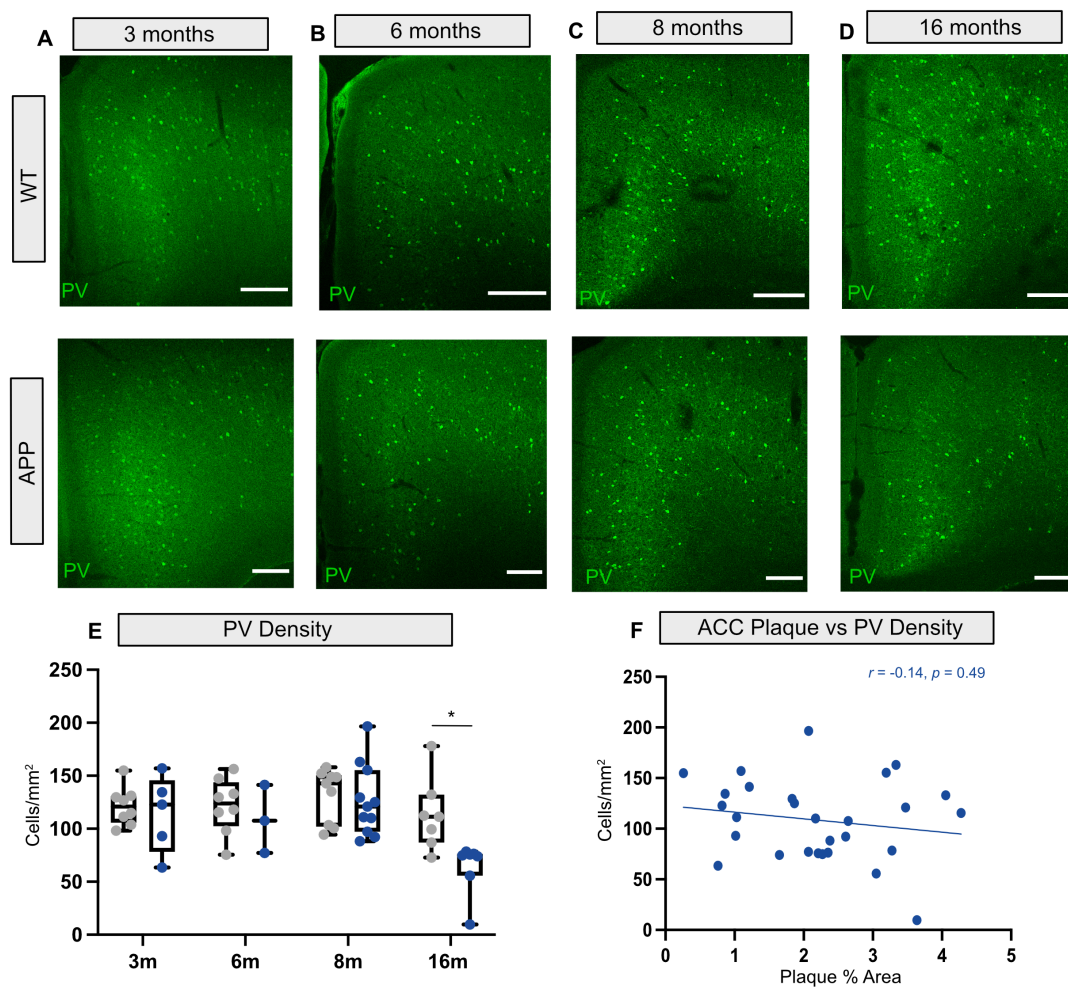


Figure 3.2.6 | PV-expressing interneuron density does not differ in APP mice compared with WT in the ACC at 3, 6, and 8 months but decreases at 16 months. A-D Representative images of PV-expressing interneurons in the ACC in WT and APP animals at 3 (A), 6 (B), 8 (C) and 16 months (D). Scale bars: 200 μ m. **E** A statistically significant main effect of genotype was identified when analysing PV-expressing interneuron activity (3m WT: 120.90 (102.40-130.10) vs APP: 122.90 (93.10-154.80), 6m WT: 123.80 (92.49-149.70) vs APP: 115.40 (92.49-137.20), 8m WT: 142.90 (102.00-150.50) vs APP: 121.00 (97.24-155.30), 16m WT: 111.30 (86.96-132.20) vs APP: 74.82 (55.71-76.35) cells/mm², $F(3,50) = 5.54$, $p = 0.02$, 2-way ANOVA). Tukey's *post-hoc* pairwise comparison revealing a statistically significant decrease in immunoreactivity in APP mice at 16m ($p = 0.04$) **F** No statistically significant correlation was found between the area covered by plaques and PV-expressing interneuron immunoreactivity in pooled APP animals ($r = -0.14$, $p = 0.49$, Spearman's correlation). Box-plots display the median, IQR and ranges. Descriptive statistics display the median. * $p < 0.05$.

3.2.4 | PV-expressing interneuron immunoreactivity in the CA1 region of the hippocampus

PV-expressing interneuron immunoreactivity was then assessed in the CA1 region of the hippocampus, with interneurons largely confined to the *Str.O* and *Str.P* layers, consistent with the localisation of axo-axonic, fast-spiking basket and bistratified interneurons (Pelkey *et al.*, 2017) (**Figure 3.2.7 A-D**). No statistically significant change in immunoreactivity was found in APP animals compared with WT controls for ages 3, 6 and 16 months. However, a statistically significant increase in PV-expressing interneuron immunoreactivity was identified in 8-month-old APP animals compared with age-matched WT controls (**Figure 3.2.7 E**). Additionally, this change in immunoreactivity did not correlate with A β ₁₋₄₂ burden in APP animals (**Figure 3.2.7 F**). Thus, it appears that the density of PV-expressing interneuron immunoreactivity in CA1 transiently increases in APP animals compared with WT controls at 8 months that then declines between the ages of 8 and 16 months.

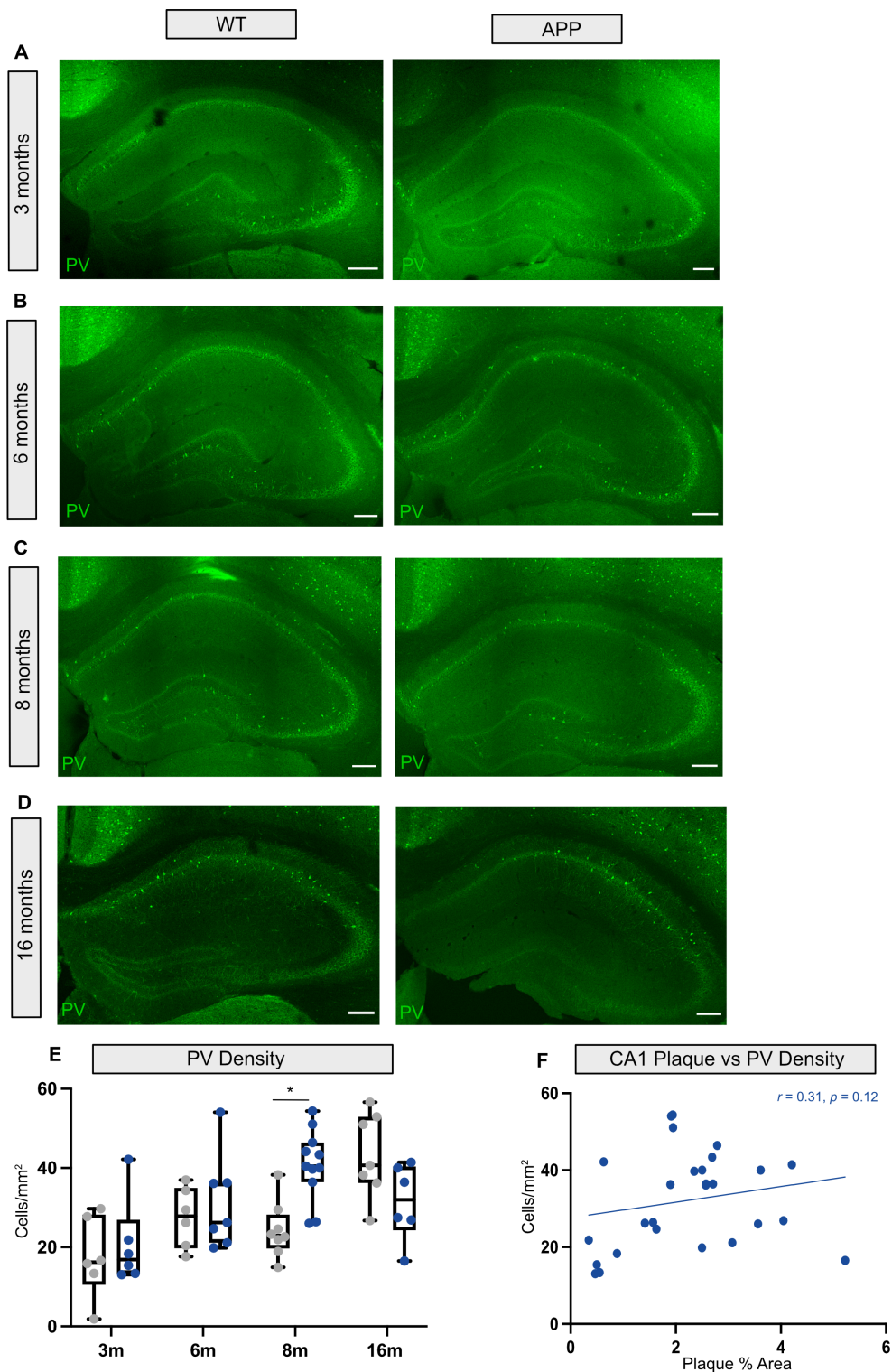


Figure 3.2.7 | PV-expressing interneuron density does not differ in APP mice compared with WT in CA1 at 3, 6, and 16 months but increases at 8 months. A-D Representative images of PV-expressing interneurons in CA1 in WT and APP animals at 3 (A), 6 (B), 8 (C) and 16 months (D). Scale bars: 200 μ m. **E** A statistically significant interaction between age with genotype was identified when analysing PV-expressing interneuron activity (3m WT: 16.23

(10.51-28.22) vs APP: 16.87 (13.29-26.91), **6m WT**: 27.84 (19.71-34.97) vs APP: 26.24 (21.14-36.28), **8m WT**: 23.26 (20.44-33.87) vs APP: 40.49 (36.40-46.41), **16m WT**: 40.70 (36.22-52.94) vs APP: 31.95 (24.30-40.36) cells/mm², $F(3,49) = 5.47$, $p = 0.002$, 2-way ANOVA). Tukey's *post-hoc* pairwise comparison revealing a statistically significant increase in immunoreactivity in APP mice at 8m ($p = 0.01$) **F** No statistically significant correlation was found between the area covered by plaques and PV-expressing interneuron immunoreactivity in pooled APP animals ($r = 0.31$, $p = 0.12$, Spearman's correlation). Box-plots display the median, IQR and ranges. Descriptive statistics display the median and IQR. * $p < 0.05$.

3.3 | Discussion

3.3.1 | Summary

The aims of these experiments were to assess PV-expressing interneuron immunoreactivity in the mPFC and CA1 region of the hippocampus at several ages in the APP^{NL-G-F} mouse model and to confirm an age-dependant increase in A β ₁₋₄₂ deposition. As expected, based on previous studies (Nilsson, Saito & Saido, 2014; Saito *et al.*, 2014), an age-dependant increase in the area covered by A β ₁₋₄₂ plaques was found in the PL cortex and ACC sub-regions of the mPFC and CA1, as was an increase in the average size of the plaques, with a trending increase found in the IL cortex. Additionally, an increase in PV-expressing interneuron immunoreactivity was identified in CA1 at 8 months and a decrease in immunoreactivity in the ACC at 16 months, both of which are novel findings.

3.3.2 | A β ₁₋₄₂ deposition in the mPFC and CA1

To generate the APP^{NL-G-F} mouse model, three different mutations associated with familial AD (FAD) were inserted into the humanised *APP* gene sequence that was knocked-in to the mouse genome to replace the endogenous mouse *APP* gene. The Swedish (KM670/671**NL**) and Beyreuther/Iberian (I716**F**) mutations increase the cleavage of the APP protein at β - and γ -sites, respectively, creating a higher proportion of A β ₁₋₄₂ protein that is more prone to aggregation, with the Arctic (E693**G**) mutation increasing the rate of deposition (Nilsson, Saito & Saido, 2014; Saito *et al.*, 2014). In the results reported in this chapter, mice homozygous for the APP^{NL-G-F} gene displayed an increase in the area covered by A β ₁₋₄₂-containing plaques as well as an increase in the average size of the plaques over the ages 3, 6, 8 and 16 months. This was evident in all mPFC sub-regions as well as in the CA1 region of the hippocampus. As expected, WT controls did not develop A β ₁₋₄₂ plaques at any age. These results are consistent with initial reports that found an increase in A β ₁₋₄₂ deposition in the cortex and hippocampus of homozygous APP^{NL-G-F} mice, over the ages of 2-10 months (Nilsson, Saito & Saido, 2014; Saito *et al.*, 2014). The current experiments further specify that A β ₁₋₄₂ deposition is observed in mPFC sub-regions and the CA1 region of the hippocampus. This deposition is consistent with the anatomical distribution of A β pathology found in humans with AD (Braak & Braak, 1991;

Grothe *et al.*, 2017), and further highlights the applicability of this mouse model in studying amyloidopathy.

3.3.3 | An increase in CA1 PV-expressing interneuron immunoreactivity

A statistically significant increase in PV-expressing interneuron immunoreactivity was identified in the CA1 region of the hippocampus in 8-month APP animals compared with WT controls. Increases in PV-expressing interneuron immunoreactivity have previously been reported in humans with AD (Saiz-Sanchez *et al.*, 2014). Additionally, an increase in PV staining intensity was found in the hippocampus of APP/PSEN1 mice, and PV-expressing interneurons were found to have a more ramified morphology (Hollnagel *et al.*, 2019). PV is a Ca²⁺ binding protein that has shown to accelerate the rate of decay of intracellular Ca²⁺ signals (Collin *et al.*, 2005). This allows neurons to be maintained close to their resting potential, preventing cumulative facilitation and allowing a stable level of inhibition to be transmitted to the post-synaptic neuron (Caillard *et al.*, 2000). An increase in PV can potentially cause interneurons to return to resting potentials quicker, allowing an increased firing rate. Indeed, the increase in PV staining intensity observed in APP/PSEN1 mice can be related to a separate study that found hyperexcitable PV-expressing interneurons at a similar age (Hijazi *et al.*, 2019). Increases in the expression levels of different interneuron protein markers have previously been documented to occur in response to aberrant network activity in the hippocampus of hAPP-J20 mice (Palop *et al.*, 2007). In the APP^{NL-G-F} mouse model, cortical epileptic discharges and a reduction in mEC fast gamma power appear before 8 months, providing evidence for a disrupted E-I balance (Nakazono *et al.*, 2017; Johnson *et al.*, 2020). Upregulation of PV could therefore be a potential compensatory effect of the network in response to an impaired E-I balance.

3.3.4 | A decrease in ACC PV-expressing interneuron immunoreactivity

PV-expressing interneuron immunoreactivity was also reduced in APP animals compared with WT in the ACC at 16 months. A loss of PV-expressing interneuron immunoreactivity, manifested as a loss of both protein and neuron, have previously been documented to occur in first-generation mouse models of amyloidopathy (Cattaudo *et al.*, 2018; Ali *et al.*, 2019; Giesers & Wirths, 2020). This loss can also be seen in humans with AD (Arai *et al.*, 1987; Brady & Mufson,

1997; Mikkonen *et al.*, 1999; Sanchez-Mejias *et al.*, 2020). Whether the loss of PV-expressing interneuron immunoreactivity in the ACC signifies a loss of protein or a loss of interneurons remains to be determined. Synaptic loss is known to occur in the APP^{NL-G-F} mouse model but it is unknown if this model displays neuronal loss too (Saito *et al.*, 2014). Staining the ACC for the neuronal nuclear protein, NeuN, and quantifying the number of fluorescent cells will give a clearer indication of what this loss represents.

Additionally, it is interesting to note that the loss of PV-expressing interneuron immunoreactivity did not correlate with amyloid plaque load. Although A β has been shown to cause neuronal death (Manseau *et al.*, 2010; Umeda *et al.*, 2011) as well as neuron and network dysfunction (Busche *et al.*, 2008, 2015; Nicole *et al.*, 2016; Chung *et al.*, 2020a; Park *et al.*, 2020), it is possible that other factors, either alone or in combination with A β , are needed to promote change in PV-expressing interneuron immunoreactivity. In fact, in one first-generation mouse model of amyloidopathy (TgCRND8), a loss of PV-expressing interneuron immunoreactivity has been reported before the onset of plaque deposition (Mahar *et al.*, 2017). Inflammation is another key feature of AD that has been linked to neuronal cell death (Wright *et al.*, 2013; Spangenberg *et al.*, 2016). Both microgliosis and astrogliosis have been reported in the APP^{NL-G-F} mouse model (Saito *et al.*, 2014). Whether these processes occur in a similar pattern to the loss of PV-expressing interneuron immunoreactivity in the ACC is unknown, but could help explain changes in immunoreactivity.

PV-expressing interneurons are known to play a role in the generation of the SWO, spindles, SWRs, as well as gamma and theta oscillations (Mann, Radcliffe & Paulsen, 2005; Sanchez-Vives *et al.*, 2010; Stark *et al.*, 2014; Amilhon *et al.*, 2015; Clemente-Perez *et al.*, 2017a). A loss of PV in PV-expressing interneurons has been shown to cause synaptic paired-pulse facilitation, which can increase the inhibitory tone, whereas a loss of the interneuron can reduce inhibition (Caillard *et al.*, 2000). Either way, a loss of protein or interneurons can affect the function of PV-expressing interneurons, potentially leading to dysfunctional oscillatory activity. Moreover, PV has been shown to play a role in the asynchronous release of the neurotransmitter GABA, which is believed to help

prevent the coordinated synchronous firing of large groups of PCs (Manseau *et al.*, 2010), a phenomenon that underlies the epileptic discharges that are a common feature in AD (Palop *et al.*, 2007; Verret *et al.*, 2012; Born, 2015; Martinez-Losa *et al.*, 2018; Brown *et al.*, 2018). Dysfunctional PV-expressing interneurons in first-generation mouse models of amyloidopathy have already been shown to impact both gamma oscillations and the occurrence of epileptic discharges (Palop *et al.*, 2007; Verret *et al.*, 2012; Martinez-Losa *et al.*, 2018). On the other hand, there is evidence for changes in hippocampal PV-expressing interneuron immunoreactivity in the APP/PSEN1 model that are not accompanied with changes to oscillatory dynamics (Hollnagel *et al.*, 2019). Therefore, pairing the observed changes in immunoreactivity with recordings of neuronal oscillations or interneuron activity will give a clearer indication of how changes in expression may affect cellular and neuronal circuit function.

3.3.4 | Similarities with other mouse models and humans

Different studies performed in first generation amyloidopathy mouse models have identified losses, gains and no change in PV-expressing interneuron immunoreactivity in cortical and hippocampal regions at various ages (Lemmens *et al.*, 2011; Cattaud *et al.*, 2018; Ali *et al.*, 2019; Hollnagel *et al.*, 2019; Giesers & Wirths, 2020). These discrepancies between studies can also be found when comparing different *post-mortem* reports from humans with AD (Arai *et al.*, 1987; Brady & Mufson, 1997; Mikkonen *et al.*, 1999; Saiz-Sanchez *et al.*, 2014; Sanchez-Mejias *et al.*, 2020). These contradictory results between studies can be due to several factors, including the mutations the different models and humans possess as well as the spread of ages used. Unfortunately, this makes it difficult to draw comparisons between models and humans. Longitudinal studies such as the one described in this chapter can help identify expression patterns of PV-expressing interneuron immunoreactivity. However, relating these patterns to AD pathology and functional changes will give a clearer indication of why these changes are occurring.

3.3.5 | Limitations and future directions

PV-expressing interneuron immunoreactivity and the area covered by A β ₁₋₄₂ plaques were manually quantified in FIJI software (see **section 2.5**) (Schindelin *et al.*, 2012). Manual quantification such as this can introduce human error and

experimenter-experimenter variability, which can potentially influence the outcome of an experiment. Several practices were therefore adopted to limit variability, such as the use of biological replicates, blinding the researcher to genotype and keeping the researcher consistent throughout quantification. Another solution would have been to use a second researcher for quantification and take an average of the results. However, this doubles the resources required to perform the analysis and due to the large volume of images analysed in this chapter, was not feasible. Automated cell counting software and FIJI plugins can also be used to overcome human error and reduce the processing time of manual quantification (Schmitz *et al.*, 2014; O'Brien, Hayder & Peng, 2016; Bal, Maureira & Arguello, 2020). However, automated results initially need to be benchmarked against manual counting to determine the accuracy of the method. Therefore, they were not considered an appropriate quantification method for these experiments.

Finally, somatostatin (SST)-expressing interneurons are another interneuron sub-type shown to be important in the generation of theta and gamma oscillations as well as the SWO (Klausberger *et al.*, 2003; Funk *et al.*, 2017; Antonoudiou *et al.*, 2020). Impairments to SST-expressing interneurons are reported in first-generation mouse models of amyloidopathy (Chung *et al.*, 2020a), as are changes to their immunoreactivity (Moreno-Gonzalez *et al.*, 2009; Trujillo-Estrada *et al.*, 2014; Sanchez-Mejias *et al.*, 2020). Additionally, a loss of SST-expressing interneuron immunoreactivity has been documented to occur in the brains of humans with AD (Saiz-Sanchez *et al.*, 2014; Sanchez-Mejias *et al.*, 2020). Therefore, assessing the expression patterns of these interneurons in the APP^{NL}-G-F mouse model in future experiments can provide valuable information about observed circuit disruptions.

3.3.6 | Conclusions

The aim of this study was to assess the expression pattern of PV-expressing interneurons in the mPFC and CA1 region of the hippocampus in the APP^{NL}-G-F mouse model and to specify an age-dependant increase in the area covered by A β ₁₋₄₂ plaques in these regions. Both the area covered by A β ₁₋₄₂ plaques and the size of A β ₁₋₄₂ plaques increased over the ages 3, 6, 8 and 16 months in mPFC

sub-regions and the CA1 region of the hippocampus. Additionally, an increase in PV-expressing interneuron immunoreactivity was identified in APP animals in the CA1 region of the hippocampus at 8 months, as was a decrease in immunoreactivity in the ACC of APP animals at 16 months. The functional implications of these changes in immunoreactivity still needs to be investigated, but further imply that a disrupted E-I balance exists in the APP^{NL-G-F} mouse model.

4 | A chemogenetic approach for targeting PV- and SST-expressing interneuron populations to ameliorate slow wave oscillation impairments in the APP^{NL-G-F} mouse model

4.1 | Introduction

During NREM sleep, the communication between the mPFC and hippocampus underlies the long-term consolidation of hippocampus-dependant memories. This is achieved through the temporal coupling of three cardinal neuronal oscillations: the SWO, spindles and SWRs (Diekelmann & Born, 2010; Maingret *et al.*, 2016b) (see **section 1.2.2.4**). In particular, the SWO provides a temporal framework for spindles and SWRs to nest within and is considered the oscillatory pacemaker of the circuit (Mölle *et al.*, 2006, 2009; Maingret *et al.*, 2016b). The SWO is composed of two distinct states: Up states and Down states (UDS). Up states are reflected in the LFP as surface positive (depth negative) deflections and are associated with the rapid firing and depolarisation of neurons. Down states can be viewed as surface negative (depth positive) deflections and are associated with long-lasting neuronal hyperpolarisations (Steriade, Nunez & Amzica, 1993a).

UDS are generated, in part, by the action of GABAergic interneurons. Fast-spiking PV-expressing basket cells have been shown to be important in the maintenance of Up states through their ability to balance the rapid firing of excitatory neurons (Haider *et al.*, 2006). These cells target the cell soma and mediate inhibition through the fast-acting GABA_A receptors, that are important in Up state maintenance (Mann, Kohl & Paulsen, 2009; Sanchez-Vives *et al.*, 2010; Pelkey *et al.*, 2017). Additionally, these cells are documented to play a role in the generation of gamma oscillations (Mann, Radcliffe & Paulsen, 2005), which can be found nested within SWO Up states (Steriade *et al.*, 1996; Valderrama *et al.*, 2012). SST-expressing interneurons are thought to be involved in initiating Down states and increase their firing and Ca²⁺ activity towards the end of an Up state (Fanselow & Connors, 2010; Niethard *et al.*, 2018). Moreover, SST-expressing interneurons mediate their effects through GABA_B receptors, that have shown to be important in Down state initiation (Mann, Kohl & Paulsen, 2009; Craig *et al.*, 2013; Craig MT, 2014; Urban-Ciecko, Fanselow & Barth, 2015), with their chemogenetic activation enhancing SWA (Funk *et al.*, 2017).

Impairments to PV-expressing interneurons have been identified in first-generation mouse models of amyloidopathy and are associated with aberrant network activity and a reduction in the power of gamma oscillations (Verret *et al.*,

2012; Martinez-Losa *et al.*, 2018). Additionally, SST-expressing OLM cells are documented to have reduced axon boutons and dendritic spines in amyloidopathy mouse models (Schmid *et al.*, 2016b). Impaired inhibition in these models has been linked to a reduction in the power, frequency and coherence of the SWO, as deficits can be rescued upon administration of GABA_A receptor agonists (Busche *et al.*, 2015; Kastanenka *et al.*, 2017; Castano-Prat *et al.*, 2019). This is consistent with reduced SWA correlating with increased amyloid burden in the brains of humans with AD (Mander *et al.*, 2015b) as well as the diminished expression of PV and SST proteins (Ambrad Giovannetti & Fuhrmann, 2019). However, the contribution of PV and SST-expressing interneurons to SWO deficits reported in AD is currently unknown.

Enhancing the activity of PV and SST-expressing interneurons has previously been shown to rescue impairments to theta and gamma oscillations caused by pathological amyloid (Verret *et al.*, 2012; Martinez-Losa *et al.*, 2018; Chung *et al.*, 2020a; Park *et al.*, 2020). Therefore, it was hypothesised that enhancing the activity of these interneurons in the mPFC could reverse deficits to the SWO in the APP^{NL-G-F} mouse model of amyloidopathy. Using Designer Receptors Exclusively Activated by Designer Drugs (DREADD) technology (Roth, 2016), these interneuron sub-populations were individually targeted in the hope that boosting their activity could ameliorate impairments to the SWO and subsequently, any potential deficits to the temporal coupling of the systems consolidation circuit. These experiments were conducted when animals were 8 months old. I originally hypothesised that disruptions to the SWO would occur at this age given that amyloid pathology began as early as 2 months and spatial memory impairments were reported at 6 months (Nilsson, Saito & Saido, 2014; Saito *et al.*, 2014; Masuda *et al.*, 2016). Additionally, the time required for breeding and ageing mice constrained the age at which experiments could be carried out to completion.

4.2 | Results

4.2.1 | Viral transduction of excitatory DREADDs

To target specific PV and SST-expressing interneuron populations in the APP^{NL-G-F} mouse model, PV-Cre and SST-Cre mice were bred with APP^{NL-G-F} mice in-house. Resultant animals were either homozygous for the APP^{NL-G-F} gene or WT littermate controls and expressed Cre-recombinase under the expression of either PV or SST promoters (**Figure 4.2.1 C**). Animals received a unilateral injection of one of two viruses in the mPFC (**Figure 4.2.1 A**). The viral vector contained either the excitatory DREADD, hM3D(Gq)_mCherry, or mCherry to act as a control, within a DIO (**Figure 4.2.1 B**). This resulted in Cre-dependant expression of hM3D(Gq) plus mCherry or mCherry only in PV or SST-expressing interneurons (**Figure 4.2.1 E**).

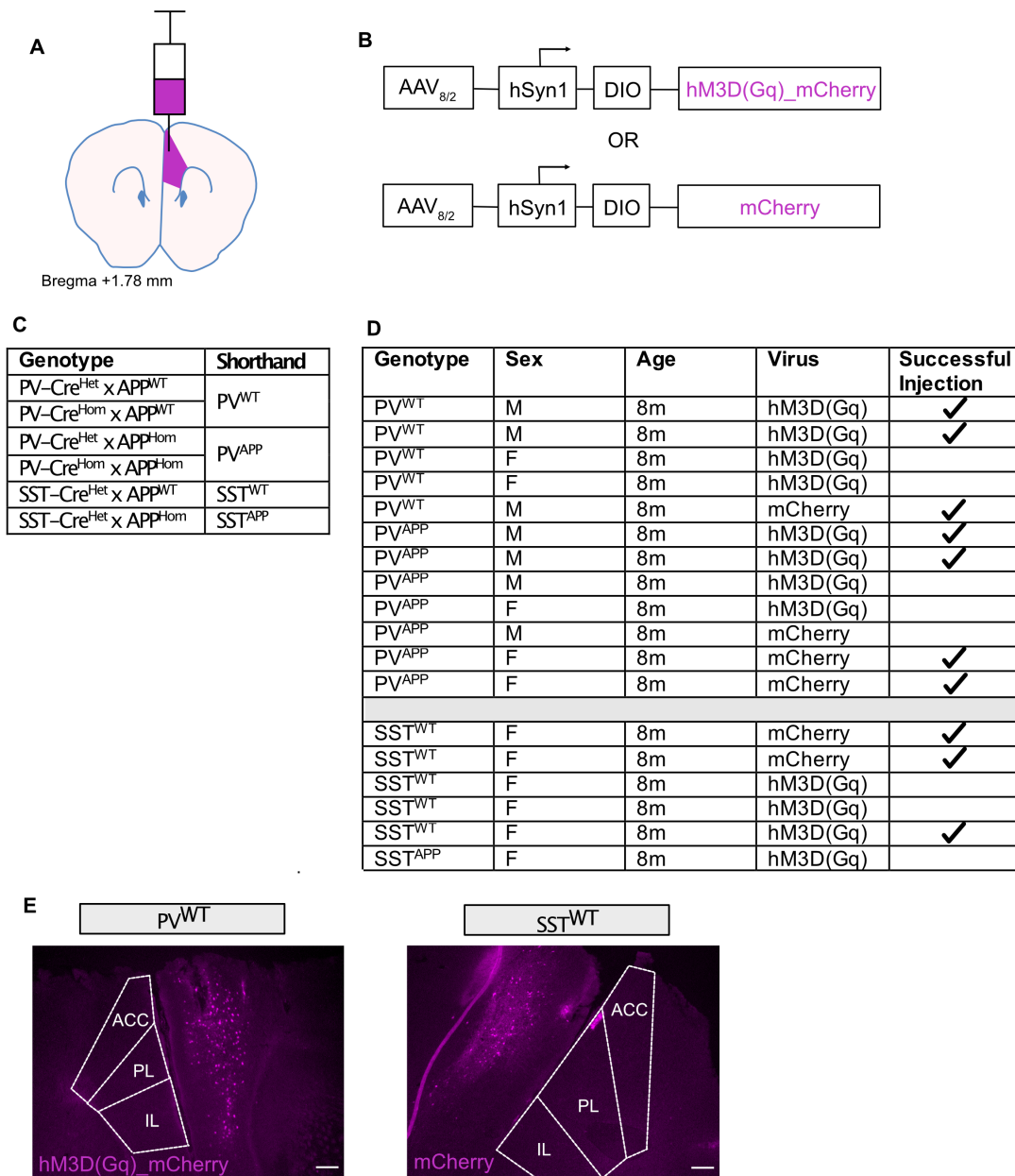


Figure 4.2.1 | Strategy for controlling PV and SST interneuron populations in the mPFC of WT and APP mice. **A** Schematic showing the target brain region. **B** Diagram showing the design of the viral vectors that were intracerebrally injected into the mice outlined in **C** and **D**. **C** Table showing the final genotypes of the mice that were bred and used in this study as well as their shorthand notation used in this chapter. **D** Table showing the animals that were used in these experiments with a tick showing the animals that had successful viral injections. **E** Representative sections showing successful transduction of both viruses illustrated in **B** within both PV and SST interneuron populations in the target brain region outlined in **A**. mPFC sub-regions are outlined in white. Scale bars: 100 μ m.

The designer drug, clozapine N-oxide (CNO), was originally created to selectively activate the designer receptors, such as hM3D(Gq) (Roth, 2016). However, CNO was later found to back-metabolise to clozapine *in vivo*, causing off-target effects (Gomez *et al.*, 2017). To overcome this, a second designer drug was created called compound 21 (Chen *et al.*, 2015). To test this drug's efficacy, Emx1-Cre mice that expressed hM3D(Gq)_mCherry in cortical PCs were given a 1 mg/Kg sub-cutaneous injection of compound 21. Mice were perfused 2 hours later and brains were processed and stained for the neural marker of activation, cFos. Co-localisation of cells expressing mCherry and cFos signify that at this dose, compound 21 can effectively increase the neural activity of cells expressing the excitatory DREADD, hM3D(Gq) (**Figure 4.2.2 A-C**). This has since been corroborated (Thompson *et al.*, 2018; Jendryka *et al.*, 2019).

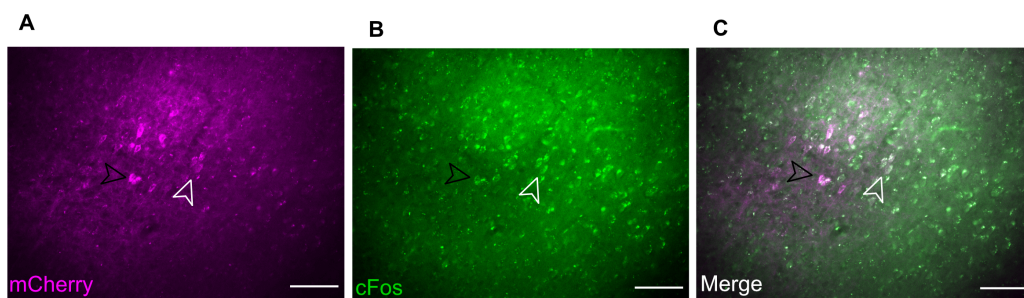


Figure 4.2.2 | Subcutaneous injection of compound 21 successfully activates neurons expressing the hM3D(Gq) excitatory DREADD as seen by the expression of the immediate early gene cFos. A Representative section of hM3D(Gq)_mCherry expression in excitatory neurons of an Emx1-cre mouse virally injected with AAV_{8/2}-hSyn1-DIO-hM3D(Gq)_mCherry. **B** Immunoreactivity in the same section for the immediate early gene cFos. Mice were injected subcutaneously with compound 21 (1 mg/Kg) and perfused 2 hours later. **C** Images from **A** and **B** were merged together to show the co-localisation of hM3D(Gq)_mCherry-expressing cells with cFOS. Black and white arrows highlight cells showing this colocalization. Scale bars: 100 μ m.

4.2.2 | Experimental approach

The animals described in **Figure 4.2.1** were used for the following experiments. To record neuronal oscillations within the mPFC-hippocampal circuit, 4-shank, 32-channel silicon microelectrodes were inserted into both mPFC and hippocampus, respectively (**Figure 4.2.3 A**). Experiments were non-recovery and conducted under isoflurane anaesthesia, as this state has previously been shown to model SWO analogous to those recorded in natural sleep (Doi *et al.*, 2007; Busche *et al.*, 2015; Dasilva *et al.*, 2021). Neural activity was recorded at baseline, after injection with 0.9% sterile saline and after injection with compound 21, with each animal acting as its own control. The depth of anaesthesia was kept as consistent as possible between conditions by maintaining a breathing rate of roughly 2 Hz and the presence of low frequency, high amplitude activity visible in the LFP. A schematic of the protocol used can be found in **Figure 4.2.3 B** and full details of experiments found in **section 2.3**.

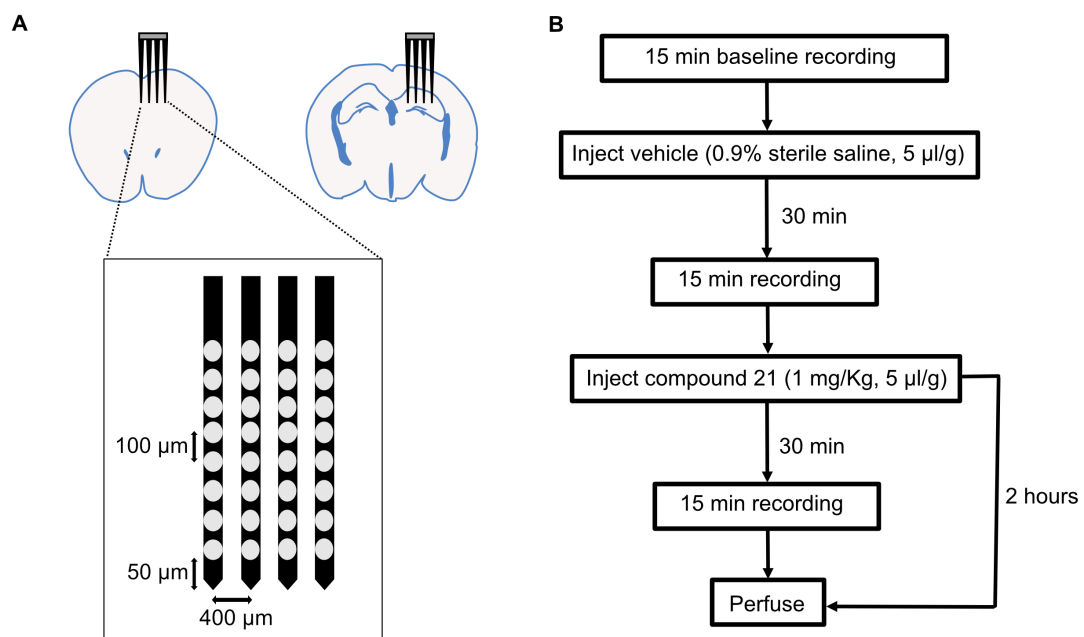


Figure 4.2.3 | Experimental protocol for chemogenetically controlling PV and SST interneuron populations to alter UDS dynamics in WT and APP mice. **A** Representative cartoon showing probe placement within the target brain structures; mPFC and dorsal CA1, plus a schematic showing the design of the microelectrodes. **B** Flow diagram describing the experimental protocol

used in these experiments. Note the 2-hour time lag between injection of compound 21 and perfusion, to allow for the expression of cFos.

4.2.3 | No difference in UDS dynamics between WT and APP mice

UDS dynamics in the mPFC were first assessed during baseline conditions. Only electrodes in the mPFC were used, with data from each channel averaged together as no difference was found between electrodes for each measure. Additionally, animals were pooled into either WT or APP animals for the following analysis, regardless of the cell type expressing Cre-recombinase or viral vector injected. No statistically significant change was found in APP animals compared with WT in the duration of Down states, Up states, combined UDS and therefore frequency of UDS (**Figure 4.2.4 A-C**). There was also no statistically significant change in APP animals compared with WT in the amplitude of Down states, Up states, total amplitude (**Figure 4.2.4 D-E**) or in the number of detected UDS (**Figure 4.2.4 F**). Very similar distributions can be seen in the cumulative probability histograms for each measure, further indicating that UDS dynamics do not appear to be altered in APP animals compared with WT at 8 months (**Figure 4.2.4 C, E**).

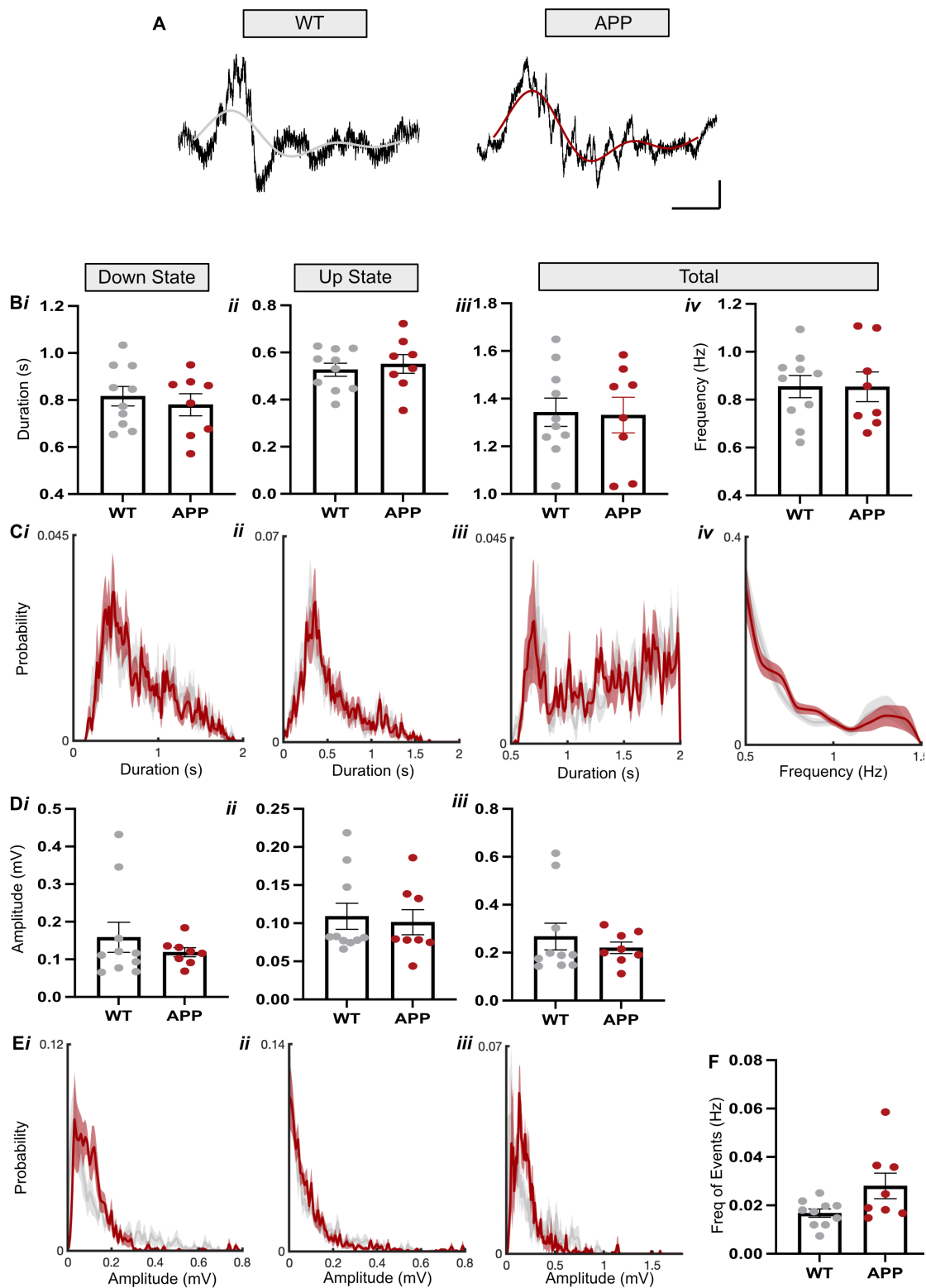


Figure 4.2.4 | Baseline UDS dynamics do change in APP animals compared with WT at 8 months under isoflurane anaesthesia. A Raw (black) and filtered (coloured) traces of detected UDS for both WT and APP mice. Scale bar: 400 ms, 100 μ V. **B** No statistically significant difference was found in APP animals compared with WT for the average Down state duration

(WT: 0.81 ± 0.04 vs APP: 0.78 ± 0.04 s, $t(16) = 0.58$, $p = 0.57$, unpaired t-test) **(i)**, Up state duration (WT: 0.52 ± 0.02 vs APP: 0.55 ± 0.03 s, $t(13.04) = 0.5$, $p = 0.62$, unpaired t-test) **(ii)**, total duration (WT: 1.3 ± 0.06 vs APP: 1.3 ± 0.07 s, $t(14.19) = 0.12$, $p = 0.90$, unpaired t-test) **(iii)**, or UDS frequency (WT: 0.85 ± 0.04 vs APP: 0.85 ± 0.06 Hz, $t(13.66) = 0.02$, $p = 0.98$, unpaired t-test) **(iv)**. **C** Average \pm SEM cumulative probability histograms of all detected UDS from both WT and APP mice. No visible difference noted in the distribution of UDS data between genotypes for the duration of Down states **(i)**, Up states **(ii)**, total duration **(iii)** or UDS frequency **(iv)**. **D** No statistically significant difference was found in APP animals compared with WT for the average Down state amplitude (WT: 0.15 ± 0.03 vs APP: 1.30 ± 0.07 mV, $t(14.19) = 0.12$, $p = 0.90$, unpaired t-test) **(i)**, Up state amplitude (WT: 0.11 ± 0.02 vs APP: 0.10 ± 0.02 mV, $t(16) = 0.32$, $p = 0.75$, unpaired t-test) **(ii)** or total amplitude (WT: 0.26 ± 0.06 vs APP: 0.22 ± 0.02 mV, $t(12.08) = 0.78$, $p = 0.45$, unpaired t-test) **(iii)**. **E** Average \pm SEM cumulative probability histograms of all detected UDS from both WT and APP mice. No visible difference noted in the distribution of UDS data between genotypes for the amplitude of Down states **(i)**, Up states **(ii)** or total amplitude **(iii)**. **F** No statistically significant difference was found in APP animals compared with WT for the frequency of detected UDS events (WT: 0.02 ± 0.001 vs APP: 0.03 ± 0.005 Hz, $t(8.42) = 2.03$, $p = 0.07$, unpaired t-test). Bar graphs and statistics display the mean \pm SEM.

To confirm that there is no effect of expressing Cre-recombinase in either PV vs SST-expressing cell populations upon the observed results, three different measures of UDS dynamics were chosen to compare between genotypes. No visible difference was seen between genotypes in the frequency of UDS, the amplitude of UDS, or in the number of detected UDS (**Figure 4.2.5 A-C**). No statistical test was performed due to the SST^{APP} group being underpowered. Additionally, it is unlikely that the expression of the viral vectors had any influence upon UDS dynamics as there is no evidence that the expression of hM3D(Gq)_mCherry alters basal neuronal activity (Roth, 2016). Therefore, there was no effect of viral transduction or expression of Cre-recombinase upon UDS dynamics.

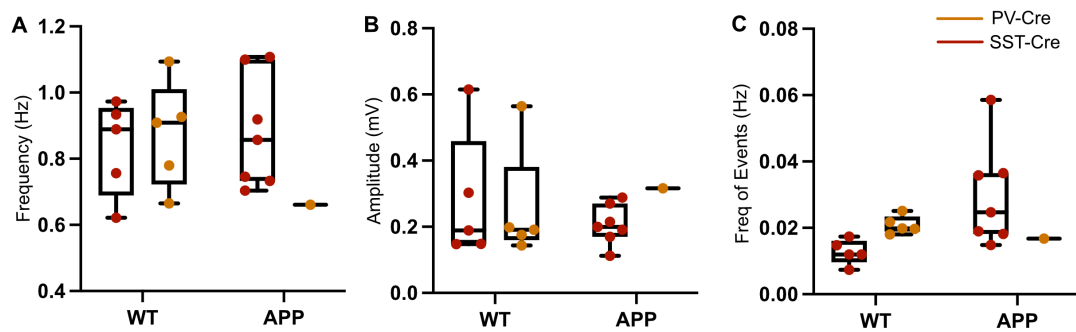


Figure 4.2.5 | Variation in baseline UDS dynamics is not due to an effect of expressing Cre-recombinase in PV or SST-expressing neurons. The expression of Cre-recombinase in PV and SST-expressing cell populations had no visible effect within and between WT and APP animals when comparing **A** UDS frequency (PV^{WT} : 0.89 (0.69-0.95), SST^{WT} : 0.91 (0.72-1.01), PV^{APP} : 0.86 (0.73-1.1), SST^{APP} : 0.66 Hz), **B** UDS amplitude (PV^{WT} : 0.19 (0.15-0.46), SST^{WT} : 0.19 (0.16-0.38), PV^{APP} : 0.2 (0.17-0.27), SST^{APP} : 0.32 mV) and **C** the number of detected UDS (PV^{WT} : 0.012 (0.01-0.02), SST^{WT} : 0.02 (0.019-0.023), PV^{APP} : 0.025 (0.2-0.04), SST^{APP} : 0.017 Hz). Box-plots display the median, IQR and ranges. Descriptive statistics display the median, IQR and ranges.

Differing isoflurane concentrations have previously been shown to exert an effect upon UDS dynamics (Doi *et al.*, 2007; Dasilva *et al.*, 2021). Therefore, it is possible that changes in anaesthesia depth can obscure differences to the SWO between genotypes by producing variability. To try and keep the depth of anaesthesia consistent between animals and between conditions, a breathing rate of roughly 2 Hz was maintained, as was the presence of large amplitude, low frequency activity in the LFP. This was typically achieved at isoflurane concentrations between 0.4-0.8%. However, it is difficult to precisely maintain these conditions. A proxy marker of anaesthesia depth is breathing rate, with higher concentrations of isoflurane depressing the number of breaths per second (measured in Hz) (Gargiulo *et al.*, 2012; Massey & Richerson, 2017). Therefore, relationships between breathing rate and three different measures of UDS dynamics were assessed to determine if there was an influence of anaesthesia depth upon the observed SWO results. No statistically significant correlation was found between breathing rate and UDS frequency, UDS amplitude or number of detected UDS events for either genotype (**Figure 4.2.6 A-C**). Therefore,

breathing rate and depth of anaesthesia had no effect upon the observed SWO results.

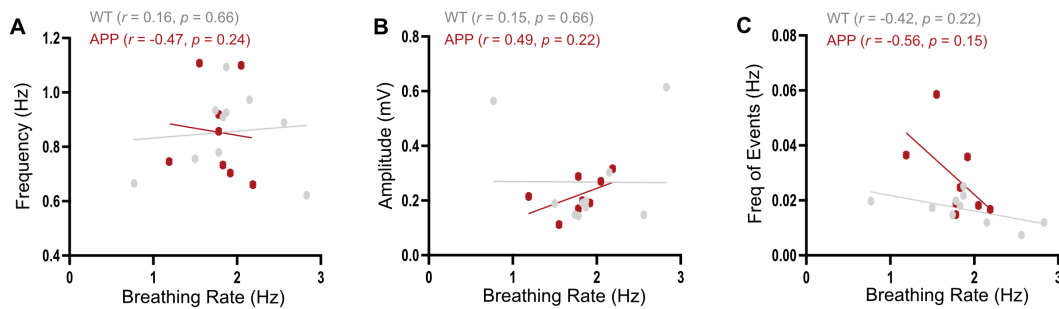


Figure 4.2.6 | No correlation between breathing rate and UDS dynamics is observed. No statistically significant correlation was found for either genotype between breathing rate and **A** UDS frequency (*WT*: $r = 0.16$, $p = 0.66$ vs *APP*: $r = -0.47$, $p = 0.24$, Spearman's correlation), **B** UDS amplitude (*WT*: $r = 0.15$, $p = 0.66$ vs *APP*: $r = 0.49$, $p = 0.22$, Spearman's correlation) and **C** the number of UDS events (*WT*: $r = -0.42$, $p = 0.22$ vs *APP*: $r = -0.56$, $p = 0.15$, Spearman's correlation). Points on each graph represent values from individual animals.

4.2.4 | Differences in UDS dynamics between baseline and saline control conditions

The difficulty in maintaining the same depth of anaesthesia between conditions can prevent observing an effect of the designer drug upon UDS dynamics when comparing with baseline and saline control conditions. Therefore, to determine if variation in UDS dynamics exists between conditions, the relationship between baseline and saline control conditions were analysed for each measure. Baseline and saline conditions were chosen as saline should theoretically have no effect upon UDS dynamics.

Assuming that UDS dynamics during baseline conditions are the roughly same after an injection of saline, a statistically significant positive correlation would be expected between baseline and saline conditions. However, this was only the case for WT Down state duration, WT total UDS duration, WT UDS frequency, WT and APP Up state amplitude and WT total amplitude (**Figure 4.2.7 A-E**). There was also no statistically significant change in the correlations in APP animals compared with WT controls for each measure (**Figure 4.2.7 B-E**).

Therefore, it appears that similar UDS dynamics cannot be reliably reproduced between conditions, within individual animals. This signifies that isoflurane is an unreliable method for measuring the effect of increasing PV and SST-expressing interneuron activity on UDS dynamics. No comparisons were made with the designer drug condition as the number of successful viral injections for each genotype was underpowered (**Figure 4.2.1 D**).

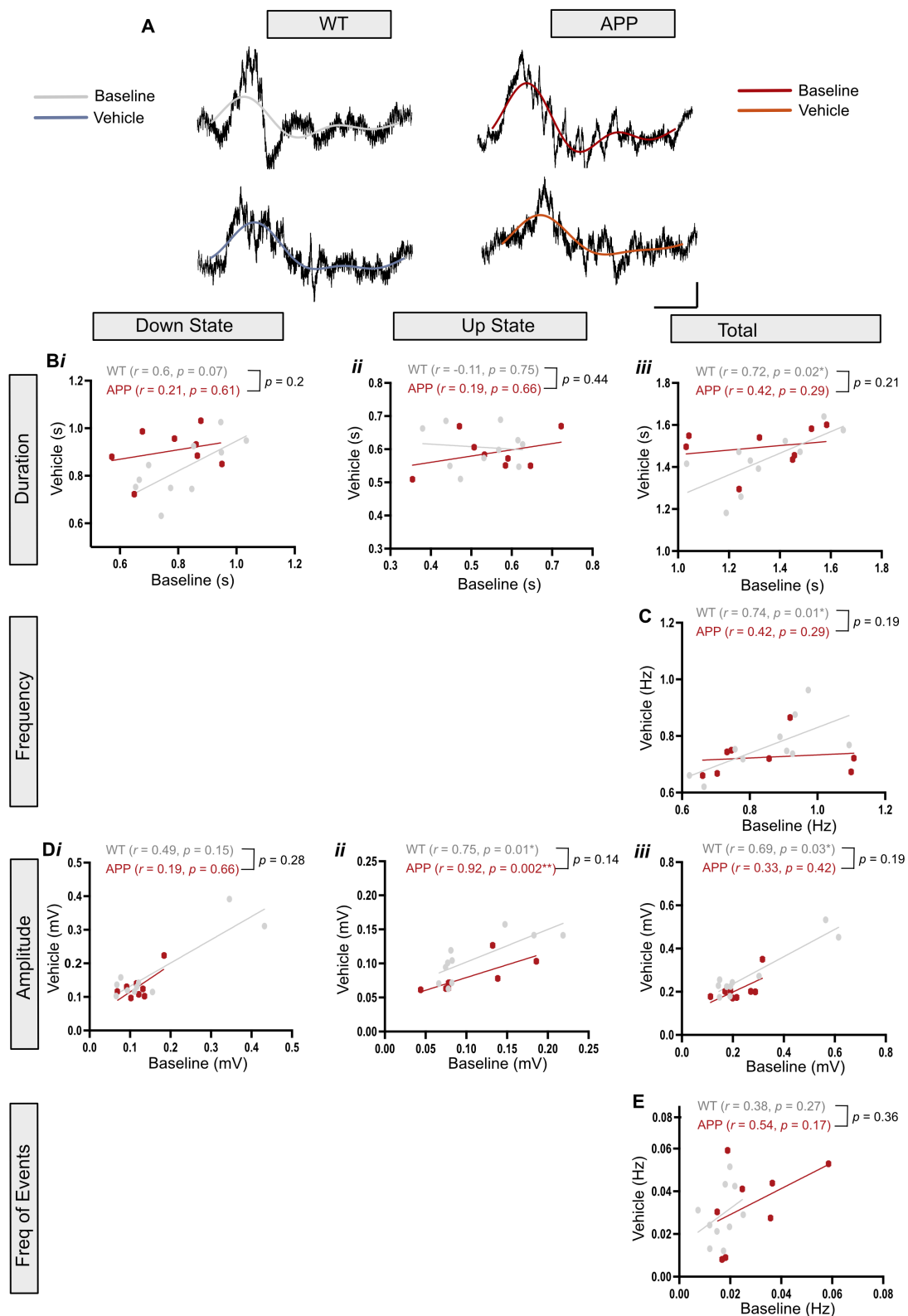


Figure 4.2.7 | UDS dynamics change between baseline and vehicle treated conditions. A Raw (black) and filtered (coloured) traces of detected UDS from WT and APP mice under both baseline and vehicle treated conditions. Scale bar: 400 ms, 100 μ V. For the data shown in figures **B-E** a statistically significant positive correlation signifies that there is no change in the UDS measured

variable between baseline and vehicle conditions. **B** A statistically significant positive correlation was found between the total UDS duration in baseline and vehicle treated conditions in WT mice ($r = 0.72$, $p = 0.02$, Spearman's correlation) but not in APP mice ($r = 0.42$, $p = 0.29$, Spearman's correlation). This difference was not found to be a function of genotype ($p = 0.21$, Fisher's transformation) (*iii*). No statistically significant correlation was found for the duration of Down states or Up states between baseline and vehicle conditions for either WT or APP mice (all $p > 0.05$, Spearman's correlation), nor was there a statistically significant difference in the r values between genotypes for each of these measures (all $p > 0.05$, Fisher's transformation) (*i-ii*). **C** A statistically significant positive correlation was found between UDS frequency in baseline and vehicle treated conditions in WT mice ($r = 0.74$, $p = 0.01$, Spearman's correlation) but not in APP mice ($r = 0.42$, $p = 0.29$, Spearman's correlation). This difference was not found to be a function of genotype ($p = 0.19$, Fisher's transformation). **D** No statistically significant correlation was found between Down state amplitude in baseline and vehicle conditions for either WT ($r = 0.49$, $p = 0.15$, Spearman's correlation) or APP mice ($r = 0.19$, $p = 0.66$, Spearman's correlation), nor was there a statistically significant difference in the r values between genotypes ($p = 0.28$, Fisher's transformation) (*i*). A statistically significant positive correlation was found between the Up state amplitude in baseline and vehicle conditions in WT ($r = 0.75$, $p = 0.01$, Spearman's correlation) and APP mice ($r = 0.92$, $p = 0.002$, Spearman's correlation). There was no statistically significant difference in the r values between genotypes ($p = 0.14$, Fisher's transformation) (*ii*). A statistically significant positive correlation was found between the total UDS amplitude in baseline and vehicle treated conditions in WT mice ($r = 0.69$, $p = 0.03$, Spearman's correlation) but not in APP mice ($r = 0.33$, $p = 0.42$, Spearman's correlation). This difference was not found to be a function of genotype ($p = 0.19$, Fisher's transformation) (*iii*). No statistically significant correlation was found between the frequency of UDS events in baseline and vehicle treated conditions in WT ($r = 0.38$, $p = 0.27$, Spearman's correlation) and APP mice ($r = 0.54$, $p = 0.17$, Spearman's correlation). There was no statistically significant difference in the r values between genotypes ($p = 0.36$, Fisher's transformation). Points on graph represent values from individual animals. * $p < 0.05$, ** $p < 0.01$.

4.2.5 | Isoflurane produces large variation in UDS dynamics compared with urethane and natural sleep

The SWO has been studied under several different types of anaesthetics, including isoflurane and urethane (Doi *et al.*, 2007; Luczak *et al.*, 2007; Busche *et al.*, 2015; Dasilva *et al.*, 2021). Differences in UDS dynamics between anaesthesia depths as well as differences between anaesthetics and natural sleep have previously been investigated (Chauvette *et al.*, 2011; Dasilva *et al.*, 2021; Torao-Angosto *et al.*, 2021). However, no comparison exists between isoflurane, urethane and natural sleep. Therefore, using WT animals that had been chronically implanted with silicon microelectrodes in the mPFC (see **section 2.2**), changes to cortical UDS dynamics were investigated during natural sleep and under isoflurane and urethane anaesthesia. No statistically significant difference was found between conditions for all measures of UDS dynamics, although a trending increase in Up state duration can be seen under urethane anaesthesia compared with natural sleep as well as a decrease in UDS frequency (**Figure 4.2.8 Bi, iv**) and occurrence (**Figure 4.2.8 F**). Interestingly, variation in UDS duration is visible under isoflurane anaesthesia, consistent with the variation in UDS duration seen in **Figure 4.2.4 B**. A Brown-Forsyth test was used to determine if the variation between groups is equal. Statistically significant unequal variation was found for Down state duration, UDS duration and UDS frequency. This is most likely due to the variation caused by isoflurane anaesthesia, yet multiple comparisons corrected Bonferroni *post-hoc* testing did not reveal any statistically significant differences between individual groups. However, visual inspection of the data revealed isoflurane to have notably larger variability compared with urethane and sleep conditions (**Figure 4.2.8 Bi, iii, iv**). Additionally, a trending statistical significance was found when comparing the variation between groups for the number of detected UDS, with larger variability noticeable under isoflurane anaesthesia (**Figure 4.2.8 F**). Finally, the different conditions appeared to have no effect on UDS amplitude (**Figure 4.2.8 D**).

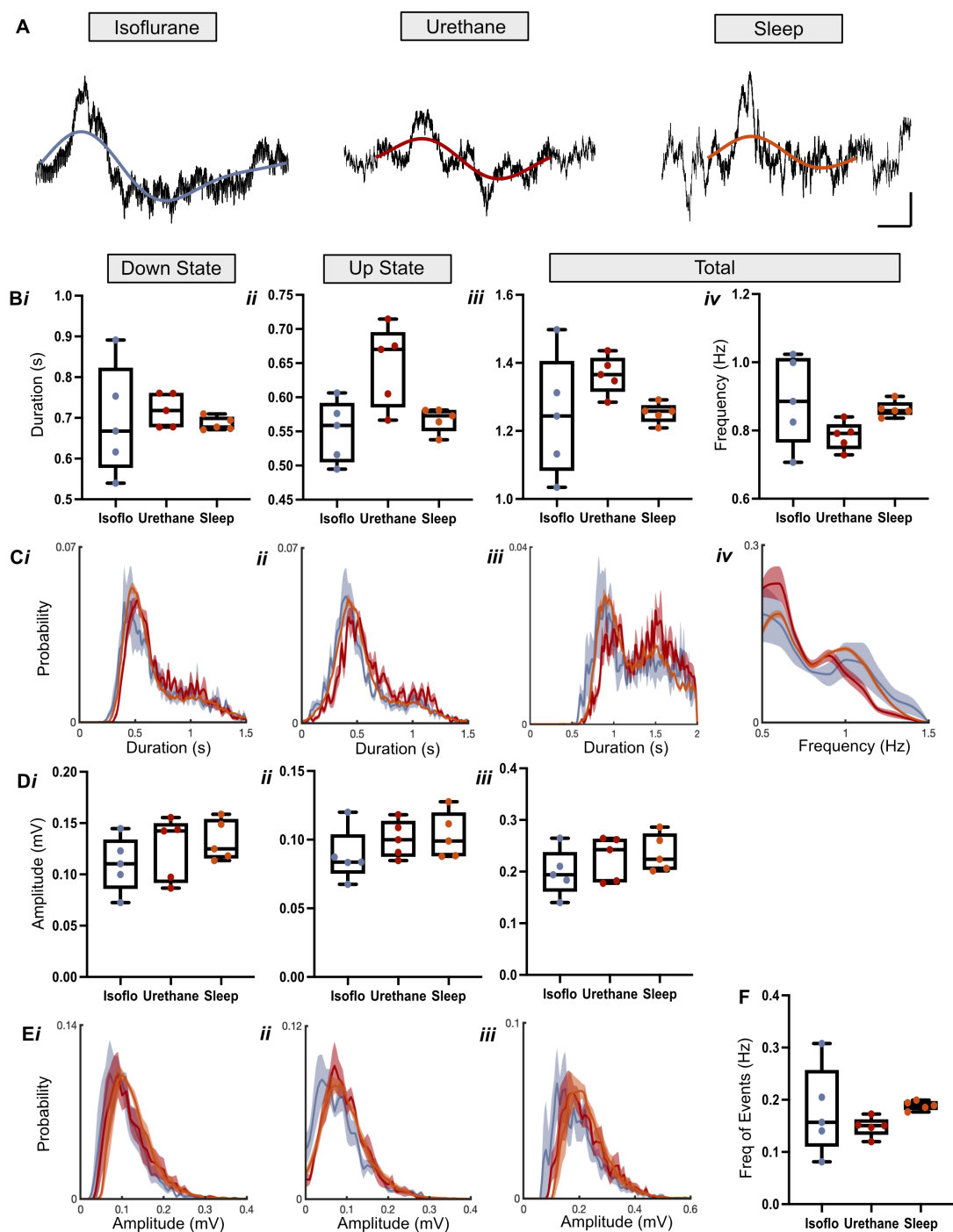


Figure 4.2.8 | UDS dynamics are highly variable under isoflurane anaesthesia. **A** Example raw (black) and filtered traces of detected UDS during isoflurane (grey) and urethane (red) anaesthesia and natural sleep (orange). Scale bar: 200 ms, 200 μ V. **B** No statistically significant difference was found between conditions for the average Down state duration (*Isofo*: 0.66 (0.58-0.82), *Urethane*: 0.72 (0.68-0.76), *Sleep*: 0.68 (0.67-0.7) s, $F_r = 2.8$, $p = 0.36$, Friedman test) (*i*), Up state duration (*Isoflo*: 0.56 (0.5-0.59), *Urethane*: 0.67 (0.59-0.69), *Sleep*: 0.57 (0.55-0.58) s, $F_r = 5.2$, $p = 0.09$, Friedman test) (*ii*),

total duration (*Isoflo*: 1.24 (1.08-1.4), *Urethane*: 1.37 (1.3-1.4), *Sleep*: 1.26 (1.23-1.28) s, $F_r = 4.8$, $p = 0.12$, Friedman test) **(iii)**, or UDS frequency (*Isoflo*: 0.89 (0.77-0.89), *Urethane*: 0.79 (0.75-0.82), *Sleep*: 0.86 (0.85-0.88) Hz, $F_r = 4.8$, $p = 0.12$, Friedman test) **(iv)**. Large variability was also found between conditions for the duration of Down states ($F(2,12) = 3.91$, $p = 0.04$, Brown-Forsythe test) **(i)**, total duration ($F(2,12) = 4.14$, $p = 0.04$, Brown-Forsythe test) **(iii)** and frequency ($F(2,12) = 5.14$, $p = 0.02$, Brown-Forsythe test) **(iv)**. **C** Average \pm SEM cumulative probability histograms of all detected UDS from all 3 conditions. No visible difference noted in the distribution of UDS data between conditions for the duration of Down states **(i)**, Up states **(ii)**, total duration **(iii)** or UDS frequency **(iv)**. However, a bimodal distribution exists for each measure, indicating two separate frequencies of UDS in all conditions. **D** No statistically significant difference in amplitude was found between conditions for Down states (*Isoflo*: 0.11 (0.09-0.13), *Urethane*: 0.14 (0.09-0.15), *Sleep*: 0.13 (0.12-0.15) mV, $F_r = 2.8$, $p = 0.36$, Friedman test) **(i)**, Up states (*Isoflo*: 0.08 (0.075-0.1), *Urethane*: 0.1 (0.09-0.11), *Sleep*: 0.1 (0.09-0.12) mV, $F_r = 2.8$, $p = 0.36$, Friedman test) **(ii)** or the total amplitude (*Isoflo*: 0.19 (0.16-0.24), *Urethane*: 0.24 (0.18-0.26), *Sleep*: 0.22 (0.2-0.27) mV, $F_r = 2.8$, $p = 0.36$, Friedman test) **(iii)**. **E** Average \pm SEM cumulative probability histograms of all detected UDS from all conditions. No visible difference noted in the distribution of UDS data between conditions for Down states **(i)**, Up states **(ii)** or total amplitude **(iii)**. **F** No statistically significant difference was found between conditions for the frequency of detected UDS (*Isoflo*: 0.16 (0.11-0.26), *Urethane*: 0.15 (0.13-0.16), *Sleep*: 0.19 (0.18-0.2) Hz, $F_r = 2.8$, $p = 0.36$, Friedman test) but a large variation within the data was found, although not statistically significant ($F(2,12) = 3.26$, $p = 0.07$, Brown-Forsythe test). Box plots show median, IQR and ranges. Descriptive statistics display the median and IQR.

4.3 | Discussion

4.3.1 | Summary

Impairments to the SWO, and the PV- and SST-expressing interneurons that help generate it, have been reported in humans with AD as well as in first-generation mouse models of amyloidopathy (Busche *et al.*, 2015; Mander *et al.*, 2015b; Schmid *et al.*, 2016a; Martinez-Losa *et al.*, 2018; Ambrad Giovannetti & Fuhrmann, 2019). The present study aimed to set up an *in vivo* model of SWA under isoflurane anaesthesia, confirm the presence of aberrant SWA in 8-month-old APP^{NL-G-F} mice, and rectify changes to the SWO by increasing the overall activity of PV- and SST-expressing interneurons using DREADD technology. Isoflurane was found to generate the SWO *in vivo*, although this method was found to be suboptimal for studying SWA. Additionally, no observable deficits to UDS dynamics were found in APP mice at 8 months, which is a novel finding. Together, these findings precluded investigation into the effect of enhancing PV- and SST-expressing interneuron activity upon the SWO. Furthermore, this data influenced the use of natural sleep for studying the SWO in future experiments (see **section 5**).

4.3.2 | UDS dynamics appear to be unaffected in 8-month APP animals

No observable changes were found to UDS dynamics in APP animals compared with WT at 8 months. This is inconsistent with previous research using first-generation mouse models of amyloidopathy that identified disruptions to the SWO frequency and coherence at a similar age (Busche *et al.*, 2015; Kastanenka *et al.*, 2017). However, the over-expression of mutated genes in first-generation mouse models can exacerbate certain phenotypes, leading to detectable deficits at younger time-points (Saito *et al.*, 2014; Nilsson, Saito & Saido, 2014; Sasaguri *et al.*, 2017). The KI strategy applied to generate the APP^{NL-G-F} mouse model overcomes this issue (Saito *et al.*, 2014; Nilsson, Saito & Saido, 2014), therefore it is possible that 8 months is too early in the APP^{NL-G-F} mouse model disease progression to observe similar deficits to those modelled by more aggressive APP over-expression mouse lines.

The lack of observable deficits to the SWO at this age meant I was unable to test my hypothesis: that chemogenetically enhancing the activity of PV- and SST-

expressing interneuron populations would ameliorate deficits to the SWO. At the time of this study, little was known about the APP^{NL-G-F} model. The hypothesis that impairments to the SWO would occur at 8-months was based on previous findings of disrupted SWA in first-generation models (Busche *et al.*, 2015; Kastanenka *et al.*, 2017), the relationship between A β load and SWA impairments in humans (Mander *et al.*, 2015b), the development of cortical A β pathology as early as 2 months in the APP^{NL-G-F} mouse model (see **section 3**) as well as spatial memory impairments occurring at 6 months (Saito *et al.*, 2014; Nilsson, Saito & Saido, 2014). Since then, spatial memory impairments occurring at 6 months have been disputed (Whyte *et al.*, 2018), with the majority of research finding subtle memory deficits from 11 months onwards (Latif-Hernandez *et al.*, 2019; Sakakibara *et al.*, 2019; Maezono *et al.*, 2020). Additionally, impaired theta-high gamma coupling is found in the mEC at 5 months (Nakazono *et al.*, 2017) that progresses to the CA1 region of the hippocampus around 12 months (Jun *et al.*, 2020). A separate study failed to notice changes to gamma oscillations in the mPFC *ex vivo* at the same age (Pervolaraki *et al.*, 2019), indicating a progression of neuronal network deficits through different brain regions and a perhaps later onset of cortical neuronal oscillation decline. Conducting experiments at later time-points is therefore necessary to better understand how SWA may be affected in this model.

4.3.3 | Anaesthetics vs natural sleep to study the SWO

4.3.3.1 | Isoflurane

Using isoflurane anaesthesia, Busche and colleagues documented impaired SWO coherence across the cortex in an APP/PSEN1 model that was rescued upon administration of a GABA_A receptor agonist, indicating impaired inhibition (Busche *et al.*, 2015). Therefore, isoflurane was chosen in these experiments to study the effects of enhancing the activity PV- and SST-expressing interneurons populations upon disrupted SWA. However, the depth of isoflurane anaesthesia could not be reliably maintained between baseline and saline control conditions. A significant positive correlation would be expected for each measure of UDS dynamics between conditions if anaesthesia depth is consistent. Yet, this was only noticeable for a few measures, with no effect of genotype. The lack of reproducible anaesthesia depth and UDS dynamics between conditions is particularly a problem when studying the effects of the designer drug upon UDS

dynamics, as it is difficult to reliably compare results with baseline and saline control conditions.

Isoflurane has already been documented to create differences in UDS dynamics with varying anaesthesia depth. The frequency of the SWO has been found to decrease and the amplitude increase with deeper anaesthesia levels (higher isoflurane concentrations) as well as fewer detectable UDS events (Doi *et al.*, 2007; Dasilva *et al.*, 2021). Interestingly, MUA across cortical regions was found to be highly coherent during deeper levels of anaesthesia but emerged as distinct, local activity during lighter anaesthesia (Dasilva *et al.*, 2021). Weight and sex differences are known to have an effect on the concentration of isoflurane required to anaesthetise mice (Gargiulo *et al.*, 2012). Therefore, to try and overcome this, breathing rate was used as a proxy measure of anaesthesia depth as deeper isoflurane anaesthesia depresses breathing rate (Gargiulo *et al.*, 2012; Massey & Richerson, 2017). However, no relationship was found between the breathing rate and UDS amplitude, frequency and occurrence. This result was surprising given the reported influence of differing isoflurane concentrations upon SWA and the relationship between isoflurane concentration and breathing rate (Doi *et al.*, 2007; Gargiulo *et al.*, 2012; Massey & Richerson, 2017; Dasilva *et al.*, 2021). It is possible that under these experimental conditions, isoflurane influences UDS dynamics through multiple interacting factors including the breathing rate as well as isoflurane concentration, age, sex and weight.

4.3.3.2 | Anaesthesia vs natural sleep

The SWO can be studied under several different types of anaesthesia such as isoflurane, urethane, ketamine/xylazine and ketamine/medetomidine as well as during natural sleep, with slight differences in UDS dynamics noted between them (Steriade, Nunez & Amzica, 1993a; Mölle *et al.*, 2004; Mukovski *et al.*, 2007; Doi *et al.*, 2007; Luczak *et al.*, 2007; Chauvette *et al.*, 2011; Castano-Prat *et al.*, 2019; Torao-Angosto *et al.*, 2021; Dasilva *et al.*, 2021). For example, ketamine/xylazine produces a faster, more rhythmic SWO compared with natural sleep (Chauvette *et al.*, 2011), whereas ketamine/medetomidine reduces the SWO frequency (Torao-Angosto *et al.*, 2021). Additionally, urethane anaesthesia produces a slower oscillation frequency compared with ketamine/xylazine (Steriade, Nunez & Amzica, 1993a) and increasing isoflurane depth also

decreases the SWO frequency (Dasilva *et al.*, 2021). Despite these differences, no study has compared UDS dynamics between natural sleep and isoflurane and urethane anaesthesia. Therefore, using WT animals that had been chronically implanted with silicon microelectrodes in the mPFC, UDS dynamics were assessed between these conditions.

No statistically significant difference was observed between the three conditions for each measure of UDS dynamics. However, a trending increase in Up state duration can be seen under urethane anaesthesia compared with natural sleep as can a reduction in UDS frequency and occurrence. Moreover, isoflurane produced the largest variation within the data compared with urethane and natural sleep when assessing the duration of UDS as well as their occurrence. This further demonstrates that isoflurane is not a reliable method for studying the SWO. Although the SWO can be recorded using certain anaesthetics, they each cause differences and variation within UDS dynamics (Crunelli & Hughes, 2010b). Additionally, they all exert their effects upon different cell receptors that can interfere with the true representation and complexity of the SWO (Hara & Harris, 2002; Zanos & Gould, 2018). Therefore, studying this oscillation under natural sleep is optimal for future experiments.

4.3.4 | Conclusions

The aims of this study were to set-up an *in vivo* model of recording SWA under isoflurane anaesthesia, to determine if SWA was impaired similar to first-generation mouse models of amyloidopathy, and to ameliorate SWO deficits in the APP^{NL-G-F} mouse model by enhancing PV- and SST-expressing interneuron populations. The first two aims were achieved; isoflurane was able to generate the SWO and no deficits were identified in APP^{NL-G-F} mice at 8 months, the latter being a novel finding. However, isoflurane was not found to be as reliable a method as originally thought for studying the SWO. The results produced from both of these aims were surprising given previously reported data, and meant that the final aim could not be achieved. Nonetheless, PV- and SST-expressing interneurons are still attractive targets for enhancing disrupted SWA in AD. Conducting similar experiments in this model under natural sleep at an age at which SWA is impaired will hopefully yield more promising results.

5 | Investigating the oscillations underlying systems consolidation in the mPFC-hippocampal circuit during NREM sleep in the APP^{NL-G-F} mouse model

5.1 | Introduction

Sleep disturbances are extremely common in the preclinical stages of AD and are a predictor of cognitive decline (Kabeshita *et al.*, 2017; Bubu *et al.*, 2017). Patients exhibit night time awakenings, sleep fragmentation and disruptions to the sleep/wake cycle, particularly a reduced time spent in NREM sleep (Vitiello *et al.*, 1990; Bubu *et al.*, 2017). During NREM sleep, the oscillations found within the mPFC-hippocampal circuit facilitate the reorganisation of our newly-acquired hippocampal memories into distributed cortical networks for long-term storage, in a process named systems consolidation (Diekelmann & Born, 2010; Maingret *et al.*, 2016b). This is achieved through the temporal coupling of 3 cardinal oscillations; the SWO, spindles and SWRs (see **section 1.2.2.4**).

In humans, the extent of amyloid pathology inversely correlates with both SWA and spindle density (Mander *et al.*, 2015a; Kam *et al.*, 2019). Additionally, impairments to the SWO power, frequency and coherence across cortical regions are found within first-generation mouse models of amyloidopathy (Busche *et al.*, 2015; Kastanenka *et al.*, 2017; Castano-Prat *et al.*, 2019), as are disruptions to SWR dynamics and density (Nicole *et al.*, 2016; Hollnagel *et al.*, 2019; Caccavano *et al.*, 2020), all of which is associated with a decline in declarative memory performance. Although each cardinal oscillator plays an individual role in systems consolidation, it is their temporal communication that drives the reorganisation of hippocampal memories to the cortex for long-term storage (Mölle *et al.*, 2006; Maingret *et al.*, 2016b). Only one study to date has investigated this coupling in a mouse model of amyloidopathy; a reduction in mPFC-hippocampal delta coherence as well as SWR-locked cortical spindle power was found using the APP/PSEN1 mouse model (Zhurakovskaya *et al.*, 2019). However, the full breadth of oscillatory coupling was not addressed in this study and an in-depth understanding of how this circuit is affected in AD is still lacking.

The aim of the following set of experiments was to assess disruptions to the oscillations and oscillatory coupling found within the mPFC-hippocampal circuit during NREM sleep in the second-generation APP^{NL-G-F} KI mouse model (see **section 1.4.5**). Although disruptions to several of the oscillations involved in this

circuit have been identified in first-generation mouse model of amyloidopathy, comparisons should not be assumed as APP over-expression artefacts may cause phenotypes not directly associated with AD (Nilsson, Saito & Saido, 2014; Sasaguri *et al.*, 2017). Experiments were carried out when mice were 16 months old, by which point extensive amyloid pathology is found in both the mPFC and hippocampus (Nilsson, Saito & Saido, 2014; Saito *et al.*, 2014) (see **section 3**). Additionally, by this time point impairments to the sleep/wake cycle have been reported (Maezono *et al.*, 2020) as well as disruptions to both theta and gamma oscillations within the hippocampus and mEC (Nakazono *et al.*, 2017; Jun *et al.*, 2020). Disruptions to these oscillations as well as cortical epileptic discharges occurring at 6 months (Johnson *et al.*, 2020) signify a breakdown in the E-I balance, similar to both first-generation mouse models and humans (Palop *et al.*, 2007; Verret *et al.*, 2012; Born, 2015). Therefore, it was hypothesised that disruptions to the cardinal oscillators and their coupling would be detected during NREM sleep at 16 months.

5.2 | Results

To assess the potential functional disruptions to the mPFC-hippocampal circuit during NREM sleep, 4-channel silicon microelectrodes were inserted into the mPFC and hippocampus, respectively, and neural activity was recorded while mice were naturally sleeping. These experiments were conducted in 16-month-old male and female mice that were homozygous for the APP^{NL-G-F} gene (APP) and their wildtype littermates as controls (WT). Electrodes in the mPFC were primarily located in the ACC and PL cortex, with data from each electrode average together within-animals as no electrophysiological differences were found between regions. Hippocampal analysis was conducted using electrodes situated in CA1 Str. P (see **section 2.2.9**).

5.2.1 | SWS detection

To reduce the signal:noise ratio produced by the mix of SWS periods with non-SWS periods, signals were split into sections defined as either non-SWS (awake, microarousals, REM sleep) or SWS using a custom-made algorithm (see **section 2.4.3**). Signals were split into 30 second epochs and the power of UDS/delta oscillations (1-4 Hz) and theta oscillations (6-12 Hz) were found and a theta:delta power ratio was created (**Figure 5.2.1 A, B**). If the power ratio in a 30 second epoch fell below the threshold (median + 1 SD of the cumulative power ratios from all epochs), signifying greater delta power over theta, and was also accompanied by a lack of movement (manually scored offline using pre-recorded videos of the mouse during the experiment), the epoch was considered SWS (**Figure 5.2.1 B-C**). If an epoch didn't make this requirement it was considered to be non-SWS, with only SWS epochs used for the subsequent analysis found in this chapter (**Figure 5.2.1 D**).

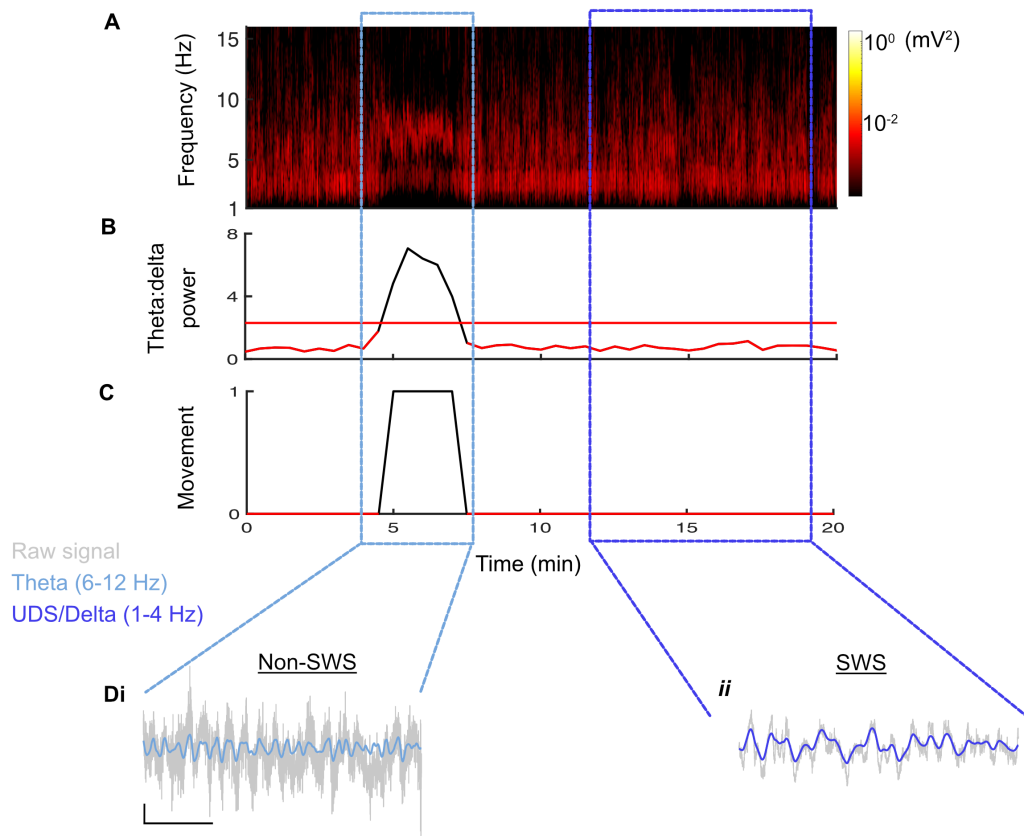


Figure 5.2.1 | Method for isolating periods of SWS. **A** Spectrogram showing power changes over time within the UDS and delta bands (1-4 Hz) and theta (6-12 Hz) band. **B** Corresponding theta:delta power ratio over time. Horizontal red line shows the threshold for distinguishing periods of non-SWS from SWS (median + 1SD). **C** Corresponding manually scored movement of the animal over time, taken as an all-or-nothing binary measure, with 1 showing movement and 0 showing no movement. **B-C** Portions of the time series highlighted in red signify periods of detected SWS that fell below the theta:delta ratio and when no movement was detected. **D** Example traces of theta oscillations in non-SWS (*i*) and UDS and delta oscillations during SWS (*ii*). Scale bars: 1 s, 200 μ V.

5.2.2 | Cortical UDS and delta oscillation power

Across the cortex during SWS, the SWO (0.5-1.25 Hz) and delta oscillations (1.25-4 Hz) dominate (Amzica & Steriade, 1998). Relative to WT mice, APP animals displayed no statistically significant difference in the power of either mPFC UDS or delta oscillations (**Figure 5.2.2 A-C**). The SWO is often misclassified as being a continuation of the delta oscillation (Sirota *et al.*, 2003; Varela & Wilson, 2020), when in fact the two are generated independently and

potentially have different physiological roles (Amzica & Steriade, 1998; Kim, Gulati & Ganguly, 2019). The SWO provides the temporal framework for spindles and SWR to nest within and is the temporal pacemaker of systems consolidation (Mölle *et al.*, 2006; Maingret *et al.*, 2016b), whereas there is evidence for delta oscillations playing a role in forgetting (Kim, Gulati & Ganguly, 2019). Therefore, for the purposes of this chapter, I will be focussing solely on the SWO (also known as UDS). Given the low frequency of the SWO (0.5-1.25 Hz), DC shifts and artefacts (e.g. animal movement, knocking the tether on the cage) within the LFP can often have similar frequencies and can therefore be falsely detected for the SWO within power spectra. The SWO is additionally not a continuous oscillation during natural sleep (Chauvette *et al.*, 2011; David *et al.*, 2013; Latchoumane *et al.*, 2017; Bukhtiyarova *et al.*, 2019). Therefore, to confirm the lack of power spectral difference, individual UDS were isolated from the LFP and analysed.

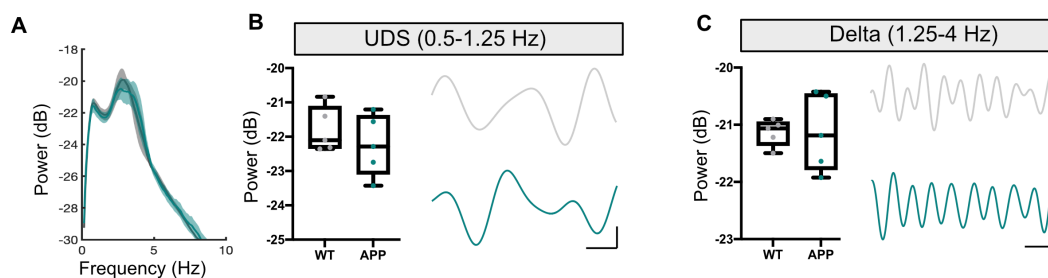


Figure 5.2.2 | The power of both UDS and delta oscillations in the mPFC is not altered in APP animals compared with WT controls. **A** Average power spectra \pm SEM of both WT (grey) and APP (turquoise) mice, showing clear peaks in the UDS and delta frequency bands. **B** No statistically significant difference in the power of UDS was found in APP animals compared with WT (WT: -22.10 (-22.33 - -21.12) vs APP: -22.29 (-23.09 - -21.38) dB, $U = 9$, $p = 0.54$, Mann-Whitney U test). Example traces show UDS bandpass filtered signals for both WT and APP mice. **C** No statistically significant difference in the power of delta oscillations was found in APP animals compared with WT (WT: -21.06 (-21.36 - -20.95) vs APP: -21.19 (-21.78 - -20.46) dB, $U = 12$, $p > 0.99$, Mann-Whitney U test). Example traces show delta bandpass filtered signals for both WT and APP mice. Box plots show median, IQR and ranges. Descriptive statistics display median and IQR. Scale bars: 500 ms, 0.1 mV.

5.2.3 | UDS dynamics

The SWO is defined by the presence of UDS that are generated, in part, by the action of interneurons (see **section 1.2.2.1**). Impaired inhibitory neurotransmission, that causes aberrant network activity and disrupted oscillations, is well documented in humans and first-generation mouse models of AD (Palop *et al.*, 2007; Verret *et al.*, 2012; Born, 2015) as are disruptions to the SWO (Mander *et al.*, 2015a; Busche *et al.*, 2015). There is also growing evidence for an impaired E-I balance in the APP^{NL-G-F} mouse model (Johnson *et al.*, 2020; Jun *et al.*, 2020), therefore it is possible that UDS dynamics are affected during SWS. However, no statistically significant difference was found in APP animals compared with WT controls when analysing the duration of Down states, Up states, the total duration of UDS and the frequency of UDS (**Figure 5.2.3 A, B**). A bimodal distribution can be seen in the cumulative probability histograms for each of these measures, showing two different frequency oscillations, one at ~0.5 Hz and one at ~1 Hz (**Figure 5.2.3 C**). The SWO has been reported to occur at both frequencies (Sanchez-Vives & McCormick, 2000; Chauvette *et al.*, 2011). Given that no visible difference was found between genotypes for either frequency and that a unimodal distribution was found in the cumulative probability histograms displaying UDS amplitude (**Figure 5.2.3 E**), the two different oscillation frequencies were grouped for further analysis and treated as one oscillation. Additionally, the amplitude of Down states, Up states and total UDS amplitude, as well the number of detected UDS events did not statistically differ in APP animals relative to WT controls (**Figure 5.2.3 A, D, F**). Therefore, it appears the SWO is unimpaired at 16 months in APP mice.

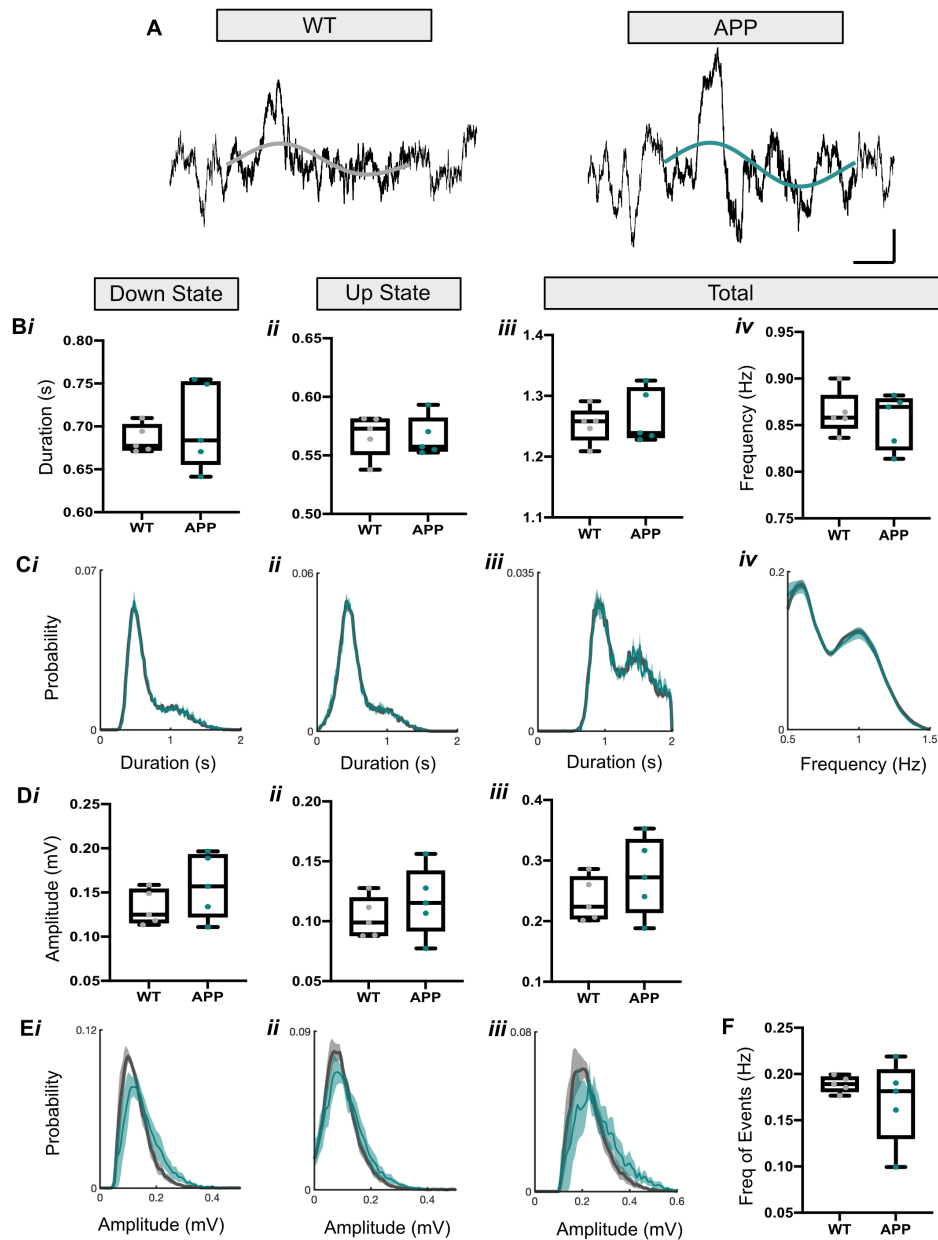


Figure 5.2.3 | UDS dynamics is not altered in APP animals compared with WT controls. **A** Example raw (black) and filtered (coloured) traces of detected UDS, for both WT and APP mice. Scale bar: 200 ms, 200 μ V. **B** No statistically significant difference was found in APP animals compared with WT for the average Down state duration (*WT*: 0.67 (0.67-0.70) vs *APP*: 0.68 (0.66-0.75) s, $U = 12$, $p = 0.99$, Mann-Whitney U test) (**i**), Up state duration (*WT*: 0.57 (0.55-0.58) vs *APP*: 0.56 (0.55-0.58) s, $U = 10$, $p = 0.69$, Mann-Whitney U test) (**ii**), total duration (*WT*: 1.26 (1.23-1.28) vs *APP*: 1.24 (1.23-1.31) s, $U = 12$, $p = 0.99$, Mann-Whitney U test) (**iii**), or UDS frequency (*WT*: 0.86 (0.85-0.88) vs *APP*: 0.87 (0.82-0.88) Hz, $U = 12$, $p = 0.99$, Mann-Whitney U test) (**iv**). **C** Average \pm SEM cumulative probability histograms of all detected UDS from

both WT and APP mice. No visible difference noted in the distribution of UDS data in APP animals relative to WT for the duration of Down states (**i**), Up states (**ii**), total duration (**iii**) or UDS frequency (**iv**). However, a bimodal distribution exists for each measure, indicating two separate frequencies of UDS in both genotypes. **D** No statistically significant difference was found between genotypes for the average Down state amplitude (*WT*: 0.13 (0.12-0.15) vs *APP*: 0.16 (0.12-0.19) mV, $U = 8$, $p = 0.42$, Mann-Whitney U test) (**i**), Up state amplitude (*WT*: 0.10 (0.09-0.12) vs *APP*: 0.12 (0.09-0.14) mV, $U = 8$, $p = 0.42$, Mann-Whitney U test) (**ii**) or total amplitude (*WT*: 0.22 (0.20-0.27) vs *APP*: 0.27 (0.21-0.33) mV, $U = 8$, $p = 0.42$, Mann-Whitney U test) (**iii**). **E** Average \pm SEM cumulative probability histograms of all detected UDS from both WT and APP mice. A slight decrease in the mean peak amplitude probability is noted in APP mice relative to WT or Down states (**i**), Up states (**ii**) or total amplitude (**iii**). **F** No statistically significant difference was found in APP animals relative to WT for the number of detected UDS events (*WT*: 0.18 (0.18-0.20) vs *APP*: 0.18 (0.13-0.20) Hz, $U = 9$, $p = 0.54$, Mann-Whitney U test). Box plots show median, IQR and ranges. Descriptive statistics display median and IQR.

5.2.4 | UDS nested gamma oscillations

Gamma oscillations (30-120 Hz) can be found nested within the Up states of the SWO (Steriade *et al.*, 1996; Valderrama *et al.*, 2012), with some considering these to be “fragments of wakefulness” (Destexhe *et al.*, 2007). Gamma oscillations are found to be disrupted in first-generation mouse models of AD (Verret *et al.*, 2012; Martinez-Losa *et al.*, 2018) and in the APP^{NL-G-F} mouse model (Jun *et al.*, 2020) during awake behaviour, therefore it is possible that they are also affected during SWS. The total power of both low gamma (30-60 Hz) and high gamma (60-120 Hz) oscillations, when nested within UDS, did not change in APP animals compared with WT controls (**Figure 5.2.4 A-C**). Although a trending increase can be seen in the power of low gamma oscillations, but due to variation within the data this is not conclusive (**Figure 5.2.4 B**). Coupling between UDS and gamma oscillations is noticeable from the LFP in humans and rodents under anaesthesia (Mukovski *et al.*, 2007; Valderrama *et al.*, 2012). However, during rodent natural sleep this relationship can be better visualised by displaying the normalised instantaneous amplitude of the gamma oscillation over

the phase of the UDS (Chauvette *et al.*, 2011). To assess the degree of this coupling, phase-amplitude coupling between the two oscillations was measured and quantified using a modulation index (MI) value (see **section 2.4.2**). However, no statistically significant difference was found in APP animals relative to WT controls when analysing the coupling of UDS with both low gamma and high gamma oscillations (**Figure 5.2.4 D, E**), indicating that UDS-locked gamma oscillations are unaltered in 16-month-old APP mice.

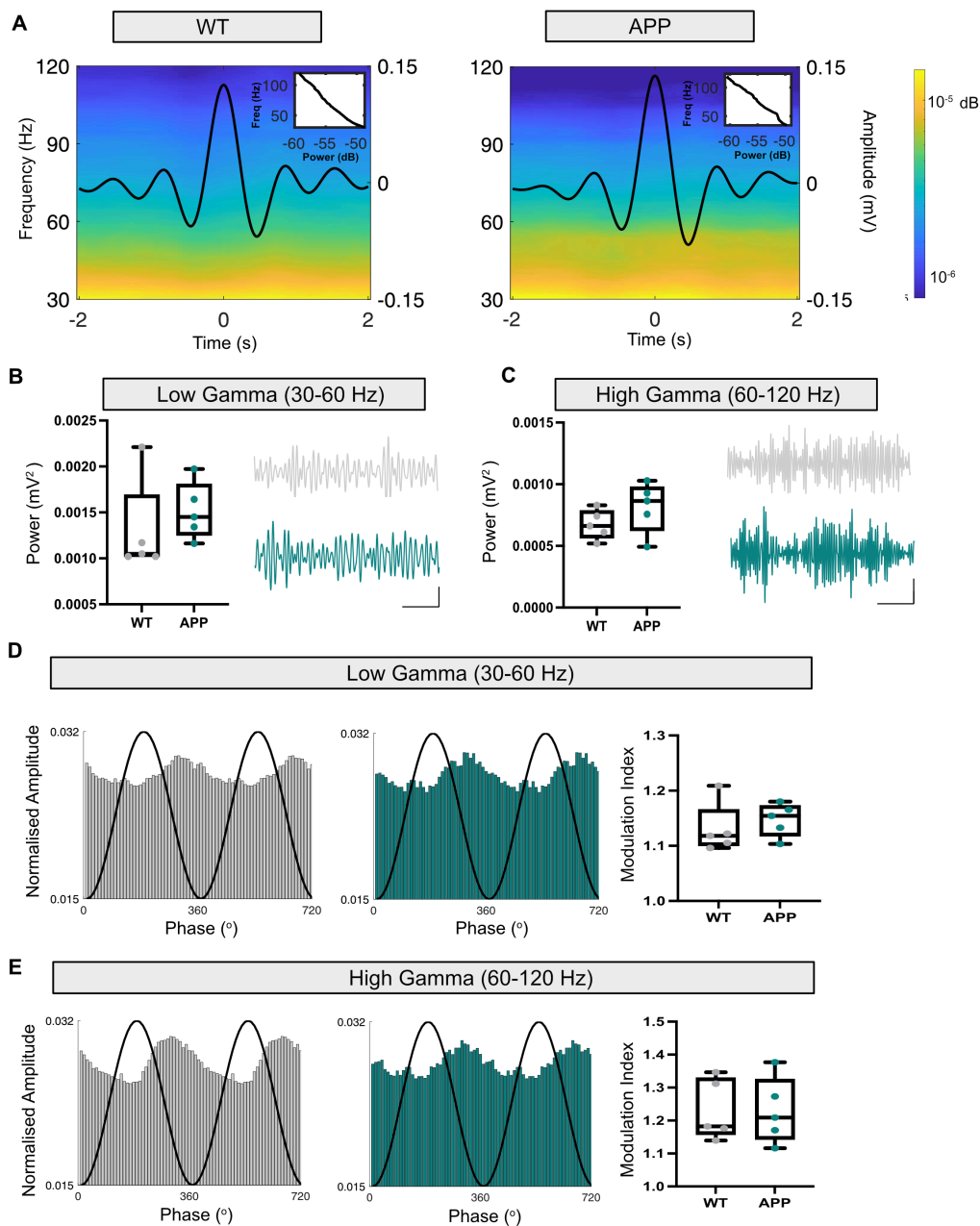


Figure 5.2.4 | No change in UDS-locked gamma power and PAC between genotypes. A Example average UDS traces (black lines) overlaid on its

corresponding power spectrum showing the power of UDS-locked gamma oscillations for both WT and APP mice. Slight modulation of low gamma power can be visualised over the UDS time course. Indented plots (top right corner) display the mean gamma power over the time-course of the LFP power spectrum. **B** No statistically significant difference in the total power of UDS-locked low gamma oscillations was found in APP animals relative to WT (*WT*: 0.0010 (0.0010-0.0017) vs *APP*: 0.0014 (0.0013-0.0018) mV^2 , $U = 6$, $p = 0.2$, Mann-Whitney U test), although a trending increase is seen within APP mice. Example traces show low gamma bandpass filtered signals for both WT (grey) and APP (turquoise) mice. **C** No statistically significant difference in the total power of UDS-locked high gamma oscillations was found in APP animals relative to WT (*WT*: 0.00066 (0.00057-0.00079) vs *APP*: 0.00087 (0.00063-0.00098) mV^2 , $U = 6$, $p = 0.22$, Mann-Whitney U test). Example traces show high gamma bandpass filtered signals for both WT and APP mice. Scale bars: 200ms, 40 μV . **D** No statistically significant difference in the PAC of UDS with low gamma oscillations was found in APP animals relative to WT (*WT*: 1.12 (1.10-1.17) vs *APP*: 1.15 (1.12-1.17) MI, $U = 8$, $p = 0.42$, Mann-Whitney U test). Shown are example histograms of the changes to the low gamma normalised amplitude (bars) over the phase of the UDS (black line) for both WT (left) and APP (right) mice. **E** No statistically significant difference in the PAC of UDS with high gamma oscillations was found in APP animals relative to WT (*WT*: 1.18 (1.16-1.33) vs *APP*: 1.21 (1.14-1.33) MI, $U = 12$, $p = 0.99$, Mann-Whitney U test). Shown are example histograms of the changes to the high gamma normalised amplitude (bars) over the phase of the UDS (black line) for both WT (left) and APP mice (right). Box plots show median, IQR and ranges. Descriptive statistics display median and IQR.

5.2.5 | Cortical and hippocampal spindles

Thalamocortical spindles (11-15 Hz) are waxing-waning oscillations that typically last between 0.5-2 s (Lüthi, 2014). Spindles occur at the start of SWO Up states (Mölle *et al.*, 2002) and act to increase intracellular Ca^{2+} in the post-synaptic cortical dendrites to facilitate plasticity-related changes (Niethard *et al.*, 2018). A statistically significant increase in the amplitude of mPFC spindles was found in APP mice compared with WT controls, with a corresponding statistically

significant increase in their total power (**Figure 5.2.5 A, B, Cii**). Note the rightward shift in the WT vs APP cumulative probability histogram showing increased spindle amplitude (**Figure 5.2.5 Dii**). No statistically significant difference was found in the total duration of spindles, their frequency, nor in the number of detected spindle events (**Figure 5.2.5 A, C, D, E**).

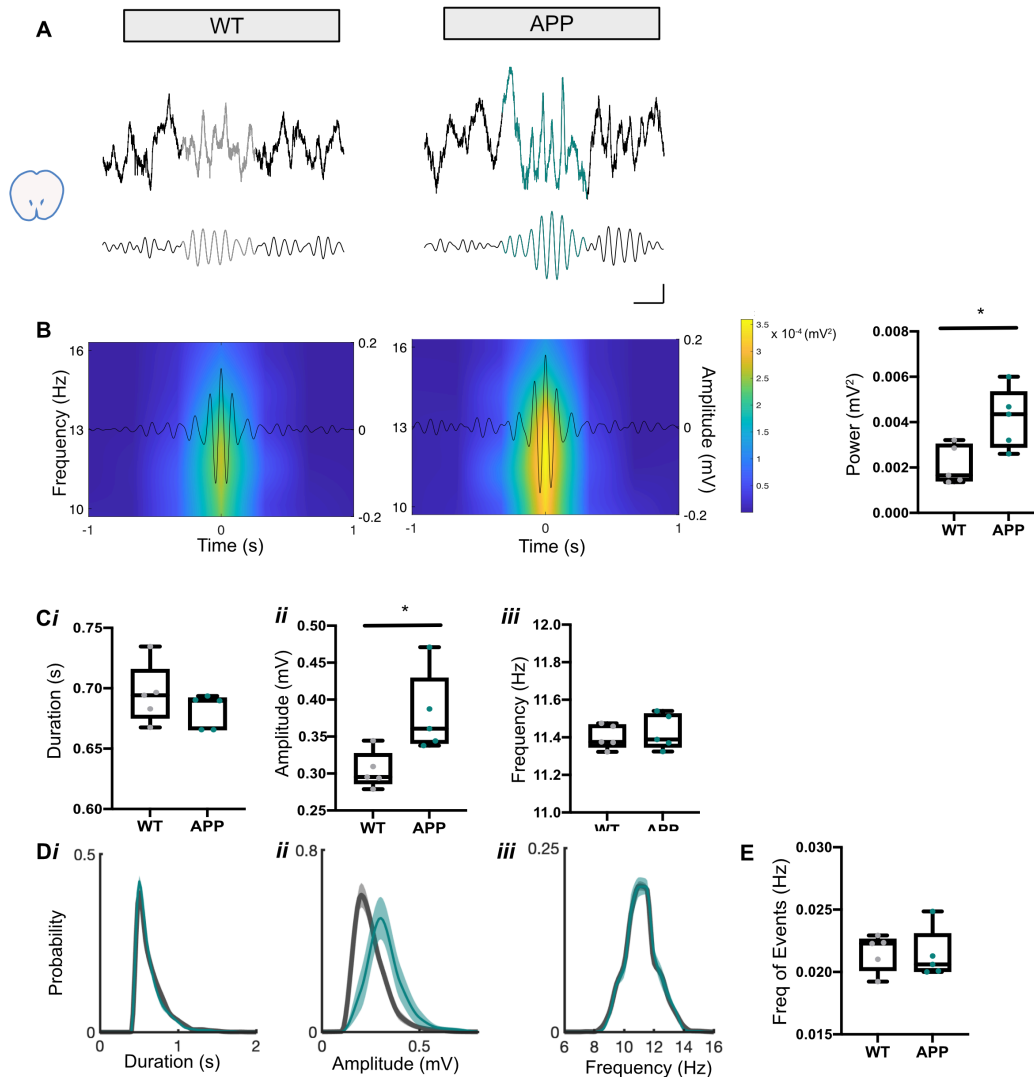


Figure 5.2.5 | A statistically significant increase in the amplitude and power of mPFC spindles in APP mice relative to WT. A Example raw (top) and 11-15 Hz bandpass filtered (bottom) traces of detected spindle events (coloured segments) from WT and APP mice. Scale bars: 250 ms, 200 μ V. **B** Example average spindle traces (black lines) overlaid on its corresponding power spectrum showing average spindle power. A statistically significant increase in the average spindle power was found in APP mice compared with WT controls (*WT*: 0.0017 (0.0014-0.0030) vs *APP*: 0.0043 (0.0029-0.0053))

mV², $U = 2.5$, $p = 0.03$, Mann-Whitney U test). **C** No statistically significant difference was found in APP animals relative to WT for the average spindle duration (WT: 0.69 (0.68-0.72) vs APP: 0.69 (0.67-0.69) s, $U = 6$, $p = 0.22$, Mann-Whitney U test) (**i**) or frequency (WT: 11.38 (11.35-11.47) vs APP: 11.39 (11.35-11.53) Hz, $U = 10$, $p = 0.69$, Mann-Whitney U test) (**iii**) but a statistically significant increase in the average spindle amplitude was found in APP mice compared with WT controls (WT: 0.30 (0.29-0.33) vs APP: 0.36 (0.34-0.43) mV, $U = 2$, $p = 0.03$, Mann-Whitney U test) (**ii**). **D** Average \pm SEM cumulative probability histograms of all detected spindle events from both WT and APP mice. No change seen in the distribution of data for both event duration (**i**) and frequency (**iii**) but a rightward shift can be seen in the distribution of spindle amplitudes in APP mice relative to WT controls (**ii**), consistent with the increase in average spindle amplitude. **E** No statistically significant difference was found in APP animals relative to WT for the number of detected spindle events (WT: 0.022 (0.020-0.023) vs APP: 0.021 (0.020-0.023) Hz, $U = 10$, $p = 0.69$, Mann-Whitney U test). Box plots show median, IQR and ranges. Descriptive statistics display median and IQR. * $p < 0.05$.

Spindles are also documented to occur within the CA1 region of the hippocampus and are thought to arrive by mEC input *via* the TA pathway (Sullivan *et al.*, 2014). Contrary to cortical spindles, a trending but not statistically significant decrease in the amplitude and overall power of hippocampal spindles was found in APP animals relative to WT (**Figure 5.2.6 A, B, Cii, Dii**). Additionally, no statistically significant difference was found in the overall duration of spindle events nor in their frequency when comparing APP animals with WT (**Figure 5.2.6 A, Ci,iii, Di,iii**). Interestingly, a statistically significant decrease in the number of detected spindle events was found in APP animals compared with WT controls (**Figure 5.2.6 E**). Since there was no evidence of decreased spindle number in mPFC, this result indicates potentially impaired mEC input to CA1 in APP mice, which would be consistent with previously reported data (Jun *et al.*, 2020).

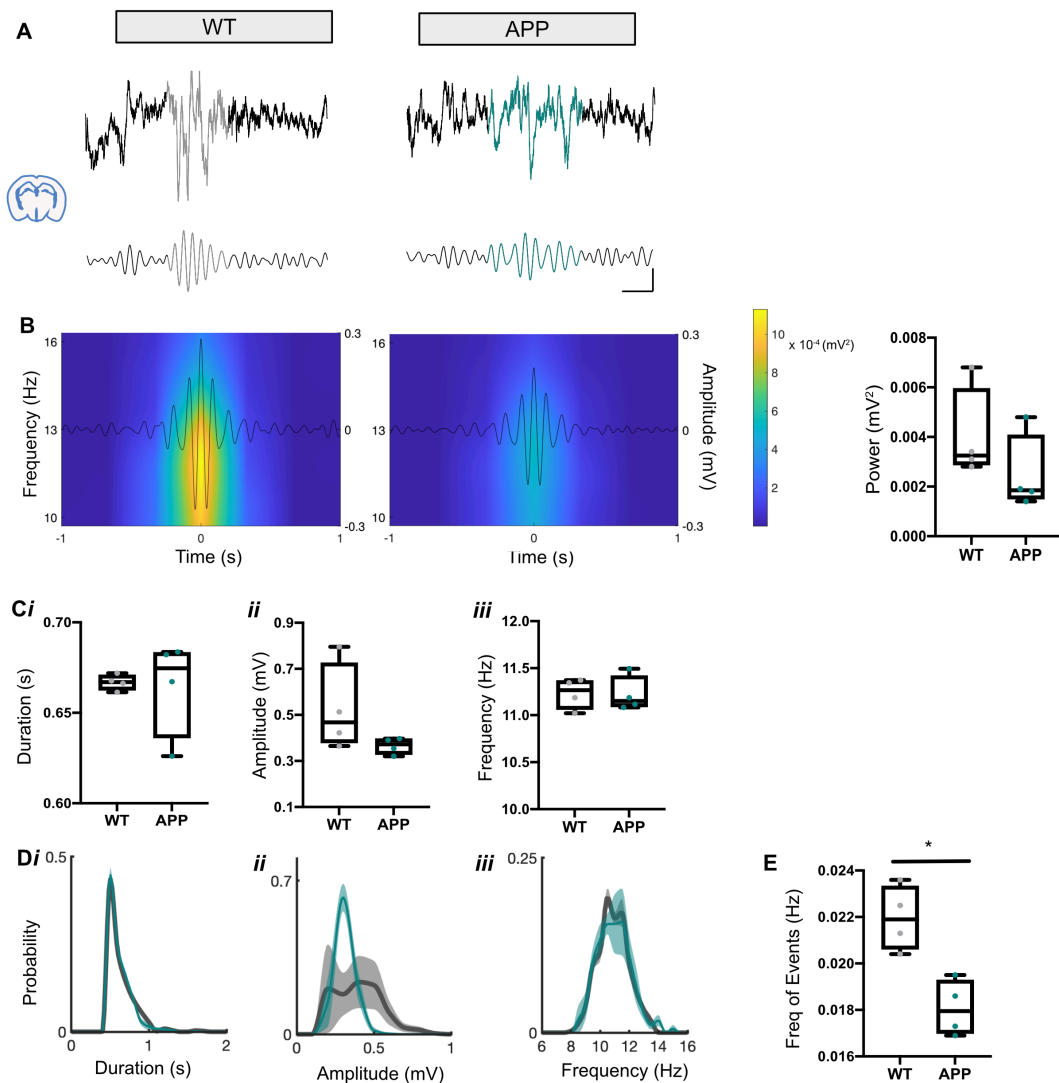


Figure 5.2.6 | A trending decrease in the amplitude and power of CA1 spindle events and statistically significant decrease in the number of detected of events in APP mice. A Example raw (top) and 11-15 Hz bandpass filtered (bottom) traces of detected hippocampal spindle events (coloured segments) from WT and APP mice. Scale bars: 250 ms, 200 μ V. **B** Example average spindle traces (black lines) overlaid on its corresponding power spectrum showing average spindle power. A trending decrease in the average spindle power can be seen in APP mice compared with WT controls (WT: 0.0033 (0.0029-0.0060) vs APP: 0.0019 (0.0015-0.0041) mV², $U = 3$, $p = 0.20$, Mann-Whitney U test). **C** No statistically significant difference was found in APP animals compared with WT for the average spindle duration (WT: 0.67 (0.66-0.67) vs APP: 0.67 (0.64-0.68) s, $U = 6$, $p = 0.68$, Mann-Whitney U test) (*i*) or frequency (WT: 11.27 (11.06-11.37) vs APP: 11.15 (11.09-11.42) Hz, $U = 7.5$, $p = 0.91$, Mann-Whitney U test) (*iii*) but a trending decrease in the average

spindle amplitude can be seen in APP animals (*WT*: 0.47 (0.38-0.72) vs *APP*: 0.37 (0.33-0.40) mV, $U = 2$, $p = 0.11$, Mann-Whitney U test) (*ii*). **D** Average \pm SEM cumulative probability histograms of all detected spindle events from both WT and APP mice. No change seen in the distribution of data for both event duration (*i*) and frequency (*iii*) but large variation can be seen in the distribution of spindle amplitudes in WT animals (*ii*). **E** A statistically significant decrease in the frequency of detected spindle events was found in APP mice compared with WT controls (*WT*: 0.021 (0.020-0.023) vs *APP*: 0.018 (0.017-0.019) Hz, $U = 0$, $p = 0.02$, Mann-Whitney U test). Box plots show median, IQR and ranges. Descriptive statistics display median and IQR. * $p < 0.05$.

Spindles are generated, in part, by PV-expressing interneurons within the TRN (Clemente-Perez *et al.*, 2017b). Optogenetic activation of PV-expressing interneurons within the anterior TRN (aTRN) has previously been shown to generate spindles in both the mPFC and CA1 (Latchoumane *et al.*, 2017). Given the importance of these neurons for spindle generation, and the impairments seen to these neurons in mouse models of amyloidopathy (Verret *et al.*, 2012), immunohistochemical staining and analysis was performed for PV-expressing interneurons within the aTRN to determine if there were any changes in protein immunoreactivity. No statistically significant difference was found in the number of immunoreactive PV-expressing interneurons in APP animals compared with WT controls (**Figure 5.2.7 A, B**).

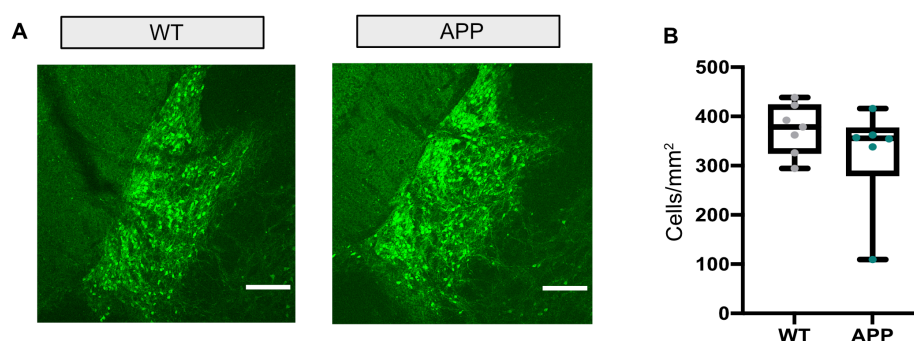


Figure 5.2.7 | PV-expressing interneuron immunoreactivity does not change in APP animals within the aTRN. A Representative images of PV-expressing interneurons within the aTRN of WT and APP mice. Scale bar: 200 μ m. **B** No statistically significant difference in the immunoreactivity between

genotypes (*WT*: 378.7 (326.1-422.5) vs *APP*: 355.5 (280.8-375.7) Cell/mm², $U = 13.5$, $p = 0.31$, Mann-Whitney U test). Box plots show median, IQR and ranges. Descriptive statistics display median and IQR.

5.2.6 | UDS nested spindles

Both cortical and hippocampal spindles occur at the beginning of the SWO Up states (Möller *et al.*, 2002; Staresina *et al.*, 2015). This coupling can be clearly seen when looking at the power of spindles relative to the UDS trace as well as looking at the normalised instantaneous spindle amplitude over UDS phase (**Figure 5.2.8 A, B**). To assess the coupling strength between UDS and both cortical and hippocampal spindles, several different parameters were measured. No statistically significant difference was found in the PAC of UDS with cortical spindles when comparing *APP* with *WT* (**Figure 5.2.8 B**). Additionally, there was no statistically significant difference in the time lag between the peak of the Down states and the peak of cortical spindle events nor was there a difference in the percentage of UDS that were coupled to a cortical spindle (**Figure 5.2.8 C, D**).

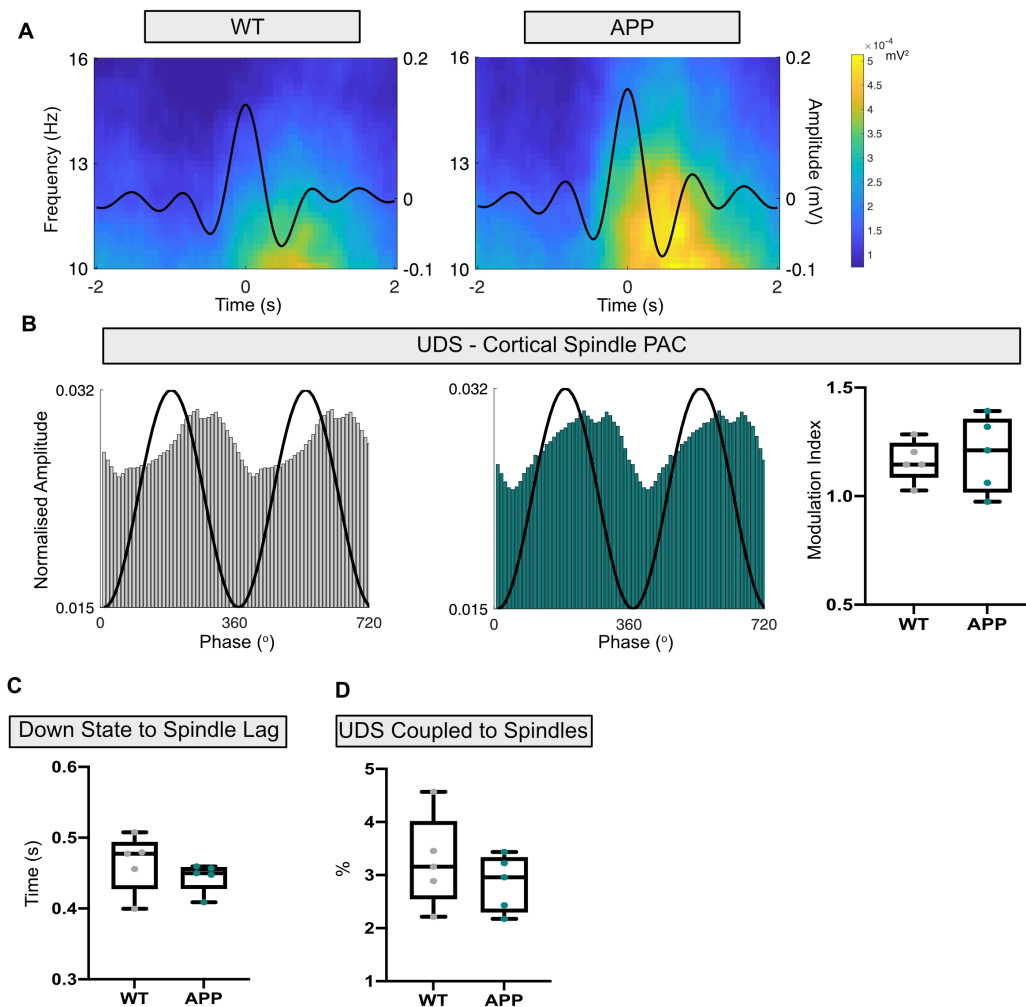


Figure 5.2.8 | No changes in the coupling of UDS with mPFC spindles. A Example average UDS traces (black lines) overlaid on its corresponding power spectrum showing the power of UDS-locked mPFC spindle oscillations for both WT and APP mice. Spindles can be seen locked to SWO Up states. **B** No statistically significant difference in the PAC of UDS with mPFC spindle oscillations was found in APP animals relative to WT (WT: 1.15 (1.09-1.24) vs APP: 1.21 (1.02-1.36) MI, $U = 10$, $p = 0.65$, Mann-Whitney U test). Shown are example histograms of the changes to the spindle normalised amplitude (bars) over the phase of the UDS (black line) for both WT (left) and APP (right) mice. **C** No statistically significant difference was found in the time lag between the peak of the Down state to the peak of the mPFC spindle event (WT: 0.48 (0.43-0.49) vs APP: 0.45 (0.43-0.46) s, $U = 7$, $p = 0.31$, Mann-Whitney U test). **D** No statistically significant difference was found in the percentage of UDS coupled to a mPFC spindle event (WT: 3.16 (2.55-4.01) vs APP: 2.96 (2.30-3.33) %, U

= 9, $p = 0.54$, Mann-Whitney U test). Box plots show median, IQR and ranges. Descriptive statistics display median and IQR.

However, a trending decrease can be seen in the PAC of UDS with hippocampal spindles in APP mice compared with WT controls (**Figure 5.2.9 A, B**). This could potentially be due to the trending decrease seen to hippocampal spindle amplitude reported previously (see **section 5.2.5**). Additionally, no statistically significant difference was found in the time lag between the peak of the Down states and the peak of hippocampal spindles (**Figure 5.2.9 C**). Yet, a trending decrease in the percentage of UDS coupled to spindles was found in APP animals compared with WT controls, that can potentially be attributed to the decrease in the frequency of detected hippocampal spindle events (**Figure 5.2.9 D**). These results therefore show that coupling between UDS and cortical spindles remains intact, whereas coupling between UDS and hippocampal spindles shows the early signs of disruption in APP mice; whether this is due to long-range communication or local impairments remains to be determined.

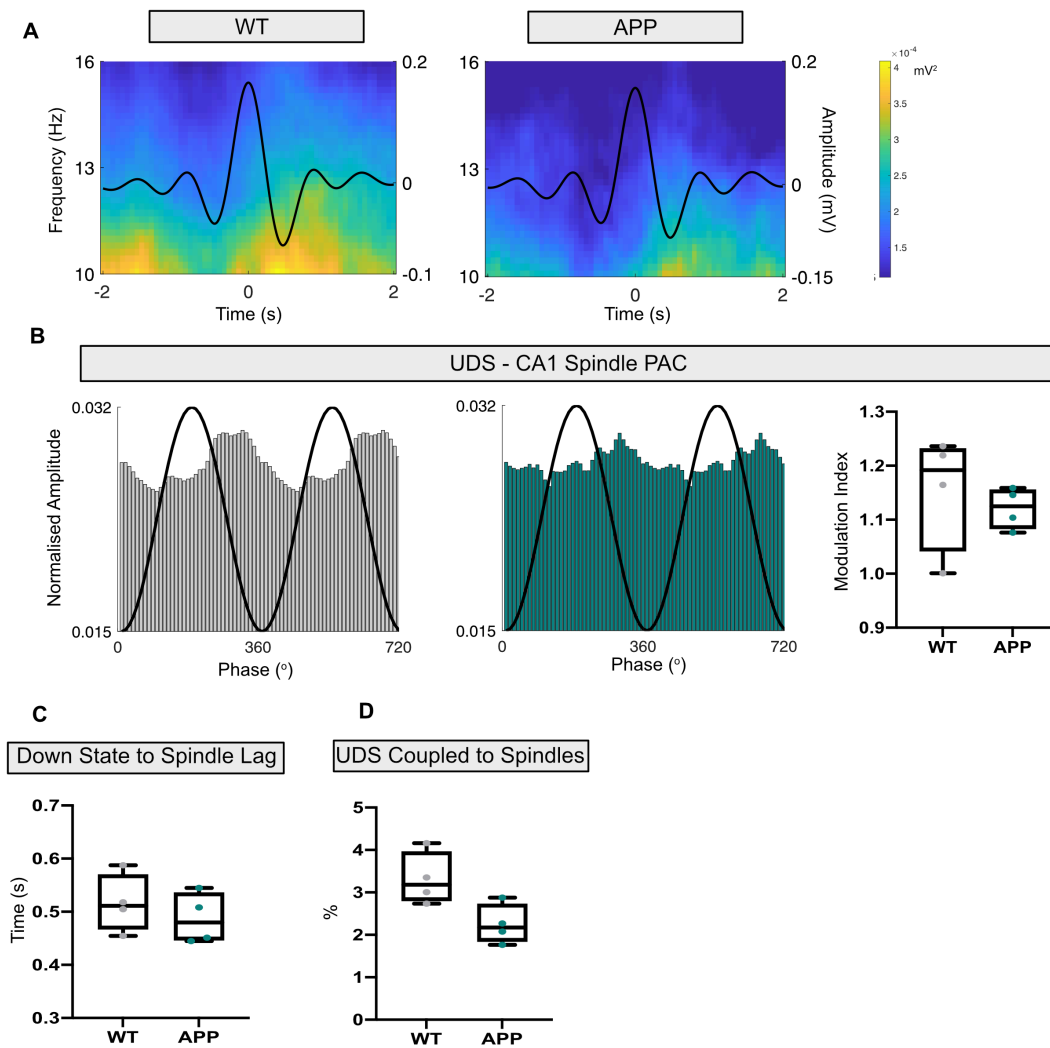


Figure 5.2.9 | Impaired UDS coupling to CA1 spindles. **A** Example average UDS traces (black lines) overlaid on its corresponding power spectrum showing the power of UDS-locked CA1 spindle oscillations for both WT and APP mice. Spindles can be seen locked to Up states. **B** A trending decrease in the PAC of UDS with CA1 spindle oscillations was found in APP animals compared with WT (*WT*: 1.19 (1.04-1.23) vs *APP*: 1.12 (1.08-1.16) MI, $U = 4$, $p = 0.34$, Mann-Whitney U test). Shown are example histograms of the changes to the spindle normalised amplitude (bars) over the phase of the UDS (black line) for both WT (left) and APP (right) mice. **C** No statistically significant difference was found in the time lag between the peak of the Down states to the peak of the CA1 spindle events (*WT*: 0.51 (0.47-0.57) vs *APP*: 0.48 (0.45-0.54) s, $U = 5$, $p = 0.48$, Mann-Whitney U test). **D** A trending decrease in the percent of UDS coupled to CA1 spindles was found in APP mice compared with WT controls (*WT*: 3.18 (2.80-3.96) vs *APP*: 2.17 (1.84-2.73) %, $U = 1$, $p = 0.05$, Mann-Whitney U test). Box

plots show median, IQR and ranges. Descriptive statistics display median and IQR.

5.2.7 | Spindle – spindle coupling

Optogenetic stimulation of PV-expressing interneurons within the aTRN can generate spindles in both the mPFC and CA1, with cortical spindles appearing first and hippocampal spindles following (Latchoumane *et al.*, 2017). The mEC appears to act as an intermediary brain region, assisting in the communication between the mPFC and hippocampus. For example, strong excitatory current sinks in CA1 *Str.LM* during hippocampal spindles suggest mEC input *via* the TA pathway (Sullivan *et al.*, 2014). Impaired communication between the mEC and CA1 has already been documented in the APP^{NL-G-F} mouse model during spatial navigation (Jun *et al.*, 2020). Therefore, it is possible that the coupling of spindles between the mPFC and CA1 is also impaired. Interestingly, no statistically significant difference was found in APP animals relative to WT when analysing the time lag between spindle events or in the percentage of cortical spindles coupled to hippocampal spindles (**Figure 5.2.10 A-C**). The latter result is surprising given that there is a statistically significant decrease in the number of hippocampal spindles (see **section 5.2.5**), suggesting that fewer hippocampal spindles occur independent of cortical spindles in APP mice compared with WT. This is in keeping with data showing that spindles are not always coherent across cortical and hippocampal structures, but can occur as local events (Nir *et al.*, 2011).

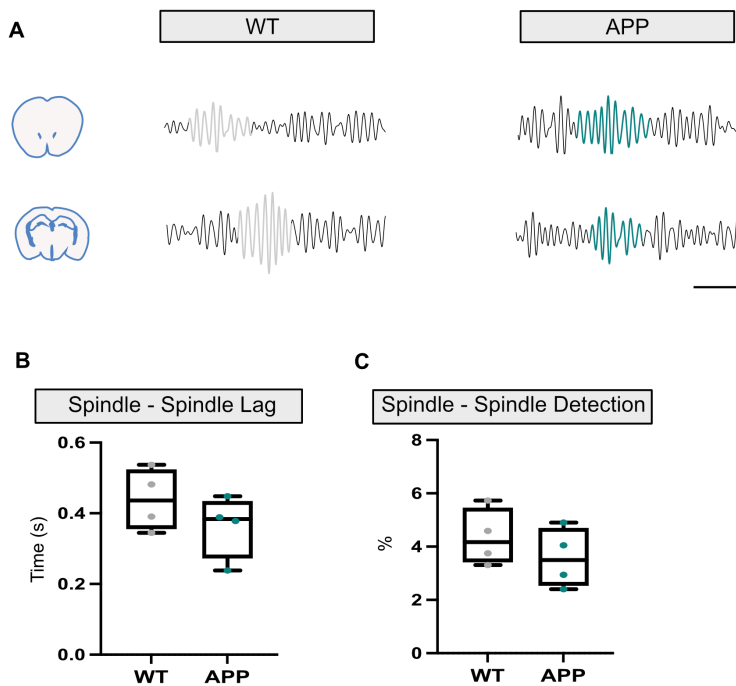


Figure 5.2.10 | Unimpaired mPFC to CA1 spindle coupling in APP mice. A Examples of 11-15 Hz bandpass filtered traces of coupled spindle events (coloured segments) in the mPFC (top) and CA1 (bottom) from WT and APP mice. Scale bars: 500 ms, 200 μ V. **B** No statistically significant difference was found in the time lag between the start of mPFC spindle events to the start of CA1 spindle events (*WT*: 0.44 (0.35-0.52) vs *APP*: 0.38 (0.27-0.43) s, $U = 4$, $p = 0.34$, Mann-Whitney U test). **C** No statistically significant difference in the percentage of cortical spindles coupled to hippocampal spindles was identified (*WT*: 4.17 (3.42-5.45) vs *APP*: 3.50 (2.54-4.69) %, $U = 5$, $p = 0.48$, Mann-Whitney U test). Box plots show median, IQR and ranges. Descriptive statistics display median and IQR.

5.2.8 | Hippocampal ripples

Hippocampal ripples are thought to represent the replay of the neuronal firing patterns associated with previously encoded information during awake behaviour (Nádasy *et al.*, 1999). The information contained within these oscillatory events is then reorganised within cortical networks during systems consolidation (Wierzynski *et al.*, 2009a; Dong, Wang & Ikemoto, 2016), with disruptions to these oscillations impairing the consolidation of hippocampus-dependant memories (Girardeau *et al.*, 2009). Additionally, SWR and the PV-expressing interneurons that contribute to their generation are impaired in first-generation mouse models

of amyloidopathy (Verret *et al.*, 2012; Hollnagel *et al.*, 2019; Caccavano *et al.*, 2020). It was therefore hypothesised that ripples would be disrupted in the APP^{NL-G-F} mouse model at 16 months. No statistically significant difference was found when comparing APP animals with WT for ripple duration or frequency (**Figure 5.2.11 A, Ci,iii, Di,iii**). However, a statistically significant decrease in ripple power was found in APP animals compared with WT controls that was not accompanied by a statistically significant change in ripple amplitude (**Figure 5.2.11 A, B, Cii, Dii**). Ripple amplitude is taken as the difference between the highest peak and the lowest trough, whereas power is measured using the short-time FFT of the whole ripple event. The fact that there is no change to the amplitude but a decrease in overall power potentially points to impairments at other points along the duration of the ripple event, indicating disrupted spike-time dynamics. Interestingly, a trending increase in the number of detected ripple events was found in APP animals compared with WT controls (**Figure 5.2.11 E**). Taken together, it can be concluded that ripple oscillations are disrupted in APP mice at 16 months old.

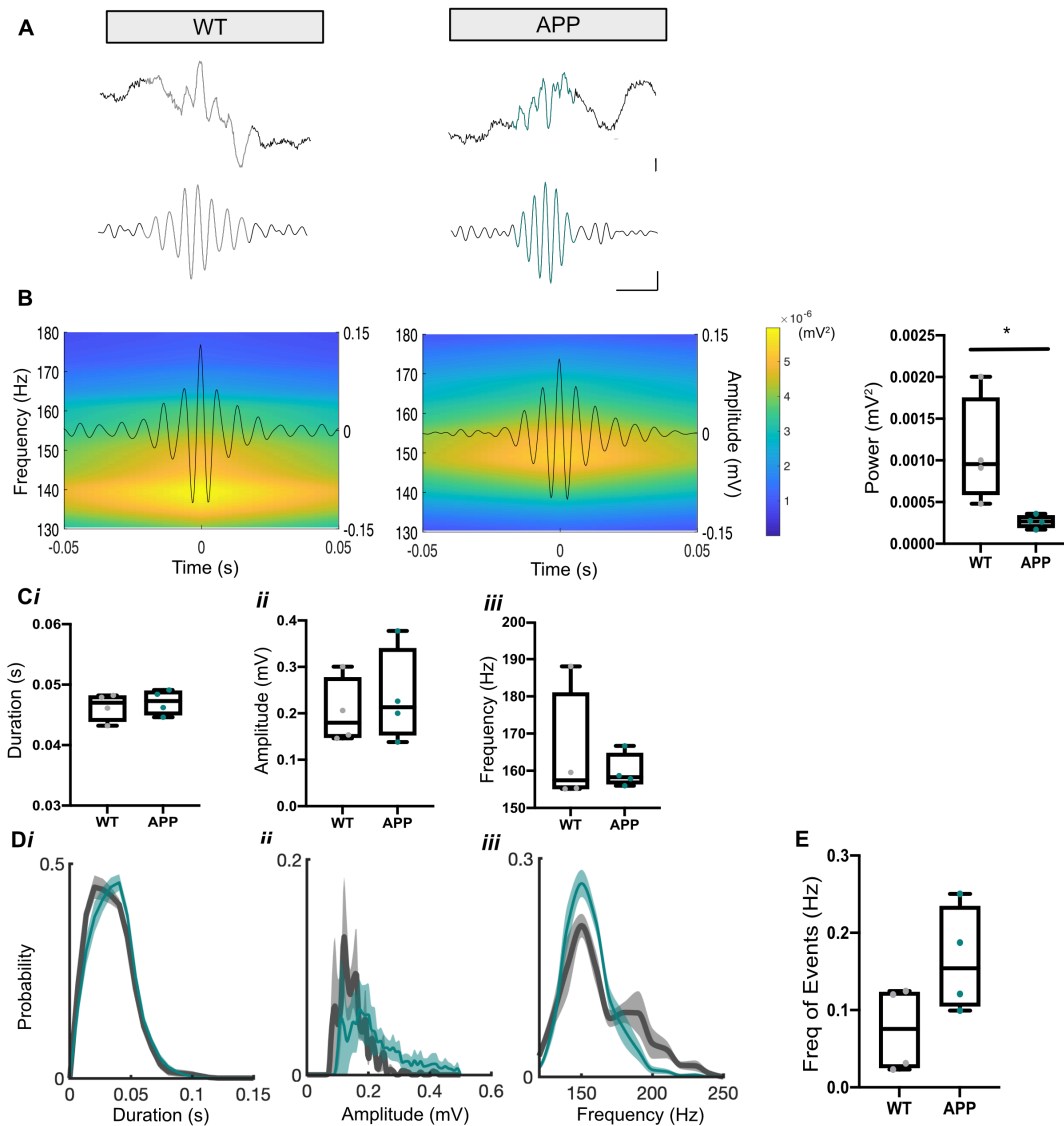


Figure 5.2.11 | A statistically significant decrease in the power of ripple events but a trending increase in ripple occurrence in APP mice. A Example raw (top) and 130-250 Hz bandpass filtered (bottom) traces of detected ripple events from WT and APP mice (coloured segments). Scale bars: 20 ms, 50 μ V (bottom), 100 μ V (top). **B** Example average ripple traces (black lines) overlaid on corresponding power spectra showing average ripple power. A statistically significant decrease in the average ripple power can be seen in APP mice compared with WT controls (*WT*: 0.00095 (0.00059-0.00175) vs *APP*: 0.00027 (0.00019-0.00034) mV², $U = 0$, $p = 0.02$, Mann-Whitney U test). **C** No statistically significant difference was found in the average ripple duration (*WT*: 0.050 (0.044-0.048) vs *APP*: 0.047 (0.045-0.049) s, $U = 5$, $p = 0.48$, Mann-Whitney U test) (*i*), amplitude (*WT*: 0.18 (0.15-0.28) vs *APP*: 0.21 (0.15-0.34) mV, $U = 7$, $p = 0.88$, Mann-Whitney U test) (*ii*) and frequency (*WT*:

157.4 (155.2-180.9) vs APP: 158.3 (156.5-164.7) %, $U = 7$, $p = 0.88$, Mann-Whitney U test) (**iii**). **D** Average \pm SEM cumulative probability histograms of all detected ripple events from both WT and APP mice. A slight rightward shift in the peak duration can be seen in APP animals (**i**) and what looks like decrease variation in ripple frequency occurring in APP animals (**iii**). Large variation in the distribution of ripple amplitudes can be seen for both genotypes (**ii**). **E** A trending increase in the occurrence of detected ripple events was found in APP mice compared with WT controls (WT: 0.08 (0.03-0.12) vs APP: 0.15 (0.10-0.23) Hz, $U = 3$, $p = 0.2$, Mann-Whitney U test). Box plots show median, IQR and ranges. Descriptive statistics display median and IQR. * $p < 0.05$.

5.2.9 | UDS nested ripples

Ripples occur towards the end of SWO Up states (Mölle *et al.*, 2006). An increase in ripple power can be seen nested within the trough of the overlying UDS (**Figure 5.2.12 A**). No statistically significant difference was found in APP animals relative to controls when looking at the PAC of ripples with UDS and when comparing the time lag between the peak of the Down states with the peak of the ripple events (**Figure 5.2.12 B, C**). However, a trending increase in the percentage of UDS coupled to ripples is found in APP animals compared with WT controls (**Figure 5.2.12 D**). This is consistent with the increased number of ripple events previously reported (see **section 5.2.8**). Interestingly, when taking a ratio of the frequency of UDS coupled to cortical spindles and ripples to the frequency of UDS coupled to ripples alone, a trending decrease is found in APP mice compared with WT controls (**Figure 5.2.12 E**). This indicates that there is a greater proportion of UDS that co-occur with ripples without cortical spindle events in APP mice. This is again consistent with the increased number of detected ripples. Given that UDS-spindle-ripple coupling seems to be necessary for systems consolidation, it is interesting to speculate on the physiological ramifications of ripples occurring without spindles, and whether they are similarly effective for memory consolidation.

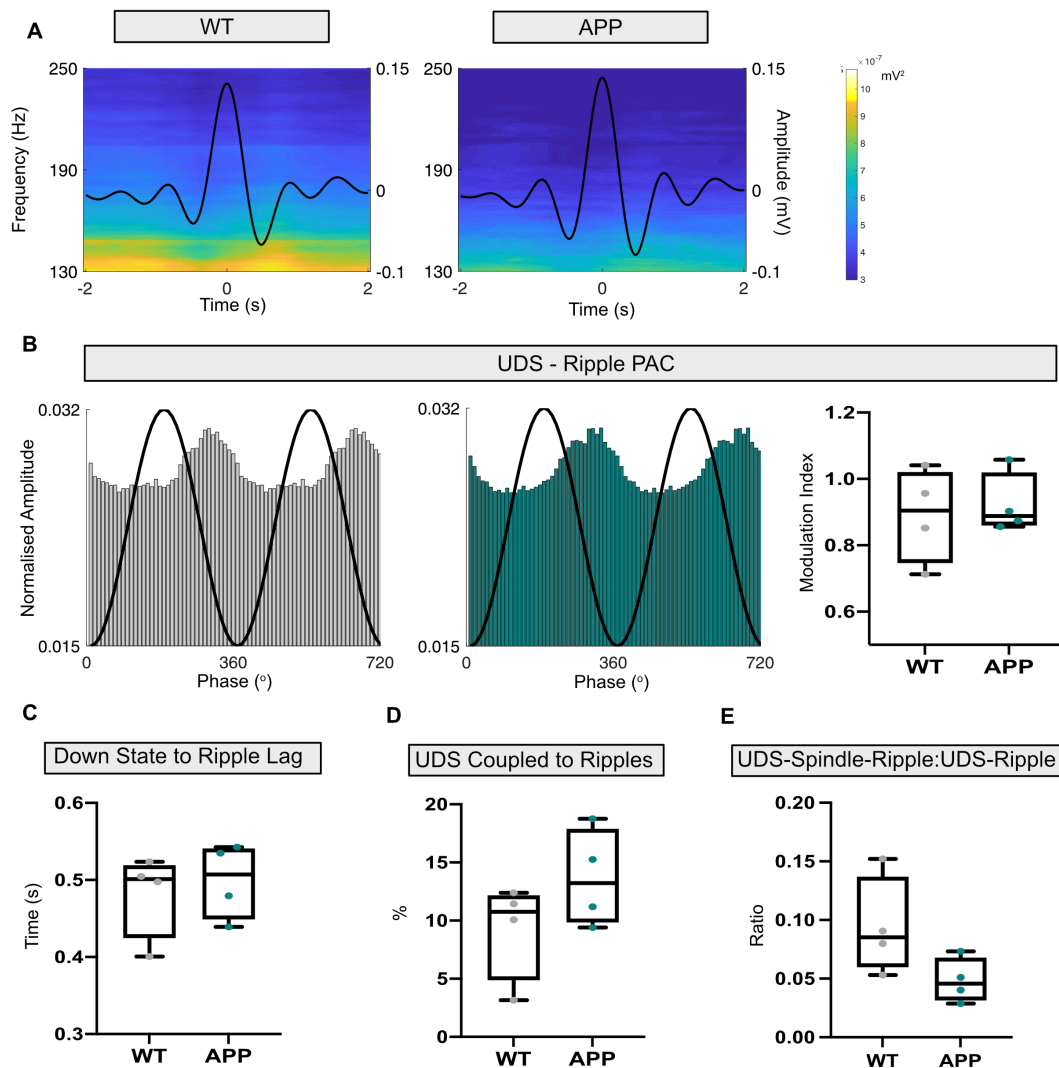


Figure 5.2.12 | A larger proportion of UDS are coupled to ripples without mPFC spindles in APP mice. **A** Example average UDS traces (black lines) overlaid on its corresponding power spectrum showing the power of UDS-locked ripple oscillations for both WT and APP mice. Ripples can be seen locked to SWO Up states. **B** No statistically significant difference in the PAC of UDS with ripple oscillations was found between in APP animals compared with WT controls (*WT*: 0.90 (0.75-1.02) vs *APP*: 0.89 (0.86-1.02) MI, $U = 6$, $p = 0.68$, Mann-Whitney U test). Shown are example histograms of the changes to the ripple normalised amplitude (bars) over the phase of the UDS (black line) for both WT (left) and APP (right) mice. **C** No statistically significant difference was found in the time lag between the peak of the Down state to the peak of the ripple event (*WT*: 0.50 (0.42-0.52) vs *APP*: 0.51 (0.44-0.54) s, $U = 6$, $p = 0.68$, Mann-Whitney U test). **D** A trending increase was found in APP mice compared with WT controls when looking at the percentage of UDS coupled to ripples

(*WT*: 10.76 (4.89-12.15) vs *APP*: 13.23 (9.86-17.88) %, $U = 5$, $p = 0.48$, Mann-Whitney U test). **E** A trending decrease in the ratio of UDS-spindle-ripple coupling to UDS-ripple coupling can be seen in *APP* animals compared with *WT* controls, signifying a larger proportion of UDS coupled to ripples without spindles, that is consistent with the trending increase in ripple events and UDS coupled to ripples (*WT*: 0.09 (0.06-0.14) vs *APP*: 0.05 (0.03-0.07), $U = 1$, $p = 0.05$, Mann-Whitney U test). Graphs show median and ranges. Box plots show median, IQR and ranges. Descriptive statistics display median and IQR.

5.2.10 | Spindle – ripple coupling

Cortical spindles occur before hippocampal ripples, and the coupling of these oscillations helps to drive systems consolidation (Siapas & Wilson, 1998; Clemens *et al.*, 2007; Xia *et al.*, 2017); spindles prime cortical neurons for plasticity-related changes with an increase in intracellular Ca^{2+} (Niethard *et al.*, 2018), ready for information to be sent from the hippocampus during a ripple (Wierzynski *et al.*, 2009a; Dong, Wang & Ikemoto, 2016). A breakdown in this coupling could therefore have disastrous consequences upon memory. No statistically significant difference was found in *APP* animals relative to *WT* controls in the time lag between the start of cortical spindles and hippocampal ripples nor in the percentage of cortical spindles coupled to ripples (**Figure 5.2.13 A-C**). However, a statistically significant decrease was found in the percentage of hippocampal ripples that were preceded by a cortical spindle (**Figure 5.2.13 D**), indicating that there is a greater proportion of ripples occurring in the hippocampus that are uncoupled to spindles in *APP* mice. This is consistent with the increase in the number of hippocampal ripple events in *APP* mice (see **section 5.2.8**), and collectively suggests that cortical spindle-ripple coupling is unaffected at the 16-month age point.

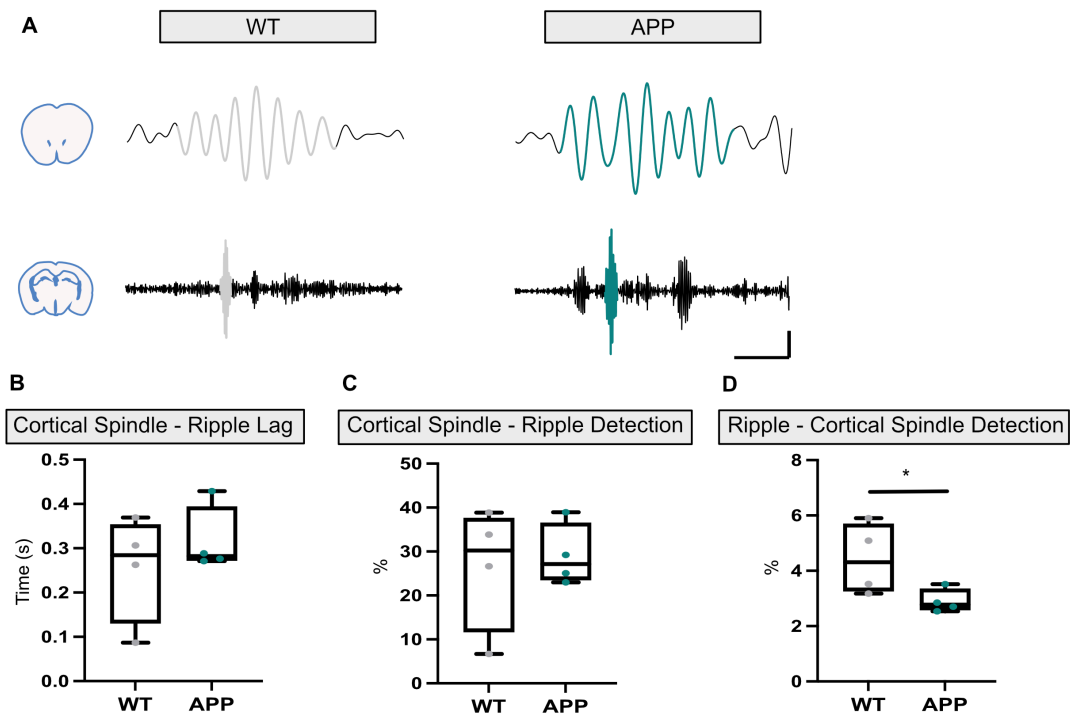


Figure 5.2.13 | A larger proportion of ripples occur without mPFC spindles in APP mice. **A** Examples of 11-15 Hz bandpass filtered traces of spindle events in the mPFC (top) coupled to 130-250 Hz bandpass filtered CA1 ripple events (bottom) from WT and APP mice (coloured segments). Scale bars: 200 ms, 100 μ V. **B** No statistically significant difference was found in the time lag between the start of mPFC spindle events to the start of CA1 ripple events (*WT*: 0.28 (0.13-0.35) vs *APP*: 0.28 (0.27-0.39) s, $U = 6$, $p = 0.68$, Mann-Whitney U test). **C** No statistically significant difference was found in the percentage of mPFC spindles coupled to CA1 ripples (*WT*: 30.24 (11.69-37.61) vs *APP*: 27.16 (23.51-36.52) %, $U = 8$, $p = 0.99$, Mann-Whitney U test). **D** A statistically significant decrease in the percentage of ripple events coupled to mPFC spindles in APP mice compared with WT controls (*WT*: 4.31 (3.26-5.70) vs *APP*: 2.78 (2.58-3.35) %, $U = 1$, $p = 0.05$, Mann-Whitney U test). Box plots show median, IQR and ranges. Descriptive statistics display median and IQR. * $p < 0.05$.

In the hippocampus, ripples nest within hippocampal spindle troughs (Ngo, Fell & Staeresina, 2020). Additionally, optogenetically-evoked hippocampal spindles are found to couple to ripples (Latchoumane *et al.*, 2017), suggesting a mechanistic link. Therefore, the relationship between these two oscillations was analysed (**Figure 5.2.14 A**). No statistically significant difference in the PAC of

hippocampal spindles with ripples was found in APP animals compared with WT controls (**Figure 5.2.14 B**). Additionally, no statistically significant difference was found in the time lag between the start of the hippocampal spindles and ripples nor in the percentage of hippocampal spindles coupled to ripples, although large variation can be seen within WT animals for the latter (**Figure 5.2.14 C, D**). Consistent with the increase in the frequency of detected ripple events in APP mice, a statistically significant decrease was found in the percentage of ripples preceded by a hippocampal spindle, further indicating that a greater proportion of ripple events occurring on their own (**Figure 5.2.14 E**). Whether spindle-ripple coupling in the hippocampus has the same physiological function to cortical spindle-ripple coupling is currently unknown, but further suggests that spindle-ripple coupling is unaffected in 16-month-old APP mice.

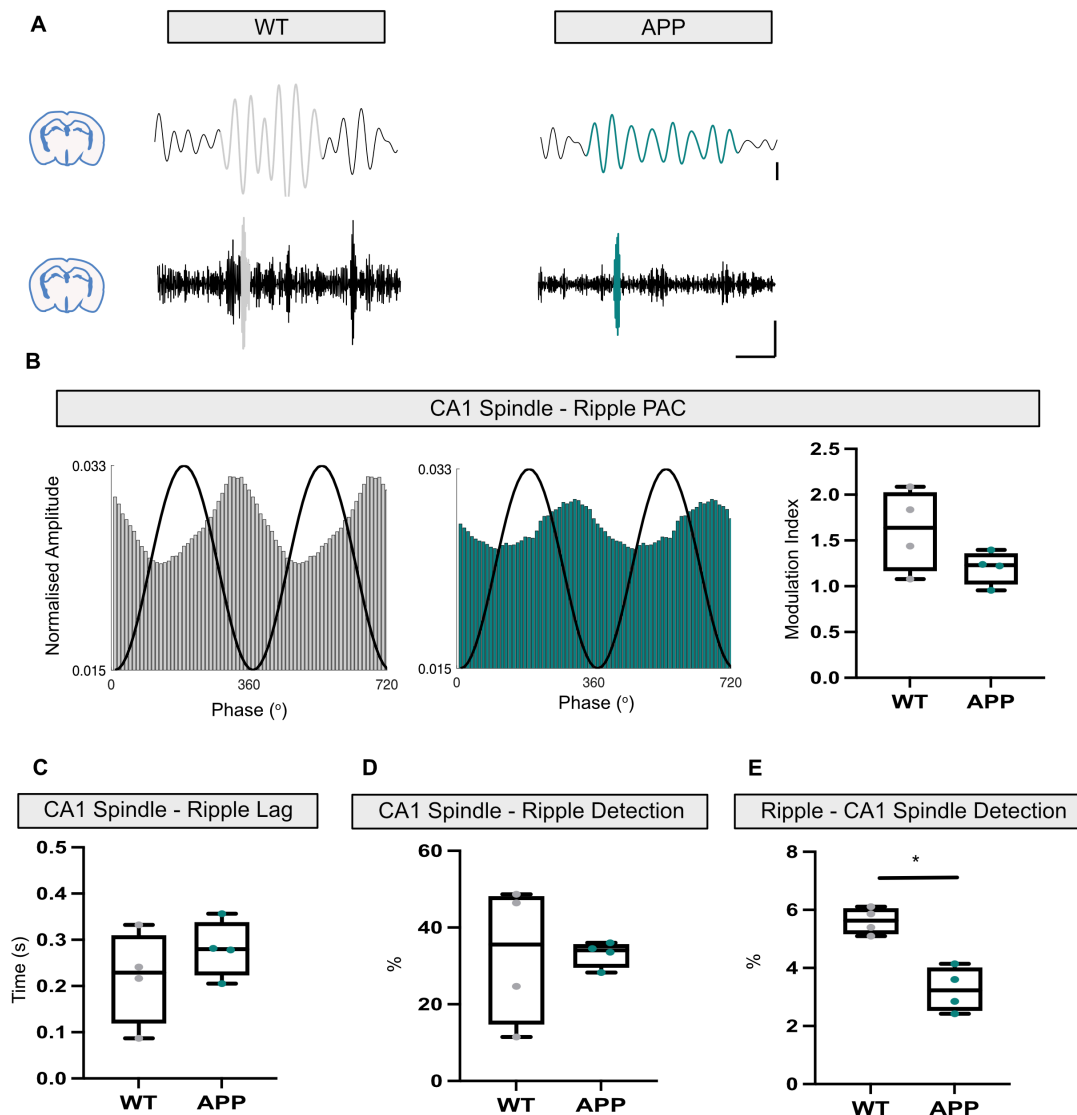


Figure 5.2.14 | A larger proportion of ripples occur without CA1 spindles in APP mice. **A** Examples of 11-15 Hz bandpass filtered traces of spindle events in CA1 (top) coupled to 130-250 Hz bandpass filtered CA1 ripple events (bottom) from WT and APP mice (coloured segments). Scale bars: 200 ms, 100 μ V (top), 50 μ V (bottom). **B** No statistically significant difference in the PAC of CA1 spindles with ripple oscillations was found in APP mice compared with WT controls (*WT*: 1.64 (1.17-2.03) vs *APP*: 1.23 (1.02-1.36) MI, $U = 3$, $p = 0.2$, Mann-Whitney U test). Shown are example histograms of the changes to the ripple normalised amplitude (bars) over the phase of the spindle event (black line) for both WT (left) and APP (right) mice. **C** No statistically significant difference was found in the time lag between the start of CA1 spindle events to the start of CA1 ripple events (*WT*: 0.23 (0.12-0.31) vs *APP*: 0.28 (0.22-0.34) s, $U = 5$, $p = 0.48$, Mann-Whitney U test). **D** No statistically significant difference

was found in the percentage of CA1 spindles coupled to ripples (*WT*: 35.55 (14.77-48.13) vs *APP*: 34.05 (29.58-35.64) %, $U = 8$, $p = 0.99$, Mann-Whitney U test). **E** A statistically significant decrease in the percentage of ripple events coupled to CA1 spindles in *APP* mice compared with *WT* controls (*WT*: 5.63 (5.17-6.05) vs *APP*: 3.23 (2.53-4.01) %, $U = 0$, $p = 0.02$, Mann-Whitney U test). Box plots show median, IQR and ranges. Descriptive statistics display median and IQR. * $p < 0.05$.

5.2.11 | UDS – spindle – ripple coupling

Finally, it is the coupling of all 3 cardinal oscillations together that facilitates systems consolidation (Diekelmann & Born, 2010). No statistically significant difference was found in the occurrence of UDS with both spindles and ripples when comparing *APP* animals with *WT* (**Figure 5.2.15 A, B**). It is interesting to note that despite the changes seen to local cortical and hippocampal spindles and hippocampal ripples, the temporal coordination of the oscillations within the mPFC-hippocampal circuit remains to be relatively intact.

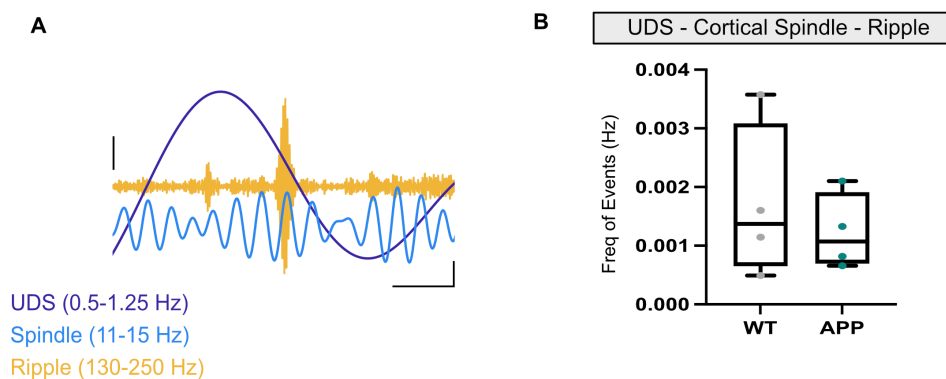


Figure 5.2.15 | No change in the frequency of the three cardinal oscillations occurring together. **A** Example of bandpass filtered traces showing the three cardinal oscillations occurring together in a *WT* mouse. UDS (0.5-1.25 Hz, purple), spindles (11-15 Hz, blue) and ripples (130-250 Hz, orange). Scale bars: 200 ms, 30 μ V (right – UDS and spindle), 100 μ V (left - ripple). **B** No statistically significant difference in the frequency of the three cardinal oscillations occurring together (*WT*: 0.00066 (0.00065-0.00308) vs *APP*: 0.0011 (0.00070-0.00190) %, $U = 7$, $p = 0.88$, Mann-Whitney U test). Box

plots show median, IQR and ranges. Descriptive statistics display median and IQR.

5.2.12 | A hippocampus-dependant memory task

Systems consolidation is important for the long-term consolidation of hippocampus-dependant memories (Diekelmann & Born, 2010). The above results suggest that the temporal precision of the circuit underlying systems consolidation remains intact, yet deficits are seen to the local spindle and ripple oscillations. To determine whether these changes are enough to confer impairments to hippocampus-dependant memory, the mice used in this study were put through a novel object location (NOL) paradigm (Antunes & Biala, 2012) (see **section 2.2.7**). In this test, mice are left to explore the location of two identical objects. To then test their short-term memory (STM), the location of one object is changed and 30 minutes later mice are left to explore. Long-term memory (LTM) is then tested by changing the location of the second object and allowing mice to explore the following day (**Figure 5.2.16 A**). Successful memory retention is defined by animals choosing to explore the novel object over the familiar, as mice prefer novel stimuli (Ennaceur, 2010), which is indicated by a discrimination index greater than 0. No statistically significant difference was found in the discrimination index for either STM or LTM in APP animals compared with WT controls (**Figure 5.2.16 C**). However, large variation is seen within WT data, therefore the results are inconclusive. It is possible that this variation is related to the general exploratory activity of the animal, so the correlation between discrimination index and time spent exploring was analysed. No statistically significant correlations were found; therefore, it is likely variation arose due to some other factor (**Figure 5.2.16 D**). Interestingly, APP mice spend more time exploring in general across sessions compared with WT animals, potentially suggesting increased locomotion in these mice at the 16-month age point (**Figure 5.2.16 B**).

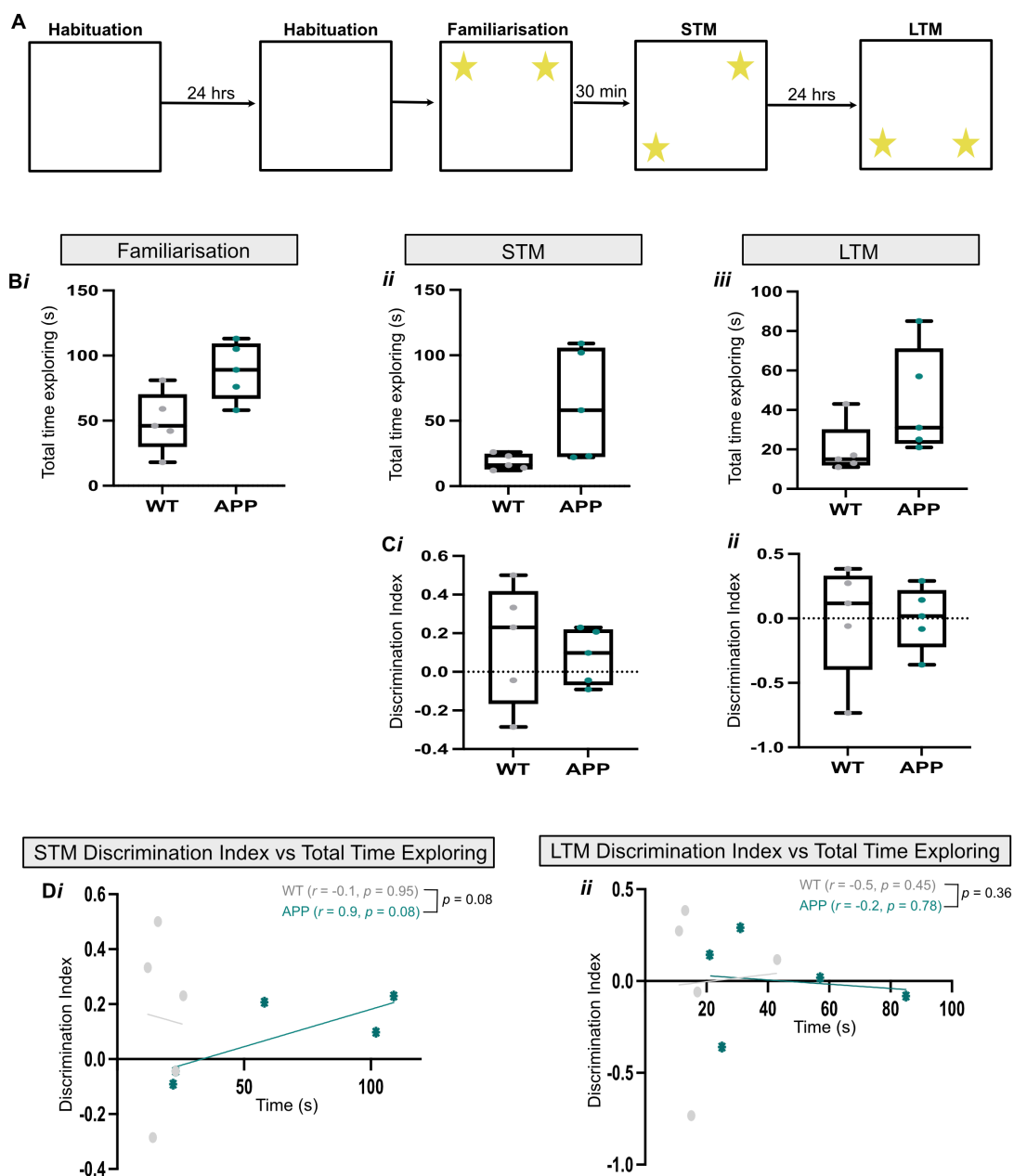


Figure 5.2.16 | Greater exploration in APP mice during NOL task. A Schematic showing the protocol used for the NOL paradigm. **B** A consistent trending increase in the amount of time spent exploring both objects was found in APP mice compared with WT controls for the familiarisation stage (*WT*: 46 (30-70) vs *APP*: 89 (67-109) s, $U = 3, p = 0.05$, Mann-Whitney U test) (**i**), the STM test (*WT*: 16 (13-24) vs *APP*: 58 (22-105) s, $U = 3.5, p = 0.06$, Mann-Whitney U test) (**ii**) and LTM test (*WT*: 15 (12-30) vs *APP*: 31 (23-71) s, $U = 3, p = 0.05$, Mann-Whitney U test) (**iii**). **C** Not all WT and APP mice were found to successfully discriminate novel vs familiar, with APP animals showing no statistical difference to WT for both the STM test (*WT*: 0.23 (-0.16-0.41) vs *APP*: 0.10 (-0.07-0.22), $U = 8.5, p = 0.45$, Mann-Whitney U test) (**i**) and LTM test

(WT: 0.11 (-0.40-0.33) vs APP: 0.02 (-0.22-0.21), $U = 11$, $p = 0.84$, Mann-Whitney U test) **(ii)**. Values above 0 indicate more time spent at the novel object. **D** No statistically significant correlation was found between the total time spent exploring and the discrimination index in the STM memory task for WT mice ($r = -0.1$, $p = 0.95$, Spearman's correlation) but a trending significant positive correlation was found for APP mice ($r = 0.9$, $p = 0.08$, Spearman's correlation) **(i)**. Strength of correlation did not change in APP animals ($p = 0.08$, Fisher's transformation). No statistically significant correlation was found between the total time spent exploring and the discrimination index in the LTM memory task for either WT mice ($r = -0.5$, $p = 0.45$, Spearman's correlation) or APP mice ($r = -0.2$, $p = 0.78$, Spearman's correlation). Strength of correlation did not change in APP animals ($p = 0.36$, Fisher's transformation) **(ii)**. Box plots show median, IQR and ranges and data points on scatter plots represent individual animals. Descriptive statistics display median and IQR.

5.3 | Discussion

5.3.1 | Summary

The data presented are the first to assess the oscillations and oscillatory coupling found in the mPFC-hippocampal circuit during NREM sleep in a mouse model of amyloidopathy, although others have made enquiries along similar lines in mice exhibiting both amyloid and tau pathology (Bentham *et al.*, 2020). Changes to cortical and hippocampal spindles and well as ripples were found to occur in the APP^{NL-G-F} mouse model at 16 months, whereas the SWO appeared to be unimpaired. Additionally, the changes to the local circuitry were not accompanied by deficits to the coupling between different oscillations throughout the circuit. Whether these subtle changes are enough to perturb systems consolidation and hippocampus-dependant memory remains to be investigated.

5.3.2 | Impaired local oscillations

5.3.2.1 | The slow wave oscillation

The SWO and its UDS dynamics were unimpaired in 16-month-old APP animals. This is consistent with the lack of SWO deficits discovered at 8 months under isoflurane anaesthesia (see **section 4**), yet is surprising given the widespread amyloid pathology (see **section 3**). Moreover, these results are inconsistent with data that report disruptions to the SWO in first-generation mouse models of amyloidopathy (Busche *et al.*, 2015; Kastanenka *et al.*, 2017; Castano-Prat *et al.*, 2019) and studies that describe a relationship between A β load and impaired SWA in humans (Mander *et al.*, 2015a). First-generation mouse models develop network deficits at a much younger age compared with second-generation models, potentially due to the over-expression of mutated genes exacerbating the phenotype (Palop *et al.*, 2007; Verret *et al.*, 2012; Sasaguri *et al.*, 2017; Jun *et al.*, 2020). It is possible that the results in this thesis show that, in the absence of over-expression, amyloid pathology does not have the same effect upon SWA. Additionally, the APP^{NL-G-F} mouse is thought to model the preclinical stages of disease progression (Sasaguri *et al.*, 2017). Therefore, 16 months may still be too young to observe changes to the SWO. Perhaps a more prolonged exposure to pathological amyloid would identify changes to SWA, as well as the development of AD-related pathologies not expressed by this model at this age.

Furthermore, the algorithm to detect UDS is typically used when analysing the communication between oscillations (Mölle *et al.*, 2009; David *et al.*, 2013; Staresina *et al.*, 2015; Latchoumane *et al.*, 2017; Niethard *et al.*, 2018). However, the two states are crudely defined and do not represent the sharp state transitions created by oscillating cortical neurons. Detecting these state transitions with precision is difficult to do during mouse natural sleep solely using the LFP. Therefore, simultaneous recording of the LFP with complementary intracellular recordings would be useful for providing greater insight into UDS dynamics (Mukovski *et al.*, 2007; Chauvette *et al.*, 2011; Bukhtiyarova *et al.*, 2019).

5.3.2.2 | Gamma oscillations

Gamma oscillations show reduced power within the cortex and hippocampus of first-generation mouse models of amyloidopathy (Verret *et al.*, 2012; Martinez-Losa *et al.*, 2018) and there is evidence for impaired CA1 high frequency gamma oscillations during navigation in the APP^{NL-G-F} model between 7-13 months (Jun *et al.*, 2020). Gamma oscillations are found nested within SWO Up states (Steriade *et al.*, 1996; Valderrama *et al.*, 2012) and disrupted SWO dynamics in first-generation mouse models can be rescued upon application of GABA_A receptor agonists (Busche *et al.*, 2015; Kastanenka *et al.*, 2017; Castano-Prat *et al.*, 2019); receptors that are crucial in mediating the effects of PV-expressing interneurons and generating gamma oscillations (Buzsaki & Wang, 2012). Therefore, it was hypothesised that gamma oscillations would be affected during the SWO. However, no statistically significant difference was found in the power of either low or high frequency gamma oscillations or in their coupling to SWO Up states. Although CA1 high frequency gamma oscillations show impairments between 7-13 months, a separate study found that mPFC *ex vivo* gamma oscillations at 12 months are not (Pervolaraki *et al.*, 2019). It is therefore possible that like the SWO, 16 months is still too young to see impairments to this oscillation within the cortex.

5.3.2.3 | Spindles

A statistically significant increase in the amplitude and power of cortical spindles was identified in APP animals compared to WT controls. Given that PV-expressing interneurons within the aTRN help generate spindles (Latchoumane

et al., 2017) and that PV interneuron function is documented to be impaired in first-generation mouse models (Verret *et al.*, 2012; Martinez-Losa *et al.*, 2018), the immunoreactivity of these interneurons was quantified. No statistically significant difference was found between genotypes. However, this does not necessarily rule out impaired function. Compensatory remodelling of interneuron networks has previously been documented to occur as a compensatory mechanism to aberrant neural activity (Palop *et al.*, 2007; Hollnagel *et al.*, 2019). Potential hyperfunction of these interneurons could cause larger IPSCs within TC neurons and subsequently larger rebound spike-bursts, that can be viewed as an increase in cortical spindle amplitude. Not only this, but compensatory mechanisms can recruit more PV-expressing interneurons during a spindle event that can in turn synapse onto more TC projections, producing the same effect.

Alternatively, as reported in **section 3.2.3**, there is a statistically significant decrease in the immunoreactivity of PV-expressing interneurons in the ACC. PV-expressing interneurons in the mPFC help gate incoming excitatory TC input during spindles, and prevent action potential propagation, localising increased Ca^{2+} to the dendrites to facilitate plasticity related changes (Peyrache *et al.*, 2011; Delevich *et al.*, 2015). A potential loss of these interneurons could impair this function and contribute to the increase in spindle amplitude. If this is the case, the failure of PV-expressing interneurons to hold Ca^{2+} within the dendrites could have disastrous ramifications for plasticity. However, these hypotheses are speculative and need to be investigated, either through optogenetic tagging of PV-expressing interneurons and recording single-units or through two-photon Ca^{2+} imaging.

Contrary to the mPFC, spindles within CA1 show a strong but not statistically significant decrease in their amplitude and power and a statistically significant decrease in the number of detected events, the latter being consistent with what is observed in patients with AD (Kam *et al.*, 2019). Spindles supposedly reach CA1 through the mEC (Sullivan *et al.*, 2014) and impairments to this pathway have already been documented to occur in this model between 7-13 months (Jun *et al.*, 2020). Disrupted communication between these regions could consequently cause a reduction in spindle power and occurrence. Hippocampal spindles are also generated through the action of PV-expressing interneurons in

the aTRN (Latchoumane *et al.*, 2017), that likely synapse on to mEC projection fibres in the NRe (Dolleman-Van Der Weel *et al.*, 2019). PV-interneuron hypofunction and impairments to the NRe are both documented in first-generation mouse models (Verret *et al.*, 2012; Martinez-Losa *et al.*, 2018; Walsh, Brown & Randall, 2020). Loss-of-function to either in the APP^{NL-G-F} model could additionally contribute to the observed effects.

Although spindle oscillations within CA1 have been documented to occur in both humans and rodents (Sullivan *et al.*, 2014; Staresina *et al.*, 2015; Latchoumane *et al.*, 2017; Ngo, Fell & Staresina, 2020), there remains some controversy as to their physiological role and nature. On one hand, hippocampal spindle oscillations (11-15 Hz) have been distinguished from the higher bounds of rodent theta (6-12 Hz) based on their differences in electrophysiological characteristics (Sullivan *et al.*, 2014), and from a morphologically atypical spindle-like oscillation found in humans, generated as a result of epileptic activity (Malow *et al.*, 1999; Nakabayashi *et al.*, 2001; Frauscher *et al.*, 2015). Furthermore, CA1 spindles have been found coupled to cortical and mEC spindles, hippocampal ripples and the SWO, and are generated upon optogenetic activation of PV-expressing interneurons within the aTRN (Sullivan *et al.*, 2014; Staresina *et al.*, 2015; Latchoumane *et al.*, 2017; Ngo, Fell & Staresina, 2020). Taken together, this suggests that hippocampal spindles represent a physiological phenomenon. Despite this evidence, it is still unknown how spindle oscillations reach the hippocampus and whether they play a similar physiological function compared with cortical spindles. It is important that these questions are addressed so that they can be better used as a metric for understanding circuit dysfunction in disease and their relation to memory consolidation during NREM sleep.

5.3.2.4 | Ripples

Ripple events located in CA1 *Str.P* exhibited a statistically significant reduction in power but interestingly, no change in amplitude. Power is taken from the short-time FFT of the whole event whereas amplitude is the difference between the highest peak and lowest trough, typically located in the centre of the ripple event. This suggests disrupted spike-time dynamics occurring elsewhere in the ripple oscillation. Indeed, CA1 PCs display impaired spiking activity relative to fast

gamma oscillations in the APP^{NL-G-F} mouse model (Jun *et al.*, 2020). Both fast gamma oscillations and ripples require the recruitment of PV-expressing interneurons to pace PC (Sohal *et al.*, 2009a; Gan *et al.*, 2017); cells that are impaired in first-generation mouse models (Verret *et al.*, 2012; Martinez-Losa *et al.*, 2018).

PV-expressing interneurons are actively involved in the recruitment of CA3 PCs for the generation of SPWs (Ellender *et al.*, 2010). SPWs then propagate to CA1, where PV-expressing interneurons contribute to pacing the ripple oscillation (Gan *et al.*, 2017). In an APP/PSEN1 model, PV-expressing interneurons show an increase in their immunoreactivity, projection patterns and co-localisation with pre- and post-synaptic markers of inhibition in both CA3 and CA1, implying compensatory alterations to the network (Hollnagel *et al.*, 2019). Interestingly, a separate study found that at a similar age, PV-expressing interneurons exhibited hyperexcitability, and an increase their inhibitory output (Hijazi *et al.*, 2019). Potentially, similar circumstances in the APP^{NL-G-F} mouse model could help explain the observed results; hyperfunction of PV-expressing interneurons in CA3 could increase the incidence of SWR (Ellender *et al.*, 2010) and in CA1, decrease the E-I balance, resulting in a reduction in oscillation power. In this instance, this hyperfunction would most likely be manifested as increased PV-expressing interneuron recruitment and gain in inhibitory output, as a lack of change in ripple frequency implies no change in firing rate. Moreover, hyperfunction can theoretically recruit more PCs during SWR events and affect the spike-time dynamics of PC recruitment. Not only can this disturb processes such as STDP, but it can affect the recruitment of neurons for the reactivation of previously encoded information, potentially interfering with consolidation.

On the other hand, PV-expressing interneuron hypofunction is observed in first-generation mouse models of amyloidopathy (Verret *et al.*, 2012; Martinez-Losa *et al.*, 2018) and has previously been found to increase the frequency and duration of CA1 ripples due to an increase in the E-I balance (Caccavano *et al.*, 2020). However, the reduced power observed in this study suggests that hypofunction may not be the cause in this instance. Possible approaches to investigate this include recording either single units or the Ca²⁺ dynamics of PV-

expressing interneurons during ripple events or, alternatively, recording the activity of these interneurons *ex vivo* using whole-cell patch clamp.

5.3.3 | Spared oscillation coupling

Although impairments can be seen to cortical and hippocampal spindles and ripples, the communication between cardinal oscillations remains relatively intact in 16-month-old APP mice. UDS coupling to cortical spindles was unaffected, suggesting that the TC feedback loop that controls their temporal communication is spared (David *et al.*, 2013). However, in APP mice, PAC of UDS with hippocampal spindles is reduced, as is the percentage of UDS that are coupled to a hippocampal spindle. This is consistent with the identified reduction in hippocampal spindle amplitude and number of events, although the functional significance of this coupling is unknown.

Coupling of spindles between the mPFC and CA1 occurs around the initiation of SWRs, with some believing that it provides a signalling mechanism (Latchoumane *et al.*, 2017; Ngo, Fell & Staesina, 2020). As discussed in **section 1.2.2.4**, I believe that it is in fact the SWO that controls the timing of SWR through the mEC perforant pathway. Nevertheless, this does not rule out a functional role of spindle-spindle coupling and it remains a good measure of communication between brain regions. Interestingly, spindle coupling between regions was unaffected, indicating spared communication. This is surprising given the reduction in hippocampal spindle events and suggests that fewer hippocampal spindles are occurring outwith the systems consolidation circuit (Nir *et al.*, 2011; Lüthi, 2014). The density of spindles in the cortex correlates with memory performance (Mölle *et al.*, 2004; Marshall *et al.*, 2006; Mölle *et al.*, 2009); whether this same holds true for the hippocampus is currently unknown.

Another indication of spared communication between brain regions comes from the lack of coupling deficits between ripples and cortical UDS, cortical spindles and hippocampal spindles. The greater proportion of ripples occurring without either cortical or hippocampal spindles can be explained by the increase in ripples events. Given that the occurrence of all 3 cardinal oscillations together remained the same between genotypes, this further suggests that the circuit is functionally

intact and the increased ripple events are occurring outwith this communication. It is unclear what effect this has upon memory consolidation, but could further allude to over-compensation of the network. Chemogenetically reducing the activity of PV-expressing interneurons can impair the coupling of cortical spindles and ripples, it is therefore plausible that a gain-of-function can enhance this coupling (Xia *et al.*, 2017). Conducting similar recordings in younger mice would give an indication of how this circuit is affected before potential compensatory mechanisms takeover. Moreover, given the reduced power of ripples, it would be interesting to look at the spiking activity of neurons in the mPFC during a ripple event, to determine if the information contained within the ripple is being effectively transmitted to the cortex (Wierzynski *et al.*, 2009a; Dong, Wang & Ikemoto, 2016).

Finally, learning induces changes to the systems consolidation circuit: increased SWA, spindle and ripple density as well as an increase in spindle-ripple coupling are observed (Mölle *et al.*, 2009). In some studies, A β -induced deficits to SWR dynamics were only identified during post-learning sleep of a hippocampus-dependant memory task as opposed to baseline conditions (Nicole *et al.*, 2016; Jura *et al.*, 2019). Although the oscillations and oscillatory coupling underlying systems consolidation can be studied under baseline conditions (Siapas & Wilson, 1998; Sirota *et al.*, 2003; Wierzynski *et al.*, 2009b; Ngo, Fell & Staerensina, 2020), it is possible A β -induced deficits are more pronounced during active consolidation of a hippocampus-dependant memory. Therefore, repeating experiments under these conditions may produce more striking deficits.

5.3.4 | Relevance to hippocampus-dependant memory

In this study mice were put through a NOL paradigm to test their hippocampus-dependant memory. An *a priori* power calculation indicated that N = 16 mice of each genotype was needed. However, given the investment needed to generate 16-month-old APP^{NL-G-F} mice, the study was run as a pilot as the mice were available from neurophysiological recordings. What can be seen from these experiments is that APP animals tended to spend more time exploring compared to WT. Increased locomotion has been documented in first-generation models (King & Arendash, 2002; Harris *et al.*, 2010) and is a potential cause for this

exploratory behaviour. However, a reduction in locomotion and exploratory behaviour can be seen in the APP^{NL-G-F} mouse model at 6 months (Whyte *et al.*, 2018). Unfortunately, due to technical difficulties, video recordings of these experiments were not captured, therefore locomotion cannot be directly assessed in this study.

Impaired performance in hippocampus-dependant memory tasks have already been reported to occur in this model by 16 months (Masuda *et al.*, 2016; Latif-Hernandez *et al.*, 2019; Jun *et al.*, 2020; Maezono *et al.*, 2020). However, the paradigms used include contextual fear conditioning, place avoidance and the Morris water maze. Spatial memories with negative emotional valence such as these more typically require ventral CA1 vs dorsal CA1 (Fanselow & Dong, 2010), with the latter being the primary target in these experiments. Additionally, emotional arousal during encoding can enhance the strength and longevity of memories (McGaugh, 2013), therefore these experiments may not represent the true extent and timeline of the changes occurring to spatial memory. Non-aversive tasks such as spontaneous alteration in the Y-maze have been conducted with some reporting deficits as early as 6 months (Saito *et al.*, 2014), yet others have been unable to replicate this (Whyte *et al.*, 2018). Nevertheless, spontaneous alteration is a measure of working memory and does not require the systems consolidation circuit. Therefore, it is currently unclear the extent at which hippocampus-dependant memory is affected in this model and is something that needs to be investigated further.

5.3.5 | Conclusions

The fact that impairments are seen to the local oscillations whereas long-range communication is spared potentially points towards the first-steps in the breakdown of mPFC-hippocampal function. Whether these disturbances lead to memory impairments is still to be determined, but it is possible that the changes occurring at this age are a good model of the preclinical phase of AD. Further experimentation is needed to decipher the underlying neuronal dysfunction contributing to oscillatory impairments and whether these impairments worsen over time. Nevertheless, this study provides valuable information about how amyloid pathology affects the circuit governing systems consolidation and adds

to existing knowledge concerning the pathophysiology of the APP^{NL-G-F} mouse model.

6 | Oscillation dynamics in CA1 and the mPFC
during exploratory behaviour in the APP^{NL-G-F}
mouse model

6.1 | Introduction

The hippocampus is crucial for episodic memory and spatial navigation and integrates spatial and non-spatial information from anatomically-connected brain regions (Drieu & Zugaro, 2019). During awake states, this integration is achieved through the theta oscillation (6-12 Hz) that, due to long conduction delays produced by its slow frequency, facilitates the transfer and processing of information (Colgin & Moser, 2010) (see **section 1.3.1**). Gamma oscillations (30-120 Hz) can be found coupled to theta oscillations, and organise neuronal firing into precise temporal windows (Colgin & Moser, 2010; Buzsaki & Wang, 2012) (see **section 1.3.2**), with the PAC between these oscillations important for binding neuronal firing across spatial and temporal scales for information transfer and processing (Lisman & Jensen, 2013) (see **section 1.3.3**).

Within hippocampal area CA1, different frequencies of gamma oscillation exist that have different physiological roles (Tort *et al.*, 2008; Belluscio *et al.*, 2012). Slow gamma oscillations, generated through CA3 input, are responsible for the retrieval of episodic and spatial information, whereas fast gamma oscillations are important for encoding and are generated through inputs arising from the mEC (Colgin *et al.*, 2009; Colgin & Moser, 2010). These different frequencies of gamma oscillation preferentially couple to different phases of the theta cycle, segregating information and preventing interference, while also integrating past with present experiences (Tort *et al.*, 2008; Scheffer-Teixeira *et al.*, 2012; Amemiya & Redish, 2018; Lopes-dos-Santos *et al.*, 2018). Additionally, CA1 theta oscillations can be found coupled to mPFC theta and gamma oscillations during goal-directed behaviours and spatial working memory, facilitating the integration of spatial information with executive control (Jones & Wilson, 2005; Tort *et al.*, 2008; Sirota *et al.*, 2008; Tamura *et al.*, 2017).

AD causes a decline in episodic, spatial and working memory, with the hippocampus and mPFC exhibiting pathological changes and dysfunctional network activity in the early stages of the disease progression (Braak & Braak, 1991; Sperling *et al.*, 2009; Bakker *et al.*, 2012; Palop & Mucke, 2016; Grothe *et al.*, 2017). Poor working memory performance in humans with AD has been linked to a generalised “slowing” of the EEG (Dauwels *et al.*, 2011), accounted for by an increase in the power of slower oscillations, such as theta (Adler, Brassens &

Jajcevic, 2003; Czigler *et al.*, 2008) and a decrease in the power of faster oscillations, such as gamma (Murty *et al.*, 2021). Moreover, patients with AD exhibit impaired theta-gamma PAC (Goodman *et al.*, 2018). Additionally, reduced functional connectivity between the hippocampus and mPFC has been identified in AD patients using fMRI (Wang *et al.*, 2006). Similar results have been found in first-generation mouse models of amyloidopathy, which show a reduction in the power of gamma oscillations in both the cortex and hippocampus (Palop *et al.*, 2007; Palop & Mucke, 2016; Martinez-Losa *et al.*, 2018; Etter *et al.*, 2019) as well as a reduction in theta-gamma PAC (Ittner *et al.*, 2014; Etter *et al.*, 2019). However, unlike humans, a reduction in the power of theta oscillations was found in these models (Ittner *et al.*, 2014; Schneider *et al.*, 2014). These changes in oscillatory dynamics were accompanied by poor performance in spatial memory and goal-directed navigation. Moreover, the application of exogenous A β oligomers has been shown to reduce the power and coupling of both gamma and theta oscillations as well as cause a decline in spatial memory (Chung *et al.*, 2020a; Park *et al.*, 2020), further implicating the role of pathological A β in causing these impairments.

It is clear from studies in humans and first-generation mouse models that impairments to theta and gamma oscillations, as well as their coupling, exist in Alzheimer's disease. However, less is known about how these oscillations are affected in second-generation mouse models of AD, such as APP^{NL-G-F}. Similarities between first- and second-generation mouse models should not be assumed, as the over expression of mutated *APP* genes is thought to produce an exacerbated phenotype (Nilsson, Saito & Saido, 2014; Saito *et al.*, 2014). Moreover, discrepancies exist between first-generation mouse models of amyloidopathy and humans with AD, such as a decrease in theta power observed in the former (Ittner *et al.*, 2014; Schneider *et al.*, 2014) and increase in the latter (Adler, Brassens & Jajcevic, 2003; Czigler *et al.*, 2008). Therefore, determining whether second-generation models better recapitulate features of AD pathophysiology as seen in humans is a crucial first-step before they can be used to understand the pathological mechanisms underpinning disrupted network activity. Research using the APP^{NL-G-F} mouse model has so far found a reduction in the power of mEC fast gamma oscillations at 5 months of age (Nakazono *et al.*, 2017) that spreads to CA1 between 7-13 months (Jun *et al.*, 2020). This

reduction in fast gamma coupling between regions was also accompanied by an increase in theta power and a reduction in the coupling between theta and fast gamma. Additionally, *ex vivo* gamma oscillations in the mPFC were found to be unimpaired at 12 months (Pervolaraki *et al.*, 2019).

As yet, it is unclear how theta and gamma oscillations in CA1 and the mPFC are affected at advanced age points in the APP^{NL-G-F} mouse model. Moreover, it is still unknown whether the communication between CA1 and the mPFC is affected in this model during awake states. Therefore, using *in vivo* electrophysiology, theta and gamma oscillations in the mPFC and CA1, as well as the communication between these regions, was investigated in 16-month-old APP^{NL-G-F} mice as they explored an open field (OF) arena.

6.2 | Results

6.2.1 | Speed-modulated theta oscillations in CA1 and the mPFC

Hippocampal theta oscillations help integrate spatial and non-spatial information across functionally-connected brain regions (Colgin & Moser, 2010; Drieu & Zugaro, 2019), such as the integration of spatial information in the hippocampus with executive decision making in the mPFC (Jones & Wilson, 2005). Evidence for theta disruption has been found in humans with AD (Adler, Brassens & Jajcevic, 2003; Czigler *et al.*, 2008) and in first-generation mouse models of amyloidopathy (Ittner *et al.*, 2014; Schneider *et al.*, 2014) and is linked to disrupted spatial navigation and working memory. In the APP^{NL-G-F} mice mouse model, an increase in the power of theta oscillations was found between 7-13 months of age (Jun *et al.*, 2020), consistent with EEG recordings in AD patients (Adler, Brassens & Jajcevic, 2003; Czigler *et al.*, 2008). To determine if this increase in power in CA1 is sustained at a more advanced stage of pathology and to understand how theta oscillations are affected in the mPFC, theta oscillations were analysed in CA1 (*Str.P*) and the mPFC at 16 months during active exploration (see **sections 2.2.6 and 2.4.8**).

Given that the frequency and power of theta oscillations in the CA1 region of the hippocampus has previously been shown to increase with running speed, theta oscillations were analysed with respect to running speed (McFarland, Teitelbaum & Hedges, 1975; Fuhrmann *et al.*, 2015). The peak theta frequency and total theta power linearly increased with running speed in both WT and APP animals (pooled data) (**Figure 6.2.1 B, Ci, Di**). The regression correlations (z-transformed R^2 values), regression line slopes and the frequency and power of the theta oscillation at the y-intercept were analysed. No statistically significant change was found in APP animals compared with WT controls for each measure (**Figure 6.2.1 A, Cii-iv, Dii-iv**). However, a trending increase in theta power can be visualised in APP animals (Adler, Brassens & Jajcevic, 2003; Czigler *et al.*, 2008).

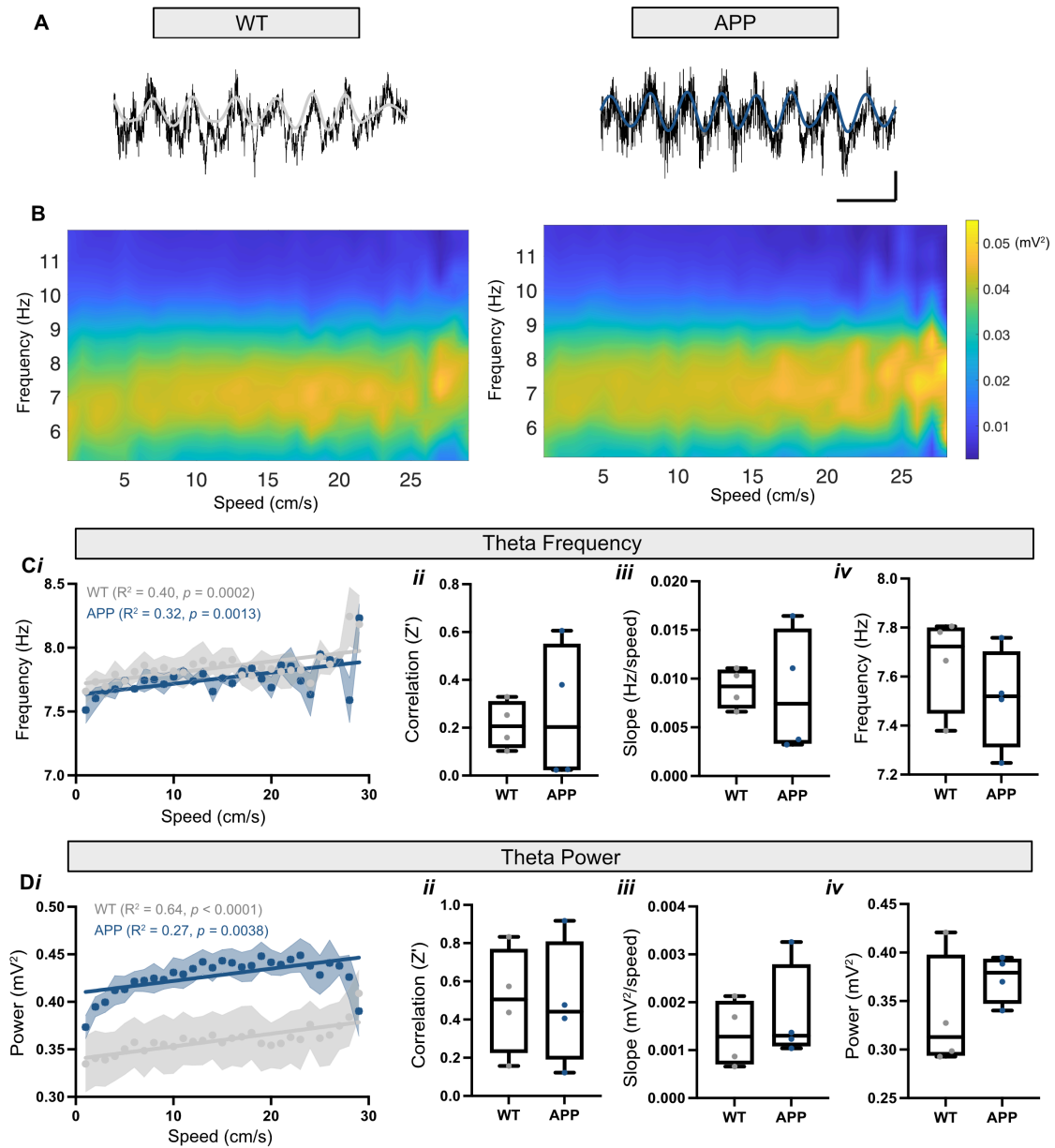


Figure 6.2.1 | Speed-modulated theta power and frequency in CA1. A Example raw traces (black) and theta filtered traces for WT (grey) and APP (blue) animals. Scale bar: 200 ms, 200 μ V. **B** Example spectrograms displaying a speed-modulated increase in theta power in WT and APP mice. **Ci** A speed-modulated increase in theta frequency was found in WT ($R^2 = 0.40$, $F(1,27) = 18.00$, $p = 0.002$, linear regression) and APP animals ($R^2 = 0.32$, $F(1,27) = 12.84$, $p = 0.001$, linear regression). APP animals displayed no statistically significant difference to WT in the regression correlation (WT: 0.21 (0.12-0.31) vs APP: 0.20 (0.02-0.55) Z' , $U = 8$, $p > 0.99$, Mann-Whitney U test) (**ii**), slope (WT: 0.009 (0.007-0.011) vs APP: 0.007 (0.003-0.015) freq/speed, $U = 7$, $p = 0.88$, Mann-Whitney U test) (**iii**) and frequency (WT: 7.72 (7.45-7.80) vs APP:

7.52 (7.31-7.70) Hz, $U = 4$, $p = 0.34$, Mann-Whitney U test) (*iv*). **Di** A speed-modulated increase in theta power was found in WT ($R^2 = 0.63$, $F(1,27) = 47.19$, $p < 0.0001$, linear regression) and APP animals ($R^2 = 0.27$, $F(1,27) = 10.06$, $p = 0.0038$, linear regression). APP animals displayed no statistically significant difference to WT in the regression correlation (WT: 0.51 (0.23-0.77) vs APP: 0.44 (0.19-0.81) Z' , $U = 7$, $p = 0.88$, Mann-Whitney U test) (*ii*), slope (WT: 0.0013 (0.0007-0.0020) vs APP: 0.0013 (0.0011-0.0028) power/speed, $U = 6$, $p = 0.68$, Mann-Whitney U test) (*iii*) and power (WT: 0.31 (0.29-0.40) vs APP: 0.38 (0.34-0.39) mV^2 , $U = 4$, $p = 0.34$, Mann-Whitney U test) (*iv*), although a trending increase in power can be seen. Box plots show median, IQR and ranges. Regression lines display the mean \pm SEM. Descriptive statistics display median and IQR.

There is also evidence for mPFC theta power to linearly increase with running speed (Adhikari, Topiwala & Gordon, 2010b), possibly through theta generating inputs arising from CA1 (Jones & Wilson, 2005; O'Neill, Gordon & Sigurdsson, 2013). Therefore, theta power and frequency in the mPFC were also analysed with respect to running speed. Interestingly, theta frequency and power were found to significantly linearly increase with running speed in WT animals, but exhibited no alteration in APP animals (pooled data) (**Figure 6.2.2 B, Ci, Di**), potentially indicating impaired theta coupling between the mPFC and CA1 at increasing locomotion velocities. However, when comparing the regression correlations and slopes of the regression lines, APP animals exhibited no statistically significant differences to WT (**Figure 6.2.2 Cii-iii, Di-iii**). Finally, no statistically significant change in the power and frequency of the theta oscillation (y-intercepts) was identified in APP animals compared with WT controls (**Figure 6.2.2 A, Civ, Div**).

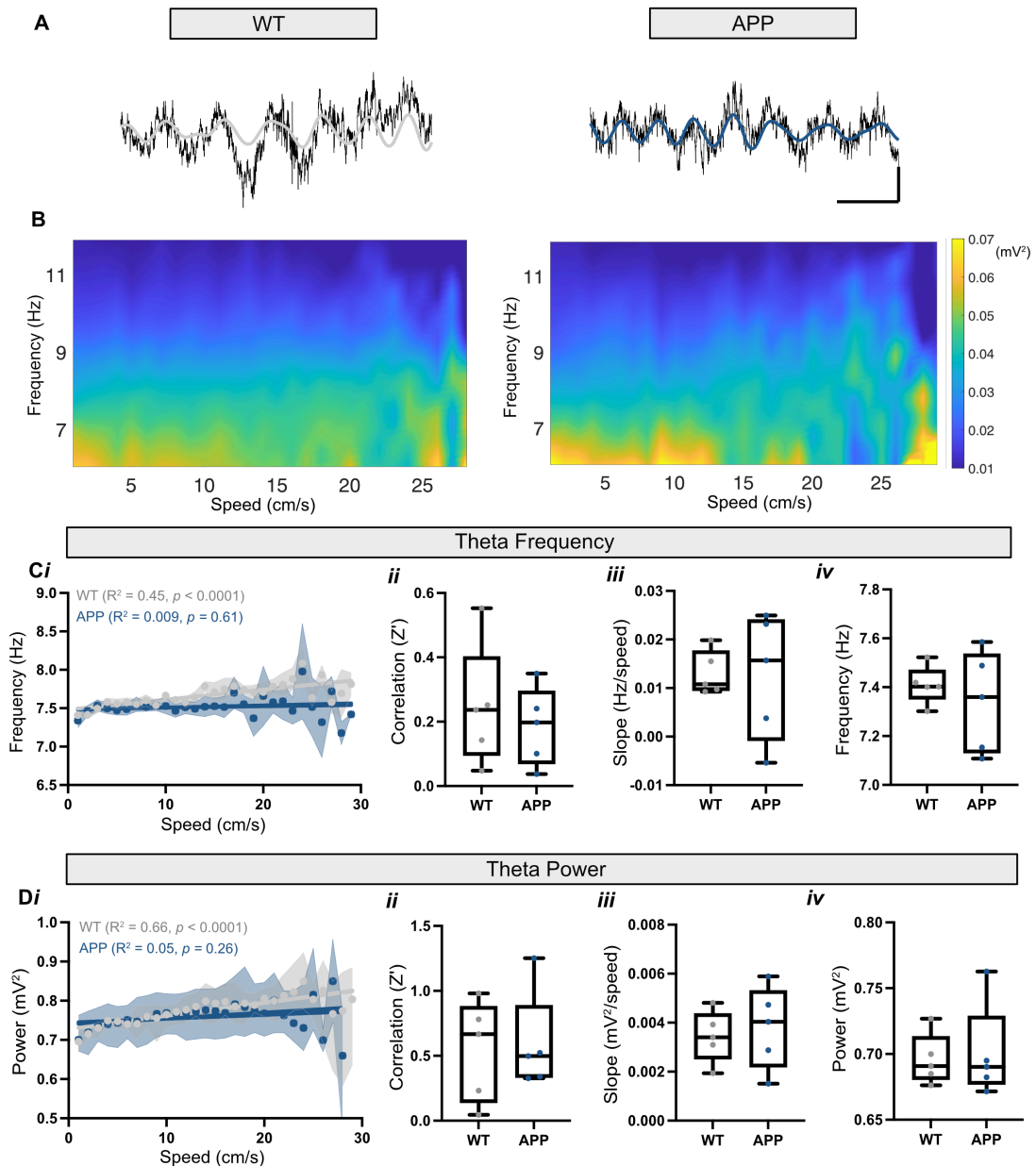


Figure 6.2.2 | Speed-modulated theta power and frequency in the mPFC. **A** Example raw traces (black) and theta filtered traces for WT (grey) and APP (blue) animals. Scale bar: 200 ms, 200 μ V. **B** Example spectrograms displaying a speed-modulated increase in theta power in WT and APP mice. **Ci** A speed-modulated increase in theta frequency was found in WT animals ($R^2 = 0.543$, $F(1,27) = 32.18$, $p < 0.0001$, linear regression) but not APP ($R^2 = 0.009$, $F(1,27) = 0.26$, $p = 0.6101$, linear regression). APP animals displayed no statistically significant difference to WT in the regression correlation (WT: 0.24 (0.10-0.40) vs APP: 0.20 (0.07-0.30) Z' , $U = 10$, $p = 0.69$, Mann-Whitney U test) (**ii**), slope (WT: 0.011 (0.009-0.018) vs APP: 0.016 (-0.001-0.024) freq/speed, $U = 11$, $p = 0.84$, Mann-Whitney U test) (**iii**) and frequency (WT: 7.40 (7.35-7.47) vs APP:

7.36 (7.13-7.54) Hz, $U = 10$, $p = 0.69$, Mann-Whitney U test) (*iv*). **Di** A speed-modulated increase in theta power was found in WT animals ($R^2 = 0.66$, $F(1,27) = 53.38$, $p < 0.0001$, linear regression) but not APP animals ($R^2 = 0.04$, $F(1,27) = 1.29$, $p = 0.2662$, linear regression). APP animals displayed no statistically significant difference to WT in the regression correlation (WT: 0.66 (0.14-0.88) vs APP: 0.50 (0.33-0.89) Z' , $U = 12$, $p > 0.99$, Mann-Whitney U test) (*ii*), slope (WT: 0.003 (0.003-0.004) vs APP: 0.004 (0.002-0.005) power/speed, $U = 11$, $p = 0.84$, Mann-Whitney U test) (*iii*) and power (WT: 0.69 (0.68-0.71) vs APP: 0.69 (0.68-0.73) mV^2 , $U = 11$, $p = 0.84$, Mann-Whitney U test) (*iv*). Box plots show median, IQR and ranges. Regression lines display the mean \pm SEM. Descriptive statistics display median and IQR.

6.2.2 | Speed-modulated gamma oscillations in CA1

Within CA1, slow gamma oscillations are driven *via* CA3 Schaffer collateral inputs and are important for the retrieval of spatial and episodic memories, whereas fast gamma oscillations are important for encoding and are generated through the mEC (Colgin *et al.*, 2009; Colgin & Moser, 2010). Broadband gamma oscillations in the hippocampus exhibit reduced power in first-generation mouse models of amyloidopathy (Palop *et al.*, 2007; Palop & Mucke, 2016; Martinez-Losa *et al.*, 2018; Etter *et al.*, 2019) and there is evidence for a reduction in the power of fast gamma but not slow gamma in APP^{NL-G-F} mice between 7-13 months (Jun *et al.*, 2020). To understand how both slow and fast gamma oscillations are affected in CA1 at more advanced stages of pathology in APP^{NL-G-F} mice, the power and frequency of both was analysed with respect to running speed at 16 months (Chen *et al.*, 2011).

The frequency of slow gamma oscillations (30-60 Hz) was found to statistically linearly decrease with respect to running speed in APP animals, but was not found to be modulated in WT (pooled data) (**Figure 6.2.3 A, Ci**). When analysing the regression correlations and slopes of the regression lines, APP animals displayed no statistically significant difference to WT (**Figure 6.2.3 Cii-iii**). Additionally, a statistically significant linear decrease in the power of slow gamma oscillations was identified in WT and APP animals (pooled data) (**Figure 6.2.3 A, B, Di**), which is contrary to previously reported data (Chen *et al.*, 2011). No statistically significant difference was found in APP animals compared with WT

when analysing the regression correlations or the slope of regression lines (**Figure 6.2.3 Dii-iii**). Furthermore, there was no statistically significant change in the frequency and power of slow gamma oscillations (y-intercepts) (**Figure 6.2.3 B, Civ, Div**), yet when looking at the power vs speed relationship, an overall decrease in power can be visualised in APP animals (**Figure 6.2.3 Di**).

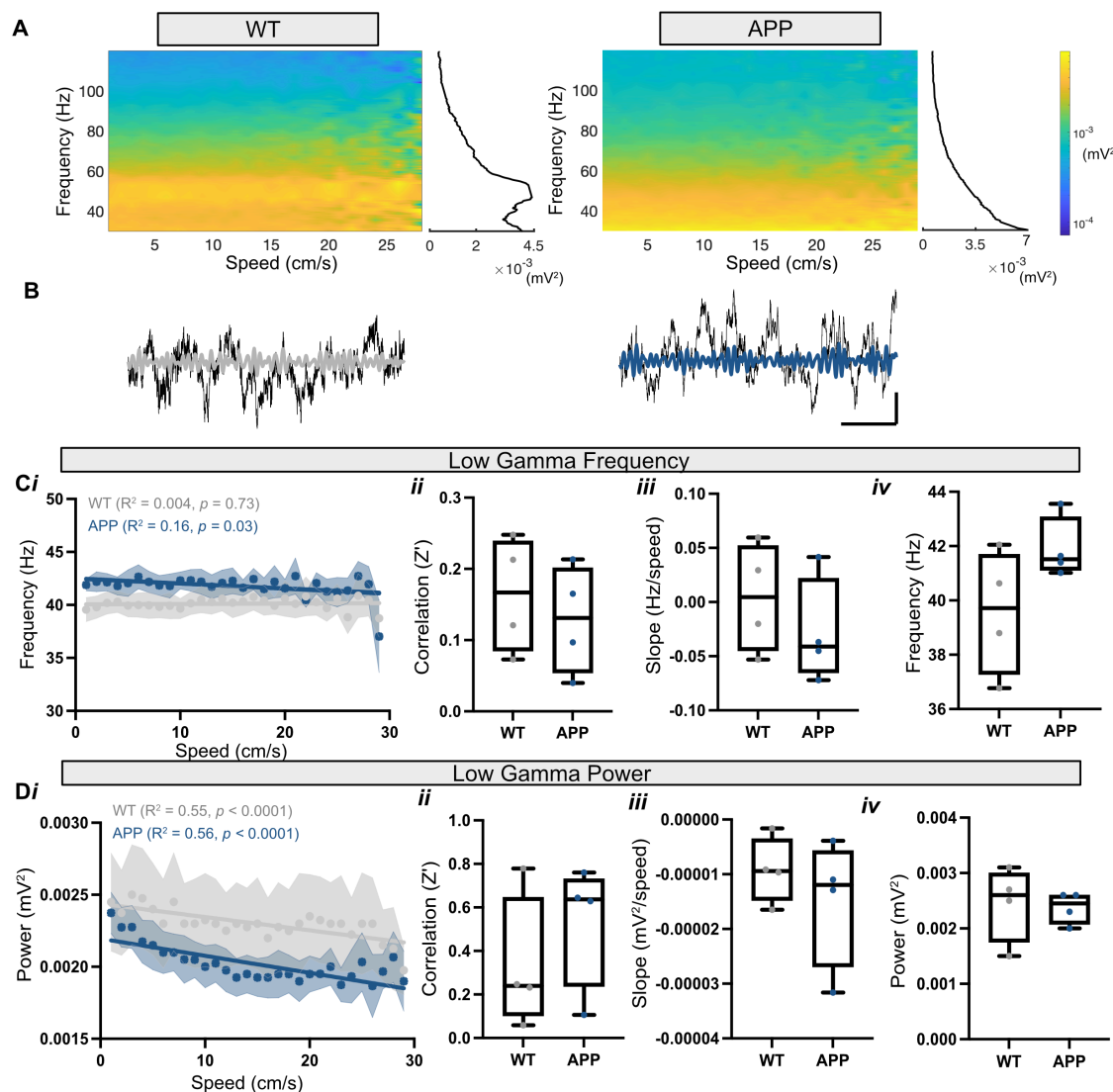


Figure 6.2.3 | Speed-modulated low gamma power and frequency in CA1.

A Example spectrograms displaying a speed-modulated low and high gamma power in WT and APP mice. **B** Example raw traces (black) and low gamma filtered traces for WT (grey) and APP (blue) animals. Scale bar: 200 ms, 200 μV . **Ci** A speed-modulated decrease in low gamma frequency was found in APP animals ($R^2 = 0.16, F(1,27) = 5.28, p = 0.02$, linear regression) but no relationship in WT ($R^2 = 0.004, F(1,27) = 0.12, p = 0.73$, linear regression). APP

animals displayed no statistically significant difference to WT in the regression correlation (*WT*: 0.16 (0.09-0.24) vs *APP*: 0.13 (0.05-0.20) *Z'*, *U* = 6, *p* = 0.69, Mann-Whitney U test) (*ii*), slope (*WT*: 0.005 (-0.045-0.052) vs *APP*: -0.041 (-0.065-0.022) freq/speed, *U* = 5, *p* = 0.49, Mann-Whitney U test) (*iii*) and frequency (*WT*: 39.71 (37.28-41.70) vs *APP*: 41.51 (41.11-43.07) Hz, *U* = 3, *p* = 0.20, Mann-Whitney U test) (*iv*). **Di** A speed-modulated decrease in low gamma power was found in WT ($R^2 = 0.55$, $F(1,27) = 32.83$, $p < 0.0001$, linear regression) and APP animals ($R^2 = 0.56$, $F(1,27) = 34.35$, $p < 0.0001$, linear regression). APP animals displayed no statistically significant difference to WT in the regression correlation (*WT*: 0.24 (0.10-0.65) vs *APP*: 0.64 (0.24-0.73) *Z'*, *U* = 6, *p* = 0.69, Mann-Whitney U test) (*ii*), slope (*WT*: -0.000009 (-0.000014 - -0.000003) vs *APP*: -0.000011 (0-0.000026 - -0.000006) power/speed, *U* = 5, *p* = 0.48, Mann-Whitney U test) (*iii*) and power (*WT*: 0.0026 (0.0018-0.0030) vs *APP*: 0.0025 (0.0021-0.0026) mV², *U* = 6, *p* = 0.62, Mann-Whitney U test) (*iv*), although a trending decrease in power can be seen. Box plots show median, IQR and ranges. Regression lines display the mean \pm SEM. Descriptive statistics display median and IQR. **p* < 0.05.

The frequency of high gamma oscillations (60-120 Hz) was found to statistically linearly increase with running speed in APP animals, yet no noticeable change was identified in WT animals (pooled data) (**Figure 6.2.3 A, Figure 6.2.4 Bi**). This most likely produced the statistically significant increase in the slope of regression line in APP animals compared with WT and the trending increase in regression correlation (**Figure 6.2.4 Bii-iii**). Additionally, the power of high gamma oscillations statistically linearly increased with respect to running speed in WT animals but not APP (pooled data) (**Figure 6.2.3 A, Figure 6.2.4 Ci**). However, no statistically significant change to the regression correlation and slope of the regression line was found (**Figure 6.2.4 Cii-iii**). Furthermore, no statistically significant change in the frequency and power of high gamma oscillations (y-intercepts) was found in APP animals compared with WT controls (**Figure 6.2.4 A, Biv, Civ**), yet when looking at the power vs speed relationship, an overall decrease in power can be visualised in APP animals (**Figure 6.2.4 Ci**). A decrease in power of high gamma oscillations would be consistent with what is observed in young APP^{NL-G-F} mice (Jun *et al.*, 2020), with the observable reduction in low gamma power being a novel finding.

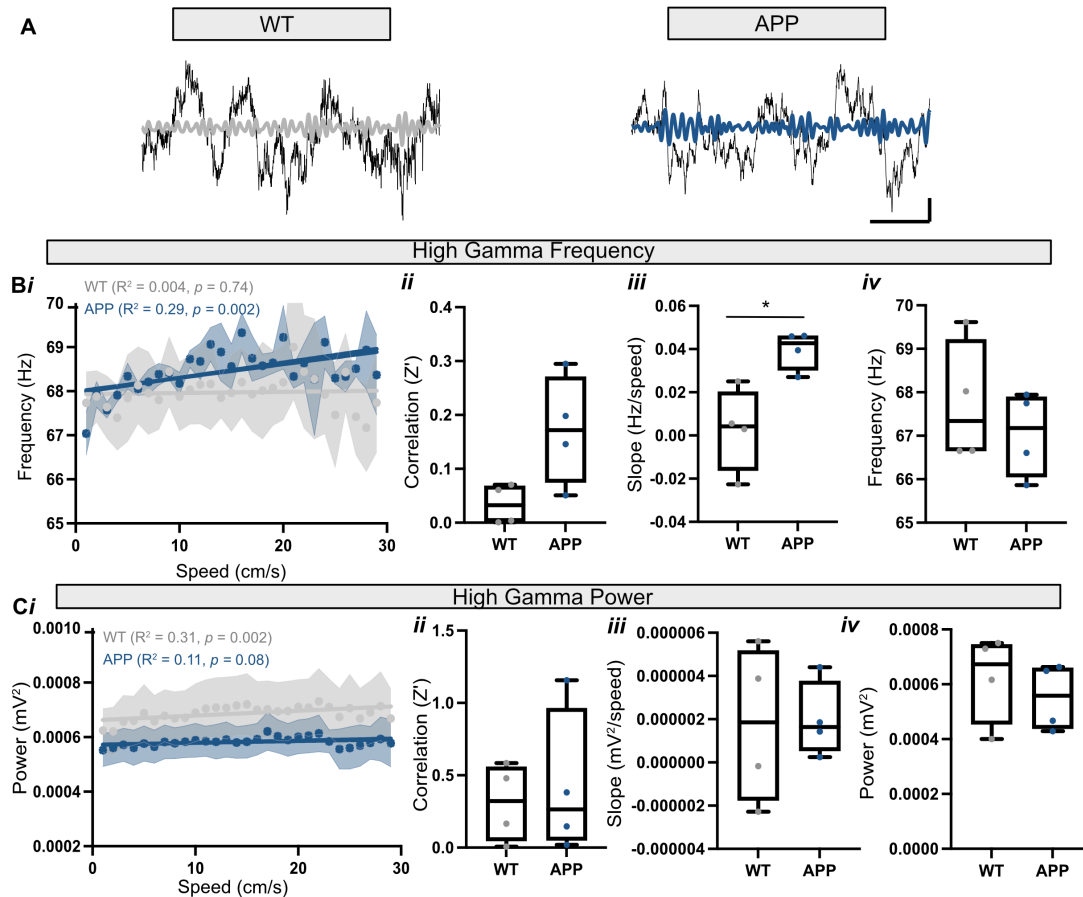


Figure 6.2.4 | Speed-modulated high gamma power and frequency in CA1.

A Example raw traces (black) and high gamma filtered traces for WT (grey) and APP (blue) animals. Scale bar: 100 ms, 100 μ V. **Bi** A speed-modulated increase in high gamma frequency was found in APP animals ($R^2 = 0.29$, $F(1,27) = 11.18$, $p = 0.002$, linear regression) but no relationship in WT ($R^2 = 0.004$, $F(1,27) = 0.11$, $p = 0.74$, linear regression). APP animals displayed no statistically significant difference to WT in the regression correlation (WT: 0.032 (0.002-0.068) vs APP: 0.172 (0.075-0.271) Z', $U = 2$, $p = 0.11$, Mann-Whitney U test) (**ii**) and in frequency (WT: 67.34 (66.65-69.22) vs APP: 67.18 (66.05-67.89) Hz, $U = 4$, $p = 0.34$, Mann-Whitney U test) (**iv**), but a statistically significant steeper slope of regression line (WT: 0.004 (-0.016-0.020) vs APP: 0.042 (0.030-0.046) freq/speed, $U = 0$, $p = 0.03$, Mann-Whitney U test) (**iii**). **Ci** A speed-modulated increase in high gamma power was found in WT animals ($R^2 = 0.31$, $F(1,27) = 11.90$, $p = 0.002$, linear regression) but not APP animals ($R^2 = 0.11$, $F(1,27) = 3.36$, $p = 0.07$, linear regression). APP animals displayed no statistically significant difference to WT in the regression correlation (WT:

0.32 (0.05-0.56) vs APP: 0.26 (0.05-0.96) Z', $U = 8$, $p > 0.99$, Mann-Whitney U test) (**ii**), slope (WT: 0.000002 (-0.000001-0.000005) vs APP: 0.000001 (0.000000-0.000003) power/speed, $U = 7$, $p = 0.89$, Mann-Whitney U test) (**iii**) and power (WT: 0.0007 (0.0005-0.0007) vs APP: 0.0006 (0.0004-0.0007) mV², $U = 6$, $p = 0.69$, Mann-Whitney U test) (**iv**). Box plots show median, IQR and ranges. Regression lines display the mean \pm SEM. Descriptive statistics display median and IQR. * $p < 0.05$.

6.2.3 | Speed-modulated gamma oscillations in the mPFC

Given that the power of hippocampal and mPFC theta oscillations increase with running speed (McFarland, Teitelbaum & Hedges, 1975; Adhikari, Topiwala & Gordon, 2010b; Fuhrmann *et al.*, 2015), and that both slow and fast mPFC gamma oscillations can be entrained by hippocampal theta oscillations (Sirota *et al.*, 2008), it was hypothesised that mPFC gamma oscillations would also be modulated by running speed. However, the frequency of slow gamma oscillations did not show a statistically significant linear relationship with respect to running speed in WT or APP animals (pooled data) (**Figure 6.2.5 A, Ci**). Additionally, no statistically significant difference was found in APP animals compared with WT when analysing the regression correlations and slope of the regression lines (**Figure 6.2.5 Cii-iii**). Furthermore, a statistically significant linear relationship between the power of slow gamma oscillations and running speed was identified in APP animals but not WT (pooled data) (**Figure 6.2.5 A, Di**). This did not result in a statistically significant difference in the regression correlations or slope of regression lines in APP animals (**Figure 6.2.5 Dii-iii**). Finally, no statistically significant change was found in the frequency and power (y-intercepts) of slow gamma oscillations in APP animals compared with WT (**Figure 6.25 B, Civ, Div**).

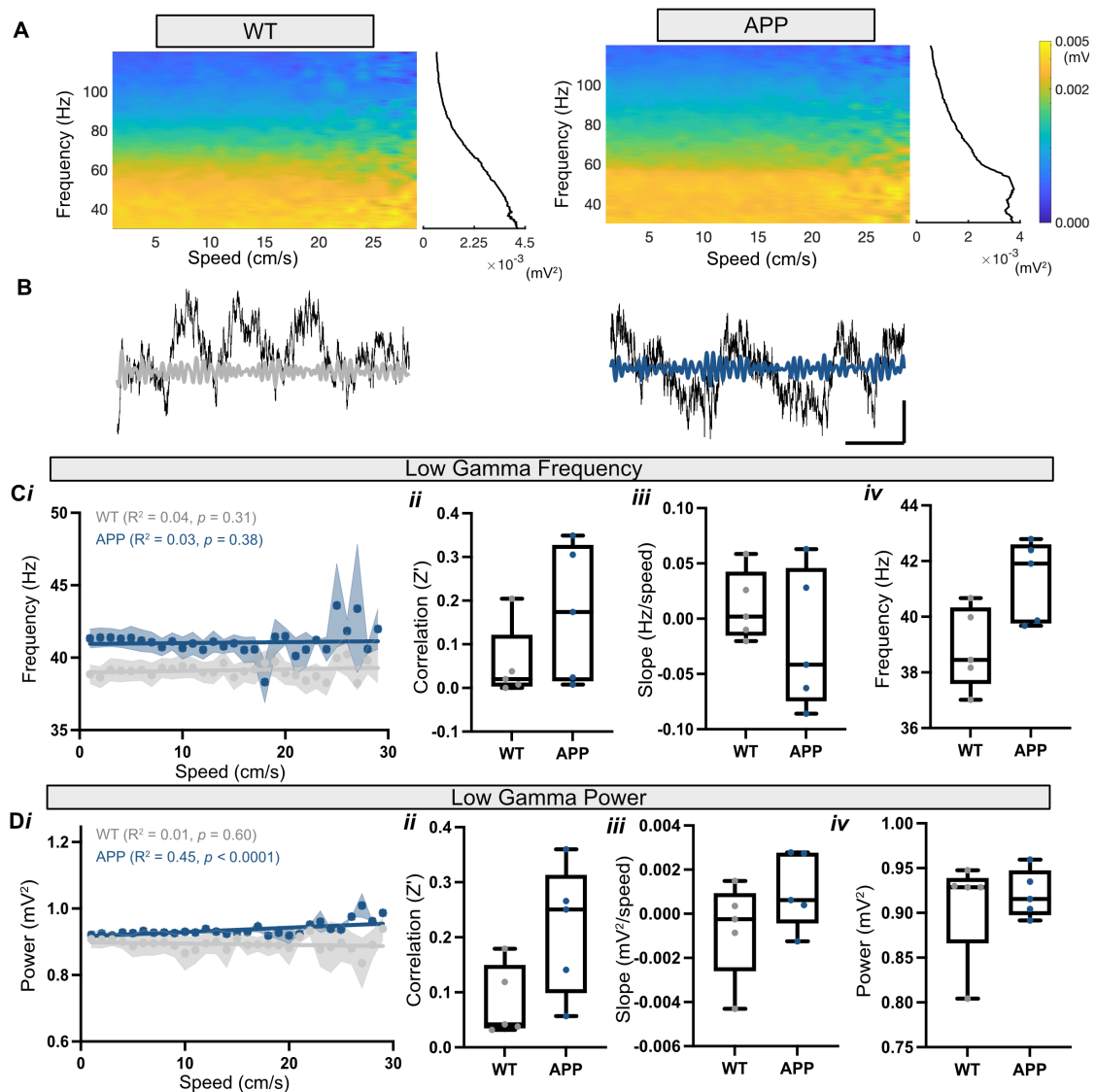


Figure 6.2.5 | Speed-modulated low gamma power and frequency in the mPFC. **A** Example spectrograms displaying a speed-modulated low and high gamma power in WT and APP mice. **B** Example raw traces (black) and low gamma filtered traces for WT (grey) and APP (blue) animals. Scale bar: 200 ms, 200 μ V. **Ci** Low gamma frequency was not found to be speed-modulated in both WT ($R^2 = 0.04, F(1,27) = 1.05, p = 0.32$, linear regression) and APP animals ($R^2 = 0.03, F(1,27) = 0.77, p = 0.38$, linear regression). APP animals displayed no statistically significant difference to WT in the regression correlation (WT: 0.020 (0.004-0.0121) vs APP: 0.174 (0.016-0.327) Z', $U = 7, p = 0.31$, Mann-Whitney U test) (ii), slope (WT: 0.001 (-0.015-0.042) vs APP: -0.041 (-0.074-0.045) freq/speed, $U = 9, p = 0.54$, Mann-Whitney U test) (iii) and frequency (WT: 38.45 (37.59-40.33) vs APP: 41.91 (39.77-42.59) Hz, $U =$

1, $p = 0.10$, Mann-Whitney U test) (*iv*), although a trending increase in frequency can be seen. **Di** Low gamma power was not found to be speed-modulated in WT animals ($R^2 = 0.01$, $F(1,27) = 0.27$, $p = 0.60$, linear regression) but linearly increased with speed in APP animals ($R^2 = 0.45$, $F(1,27) = 22.51$, $p < 0.0001$, linear regression). APP animals displayed no statistically significant difference to WT in the regression correlation (WT: 0.04 (0.04-0.15) vs APP: 0.25 (0.09-0.31) Z' , $U = 3$, $p = 0.05$, Mann-Whitney U test) (*ii*), slope (WT: -0.0002 (-0.0026-0.0009) vs APP: 0.0006 (-0.0004-0.0028) power/speed, $U = 6$, $p = 0.22$, Mann-Whitney U test) (*iii*) and power (WT: 0.93 (0.87-0.94) vs APP: 0.92 (0.90-0.95) mV^2 , $U = 12$, $p > 0.99$, Mann-Whitney U test) (*iv*), although a trending increase in correlation can be seen. Box plots show median, IQR and ranges. Regression lines display the mean \pm SEM. Descriptive statistics display median and IQR.

The peak frequency of fast gamma oscillations was found to linearly increase with respect to running speed in WT and APP animals (pooled data) (**Figure 6.2.5 A**, **Figure 6.2.6 Bi**), with no statistically significant change in the regression correlations and slope of the regression lines identified in APP animals compared with WT (**Figure 6.2.6 Bii-iii**). Additionally, a statistically linear increase in the power of fast gamma oscillations with respect to running speed was found in APP animals but not WT (pooled data) (**Figure 6.2.5 A**, **Figure 6.2.6 Ci**). This did not result in a statistically significant change in the regression correlation and slope of regression line in APP animals compared with WT (**Figure 6.2.6 Cii-iii**). Lastly, no statistically significant or trending change in the power and frequency (y-intercepts) of fast gamma oscillations was identified in APP animals compared with WT (**Figure 6.2.6 A**, **Biv**, **Civ**). This result is contrary to what is found in CA1 and potentially reflects regional differences in AD pathophysiology.

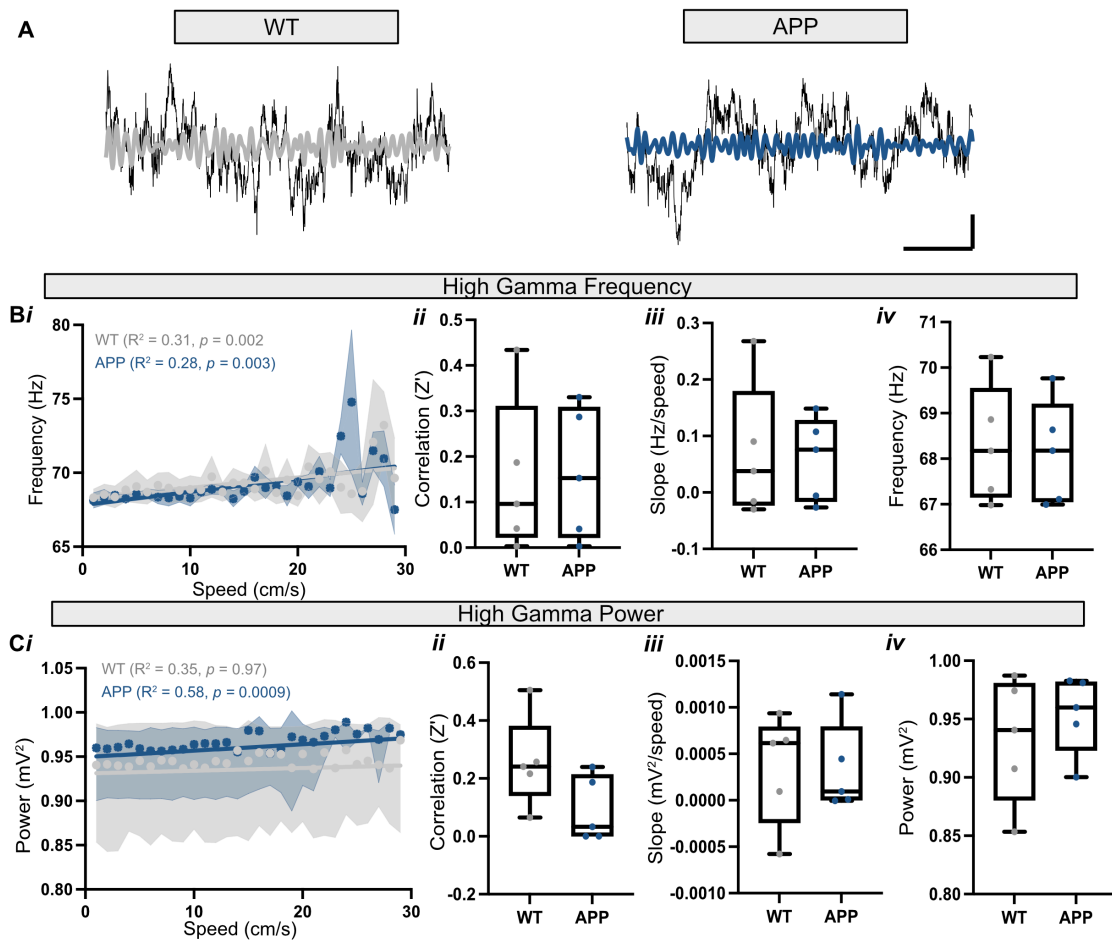


Figure 6.2.6 | Speed-modulated high gamma power and frequency in the mPFC. **A** Example raw traces (black) and high gamma filtered traces for WT (grey) and APP (blue) animals. Scale bar: 100 ms, 100 μ V. **Bi** A speed-modulated increase in high gamma frequency was found in both WT ($R^2 = 0.31$, $F(1,27) = 11.98$, $p = 0.002$, linear regression) and APP animals ($R^2 = 0.28$, $F(1,27) = 10.48$, $p = 0.003$, linear regression). APP animals displayed no statistically significant difference to WT in the regression correlation (WT: 0.09 (0.02-0.31) vs APP: 0.15 (0.02-0.31) Z', $U = 21.5$, $p > 0.99$, Mann-Whitney U test) (ii), slope (WT: 0.04 (-0.02-0.18) vs APP: 0.08 (-0.02-0.13) freq/speed, $U = 11$, $p = 0.84$, Mann-Whitney U test) (iii), and in frequency (WT: 68.17 (67.15-69.55) vs APP: 68.18 (67.05-69.20) Hz, $U = 12$, $p > 0.99$, Mann-Whitney U test) (iv). **Ci** A speed-modulated increase in high gamma power was found in both WT ($R^2 = 0.35$, $F(1,27) = 14.69$, $p = 0.0007$, linear regression) and APP animals ($R^2 = 0.58$, $F(1,27) = 37.01$, $p < 0.0001$, linear regression). APP animals displayed no statistically significant difference to WT in the regression correlation (WT: 0.24 (0.14-0.38) vs APP: 0.03 (0.00-0.21) Z', $U = 3$, $p = 0.05$,

Mann-Whitney U test) (*ii*), slope (*WT*: 0.0006 (-0.0002-0.0008) vs *APP*: 0.0001 (0.000002-0.0008) power/speed, $U = 11$, $p = 0.84$, Mann-Whitney U test) (*iii*) and power (*WT*: 0.94 (0.88-0.98) vs *APP*: 0.96 (0.92-0.98) mV^2 , $U = 10$, $p = 0.69$, Mann-Whitney U test) (*iv*), although a trending decrease in correlation can be seen. Box plots show median, IQR and ranges. Regression lines display the mean \pm SEM. Descriptive statistics display median and IQR.

6.2.4 | Theta-gamma coupling in CA1

In CA1, slow and fast gamma oscillations can be found coupled to different phases of the theta cycle, segregating information and preventing interference, while also integrating past (slow) with present (fast) experiences (Tort *et al.*, 2008; Scheffer-Teixeira *et al.*, 2012; Amemiya & Redish, 2018; Lopes-dos-Santos *et al.*, 2018). The PAC between these oscillations is thought to be a marker of cognitive performance, with an increase in theta-gamma coupling occurring during successful spatial memory retrieval and during working memory in both humans and rodents (Schack *et al.*, 2002; Tort *et al.*, 2009; Shirvalkar, Rapp & Shapiro, 2010). A reduction in theta-gamma coupling can be found in humans with AD and is related to poor performance in a working memory task (Goodman *et al.*, 2018). This relationship has also been found in first-generation mouse models of amyloidopathy (Ittner *et al.*, 2014; Etter *et al.*, 2019). Moreover, a reduction in the coupling of theta with fast gamma in CA1 has been found in the APP^{NL-G-F} mouse model between 7-13 months of age (Jun *et al.*, 2020). To understand how this coupling is affected at later ages, and to determine if these deficits extend to slow gamma oscillations, theta-gamma coupling was analysed at 16 months of age in APP^{NL-G-F} mice.

The PAC between theta and both slow and fast gamma oscillations was not found to change with respect to running speed in CA1, therefore analysis was conducted on the full signal (pooled data) (**Figure 6.275 B, C**). No statistically significant change in the PAC of theta with slow or fast gamma oscillations was found in APP animals compared with WT controls (**Figure 6.2.7 A, D, E**). Although theta-gamma PAC has also been reported to occur in the mPFC and between hippocampal theta and mPFC gamma, no noticeable change was detected when visualising the average instantaneous amplitude over theta phase

(Schack *et al.*, 2002; O'Neill, Gordon & Sigurdsson, 2013; Tamura *et al.*, 2017). Therefore, this was not analysed further.

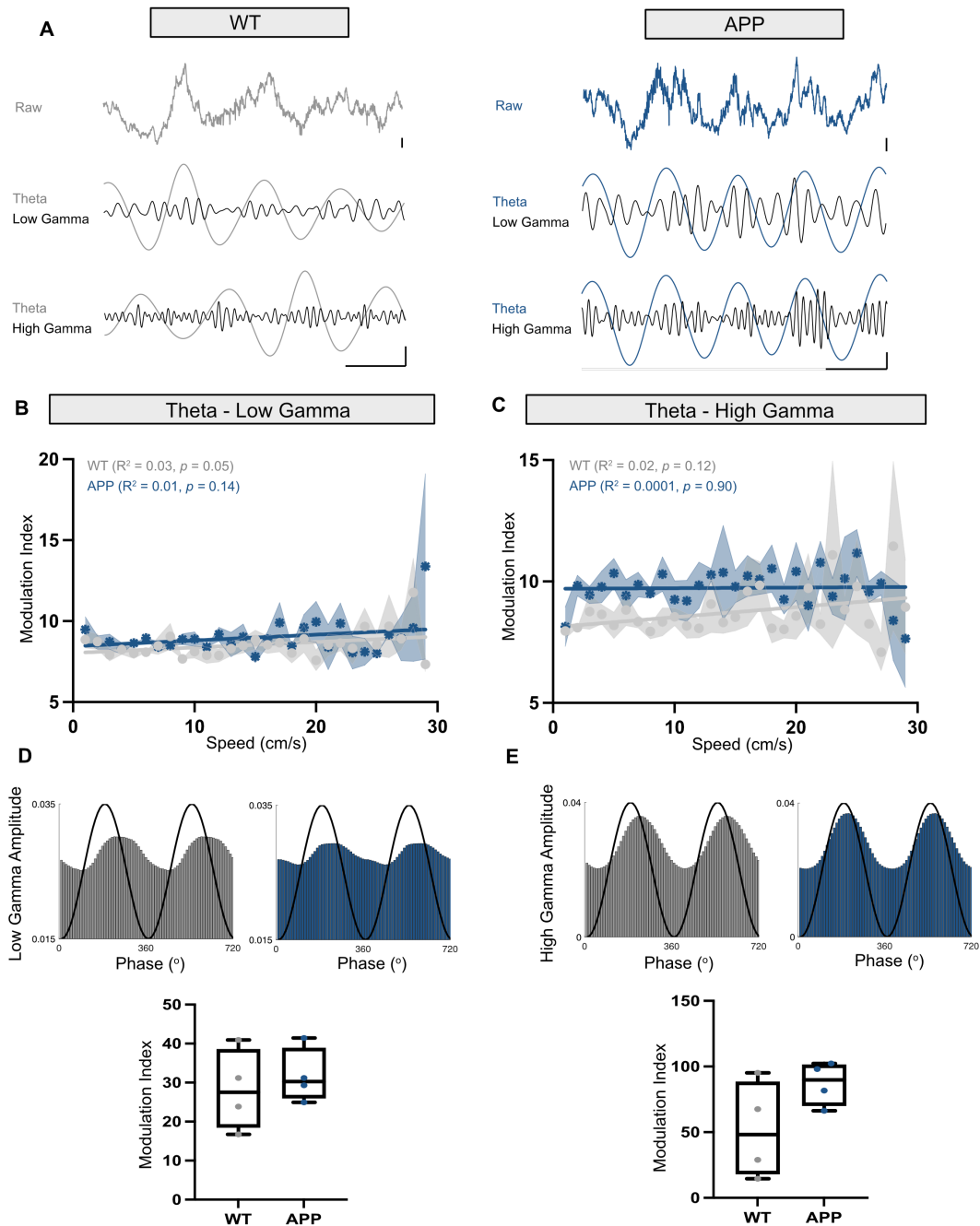


Figure 6.2.7 | Theta-gamma PAC is comparable between APP and WT animals in CA1. **A** Example traces displaying the PAC between theta oscillations and both low and high gamma oscillations in WT and APP animals. WT scale bars: 100 ms, 200 μ V, APP scale bars: 100 ms, 50 μ V (filtered), 100 μ V (raw). **B** Theta-low gamma coupling was not speed modulated in both WT

($R^2 = 0.03$, $F(1,27) = 3.81$, $p = 0.053$, linear regression) and APP animals ($R^2 = 0.02$, $F(1,27) = 2.14$, $p = 0.14$, linear regression). **C** Theta-high gamma coupling was not speed modulated in both WT ($R^2 = 0.02$, $F(1,27) = 2.43$, $p = 0.12$, linear regression) and APP animals ($R^2 = 0.0001$, $F(1,27) = 0.02$, $p = 0.90$, linear regression). **D** Theta-low gamma coupling was comparable between APP animals compared with WT (WT: 27.53 (18.52-38.51) vs APP: 30.26 (26.04-38.87), $U = 5$, $p = 0.49$, Mann-Whitney U test). Representative graphs (top) display the changing low gamma instantaneous amplitude (bars) over the phase of theta (black line). **E** Theta-high gamma coupling did not change in APP animals compared with WT when analysing the full signal (WT: 48.24 (18.18-88.29) vs APP: 89.87 (70.15-101.3), $U = 3$, $p = 0.20$, Mann-Whitney U test). Representative graphs (top) display the changing high gamma instantaneous amplitude (bars) over the phase of theta (black line). Box plots show median, IQR and ranges. Regression lines display the mean \pm SEM. Descriptive statistics display median and IQR.

6.2.5 | Theta coherence between CA1 and the mPFC

Communication between CA1 and the mPFC through theta oscillations is thought to be important for integrating spatial information with executive decision making (Jones & Wilson, 2005). The hippocampus leads this coherence, with an increase in theta coupling apparent when mice make a correct choice in a T- or Y-maze task, while a decrease in coupling occurs when an error is made (Jones & Wilson, 2005; Liu *et al.*, 2018). Less is currently known about how these regions communicate during active exploration in an OF, although evidence suggests that significant hippocampal-prefrontal coupling does exist under these conditions (Siapas, Lubenov & Wilson, 2005; Sirota *et al.*, 2008; Adhikari, Topiwala & Gordon, 2010b). Therefore, to understand how theta communication between CA1 and the mPFC is affected in the APP^{NL-G-F} mouse model at 16 months, theta coherence was analysed between these regions with respect to running speed.

A statistically significant linear increase in theta coherence was found with respect to running speed in WT animals (**Figure 6.2.8 A-C, Di**). However, no statistically significant linear increase was found in APP animals (pooled data) (**Figure 6.2.8 A-C, Di**). This potentially suggests that at faster running speeds,

theta communication between CA1 and mPFC is reduced. This is consistent with results that showed no statistically significant increase in the power and frequency of theta oscillations with respect to running speed in APP animals compared with WT (**Figure 6.2.2 Ci, Di**). However, when analysing the regression correlations and slopes of the regression lines, no statistically significant change was found in APP animals compared with WT (**Figure 6.2.8 Dii-iii**). Furthermore, no statistically significant change in coherence was found in APP animals compared with WT when analysing the y-intercepts (**Figure 6.2.8 Div**). Taken together, these results suggest that long-range communication between the hippocampus and mPFC is relatively intact in 16-month APP animals.

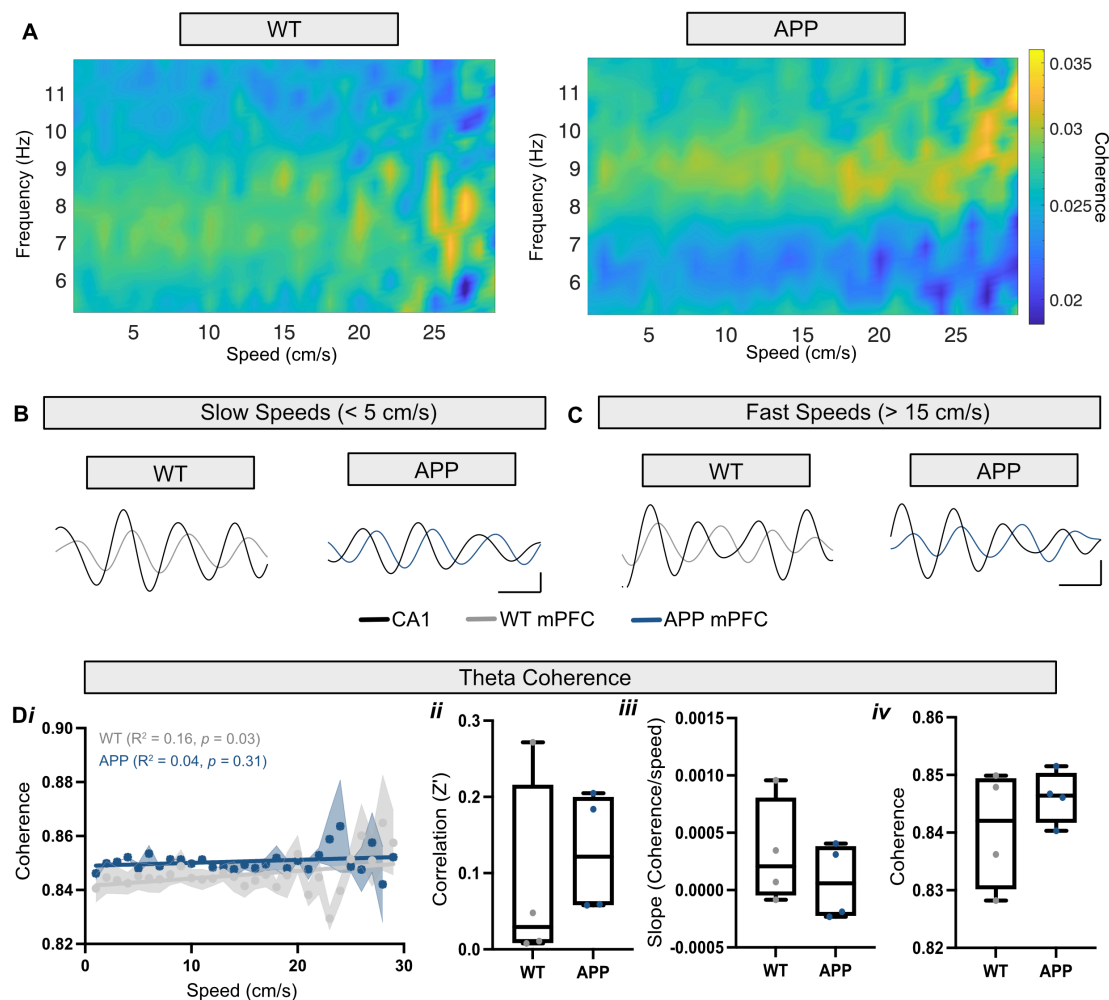


Figure 6.2.8 | Speed-modulated theta coherence between CA1 and the mPFC. **A** Example coherograms displaying a speed-modulated theta coherence between CA1 and the mPFC in WT and APP mice. **B** Example theta

filtered traces displaying theta correlation between CA1 (black) and the mPFC in WT (grey) and APP (blue) animals at slow running speeds. **C** Example theta filtered traces displaying theta correlation between CA1 (black) and the mPFC in WT (grey) and APP (blue) animals at fast running speeds. Scale bars: 100 ms, 100 μ V. **Di** Theta coherence between CA1 and the mPFC was found to linearly increase with speed in WT animals ($R^2 = 0.16$, $F(1,27) = 5.27$, $p = 0.03$, linear regression) but not in APP ($R^2 = 0.04$, $F(1,27) = 1.09$, $p = 0.31$, linear regression). APP animals displayed no statistically significant difference to WT in the regression correlation (WT: 0.029 (0.009-0.215) vs APP: 0.121 (0.058-0.200) Z' , $U = 4$, $p = 0.34$, Mann-Whitney U test) (**ii**), slope (WT: 0.0002 (-0.00004-0.0008) vs APP: 0.00006 (-0.0002-0.0004) freq/speed, $U = 5$, $p = 0.48$, Mann-Whitney U test) (**iii**) and coherence (WT: 0.84 (0.83-0.85) vs APP: 0.85 (0.84-0.85) Hz, $U = 6$, $p = 0.68$, Mann-Whitney U test) (**iv**). Box plots show median, IQR and ranges. Regression lines display the mean \pm SEM. Descriptive statistics display median and IQR.

6.2.6 | Locomotor activity in the Open Field

Both WT and APP animals successfully habituated to the OF arena, as evidenced by a statistically significant decline in the distance travelled over the 1-hour (**Figure 6.2.9 A**). Additionally, no statistically significant difference in the average distance travelled (**Figure 6.2.9 B, C**) or average running speed (**Figure 6.2.9 D, E**) was found in APP animals compared with WT controls, although APP animals, on average, trended towards increased locomotor activity (**Figure 6.2.9 A, B**).

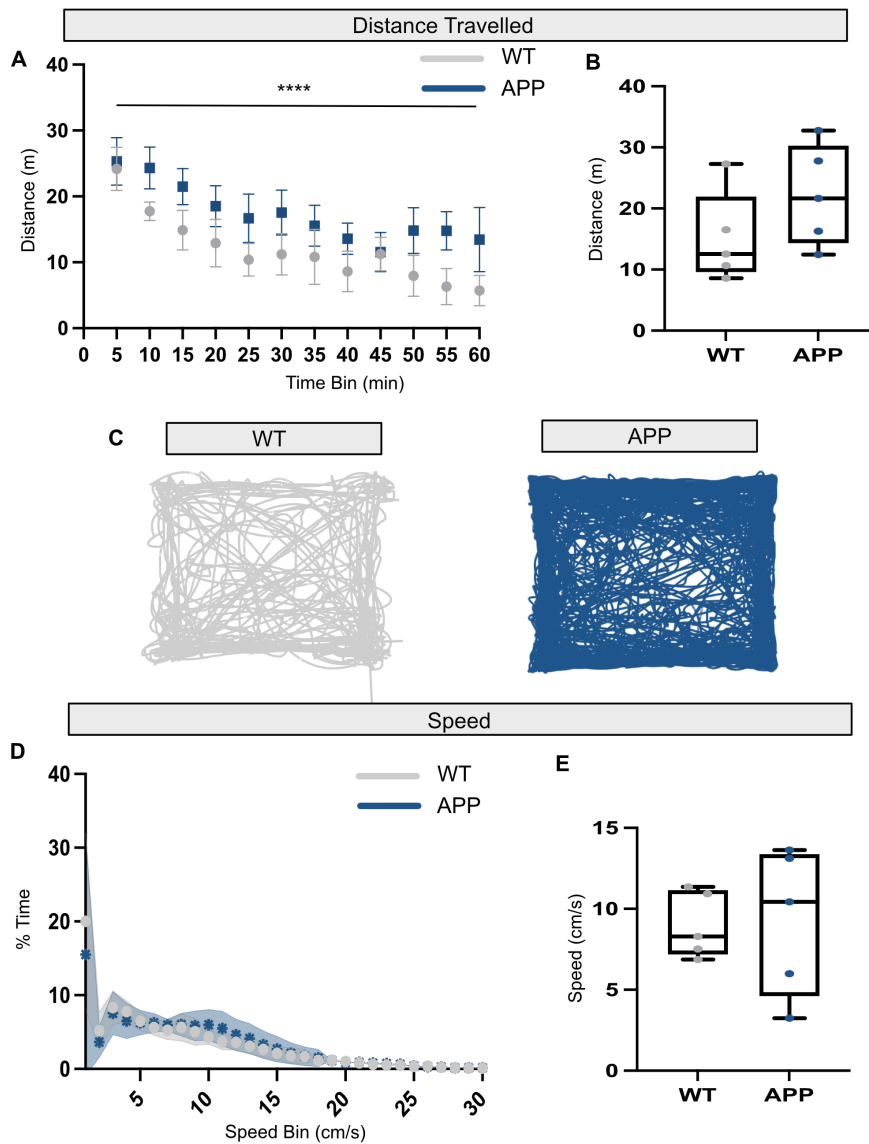


Figure 6.2.9 | Locomotor activity of WT and APP animals in an OF arena.

A Both WT and APP animals habituated to the OF arena, as evidenced by the statistically significant reduction in the distance travelled over time ($F(4,37) = 15.62$, $p < 0.0001$, Two-way repeated measured ANOVA). **B** No statistically significant difference in the total distance travelled was found in APP animals compared with WT controls (WT: 12.56 (9.62-21.91) vs APP: 21.64 (14.37-30.26), $U = 6$, $p = 0.22$, Mann-Whitney U test). **C** Example traces showing the exploratory path that a WT and APP animal took during the 60 minute OF task. **D** Graph depicting the % time spent in each speed bin for both WT and APP animals. **E** No statistically significant difference in the average running speed was found in APP animals compared with WT controls (WT: 8.29 (7.19-11.14) vs APP: 10.43 (4.61-13.37), $U = 12$, $p > 0.99$, Mann-Whitney U test). Graphs **A** and **D** display the mean \pm SEM. Box-plots display the median, IQR and range.

Non-parametric descriptive statistics display the median and IQR. **** $p < 0.0001$.

6.3 | Discussion

6.3.1 | Summary

The present study aimed to assess how the neuronal oscillations underlying exploratory behaviour in the mPFC-hippocampal circuit are affected in the APP^{NL-G-F} mouse model at 16 months. A trending increase in the power of theta oscillations and decrease in the power of low and high gamma oscillations was found in CA1, with no change in the PAC between oscillations observed, the former being consistent with previously reported data in younger animals. Theta and both low and high gamma oscillations in the mPFC were not found to change in APP animals compared with WT controls. Lastly, a slight decrease in theta coherence between CA1 and mPFC was noted with respect to running speed in APP animals, potentially indicating a mild impairment in communication between brain regions.

6.3.2 | Increased theta power in CA1

Consistent with previously reported data, a linear increase in the power and frequency of theta oscillations with respect to running speed was found in the CA1 region of the hippocampus in both WT and APP animals (McFarland, Teitelbaum & Hedges, 1975; Fuhrmann *et al.*, 2015). When analysing theta oscillation power, a trending increase was identified in APP animals compared with WT controls. This increase in theta power has previously been identified in younger APP animals (7-13 months), and was linked to impaired spatial memory (Jun *et al.*, 2020). What the current experiments do is show that this increase in power is sustained at 16 months. An increase in theta power can be seen in the brains of patients with AD (Adler, Brassens & Jajcevic, 2003; Czigler *et al.*, 2008), yet a decrease has been reported in first-generation mouse models of amyloidopathy (Ittner *et al.*, 2014; Schneider *et al.*, 2014). This demonstrates that the APP^{NL-G-F} mouse model better recapitulates the human condition compared with first-generation models (Nilsson, Saito & Saido, 2014; Sasaguri *et al.*, 2017), at least when studying neuronal oscillations.

There are several potential mechanisms that could account for the increase in theta power. The first potential cause comes from the glutamatergic afferents originating from the MS-DBB, which control the increase in theta power

accompanying locomotion velocity in CA1 (Fuhrmann *et al.*, 2015). These projections synapse onto OLM interneurons that disinhibit the feed-forward inhibiting interneurons of Schaffer-collateral (CA3) and perforant (mEC) pathways, causing the increase in PC firing rate seen with increased running speeds. The sustained activation of OLM interneurons through increased glutamatergic input could in turn increase the magnitude and frequency of PC action potentials, producing an increase in theta power. Hyperactivity of glutamatergic neurons can be found in first-generation mouse models of amyloidopathy (Busche *et al.*, 2008, 2012), yet it is currently unknown if the same is true for the APP^{NL-G-F} mouse model. However, epileptic discharges can be observed at around 6-8 months in this model (Johnson *et al.*, 2020), which are a product of neuronal hyperactivity and the synchronous discharging of neurons, potentially suggesting altered glutamatergic neuron activity (Palop & Mucke, 2010, 2016). Alternatively, an increase in the activity of OLM interneurons themselves could have the same effect, with compensatory remodelling of inhibitory synapses identified in first-generation mouse models (Palop *et al.*, 2007; Hollnagel *et al.*, 2019).

Moreover, local PV-expressing interneurons within CA1 and long-range projecting PV-expressing interneurons originating in the MS-DBB have shown to be important in generating and pacing the theta oscillation (Freund & Antal, 1988; Simon *et al.*, 2006; Hangya *et al.*, 2009; Amilhon *et al.*, 2015). Impairments to the inhibitory control of the brain in AD has been well documented (Busche *et al.*, 2008; Palop & Mucke, 2016; Ambrad Giovannetti & Fuhrmann, 2019), with PV-expressing interneurons exhibiting both hypofunction (Verret *et al.*, 2012; Martinez-Losa *et al.*, 2018) and hyperfunction (Hijazi *et al.*, 2019) in different mouse models of amyloidopathy. It is possible that a reduction in the activity of these interneurons in CA1 could cause an increase in the E-I balance, generating greater theta power. On the other hand, hyperfunction of PV-expressing interneurons in CA1 can potentially cause larger post-synaptic IPSPs and rebound spike-bursts in PCs, increasing the amplitude of theta. Indeed, hyperfunction of PV-expressing interneurons would further fit with the observed changes occurring to ripple events (see **section 5.2.3.4**). Furthermore, the spike-time relationship of PCs with the theta oscillation was found to be impaired in younger APP animals, potentially suggesting impairments to the inhibitory

pacemaker of the circuit (Jun *et al.*, 2020). Any alterations to PV-expressing interneuron activity in CA1 and the MS-DBB could impair this spike-time relationship. Repeating these experiments with single-unit or Ca²⁺ imaging of different interneuron populations will give a clearer indication how inhibition in CA1 is contributing to the increase in theta power.

6.3.3 | Mild impairments to theta communication between CA1 and the mPFC during increasing locomotion velocity

A statistically significant linear increase in the frequency and power of theta oscillations was found with respect to running speed in the mPFC of WT animals, yet was not altered in APP animals. Additionally, theta coherence between brain regions was found to linearly increase with respect to running speed in WT but not APP animals. These results collectively point towards a mild impairment in theta coupling between CA1 and the mPFC, specifically during increasing locomotion velocity in APP animals. It is possible that at faster running speeds in APP animals, when the hippocampus is modulating its neuronal firing rates to increase input sensitivity (Fuhrmann *et al.*, 2015), hippocampal output suffers, and cannot function as effectively.

Furthermore, when analysing the coherence at the y-intercept, no statistically significant difference was found in APP animals compared with WT controls. Therefore, it appears that communication between the hippocampus and mPFC is relatively unaffected in 16-month APP animals, consistent with the absence of communication deficits seen during SWS (see **section 5.3.3**). This is contrary to humans in which a decrease in functional connectivity between the hippocampus and mPFC has been found early on in the disease progression (Wang *et al.*, 2006). However, these experiments were conducted using resting state fMRI, which could potentially cause differences in results.

Finally, no change in theta power was identified in the mPFC, yet a trending increase was found in CA1. A progression of decline can be viewed when studying gamma oscillations in the APP^{NL-G-F} mouse model; impairments begin in the mEC at 5 months (Nakazono *et al.*, 2017), progress to CA1 between 7-13 months (Jun *et al.*, 2020), with no change in gamma power found in the mPFC at

12 months (Pervolaraki *et al.*, 2019). This suggests that impairments to mPFC theta oscillations may occur at ages greater than 16 months.

6.3.4 | Gamma oscillation power and frequency in CA1 and the mPFC

Changes to the power and frequency of low and high gamma oscillations with respect to running speed were analysed in CA1. An overall decrease in the power of low and high gamma was observed in APP animals compared with WT controls when visualising the power vs speed relationship. A decrease in high gamma power has previously been reported in younger APP animals (Jun *et al.*, 2020), with the trending decrease in low gamma power at 16 months further showing a progression of decline in this model. This is consistent with previous results conducted in first-generation mouse models, which displayed a reduction in broadband gamma power that was associated with poor spatial memory performance (Palop *et al.*, 2007; Palop & Mucke, 2016; Martinez-Losa *et al.*, 2018; Etter *et al.*, 2019). Moreover, decreased gamma power can be found in humans with AD (Murty *et al.*, 2021).

A reduction in low gamma power in CA1 could potentially point towards impairments in the Schaffer-collateral pathway, that can be identified by measuring the coherence of slow gamma oscillations between CA3 and CA1. Alternatively, changes in CA1 PV-expressing interneuron activity may be occurring. PV-expressing interneurons are crucial for gamma generation and pace the activity of PCs (Mann, Radcliffe & Paulsen, 2005; Sohal *et al.*, 2009b). In an APP/PSEN1 model, PV-expressing interneurons have shown to increase their expression of PV, ramify their morphology and increase their firing frequency, implying compensatory remodelling of the network (Hijazi *et al.*, 2019; Hollnagel *et al.*, 2019). PV-expressing interneuron hyperfunction in CA1 could theoretically decrease the E-I balance, causing reduced gamma power. Indeed, PC phase-locked firing to high gamma oscillations was found to be impaired in young APP mice, potentially indicating disrupted PV-expressing interneuron activity (Jun *et al.*, 2020). Moreover, hyperfunction of these interneurons would be in-keeping with the increase in CA1 theta power (see **section 6.3.2**) and decrease in ripple power (see **section 5.2.3.4**) already observed. Recording the single-units of PV-expressing interneurons with respect to these oscillations will

give a clearer indication of how their activity is contributing to the observed changes in oscillatory power. Disruptions to PV-expressing interneuron have already been linked to impaired gamma oscillations in first-generation mouse models, making them attractive targets for future experiments (Verret *et al.*, 2012; Martinez-Losa *et al.*, 2018).

Identical analysis was performed on low and high gamma oscillations in the mPFC, yet APP animals exhibited no change to gamma oscillations compared with WT. This is consistent with previously reported literature showing that gamma oscillations were unaffected in 12-month-old APP^{NL-G-F} mice (Pervolaraki *et al.*, 2019).

6.3.5 | Gamma oscillation power and frequency with respect to running speed in the mPFC and CA1

Gamma oscillation power has been shown to linearly increase with locomotion velocity in CA1 (Chen *et al.*, 2011). It was also thought the same would be true for mPFC gamma oscillations, as theta power in both regions also exhibits a linear increase with running speed (McFarland, Teitelbaum & Hedges, 1975; Adhikari, Topiwala & Gordon, 2010b; Fuhrmann *et al.*, 2015) and there is evidence for hippocampal theta entraining both mPFC theta and gamma oscillations (Jones & Wilson, 2005; Tort *et al.*, 2008; Sirota *et al.*, 2008; Tamura *et al.*, 2017). Therefore, gamma oscillations were analysed with respect to running speed in both brain regions.

The frequency of low gamma oscillations was not found to change with respect to running speed for WT animals in CA1 and for both genotypes in the mPFC. However, the total power of low gamma oscillations was found to linearly decrease with respect to running speed in CA1 and increase in the mPFC, but only in APP animals. Additionally, the frequency of high gamma oscillations was found to linearly increase with speed in both brain regions, but only in APP animals in CA1, with a linear increase in power with running speed only occurring in the mPFC of APP animals. The lack of relationship between the power and frequency of gamma and running speed in WT animals makes this data hard to

interpret. Potentially, this could be due to larger variation in WT data compared with APP.

Based on previous literature, an increase in the power of low and high gamma oscillations would be expected to occur with respect to locomotion speed in CA1 (Chen *et al.*, 2011). However, the linear decrease in power of low gamma oscillations is more reminiscent of a separate study conducted in rats, that found a decrease in the power of low gamma oscillations and increase in the power of high gamma, along with a linear increase in the frequency of both (Ahmed & Mehta, 2012). Increasing the frequency of gamma oscillations, and neuronal firing, increases the sensitivity of neurons to rapidly integrate spatial information at faster running speeds (Ahmed & Mehta, 2012; Fuhrmann *et al.*, 2015). Particularly, spatial information arriving from the mEC, producing a larger increase in high gamma power (Ahmed & Mehta, 2012). These differences in findings can be attributed to the slightly different circuitry between rodents, and the methods used to determine changes in gamma oscillations with locomotion velocity (Chen *et al.*, 2011; Ahmed & Mehta, 2012). Nevertheless, these differences do not negate the observed changes to gamma power and frequency detailed in **section 6.3.4**.

6.3.6 | Theta-gamma coupling in CA1

Theta-gamma PAC binds neuronal firing across spatial and temporal scales and is a marker of cognitive performance (Lisman & Jensen, 2013), with greater PAC occurring during spatial memory retrieval and working memory tasks (Schack *et al.*, 2002; Tort *et al.*, 2009; Shirvalkar, Rapp & Shapiro, 2010). Within CA1, slow and fast gamma oscillations can be found coupled to different phases of the theta cycle, segregating information to prevent interference while also integrating past (slow) with present (fast) experiences (Zhang *et al.*, 2019; López-Madróna *et al.*, 2020). In the current experiments, the PAC of theta with both slow and fast gamma was not found to linearly increase with respect to locomotion velocity, which is inconsistent with previously reported literature (Chen *et al.*, 2011). Therefore, the PAC between these oscillations was analysed for the full signal. No change in the coupling between theta and both frequencies of gamma was found in APP animals compared with WT controls.

Reduced theta-gamma coupling is considered a biomarker for AD in humans (Kitchigina, 2018; Goodman *et al.*, 2018). Changes in this coupling have additionally been identified in first-generation mouse models and have been linked to impaired spatial memory (Iltner *et al.*, 2014; Etter *et al.*, 2019). Furthermore, a reduction in the PAC between theta and high gamma was previously identified in younger APP mice (Jun *et al.*, 2020). Discrepancies between the results described in this chapter and previous findings can potentially be attributed to the differences in the methods used to analyse PAC; in the experiments described in this chapter, PAC was carried out on the full signal, whereas only algorithm-detected theta-gamma episodes were used in younger animals.

Furthermore, although both theta and gamma oscillations were found in the mPFC, no noticeable PAC between them was identified when visualising the instantaneous amplitude over the phase of theta. The same can be said for hippocampal theta oscillations with mPFC gamma oscillations, that have previously shown to be coupled (Sirota *et al.*, 2008; Tamura *et al.*, 2017). Therefore, both pieces of analysis were omitted. The lack of PAC is unlikely to be due to the method used (see **section 2.4.2**), as evidenced by its efficacy in detecting PAC in CA1. Theta-gamma coupling in the mPFC and between CA1 and the mPFC is more commonly studied during working memory tasks and goal-directed spatial navigation (Schack *et al.*, 2002; O'Neill, Gordon & Sigurdsson, 2013; Tamura *et al.*, 2017). Although these oscillations and inter-region communication occur during exploratory behaviour (Siapas, Lubenov & Wilson, 2005; Sirota *et al.*, 2008), it is possible that paradigms that involve spatial working memory and goal-directed spatial navigation may produce more noticeable PAC. Recording mPFC-hippocampal communication during these tasks in APP animals will further our understanding how these memory systems are affected in this model.

6.3.7 | Ambulatory activity in the OF paradigm

In these experiments, mice were left to explore an OF arena for 1 hour as exploratory behaviour generates the neuronal oscillations and brain communication that are the focus of these experiments (Siapas, Lubenov &

Wilson, 2005; Sirota *et al.*, 2008; Scheffer-Teixeira *et al.*, 2012). When analysing the average distance travelled by animals and the average locomotion velocity, APP animals did not have altered ambulatory activity compared with WT controls. Locomotor hyperactivity has previously been described in several first-generation mouse models (Dumont *et al.*, 2004; Walker *et al.*, 2011; Oblak *et al.*, 2021) and is thought to mirror the restless observed in patients with AD (Lanari *et al.*, 2006). Although, a trending increase in the distance travelled by APP animals can be found during exploratory activity in the OF arena and during the NOL paradigm (see **section 5.2.12**). Reduced locomotion has previously identified in APP animals at 6 months (Whyte *et al.*, 2018), that was not found in a separate study conducted at 8 months (Pervolaraki *et al.*, 2019). Finally, both WT and APP animals reduced their activity throughout over 1 hour, indicating successful habituation.

6.3.9 | Conclusions

Impairments to the local oscillations in CA1 were identified during exploratory behaviour, with the oscillations of the mPFC and communication between these regions relatively unaffected in APP animals at 16 months. This is consistent with the results found studying this circuit during SWS (see **section 5.3**). Although the mechanisms underlying the changes to hippocampal oscillations are still to be investigated, these results provide a clear indication that circuit alterations are taking place, and provide a platform for which additionally hypotheses can be formed and tested.

7 | Final discussion and conclusions

7.1 | Key findings

7.1.1 | Original hypotheses

The original hypotheses as stated in **section 1.5** are as follows:

- 1) Within the mPFC-hippocampal circuit, the oscillations involved in systems consolidation and their coupling are disrupted in the APP^{NL-G-F} mouse model of familial AD.
- 2) The oscillations involved in spatial memory in both the hippocampus and mPFC are disrupted in the APP^{NL-G-F} mouse model, similar to first-generation models of amyloidopathy.
- 3) The function of PV- and SST-expressing interneurons is perturbed in the APP^{NL-G-F} mouse model, contributing to disrupted SWA.

7.1.2 | Key findings investigating hypothesis 1

The work carried out in **Chapter 5** addressed *hypothesis 1*. In the preclinical stages of AD, sleep disturbances are extremely common and are a predictor of cognitive decline (Kabeshita *et al.*, 2017; Bubu *et al.*, 2017). Patients exhibit night-time awakenings, sleep fragmentation and disruptions to the sleep-wake cycle, particularly a reduced time spent in NREM sleep (Vitiello *et al.*, 1990; Bubu *et al.*, 2017). During NREM sleep, the communication between the hippocampus and mPFC facilitates the reorganisation of newly encoded hippocampal memories into cortical networks for long-term consolidation, a process called systems consolidation. This is achieved through the temporal communication of 3 cardinal oscillations; the SWO, spindles and SWRs (Diekelmann & Born, 2010; Maingret *et al.*, 2016b). An inverse relationship between amyloid load and the density of the SWO and spindles can be found in humans with AD (Mander *et al.*, 2015a; Kam *et al.*, 2019), as well as reduced functional coupling between the hippocampus and mPFC (Wang *et al.*, 2006). Additionally, there is accumulating evidence from first-generation mouse models of amyloidopathy and tauopathy for disruptions to several cardinal oscillations and their coupling, which are linked to impairments in declarative memory (Busche *et al.*, 2015; Nicole *et al.*, 2016; Kastanenka *et al.*, 2017; Castano-Prat *et al.*, 2019; Hollnagel *et al.*, 2019; Zhurakovskaya *et al.*, 2019; Caccavano *et al.*, 2020; Benthem *et al.*, 2020).

However, a characterisation of this circuit in second-generation mouse models of amyloidopathy has yet to be described. Therefore, using the APP^{NL-G-F} mouse model, the oscillatory activity of this circuit was studied using *in vivo* electrophysiology while mice slept naturally.

The outcome of this research project was the identification of impairments to the local oscillations found in CA1 and the mPFC during SWS at 16 months of age in APP^{NL-G-F} mice, while their temporal coupling was unimpaired. Specifically, an increase in the power of mPFC spindle events, a reduction in the power and number of detected hippocampal spindles, as well a reduction in the power and increase in the number of detected hippocampal ripples were identified (**Figure 7.1.1**). This partially confirms the hypothesis that disruptions to the oscillations involved in systems consolidation are occurring, but rejects the hypothesis that disruptions would also be identified in their coupling. Although this circuit has been investigated in the context of dementia prior to the present study (Zhurakovskaya *et al.*, 2019; Benthem *et al.*, 2020), this is the first characterisation of the mPFC-hippocampal circuit during SWS in a second-generation mouse model of amyloidopathy. These findings provide valuable information about how impairments to systems consolidation caused by pathological amyloid can relate to memory decline in the APP^{NL-G-F} mouse model. Additionally, they deliver a platform to study the underlying neuronal circuit alterations in a mouse model that is thought to better recapitulate the preclinical stages of AD (Sasaguri *et al.*, 2017).

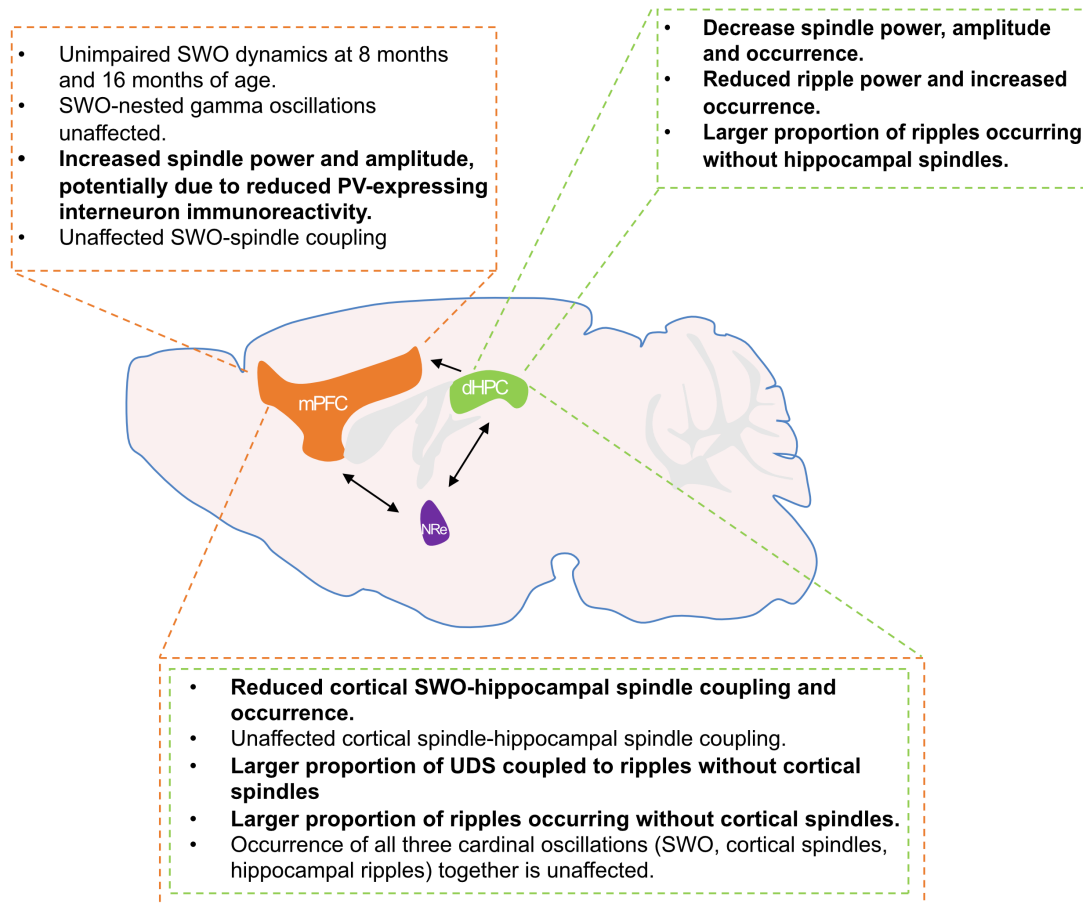


Figure 7.1.1 | Summary of results: mPFC-hippocampal circuit during SWS. Colour coded boxes detail the key findings investigating the oscillations within the corresponding brain regions during SWS in the APP^{NL-G-F} mouse model. The box that has two colours represents the coupling between brain regions. In bold are the impairments identified in APP mice. Image of brain adapted from the Allen Brain Atlas (<https://mouse.brain-map.org/>).

7.1.3 | Key findings investigating hypothesis 2

The work carried out in **Chapter 6** addressed *hypothesis 2*. The hippocampus is crucial for episodic and spatial memory and integrates spatial and non-spatial information processed by anatomically-connected brain regions (Drieu & Zugaro, 2019). Theta oscillations facilitate this integration and can be found coupled to gamma oscillations, which bind neuronal firing into precise temporal windows for information encoding and retrieval (Colgin & Moser, 2010; Buzsaki & Wang, 2012). In the hippocampus, the coupling of gamma to theta oscillations is important for the encoding and retrieval of spatial and episodic information (Tort

et al., 2008; Scheffer-Teixeira *et al.*, 2012; Amemiya & Redish, 2018; Lopes-dos-Santos *et al.*, 2018). Communication between the hippocampus and mPFC through theta oscillations combines spatial information with executive control and is important for spatial working memory and goal-directed spatial navigation (Jones & Wilson, 2005; Tort *et al.*, 2008; Sirota *et al.*, 2008; Tamura *et al.*, 2017). Episodic, spatial and working memory are all subject to decline in AD. Moreover, humans with AD display evidence for disruptions to theta and gamma oscillations as well as their coupling (Adler, Brassens & Jajcevic, 2003; Czigler *et al.*, 2008; Goodman *et al.*, 2018; Murty *et al.*, 2021). Similar impairments can also be found in first-generation mouse models of amyloidopathy (Palop *et al.*, 2007; Ittner *et al.*, 2014; Schneider *et al.*, 2014; Palop & Mucke, 2016; Martinez-Losa *et al.*, 2018; Etter *et al.*, 2019). However, less is known about how the oscillations in this circuit are affected in the APP^{NL-G-F} mouse model, as similarities should not be assumed. Validating prior research conducted in first-generation mouse models is not only important for determining how well second-generation mouse models recapitulate features of human AD pathophysiology, but is a crucial first-step before they can be used to understand the pathological mechanisms underpinning disrupted network activity. Therefore, the oscillatory activity of this circuit was investigated in 16-month APP^{NL-G-F} mice as they explored an OF arena.

The primary outcomes of this research were that disruptions were seen to the local oscillations found in CA1, yet the oscillations found in the mPFC were unaffected and communication between CA1 and the mPFC was only mildly impaired. More specifically, a trending increase in theta power but decrease in the power of slow and fast gamma oscillations were found in CA1. Additionally, theta coherence between regions was found to decline at higher locomotion velocities, potentially suggesting early signs of impaired communication (**Figure 7.1.2**). Overall, this experiment partially confirms the hypothesis that disruptions would be seen to the oscillations involved in spatial working memory in CA1. These results further our understanding of the timeline of network decline in the APP^{NL-G-F} mouse model and provide a basis for which further research investigating the underlying causes can be conducted.

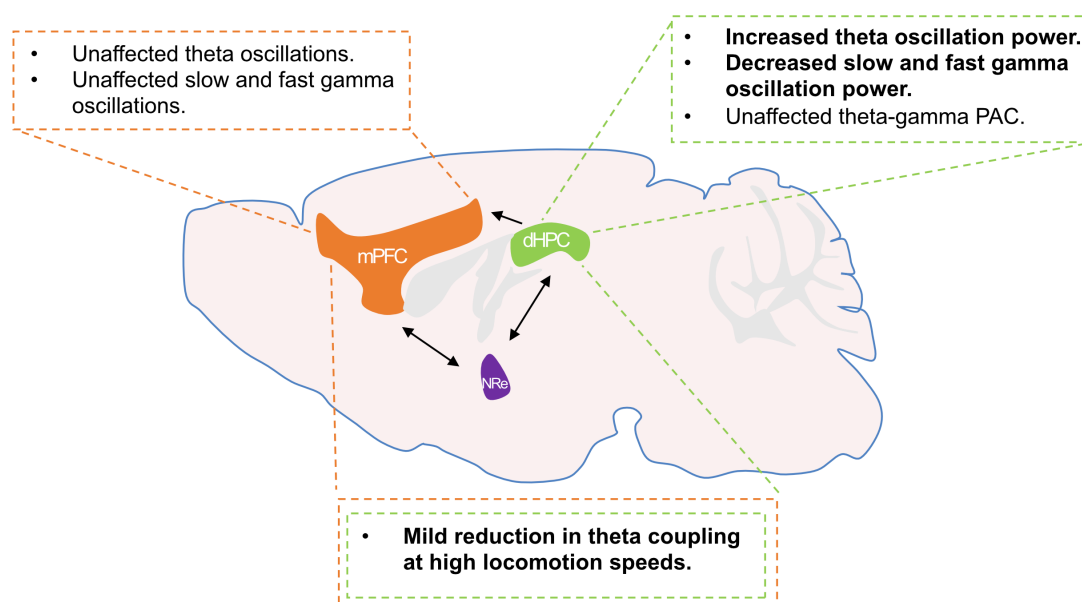


Figure 7.1.2 | Summary of results: mPFC-hippocampal circuit during exploratory behaviour. Colour coded boxes detail the key findings investigating the oscillations within the corresponding brain regions during exploratory behaviour in the APP^{NL-G-F} mouse model. The box that has two colours represents the coupling between brain regions. In bold are the impairments identified in APP mice. Image of brain adapted from the Allen Brain Atlas (<https://mouse.brain-map.org/>).

7.1.4 | Key findings investigating hypothesis 3

The work described in **Chapters 3 and 4** was designed to address *hypothesis 3*. GABAergic inhibitory interneurons are an extremely diverse family of cells that shape the firing of excitatory neurons, generating neuronal oscillations (Pelkey *et al.*, 2017). Evidence for disruptions to the inhibitory control of the brain have already been found in both humans with AD and mouse models of amyloidopathy, causing epileptic discharges and alerted neuronal activity (Busche *et al.*, 2008; Palop & Mucke, 2016). In particular, disruptions have been found to the SWO, gamma and theta oscillations, with particular emphasis on the PV- and SST-expressing interneurons that shape them (Verret *et al.*, 2012; Schneider *et al.*, 2014; Busche *et al.*, 2015; Schmid *et al.*, 2016a; Martinez-Losa *et al.*, 2018; Etter *et al.*, 2019). However, the contribution of disrupted inhibition

to the epileptiform discharges and impaired oscillations already identified in the APP^{NL-G-F} mouse model have not yet been assessed (Nakazono *et al.*, 2017; Johnson *et al.*, 2020; Jun *et al.*, 2020). Therefore, my first aim was to identify any changes in the density or distribution of PV- and SST-expressing interneurons in CA1 and the mPFC, so that this might aid interpretation of electrophysiological data. Furthermore, enhancing the activity of these interneurons has previously shown efficacy in ameliorating deficits to gamma and theta oscillations (Verret *et al.*, 2012; Iaccarino *et al.*, 2016; Martinez-Losa *et al.*, 2018; Chung *et al.*, 2020b; Park *et al.*, 2020). Thus, my second aim was to increase the function of these interneuron populations using chemogenetics (Roth, 2016) and ameliorate the hypothesised disruptions to SWA in the APP^{NL-G-F} mouse model.

These experiments generated several key findings. First, the age-dependant increase in A β ₁₋₄₂ pathology found in this model (Nilsson, Saito & Saido, 2014; Saito *et al.*, 2014) was localised to both CA1 and the sub-regions of the mPFC. Second, an increase of PV-expressing interneuron immunoreactivity was identified in CA1 at 8 months, and a loss was found in the ACC sub-region of the mPFC at 16 months, the latter aiding the interpretation of data from *hypotheses 1*. Third, no deficits to SWA were found in the mPFC at 8 months. Fourth, the use of isoflurane anaesthesia was discovered to be an unreliable model for studying the SWO. Due to the changes in PV-expressing interneuron immunoreactivity, part of the original hypothesis can be confirmed, as these interneurons are affected in the APP^{NL-G-F} mouse model. However, the outcome of these experiments cannot conclusively accept or reject the hypotheses that SST-expressing interneurons are affected in this model and that both PV- and SST-expressing interneurons contribute to disrupted SWA. This was due to the lack of SWA deficits at 8 months of age in APP^{NL-G-F} mice, and the discovery that isoflurane is an unreliable model for investigating the SWO. Nevertheless, these are both novel scientific contributions, and were crucial to informing the experimental design of the research outlined in **Chapter 5** (*hypothesis 1*).

7.1.5 | Summary of new knowledge about the mPFC-hippocampal circuit in the APP^{NL-G-F} mouse model

If the use of second-generation mouse models of familial AD, such as the APP^{NL-G-F} mouse, is to become the standard in AD research (Sasaguri *et al.*, 2017), it is

important to build a timeline of evidence that describes the occurring circuit-level changes as well as their relationship with behaviour. This is essential to enable comparisons with human data, so that the validity of the model in recapitulating the pathophysiology of the disease can be assessed, and also to provide a basis from which researchers can begin using these models to understand the causes of network dysfunction, so that potential treatments may be developed. Taken together, the research outlined in this thesis aids this knowledge generation. First, it furthers our understanding of the circuit-level changes occurring in this model at both 8 and 16 months of age and, along with previously published data, shows a clear progression of decline (Nakazono *et al.*, 2017; Pervolaraki *et al.*, 2019; Jun *et al.*, 2020). Second, it shows that at 16 months, changes to the local circuitry in CA1 and the mPFC are occurring during SWS and awake behaviour, yet long-range communication is relatively unimpaired. Moreover, the changes to the local circuitry appear to be region specific, potentially due to functional differences. Third, the deficits to the neuronal oscillations and the changes in PV-expressing interneuron immunoreactivity allow further hypotheses to be formed and tested to understand the underlying mechanisms of disruption.

7.2 | Limitations of mouse models of Alzheimer's disease

7.2.1 | Limitations of first-generation mouse models

Despite efforts, most potential new disease-modifying medications for the treatment of AD fail to show efficacy in phase 3 clinical trials. This is thought to be due to several reasons, such as the inappropriate timing of medical intervention, shortage of accurate biomarkers and the translational gap that exists between animal models and humans (Sasaguri *et al.*, 2017; Long & Holtzman, 2019). Although animal models of disease exist using several different species, the majority of scientific breakthroughs have occurred in mice (Ashe & Zahs, 2010; Sasaguri *et al.*, 2017). Mouse models of AD are created based on the mutations associated with FAD, typically those occurring on the *APP* and *PSEN1* gene sequence. Humanised versions of these genes, carrying disease-related mutations with expression controlled *via* a variety of different promoters, are over-expressed in first-generation models alongside the endogenous murine version of the genes. Several different first-generation mouse models of Alzheimer's disease exist that utilise different combinations of mutations (Sasaguri *et al.*,

2017). Unfortunately, this strategy of model creation leads to the development of several unwanted over-expression artefacts, such as exacerbated pathology, the expression of mutated genes in cell types that don't typically express the gene, interference with normal cellular gene transcription and increases in pathogenic APP protein fragments other than A β (Nilsson, Saito & Saido, 2014; Saito *et al.*, 2014; Sasaguri *et al.*, 2017).

7.2.2 | Second-generation mouse models

To overcome the limitations of first-generation mouse models, second-generation mouse models have been created that employ a knock-in strategy for model creation (Malthankar-Phatak *et al.*, 2012; Li *et al.*, 2014; Nilsson, Saito & Saido, 2014; Saito *et al.*, 2014). This results in the replacement of endogenous murine gene(s) with humanised versions that incorporate polymorphisms associated with FAD. The APP^{NL-G-F} mouse model used in this thesis is one such second-generation mouse model, which expresses humanised *APP* containing the Swedish (KM670/671**NL**), Beyreuther/Iberian (I716**F**) and Arctic (E693**G**) mutations. Together, these mutations lead to increased production and deposition of A β ₁₋₄₂ protein fragments, which are more prone to aggregation. The same group that generated APP^{NL-G-F} mice also produced two other knock-in models: one containing only the Swedish and Beyreuther/Iberian mutations (APP^{NL-F}) and another containing only the Swedish mutation (APP^{NL}). The latter model was used as a control to demonstrate that the increased production of CTF β and sAPP β by the Swedish mutation does not result in extracellular deposition of A β plaques, at least over the lifespan of a mouse (Nilsson, Saito & Saido, 2014; Saito *et al.*, 2014; Shah *et al.*, 2018). APP^{NL-G-F} mice were found to have an accelerated rate of AD-related pathology compared with APP^{NL-F} mice, suggesting that APP^{NL-G-F} mice are more appropriate for studying the pathogenic effects of increased A β ₁₋₄₂, whereas APP^{NL-F} mice should be used for studying the mechanisms of deposition (Nilsson, Saito & Saido, 2014; Saito *et al.*, 2014; Sasaguri *et al.*, 2017).

There is accumulating evidence of phenotypic similarities between the APP^{NL-G-F} mouse model and human AD, such as extracellular plaques composed of A β ₁₋₄₂ protein fragments, signs of neuroinflammation, synaptic loss (Nilsson, Saito &

Saido, 2014; Saito *et al.*, 2014; De Strooper & Karran, 2016; Hefter *et al.*, 2019), epileptic discharges (Born, 2015; Johnson *et al.*, 2020), sleep-cycle disruptions (Bubu *et al.*, 2017; Maezono *et al.*, 2020) and impairments to neuronal oscillations (Mander *et al.*, 2015a; Nakazono *et al.*, 2017; Jun *et al.*, 2020; Murty *et al.*, 2021). However, like first-generation mouse models, they do not develop NFTs, potentially due to mice not living as long as humans or the lack of a human copy of the *MAPT* gene. However, in people, A β pathology develops for decades before the onset of tau pathology and the acceleration of irreversible neurodegeneration (Hardy & Higgins, 1992; De Strooper & Karran, 2016). Once degeneration and clinical symptoms start to appear, the disease becomes harder to treat, prompting researchers to focus their efforts on the preclinical stages. Therefore, the lack of NFTs and appearance of only mild cognitive impairments lead to the proposal that knock-in mice, such as APP^{NL-G-F} most accurately model the prodromal stages of AD, for the development of early treatment strategies and discovery of novel biomarkers (Sasaguri *et al.*, 2017).

Whether knock-in models, such as APP^{NL-G-F}, are valid models of clinical AD is still being investigated. Behavioural correlates of memory loss are necessary for determining the extent of MCI, yet so far there are discrepancies in the literature regarding memory impairments in the APP^{NL-G-F} mouse model. The study that first characterised this model identified spatial memory impairments in the Y-maze as early as 6 months of age (Nilsson, Saito & Saido, 2014; Saito *et al.*, 2014) that others have failed to replicate (Whyte *et al.*, 2018), potentially due to differences in the environmental enrichment used at different institutions (Bayne, 2018). Additionally, several studies have identified spatial memory impairments from 11 months onwards, yet as discussed in **section 5.3.4**, these studies all use aversive behavioural paradigms, such as contextual fear conditioning, place avoidance and the Morris water maze (Masuda *et al.*, 2016; Latif-Hernandez *et al.*, 2019; Jun *et al.*, 2020; Maezono *et al.*, 2020). Behaviours that carry negative emotional valence are likely to generate strong memories that only partially reflect the nature of memory function, and therefore putative do not represent an accurate depiction of memory decline, in APP^{NL-G-F} mice (McGaugh, 2013). Moreover, the use of inappropriate controls can be found in several studies assessing spatial memory, such as comparisons with other KI models (APP^{NL-F} and APP^{NL}) and non-littermate controls (Masuda *et al.*, 2016; Sakakibara *et al.*, 2018; Latif-

Hernandez *et al.*, 2019; Jacob *et al.*, 2019). Therefore, a more thorough characterisation of memory decline in APP^{NL-G-F} mice is required before it can be considered a valid model of preclinical AD.

Finally, AD is a systems disorder, and therefore has characteristics that extend beyond the expression of protein-based pathologies and associated neuroinflammation (De Strooper & Karran, 2016). It is therefore difficult to recreate the full breadth of phenotypes observed in the human condition in mouse models. Moreover, mouse models are created based on mutations found in FAD. Sporadic AD makes up the majority of AD cases and is associated with a reduction in the clearance of A β , whereas FAD causes an increase in A β deposition (Hardy & Selkoe, 2002). Although the pathological hallmarks are similar between the two forms of AD, it is currently unknown how well current models recreate sporadic AD. However, sporadic AD also has a genetic component; individuals who carry the APOE- ϵ 4 allele (Kim, Basak & Holtzman, 2009) or rare variants of the triggering receptor expressed on myeloid cells 2 (TREM2) gene (Gratuze, Leyns & Holtzman, 2018) have a greater risk of developing AD. Incorporating these variants and alleles into the mouse genome, either in combination with mutated *APP* genes, alone, or with unmutated, humanised *APP* gene sequences, could provide insight into the pathophysiology of sporadic forms of AD (Kim, Basak & Holtzman, 2009; Gratuze, Leyns & Holtzman, 2018). Moreover, different lifestyle and environmental factors accruing over an individual's lifetime can influence their susceptibility for developing sporadic AD (Long & Holtzman, 2019). Not only do mice not live as long, but it is difficult to recreate similar lifestyle factors. Interestingly, cats have been shown to naturally develop AD, potentially due to being exposed to lifestyle and environmental factors similar to humans (Fiock *et al.*, 2020). Nevertheless, second-generation knock-in AD mouse models overcome many of the limitations of first-generation models, and research to date indicates that these second-generation mice broadly exhibit phenotypes similar with human AD. Therefore, knock-in models should be considered the preferred method for studying the effects of pathological amyloid caused by mutations associated with FAD.

7.3 | Broader impact within Alzheimer's disease research

Neuronal oscillations have shown to be important for myriad cognitive tasks and are created through the delicate balance between excitation and inhibition (Buzsáki & Draguhn, 2004). Disruptions to several neuronal oscillations can be found in AD that are thought to occur due to impairments in the inhibitory modulation of neuronal activity, leading to a decline in cognition (Czigler *et al.*, 2008; Mander *et al.*, 2015a; Palop & Mucke, 2016; Murty *et al.*, 2021). Therefore, both interneurons and neuronal oscillations have become attractive targets for potential AD therapies. In first-generation mouse models of amyloidopathy, dysfunctional inhibition has also been shown to lead to disrupted neuronal oscillations and epileptic activity (Busche *et al.*, 2008; Palop & Mucke, 2016). A reduction in the Nav1.1 voltage-gated Na⁺ channel subunit in PV-expressing interneurons has been identified in several first-generation mouse models and is thought to contribute to a decrease in gamma oscillation power (Kim *et al.*, 2007; Verret *et al.*, 2012; Corbett *et al.*, 2013). Over-expressing the Nav1.1 subunit in PV-expressing interneurons was shown to not only ameliorate gamma dysfunction, but improve memory performance in a spatial memory task (Verret *et al.*, 2012; Martinez-Losa *et al.*, 2018). Additionally, the optogenetic activation of both PV- and SST-expressing interneurons has shown efficacy in improving theta and gamma oscillation impairments caused by pathological amyloid (Iaccarino *et al.*, 2016; Chung *et al.*, 2020b; Park *et al.*, 2020). Moreover, disruptions to SWA and epileptic activity can be improved by administering GABA_A receptor agonists (Busche *et al.*, 2008, 2015).

Potentiating neuronal oscillations themselves also offers up therapeutic potential. Dysfunctional SWA in humans precedes cognitive decline in AD and is associated with greater A β burden (Mander *et al.*, 2015a). Potentiating the SWO using tDCS has previously been shown to enhance SWA and improve performance in a declarative memory task (Marshall *et al.*, 2006; Westerberg *et al.*, 2015). Applying this method in AD therefore has the potential to clear A β from the brain as well as improve cognition (Ju *et al.*, 2017; Lee *et al.*, 2020). In fact, stimulating the SWO in a first-generation mouse model of amyloidopathy restored SWA and halted the deposition of plaques (Kastanenka *et al.*, 2017).

Furthermore, driving gamma oscillations in mouse models of amyloidopathy and neurodegeneration using a method called ‘gamma entrainment using sensory stimulation (GENUS)’, such as visual or auditory stimulation, reduced the amount of A β ₁₋₄₂ in the brain, mitigated plaque burden, enhanced microglial activation and shifted neurons into a less degenerative state (Iaccarino *et al.*, 2016; Adaikkan *et al.*, 2019; Martorell *et al.*, 2019).

Given the success of targeting interneurons and oscillations in first-generation mouse models, it is important that findings are validated in second-generation models, as the unwanted over-expressing artefacts produced by first-generation models may confound results (Nilsson, Saito & Saido, 2014; Saito *et al.*, 2014). Encouragingly, previously characterised disruptions to neuronal oscillations and epileptic activity have been reproduced in the APP^{NL-G-F} mouse model (Nakazono *et al.*, 2017; Johnson *et al.*, 2020; Jun *et al.*, 2020). These changes, along with a disrupted spike-time relationship between PCs and gamma oscillations, indicate impaired inhibitory modulation of neuronal activity (Jun *et al.*, 2020). The results from this thesis corroborate and extend these findings by showing disruptions to several neuronal oscillations and changes in PV-expressing interneuron immunoreactivity. Identifying these dysfunctions is an important first-step before experiments can be conducted in an attempt to ameliorate the observed impairments. Given that similar signs of disrupted inhibitory neurotransmission and dysfunctional oscillatory activity are also viewed in the brains of humans with AD (Mander *et al.*, 2015a; Palop & Mucke, 2016; Ambrad Giovannetti & Fuhrmann, 2019; Murty *et al.*, 2021), the success of targeting interneurons and potentiating oscillations in mice may provide therapeutic applications for humans. Stimulating oscillations having the added benefit of being non-invasive, with acoustic entrainment of SWA and GENUS methods having already been tested in humans (Papalambros *et al.*, 2017; Lee *et al.*, 2021). However, better biomarkers of impaired inhibition and changes in oscillatory activity are needed to establish a timeline of disruption so that appropriate timing of intervention can occur.

7.4 | Future directions

The results detailed in this thesis further our understanding of how amyloid pathology contributes to changes in neuronal oscillatory activity in the mPFC-hippocampal circuit. Additionally, they add to the growing body of knowledge about the circuit-level dysfunctions occurring in the APP^{NL-G-F} mouse model. Furthermore, these findings raise questions that are potential areas for future research:

- The changes seen to theta, gamma, spindle and ripple oscillations in CA1 and the mPFC suggest impairments to inhibitory neurotransmission. Given that PV-expressing interneurons are integral in generating these oscillations (Mann, Radcliffe & Paulsen, 2005; Amilhon *et al.*, 2015; Gan *et al.*, 2017; Clemente-Perez *et al.*, 2017a), exhibit immunohistochemical changes (Sanchez-Mejias *et al.*, 2020), and are impaired in first-generation mouse models of amyloidopathy (Verret *et al.*, 2012; Martinez-Losa *et al.*, 2018), they are an attractive candidate for explaining the oscillatory alterations. A combination of field recordings with optogenetic-tagging and single-unit recording of PV-expressing interneurons during SWS and exploratory behaviour will give a clearer indication of how the activity of these interneurons is affected and contributes to the changes in ripples, spindles, theta and gamma oscillations. Moreover, this preparation would allow these interneurons to be optogenetically-activated at these oscillation frequencies, potentially ameliorating deficits.
- Although less integral than PV-expressing interneurons to the generation of theta and gamma oscillations, SST-expressing interneurons spike in a manner phase-locked to these oscillations (Klausberger *et al.*, 2004; Hájos *et al.*, 2004). Additionally, SST-expressing interneurons have also been shown to be affected in both humans with AD and in first-generation mouse models of amyloidopathy (Schmid *et al.*, 2016a; Sanchez-Mejias *et al.*, 2020). Assessing their immunohistochemical profile in APP^{NL-G-F} mice and conducting similar experiments to those detailed above will provide valuable information about whether these interneurons contribute to the observed deficits to theta and gamma oscillations.

- A definitive timeline of behavioural deficits is currently lacking in the APP^{NL-G-F} mouse model. Performing non-aversive behavioural tasks that assess spatial working and long-term memory at different ages will aid in the interpretation of electrophysiological data, better inform future experiments and help determine the validity of this model for clinical AD.
- Finally, the known electrophysiological changes occurring to the mPFC-hippocampal circuit in APP^{NL-G-F} animals occur from ages younger than 12 months, and now 16 months (Nakazono *et al.*, 2017; Jun *et al.*, 2020). To determine how the circuitry changes within that time-frame, longitudinal *in vivo* LFP recordings should be conducted during SWS and exploratory behaviour.

7.5 | Final conclusions

The experiments carried out in this thesis have addressed important questions within the field of AD and provided a valuable platform from which research using the APP^{NL-G-F} mouse model can be continued. Disruptions to key oscillations within the mPFC-hippocampal circuit responsible for systems consolidation and spatial memory were identified, whereas the communication between these brain regions was unaffected. Not only does this further our understanding of how pathological amyloid affects oscillatory activity, but it sheds light on the progression of decline and how it reflects changes in cognition. Moreover, the changes to PV-expressing interneuron immunoreactivity and impaired oscillations provides a basis for which future research can be conducted; to investigate the underlying circuit disruptions and to test methods to ameliorate dysfunctional activity, so that potential therapeutics for AD can be developed.

References

- Adaikkan, C., Middleton, S.J., Marco, A., Boyden, E.S., et al. (2019) Gamma Entrainment Binds Higher-Order Brain Regions and Offers Neuroprotection Article Gamma Entrainment Binds Higher-Order Brain Regions and Offers Neuroprotection. *Neuron*. [Online] 102 (5), 929-943.e8. Available from: doi:10.1016/j.neuron.2019.04.011.
- Adamantidis, A. & Lüthi, A. (2019) Optogenetic Dissection of Sleep-Wake States In Vitro and In Vivo. In: *Handbook of Experimental Pharmacology*. [Online]. Springer New York LLC. pp. 125–151. Available from: doi:10.1007/164_2018_94.
- Adamantidis, A.R., Gutierrez Herrera, C. & Gent, T.C. (2019) Oscillating circuitries in the sleeping brain. *Nature Reviews Neuroscience*. [Online] 20 (December). Available from: doi:10.1038/s41583-019-0223-4.
- Adhikari, A., Topiwala, M.A. & Gordon, J.A. (2010a) Synchronized activity between the ventral hippocampus and the medial prefrontal cortex during anxiety. *Neuron*. [Online] 65 (2), 257. Available from: doi:10.1016/J.NEURON.2009.12.002 [Accessed: 1 September 2021].
- Adhikari, A., Topiwala, M.A. & Gordon, J.A. (2010b) Synchronized activity between the ventral hippocampus and the medial prefrontal cortex during anxiety. *Neuron*. [Online] 65 (2), 257. Available from: doi:10.1016/J.NEURON.2009.12.002 [Accessed: 10 September 2021].
- Adler, G., Brassens, S. & Jajcevic, A. (2003) EEG coherence in Alzheimer's dementia. *Journal of Neural Transmission* 2003 110:9. [Online] 110 (9), 1051–1058. Available from: doi:10.1007/S00702-003-0024-8 [Accessed: 10 September 2021].
- Ahmed, O.J. & Mehta, M.R. (2012) Running speed alters the frequency of hippocampal gamma oscillations. *Journal of Neuroscience*. [Online] 32 (21), 7373–7383. Available from: doi:10.1523/JNEUROSCI.5110-11.2012.
- Ali, F., Baringer, S.L., Neal, A., Choi, E.Y., et al. (2019) Parvalbumin-positive neuron loss and amyloid-beta deposits in the frontal cortex of Alzheimer's disease-related mice. *Journal of Alzheimer's disease : JAD*. [Online] 72 (4), 1323. Available from: doi:10.3233/JAD-181190 [Accessed: 13 August 2021].
- Alperin, N., Wiltshire, J., Lee, S.H., Ramos, A.R., et al. (2019) Effect of sleep quality on amnesic mild cognitive impairment vulnerable brain regions in cognitively normal elderly individuals. *Sleep*. [Online] 42 (3). Available from:

- doi:10.1093/sleep/zsy254 [Accessed: 18 June 2021].
- Ambrad Giovannetti, E. & Fuhrmann, M. (2019) Unsupervised excitation: GABAergic dysfunctions in Alzheimer's disease. *Brain Research*. [Online] 1707, 216–226. Available from: doi:10.1016/J.BRAINRES.2018.11.042 [Accessed: 16 December 2018].
- Amemiya, S. & Redish, A.D. (2018) Hippocampal Theta-Gamma Coupling Reflects State-Dependent Information Processing in Decision Making. *Cell Reports*. [Online] 22 (12), 3328–3338. Available from: doi:10.1016/J.CELREP.2018.02.091 [Accessed: 14 October 2019].
- Amilhon, B., Huh, C.Y.L., Manseau, F., Ducharme, G., et al. (2015) Parvalbumin Interneurons of Hippocampus Tune Population Activity at Theta Frequency. *Neuron*. [Online] 86 (5), 1277–1289. Available from: doi:10.1016/J.NEURON.2015.05.027 [Accessed: 30 June 2019].
- Amzica, F. & Steriade, M. (1998) Electrophysiological correlates of sleep delta waves. *Electroencephalography and Clinical Neurophysiology*. [Online] 107 (2), 69–83. Available from: doi:10.1016/S0013-4694(98)00051-0.
- Antonoudiou, P., Tan, Y.L., Kontou, G., Upton, A.L., et al. (2020) Parvalbumin and Somatostatin Interneurons Contribute to the Generation of Hippocampal Gamma Oscillations. *The Journal of Neuroscience*. [Online] JN-RM-0261-20. Available from: doi:10.1523/JNEUROSCI.0261-20.2020 [Accessed: 1 September 2020].
- Antunes, M. & Biala, G. (2012) The novel object recognition memory: neurobiology, test procedure, and its modifications. *Cognitive Processing*. [Online] 13 (2), 93. Available from: doi:10.1007/S10339-011-0430-Z [Accessed: 16 July 2021].
- Arai, H., Emson, P.C., Mountjoy, C.Q., Carassco, L.H., et al. (1987) Loss of parvalbumin-immunoreactive neurones from cortex in Alzheimer-type dementia. *Brain Research*. [Online] 418 (1), 164–169. Available from: doi:10.1016/0006-8993(87)90974-7.
- Ashe, K.H. & Zahs, K.R. (2010) Probing the biology of Alzheimer's disease in mice. *Neuron*. [Online] 66 (5), 631. Available from: doi:10.1016/J.NEURON.2010.04.031 [Accessed: 17 September 2021].
- Bacci, A., Huguenard, J.R. & Prince, D.A. (2002) Differential modulation of synaptic transmission by neuropeptide Y in rat neocortical neurons. *Proceedings of the National Academy of Sciences of the United States of*

- America*. [Online] 99 (26), 17125–17130. Available from: doi:10.1073/pnas.012481899 [Accessed: 13 April 2018].
- Bakker, A., Krauss, G.L., Albert, M.S., Speck, C.L., et al. (2012) Reduction of Hippocampal Hyperactivity Improves Cognition in Amnestic Mild Cognitive Impairment. *Neuron*. [Online] 74 (3), 467–474. Available from: doi:10.1016/j.neuron.2012.03.023 [Accessed: 22 March 2021].
- Bal, A., Maureira, F. & Arguello, A.A. (2020) SimpylCellCounter: an automated solution for quantifying cells in brain tissue. *Scientific Reports* 2020 10:1. [Online] 10 (1), 1–10. Available from: doi:10.1038/s41598-020-68138-4 [Accessed: 23 August 2021].
- Bartsch, U., Simpkin, A.J., Demanuele, C., Wamsley, E., et al. (2019) Distributed slow-wave dynamics during sleep predict memory consolidation and its impairment in schizophrenia. *npj Schizophrenia*. [Online] 5 (1), 1–11. Available from: doi:10.1038/s41537-019-0086-8 [Accessed: 1 September 2021].
- Bayne, K. (2018) Environmental enrichment and mouse models: Current perspectives. *Animal Models and Experimental Medicine*. [Online] 1 (2), 82. Available from: doi:10.1002/AME2.12015 [Accessed: 27 September 2021].
- Beenhakker, M.P. & Huguenard, J.R. (2009) Neurons that Fire Together Also Conspire Together: Is Normal Sleep Circuitry Hijacked to Generate Epilepsy? *Neuron*. [Online]. 62 (5) pp.612–632. Available from: doi:10.1016/j.neuron.2009.05.015 [Accessed: 2 June 2021].
- Belluscio, M.A., Mizuseki, K., Schmidt, R., Kempster, R., et al. (2012) Cross-frequency phase-phase coupling between theta and gamma oscillations in the hippocampus. *Journal of Neuroscience*. [Online] 32 (2), 423–435. Available from: doi:10.1523/JNEUROSCI.4122-11.2012 [Accessed: 11 May 2021].
- Beltramo, R., D’Urso, G., Dal Maschio, M., Farisello, P., et al. (2013) Layer-specific excitatory circuits differentially control recurrent network dynamics in the neocortex. *Nature Neuroscience*. [Online] 16 (2), 227–234. Available from: doi:10.1038/nn.3306 [Accessed: 3 September 2020].
- Bentham, S.D., Skelin, I., Moseley, S.C., Stimmell, A.C., et al. (2020) Impaired Hippocampal-Cortical Interactions during Sleep in a Mouse Model of Alzheimer’s Disease. *Current Biology*. [Online] 30 (13), 2588-2601.e5. Available from: doi:10.1016/J.CUB.2020.04.087 [Accessed: 16 September

2021].

- Binder, S., Rawohl, J., Born, J. & Marshall, L. (2014) Transcranial slow oscillation stimulation during NREM sleep enhances acquisition of the radial maze task and modulates cortical network activity in rats. *Frontiers in Behavioral Neuroscience*. [Online] 7 (JAN), 220. Available from: doi:10.3389/fnbeh.2013.00220 [Accessed: 1 June 2020].
- Bokil, H., Andrews, P., Kulkarni, J.E., Mehta, S., et al. (2010) Chronux: A Platform for Analyzing Neural Signals. *Journal of neuroscience methods*. [Online] 192 (1), 146. Available from: doi:10.1016/J.JNEUMETH.2010.06.020 [Accessed: 27 August 2021].
- Bonjean, M., Baker, T., Lemieux, M., Timofeev, I., et al. (2011) Corticothalamic feedback controls sleep spindle duration in vivo. *Journal of Neuroscience*. [Online] 31 (25), 9124–9134. Available from: doi:10.1523/JNEUROSCI.0077-11.2011.
- Born, H.A. (2015) Seizures in Alzheimer's disease. *Neuroscience*. [Online]. 286 pp.251–263. Available from: doi:10.1016/j.neuroscience.2014.11.051.
- Boyce, R., Glasgow, S.D., Williams, S. & Adamantidis, A. (2016) Causal evidence for the role of REM sleep theta rhythm in contextual memory consolidation. *Science (New York, N.Y.)*. [Online] 352 (6287), 812–816. Available from: doi:10.1126/science.aad5252 [Accessed: 30 June 2019].
- Braak, H. & Braak, E. (1991) Neuropathological staging of Alzheimer-related changes. *Acta Neuropathol.* [Online]. 82. Available from: <https://link.springer.com/content/pdf/10.1007%2F0308809.pdf> [Accessed: 12 October 2018].
- Braak, H. & Del Tredici, K. (2011) The pathological process underlying Alzheimer's disease in individuals under thirty. *Acta Neuropathologica*. [Online] 121 (2), 171–181. Available from: doi:10.1007/s00401-010-0789-4 [Accessed: 15 June 2021].
- Brady, D.R. & Mufson, E.J. (1997) Parvalbumin-immunoreactive neurons in the hippocampal formation of Alzheimer's diseased brain. *Neuroscience*. [Online] 80 (4), 1113–1125. Available from: doi:10.1016/S0306-4522(97)00068-7.
- Brioni, J.D., Decker, M.W., Gamboa, L.P., Izquierdo, I., et al. (1990) Muscimol injections in the medial septum impair spatial learning. *Brain Research*. [Online] 522 (2), 227–234. Available from: doi:10.1016/0006-

8993(90)91465-S.

- Brown, R., Lam, A.D., Gonzalez-Sulser, A., Ying, A., et al. (2018) Circadian and brain state modulation of network hyperexcitability in Alzheimer's disease. *eNeuro*. [Online] 5 (2), 426–443. Available from: doi:10.1523/ENEURO.0426-17.2018 [Accessed: 11 May 2021].
- Bubu, O., Brannick, M., Mortimer, J., Umasabor-Bubu, O., et al. (2017) Sleep, Cognitive impairment, and Alzheimer's disease: A Systematic Review and Meta-Analysis. *Sleep*. [Online]. 40 (1) pp.1–18. Available from: <http://dx.doi.org/10.1093/sleep/> [Accessed: 18 June 2021].
- Bukhtiyarova, O., Soltani, S., Chauvette, S. & Timofeev, I. (2019) Slow wave detection in sleeping mice: Comparison of traditional and machine learning methods. *Journal of Neuroscience Methods*. [Online] 316, 35–45. Available from: doi:10.1016/j.jneumeth.2018.08.016.
- Busche, M.A., Chen, X., Henning, H.A., Reichwald, J., et al. (2012) Critical role of soluble amyloid- β for early hippocampal hyperactivity in a mouse model of Alzheimer's disease. *PNAS*. [Online] 109 (22), 8740–8745. Available from: doi:10.1073/pnas.1206171109 [Accessed: 5 September 2018].
- Busche, M.A., Eichhoff, G., Adelsberger, H., Abramowski, D., et al. (2008) Clusters of Hyperactive neurons Near Amyloid Plaques in a mouse model of Alzheimer's disease. *Science*. [Online] 321, 1686–1689. Available from: <http://www.ncbi.nlm.nih.gov/pubmed/12702875> [Accessed: 13 November 2017].
- Busche, M.A., Kekuš, M., Adelsberger, H., Noda, T., et al. (2015) Rescue of long-range circuit dysfunction in Alzheimer's disease models. *Nature neuroscience*. [Online] 18 (11), 1623–1630. Available from: doi:10.1038/nn.4137.
- Buzsáki, G. (2015) Hippocampal sharp wave-ripple: A cognitive biomarker for episodic memory and planning. *Hippocampus*. [Online] 25 (10), 1073–1188. Available from: doi:10.1002/hipo.22488 [Accessed: 27 October 2018].
- Buzsáki, G. (1986) Hippocampal sharp waves: Their origin and significance. *Brain Research*. [Online] 398 (2), 242–252. Available from: doi:10.1016/0006-8993(86)91483-6.
- Buzsáki, G. (2002) Theta Oscillations in the Hippocampus. *Neuron*. [Online] 33 (3), 325–340. Available from: doi:10.1016/S0896-6273(02)00586-X

- [Accessed: 24 September 2019].
- Buzsáki, G., Anastassiou, C.A. & Koch, C. (2012) The origin of extracellular fields and currents--EEG, ECoG, LFP and spikes. *Nature reviews. Neuroscience*. [Online] 13 (6), 407–420. Available from: doi:10.1038/nrn3241 [Accessed: 22 February 2018].
- Buzsáki, G. & Draguhn, A. (2004) Neuronal oscillations in cortical networks. *Science (New York, N.Y.)*. [Online] 304 (5679), 1926–1929. Available from: doi:10.1126/science.1099745 [Accessed: 12 November 2018].
- Buzsáki, G., Haas, H.L. & Anderson, E.G. (1987) Long-term potentiation induced by physiologically relevant stimulus patterns. *Brain Research*. [Online] 435 (1–2), 331–333. Available from: doi:10.1016/0006-8993(87)91618-0.
- Buzsáki, G., Horvath, Z., Urioste, R., Hetke, J., et al. (1992) High-Frequency Network Oscillation in the Hippocampus. *Science*. [Online] 256, 1025–1027. Available from: <http://science.sciencemag.org/> [Accessed: 24 June 2019].
- Buzsáki, G., Lai-Wo S., L. & Vanderwolf, C.H. (1983) Cellular bases of hippocampal EEG in the behaving rat. *Brain Research Reviews*. [Online]. 6 (2) pp.139–171. Available from: doi:10.1016/0165-0173(83)90037-1 [Accessed: 7 June 2021].
- Buzsáki, G., Logothetis, N. & Singer, W. (2013) Scaling brain size, keeping timing: Evolutionary preservation of brain rhythms. *Neuron*. [Online]. 80 (3) pp.751–764. Available from: doi:10.1016/j.neuron.2013.10.002 [Accessed: 30 June 2021].
- Buzsáki, G. & Wang, X.-J. (2012) Mechanisms of Gamma Oscillations. *Annual review of neuroscience*. [Online] 6 (9), 2166–2171. Available from: doi:10.1021/nl061786n.Core-Shell.
- Caccavano, A., Bozzelli, P.L., Forcelli, P.A., Pak, D.T.S., et al. (2020) Inhibitory Parvalbumin Basket Cell Activity is Selectively Reduced during Hippocampal Sharp Wave Ripples in a Mouse Model of Familial Alzheimer’s Disease. *Journal of Neuroscience*. [Online] 40 (26), 5116–5136. Available from: doi:10.1523/JNEUROSCI.0425-20.2020 [Accessed: 16 July 2021].
- Caillard, O., Moreno, H., Schwaller, B., Llano, I., et al. (2000) Role of the calcium-binding protein parvalbumin in short-term synaptic plasticity.

- Proceedings of the National Academy of Sciences*. [Online] 97 (24), 13372–13377. Available from: doi:10.1073/PNAS.230362997 [Accessed: 23 August 2021].
- Canolty, R.T., Edwards, E., Dalal, S.S., Soltani, M., et al. (2006) High Gamma Power Is Phase-Locked to Theta Oscillations in Human Neocortex. *Science*. [Online] 313 (5793), 1626–1628. Available from: doi:10.1126/SCIENCE.1128115 [Accessed: 27 August 2021].
- Canolty, R.T. & Knight, R.T. (2010) The functional role of cross-frequency coupling. *Trends in cognitive sciences*. [Online] 14 (11), 506–515. Available from: doi:10.1016/j.tics.2010.09.001 [Accessed: 1 October 2019].
- Caporale, N. & Dan, Y. (2008) Spike timing-dependent plasticity: A Hebbian learning rule. *Annual Review of Neuroscience*. [Online]. 31 pp.25–46. Available from: doi:10.1146/annurev.neuro.31.060407.125639 [Accessed: 26 May 2021].
- Castano-Prat, P., Perez-Mendez, L., Perez-Zabalza, M., Sanfeliu, C., et al. (2019) Altered slow (δ1 Hz) and fast (beta and gamma) neocortical oscillations in the 3xTg-AD mouse model of Alzheimer’s disease under anesthesia. *Neurobiology of Aging*. [Online] 79, 142–151. Available from: doi:10.1016/j.neurobiolaging.2019.02.009 [Accessed: 24 May 2019].
- Cattaud, V., Bezzina, C., Rey, C.C., Lejards, C., et al. (2018) Early disruption of parvalbumin expression and perineuronal nets in the hippocampus of the Tg2576 mouse model of Alzheimer’s disease can be rescued by enriched environment. *Neurobiology of Aging*. [Online] 72, 147–158. Available from: doi:10.1016/J.NEUROBIOLAGING.2018.08.024.
- Cedernaes, J., Osorio, R.S., Varga, A.W., Kam, K., et al. (2017) Candidate mechanisms underlying the association between sleep-wake disruptions and Alzheimer’s disease. *Sleep Medicine Reviews*. [Online] 31, 102–111. Available from: doi:10.1016/j.smr.2016.02.002 [Accessed: 23 January 2018].
- Cellini, N. (2017) Memory consolidation in sleep disorders. *Sleep Medicine Reviews*. [Online]. 35 pp.101–112. Available from: doi:10.1016/j.smr.2016.09.003.
- Chauvette, S., Crochet, S., Volgushev, M. & Timofeev, I. (2011) Properties of slow oscillation during slow-wave sleep and anesthesia in cats. *The Journal of neuroscience*. [Online] 31 (42), 14998–15008. Available from:

- doi:10.1523/JNEUROSCI.2339-11.2011 [Accessed: 13 November 2018].
- Chauvette, S., Seigneur, J. & Timofeev, I. (2012) Sleep oscillations in the thalamocortical system induce long-term neuronal plasticity. *Neuron*. [Online] 75 (6), 1105–1113. Available from: doi:10.1016/j.neuron.2012.08.034 [Accessed: 16 December 2018].
- Chauvette, S., Volgushev, M. & Timofeev, I. (2010) Origin of Active States in Local Neocortical Networks during Slow Sleep Oscillation. *Cerebral Cortex*. [Online] 20, 2660–2674. Available from: doi:10.1093/cercor/bhq009 [Accessed: 13 December 2017].
- Chen, J.-Y., Chauvette, S., Skorheim, S., Timofeev, I., et al. (2012) Interneuron-mediated inhibition synchronizes neuronal activity during slow oscillation. *The Journal of Physiology*. [Online] 590 (16), 3987–4010. Available from: doi:10.1113/jphysiol.2012.227462 [Accessed: 1 June 2020].
- Chen, X., Choo, H., Huang, X.-P., Yang, X., et al. (2015) The First Structure–Activity Relationship Studies for Designer Receptors Exclusively Activated by Designer Drugs. *ACS Chemical Neuroscience*. [Online] 6 (3), 476. Available from: doi:10.1021/CN500325V [Accessed: 22 September 2021].
- Chen, Z., Resnik, E., McFarland, J.M., Sakmann, B., et al. (2011) Speed Controls the Amplitude and Timing of the Hippocampal Gamma Rhythm. *PLOS ONE*. [Online] 6 (6), e21408. Available from: doi:10.1371/JOURNAL.PONE.0021408 [Accessed: 10 September 2021].
- Chávez-Gutiérrez, L., Bammens, L., Benilova, I., Vandersteen, A., et al. (2012) The mechanism of γ -Secretase dysfunction in familial Alzheimer disease. *EMBO Journal*. [Online] 31 (10), 2261–2274. Available from: doi:10.1038/emboj.2012.79 [Accessed: 16 June 2021].
- Chittajallu, R., Wester, J.C., Craig, M.T., Barksdale, E., et al. (2017) Afferent specific role of NMDA receptors for the circuit integration of hippocampal neurogliaform cells. *Nature Communications 2017 8:1*. [Online] 8 (1), 1–13. Available from: doi:10.1038/s41467-017-00218-y [Accessed: 22 September 2021].
- Chrobak, J.J. & Buzsáki, G. (1998) Gamma oscillations in the entorhinal cortex of the freely behaving rat. *Journal of Neuroscience*. [Online] 18 (1), 388–398. Available from: doi:10.1523/jneurosci.18-01-00388.1998 [Accessed: 1 July 2021].
- Chung, H., Park, K., Jang, H.J., Kohl, M.M., et al. (2020a) Dissociation of

- somatostatin and parvalbumin interneurons circuit dysfunctions underlying hippocampal theta and gamma oscillations impaired by amyloid β oligomers in vivo. *Brain Structure and Function*. [Online] 225 (3), 935–954. Available from: doi:10.1007/S00429-020-02044-3 [Accessed: 21 July 2021].
- Chung, H., Park, K., Jang, H.J., Kohl, M.M., et al. (2020b) Dissociation of somatostatin and parvalbumin interneurons circuit dysfunctions underlying hippocampal theta and gamma oscillations impaired by amyloid β oligomers in vivo. *Brain Structure and Function*. [Online] 225 (3), 935–954. Available from: doi:10.1007/s00429-020-02044-3 [Accessed: 28 September 2020].
- Clemens, Z., Molle, M., Eross, L., Barsi, P., et al. (2007) Temporal coupling of parahippocampal ripples, sleep spindles and slow oscillations in humans. *Brain*. [Online] 130 (11), 2868–2878. Available from: doi:10.1093/brain/awm146 [Accessed: 18 January 2021].
- Clemente-Perez, A., Makinson, S.R., Higashikubo, B., Brovarney, S., et al. (2017a) Distinct Thalamic Reticular Cell Types Differentially Modulate Normal and Pathological Cortical Rhythms. *Cell Reports*. [Online] 19 (10), 2130–2142. Available from: doi:10.1016/j.celrep.2017.05.044 [Accessed: 9 February 2021].
- Clemente-Perez, A., Makinson, S.R., Higashikubo, B., Szló, L., et al. (2017b) Distinct Thalamic Reticular Cell Types Differentially Modulate Normal and Pathological Cortical Rhythms. *Cell Reports*. [Online] 19, 2130–2142. Available from: doi:10.1016/j.celrep.2017.05.044 [Accessed: 5 July 2018].
- Colgin, L.L., Denninger, T., Fyhn, M., Hafting, T., et al. (2009) Frequency of gamma oscillations routes flow of information in the hippocampus. *Nature*. [Online] 462 (7271), 353–357. Available from: doi:10.1038/nature08573 [Accessed: 23 September 2020].
- Colgin, L.L. & Moser, E.I. (2010) Gamma Oscillations in the Hippocampus. *Physiology*. [Online] 25 (5), 319–329. Available from: doi:10.1152/physiol.00021.2010 [Accessed: 24 September 2019].
- Collin, T., Chat, M., Lucas, M.G., Moreno, H., et al. (2005) Developmental Changes in Parvalbumin Regulate Presynaptic Ca^{2+} Signaling. *The Journal of Neuroscience*. [Online] 25 (1), 96. Available from: doi:10.1523/JNEUROSCI.3748-04.2005 [Accessed: 23 August 2021].

- Contreras, D., Destexhe, A., Sejnowski, T.J. & Steriade, M. (1996) Control of spatiotemporal coherence of a thalamic oscillation by corticothalamic feedback. *Science*. [Online] 274 (5288), 771–774. Available from: doi:10.1126/science.274.5288.771 [Accessed: 2 June 2021].
- Contreras, D. & Steriade, M. (1995) Cellular basis of EEG slow rhythms: A study of dynamic corticothalamic relationships. *Journal of Neuroscience*. [Online] 15 (1 II), 604–622. Available from: doi:10.1523/jneurosci.15-01-00604.1995.
- Contreras, D. & Steriade, M. (1996) Spindle oscillation in cats: the role of corticothalamic feedback in a thalamically generated rhythm. *Journal of Physiology*. [Online] 490 (1), 159–179. Available from: <https://www.ncbi.nlm.nih.gov/pmc/articles/PMC1158654/pdf/jphysiol00300-0155.pdf> [Accessed: 5 January 2018].
- Corbett, B.F., Leiser, S.C., Ling, H.-P., Nagy, R., et al. (2013) Sodium Channel Cleavage Is Associated with Aberrant Neuronal Activity and Cognitive Deficits in a Mouse Model of Alzheimer’s Disease. *Journal of Neuroscience*. [Online] 33 (16), 7020–7026. Available from: doi:10.1523/JNEUROSCI.2325-12.2013 [Accessed: 18 September 2021].
- Coulon, P., Budde, T. & Pape, H.C. (2012) The sleep relay-the role of the thalamus in central and decentral sleep regulation. *Pflugers Archiv European Journal of Physiology*. [Online]. 463 (1) pp.53–71. Available from: doi:10.1007/s00424-011-1014-6 [Accessed: 2 June 2021].
- Craig, M.T., Mayne, E.W., Bettler, B., Paulsen, O., et al. (2013) Distinct roles of GABAB1a- and GABAB1b-containing GABAB receptors in spontaneous and evoked termination of persistent cortical activity. *The Journal of physiology*. [Online] 591 (Pt 4), 835–843. Available from: doi:10.1113/jphysiol.2012.248088.
- Craig, M.T. & McBain, C.J. (2015) Fast gamma oscillations are generated intrinsically in CA1 without the involvement of fast-spiking basket cells. *The Journal of neuroscience : the official journal of the Society for Neuroscience*. [Online] 35 (8), 3616–3624. Available from: doi:10.1523/JNEUROSCI.4166-14.2015 [Accessed: 10 October 2019].
- Craig MT, M.C. (2014) The emerging role of GABAB receptors as regulators of network dynamics: fast actions from a ‘slow’ receptor? *Current opinion in neurobiology*. [Online] 36, 15–21. Available from:

doi:10.1124/dmd.107.016501.CYP3A4-Mediated.

- Cruikshank, S.J., Landisman, C.E., Mancilla, J.G. & Connors, B.W. (2005) Connexon connexions in the thalamocortical system. In: *Progress in Brain Research*. [Online]. 1 January 2005 Elsevier. pp. 41–57. Available from: doi:10.1016/S0079-6123(05)49004-4.
- Crunelli, V. & Hughes, S.W. (2010a) The slow (<1 Hz) rhythm of non-REM sleep: a dialogue between three cardinal oscillators. *Nature Neuroscience*. [Online] 13 (1). Available from: doi:10.1038/nn.2445 [Accessed: 3 October 2017].
- Crunelli, V. & Hughes, S.W. (2010b) The slow (<1 Hz) rhythm of non-REM sleep: a dialogue between three cardinal oscillators. *Nature Neuroscience*. [Online] 13 (1), 9–17. Available from: doi:10.1038/nn.2445 [Accessed: 14 February 2018].
- Csicsvari, J., Hirase, H., Mamiya, A. & Buzsáki, G. (2000) Ensemble patterns of hippocampal CA3-CA1 neurons during sharp wave-associated population events. *Neuron*. [Online] 28 (2), 585–594. Available from: doi:10.1016/S0896-6273(00)00135-5.
- Czigler, B., Csikós, D., Hidasi, Z., Anna Gaál, Z., et al. (2008) Quantitative EEG in early Alzheimer's disease patients — Power spectrum and complexity features. *International Journal of Psychophysiology*. [Online] 68 (1), 75–80. Available from: doi:10.1016/J.IJPSYCHO.2007.11.002.
- Dasilva, M., Camassa, A., Navarro-Guzman, A., Pazienti, A., et al. (2021) Modulation of cortical slow oscillations and complexity across anesthesia levels. *NeuroImage*. [Online] 224, 117415. Available from: doi:10.1016/j.neuroimage.2020.117415.
- Dauwels, J., Srinivasan, K., Reddy, M.R., Musha, T., et al. (2011) Slowing and Loss of Complexity in Alzheimer's EEG: Two Sides of the Same Coin? *International Journal of Alzheimer's Disease*. [Online] 2011, 1–10. Available from: /pmc/articles/PMC3090755/ [Accessed: 27 September 2021].
- David, F., Schmiedt, J.T., Taylor, H.L., Orban, G., et al. (2013) Essential thalamic contribution to slow waves of natural sleep. *The Journal of Neuroscience*. [Online] 33 (50), 19599–19610. Available from: doi:10.1523/JNEUROSCI.3169-13.2013 [Accessed: 28 September 2018].
- Delevich, K., Tucciarone, J., Huang, Z.J. & Li, B. (2015) The mediodorsal thalamus drives feedforward inhibition in the anterior cingulate cortex via

- parvalbumin interneurons. *Journal of Neuroscience*. [Online] 35 (14), 5743–5753. Available from: doi:10.1523/JNEUROSCI.4565-14.2015 [Accessed: 21 June 2018].
- Denninger, J.K., Smith, B.M. & Kirby, E.D. (2018) Novel Object Recognition and Object Location Behavioral Testing in Mice on a Budget. *Journal of visualized experiments : JoVE*. [Online] 2018 (141). Available from: doi:10.3791/58593 [Accessed: 1 September 2021].
- Destexhe, A., Hughes, S.W., Rudolph, M. & Crunelli, V. (2007) Are corticothalamic UP states fragments of wakefulness? *Trends in Neurosciences*. [Online] 30 (7), 334–342. Available from: doi:10.1016/j.tins.2007.04.006 [Accessed: 26 September 2017].
- Diba, K. & Buzsáki, G. (2007) Forward and reverse hippocampal place-cell sequences during ripples. *Nature Neuroscience*. [Online] 10 (10), 1241–1242. Available from: doi:10.1038/nn1961 [Accessed: 7 June 2021].
- Diekelmann, S. & Born, J. (2010) The memory function of sleep. *Nature Reviews Neuroscience*. [Online] 11 (2), 114–126. Available from: doi:10.1038/nrn2762 [Accessed: 30 June 2019].
- Doi, A., Mizuno, M., Katafuchi, T., Furue, H., et al. (2007) Slow oscillation of membrane currents mediated by glutamatergic inputs of rat somatosensory cortical neurons: in vivo patch-clamp analysis. *European Journal of Neuroscience*. [Online] 26 (9), 2565–2575. Available from: doi:10.1111/J.1460-9568.2007.05885.X [Accessed: 23 July 2021].
- Dolleman-Van Der Weel, M.J., Griffin, A.L., Ito, H.T., Shapiro, M.L., et al. (2019) The nucleus reuniens of the thalamus sits at the nexus of a hippocampus and medial prefrontal cortex circuit enabling memory and behavior. *Learning and Memory*. [Online]. 26 (7) pp.191–205. Available from: doi:10.1101/lm.048389.118 [Accessed: 19 January 2021].
- Dolleman-van der Weel, M.J., Lopes da Silva, F.H. & Witter, M.P. (2017) Interaction of nucleus reuniens and entorhinal cortex projections in hippocampal field CA1 of the rat. *Brain Structure and Function*. [Online] 222 (5), 2421–2438. Available from: doi:10.1007/s00429-016-1350-6 [Accessed: 4 July 2021].
- Dong, X., Wang, V. & Ikemoto, X.S. (2016) Coordinated Interaction between Hippocampal Sharp-Wave Ripples and Anterior Cingulate Unit Activity. *Journal of Neuroscience*. [Online] 36 (41), 10663–10672. Available from:

- doi:10.1523/JNEUROSCI.1042-16.2016 [Accessed: 2 May 2019].
- Drieu, C. & Zugaro, M. (2019) Hippocampal sequences during exploration: Mechanisms and functions. *Frontiers in Cellular Neuroscience*. [Online]. 13 p.232. Available from: doi:10.3389/fncel.2019.00232.
- Dumont, M., Strazielle, C., Staufenbiel, M. & Lalonde, R. (2004) Spatial learning and exploration of environmental stimuli in 24-month-old female APP23 transgenic mice with the Swedish mutation. *Brain Research*. [Online] 1024 (1–2), 113–121. Available from: doi:10.1016/J.BRAINRES.2004.07.052.
- Duyckaerts, C., Delatour, B. & Potier, M.C. (2009) Classification and basic pathology of Alzheimer disease. *Acta Neuropathologica*. [Online]. 118 (1) pp.5–36. Available from: doi:10.1007/s00401-009-0532-1 [Accessed: 16 June 2021].
- Ellender, T.J., Nissen, W., Colgin, L.L., Mann, E.O., et al. (2010) Priming of hippocampal population bursts by individual perisomatic- targeting interneurons. *Journal of Neuroscience*. [Online] 30 (17), 5979–5991. Available from: doi:10.1523/JNEUROSCI.3962-09.2010 [Accessed: 18 March 2021].
- Ennaceur, A. (2010) One-trial object recognition in rats and mice: Methodological and theoretical issues. *Behavioural Brain Research*. [Online] 215 (2), 244–254. Available from: doi:10.1016/J.BBR.2009.12.036.
- Van Erum, J., Van Dam, D. & De Deyn, P.P. (2018) Sleep and Alzheimer's disease: A pivotal role for the suprachiasmatic nucleus. *Sleep Medicine Reviews*. [Online]. 40 pp.17–27. Available from: doi:10.1016/j.smrv.2017.07.005.
- Eschenko, O., Magri, C., Panzeri, S. & Sara, S.J. (2012) Noradrenergic neurons of the locus coeruleus are phase locked to cortical up-down states during sleep. *Cerebral Cortex*. [Online] 22 (2), 426–435. Available from: doi:10.1093/cercor/bhr121 [Accessed: 1 September 2020].
- Etter, G., van der Veldt, S., Manseau, F., Zarrinkoub, I., et al. (2019) Optogenetic gamma stimulation rescues memory impairments in an Alzheimer's disease mouse model. *Nature Communications*. [Online] 10 (1), 1–11. Available from: doi:10.1038/s41467-019-13260-9.
- Fanselow, E.E. & Connors, B.W. (2010) The Roles of Somatostatin-Expressing (GIN) and Fast-Spiking Inhibitory Interneurons in UP-DOWN States of Mouse Neocortex. *J Neurophysiol*. [Online] 104, 596–606. Available from:

- doi:10.1152/jn.00206.2010 [Accessed: 29 September 2017].
- Fanselow, E.E., Richardson, K.A. & Connors, B.W. (2008) Selective, State-Dependent Activation of Somatostatin-Expressing Inhibitory Interneurons in Mouse Neocortex. *Journal of Neurophysiology*. [Online] 100 (5), 2640–2652. Available from: doi:10.1152/jn.90691.2008 [Accessed: 23 November 2018].
- Fanselow, M.S. & Dong, H.-W. (2010) Are The Dorsal and Ventral Hippocampus functionally distinct structures? *Neuron*. [Online] 65 (1), 7. Available from: doi:10.1016/J.NEURON.2009.11.031 [Accessed: 19 July 2021].
- Fiock, K.L., Smith, J.D., Crary, J.F. & Hefti, M.M. (2020) β -amyloid and Tau Pathology in the Aging Feline Brain. *The Journal of comparative neurology*. [Online] 528 (1), 108. Available from: doi:10.1002/CNE.24741 [Accessed: 27 September 2021].
- Flores-Martínez, E. & Penã-Ortega, F. (2017) Amyloid β Peptide-Induced Changes in Prefrontal Cortex Activity and Its Response to Hippocampal Input. *International Journal of Peptides*. [Online] 2017. Available from: doi:10.1155/2017/7386809.
- Foster, D.J. & Wilson, M.A. (2006) Reverse replay of behavioural sequences in hippocampal place cells during the awake state. *Nature*. [Online] 440 (7084), 680–683. Available from: doi:10.1038/nature04587 [Accessed: 7 June 2021].
- Frauscher, B., Bernasconi, N., Caldarou, B., von Ellenrieder, N., et al. (2015) Interictal Hippocampal Spiking Influences the Occurrence of Hippocampal Sleep Spindles. *Sleep*. [Online] 38 (12), 1927–1933. Available from: doi:10.5665/SLEEP.5242 [Accessed: 21 February 2022].
- Freund, T.F. & Antal, M. (1988) GABA-containing neurons in the septum control inhibitory interneurons in the hippocampus. *Nature*. [Online] 336 (6195), 170–173. Available from: doi:10.1038/336170a0 [Accessed: 30 June 2021].
- Fuentealba, P. & Steriade, M. (2005) The reticular nucleus revisited: Intrinsic and network properties of a thalamic pacemaker. *Progress in Neurobiology*. [Online]. 75 (2) pp.125–141. Available from: doi:10.1016/j.pneurobio.2005.01.002.
- Fuentealba, P., Timofeev, I. & Steriade, M. (2004) Prolonged hyperpolarizing potentials precede spindle oscillations in the thalamic reticular nucleus.

- Proceedings of the National Academy of Sciences of the United States of America*. [Online] 101 (26), 9816–9821. Available from: doi:10.1073/pnas.0402761101 [Accessed: 2 June 2021].
- Fuhrmann, F., Justus, D., Sosulina, L., Kaneko, H., et al. (2015) Locomotion, Theta Oscillations, and the Speed-Related Firing of Hippocampal Neurons Are Controlled by a Medial Septal Glutamatergic Circuit. *Neuron*. [Online] 86 (5), 1253–1264. Available from: doi:10.1016/j.neuron.2015.05.001.
- Fukuda, T. & Kosaka, T. (2000) Gap junctions linking the dendritic network of GABAergic interneurons in the hippocampus. *Journal of Neuroscience*. [Online] 20 (4), 1519–1528. Available from: doi:10.1523/jneurosci.20-04-01519.2000 [Accessed: 7 June 2021].
- Funk, C.M., Peelman, K., Bellesi, M., Marshall, W., et al. (2017) Role of somatostatin-positive cortical interneurons in the generation of sleep slow waves. *J. Neurosci.* [Online] 10 (1523), 1303–1317. Available from: doi:10.1523/JNEUROSCI.1303-17.2017 [Accessed: 25 September 2017].
- Games, D., Adams, D., Alessandrini, R., Barbour, R., et al. (1995) Alzheimer-type neuropathology in transgenic mice overexpressing V717F β -amyloid precursor protein. *Nature* 1995 373:6514. [Online] 373 (6514), 523–527. Available from: doi:10.1038/373523a0 [Accessed: 26 July 2021].
- Gan, J., Weng, S. ming, Pernía-Andrade, A.J., Csicsvari, J., et al. (2017) Phase-Locked Inhibition, but Not Excitation, Underlies Hippocampal Ripple Oscillations in Awake Mice In Vivo. *Neuron*. [Online] 93 (2), 308–314. Available from: doi:10.1016/j.neuron.2016.12.018 [Accessed: 11 June 2021].
- Gardner, R.J., Hughes, S.W. & Jones, M.W. (2013) Differential spike timing and phase dynamics of reticular thalamic and prefrontal cortical neuronal populations during sleep spindles. *Journal of Neuroscience*. [Online] 33 (47), 18469–18480. Available from: doi:10.1523/JNEUROSCI.2197-13.2013 [Accessed: 22 March 2021].
- Gargiulo, S., Greco, A., Gramanzini, M., Esposito, S., et al. (2012) Mice Anesthesia, Analgesia, and Care, Part I: Anesthetic Considerations in Preclinical Research. *ILAR Journal*. [Online] 53 (1), E55–E69. Available from: doi:10.1093/ILAR.53.1.55 [Accessed: 28 July 2021].
- Gent, T.C., Bandarabadi, M., Herrera, C.G. & Adamantidis, A.R. (2018)

- Thalamic dual control of sleep and wakefulness. *Nature Neuroscience*. [Online] 21, 974–984. Available from: doi:10.1038/s41593-018-0164-7 [Accessed: 13 June 2018].
- Giesers, N.K. & Wirths, O. (2020) Loss of Hippocampal Calretinin and Parvalbumin Interneurons in the 5XFAD Mouse Model of Alzheimer’s Disease: <https://doi.org/10.1177/1759091420925356>. [Online] 12. Available from: doi:10.1177/1759091420925356 [Accessed: 13 August 2021].
- Girardeau, G., Benchenane, K., Wiener, S.I., Buzsáki, G., et al. (2009) Selective suppression of hippocampal ripples impairs spatial memory. *Nature Neuroscience*. [Online] 12 (10), 1222–1223. Available from: doi:10.1038/nn.2384 [Accessed: 4 July 2021].
- Girardeau, G. & Zugaro, M. (2011) Hippocampal ripples and memory consolidation. *Current Opinion in Neurobiology*. [Online]. 21 (3) pp.452–459. Available from: doi:10.1016/j.conb.2011.02.005.
- Gomez, J.L., Bonaventura, J., Lesniak, W., Mathews, W.B., et al. (2017) Chemogenetics revealed: DREADD occupancy and activation via converted clozapine. *Science*. [Online] 357 (503–507). Available from: <http://science.sciencemag.org/content/sci/357/6350/503.full.pdf> [Accessed: 26 February 2018].
- González-Rueda, A., Pedrosa, V., Feord, R.C., Clopath, C., et al. (2018) Activity-Dependent Downscaling of Subthreshold Synaptic Inputs during Slow-Wave-Sleep-like Activity In Vivo. *Neuron*. [Online] 97 (6), 1244–1252.e5. Available from: doi:10.1016/j.neuron.2018.01.047 [Accessed: 10 April 2018].
- Goodman, M.S., Kumar, S., Zomorodi, R., Ghazala, Z., et al. (2018) Theta-Gamma Coupling and Working Memory in Alzheimer’s Dementia and Mild Cognitive Impairment. *Frontiers in Aging Neuroscience*. [Online] 10 (APR), 101. Available from: doi:10.3389/fnagi.2018.00101 [Accessed: 23 September 2020].
- Gratuzé, M., Leyns, C.E.G. & Holtzman, D.M. (2018) New insights into the role of TREM2 in Alzheimer’s disease. *Molecular Neurodegeneration* 2018 13:1. [Online] 13 (1), 1–16. Available from: doi:10.1186/S13024-018-0298-9 [Accessed: 27 September 2021].
- Grau-Rivera, O., Operto, G., Falcón, C., Sánchez-Benavides, G., et al. (2020) Association between insomnia and cognitive performance, gray matter

- volume, and white matter microstructure in cognitively unimpaired adults. *Alzheimer's Research and Therapy*. [Online] 12 (1). Available from: doi:10.1186/s13195-019-0547-3 [Accessed: 18 June 2021].
- Grey Walter, W. & Wyllie, W.G.V.R. (1936) The Electro-encephalogram in the Diagnosis of Cerebral Pathology. *Proceedings of the Royal Society of Medicine*. 30, 578–579.
- Grothe, M.J., Barthel, H., Sepulcre, J., Dyrba, M., et al. (2017) In vivo staging of regional amyloid deposition. *Neurology*. [Online] 89 (20), 2031–2038. Available from: doi:10.1212/WNL.0000000000004643 [Accessed: 5 July 2021].
- H. Ferreira-Vieira, T., M. Guimaraes, I., R. Silva, F. & M. Ribeiro, F. (2016) Alzheimer's disease: Targeting the Cholinergic System. *Current Neuropharmacology*. [Online] 14 (1), 101–115. Available from: doi:10.2174/1570159x13666150716165726 [Accessed: 18 June 2021].
- Hahn, T.T.G., McFarland, J.M., Berberich, S., Sakmann, B., et al. (2012) Spontaneous persistent activity in entorhinal cortex modulates cortico-hippocampal interaction in vivo. *Nature Neuroscience*. [Online] 15 (11), 1531–1538. Available from: doi:10.1038/nn.3236 [Accessed: 4 July 2021].
- Hahn, T.T.G., Sakmann, B. & Mehta, M.R. (2007) Differential responses of hippocampal subfields to cortical up-down states. *PNAS*. [Online] 104 (12), 5169–5174. Available from: www.pnas.org/cgi/doi/10.1073/pnas.0700222104 [Accessed: 24 June 2019].
- Hahn, T.T.G., Sakmann, B. & Mehta, M.R. (2006) Phase-locking of hippocampal interneurons' membrane potential to neocortical up-down states. *Nature Neuroscience*. [Online] 9 (11), 1359–1361. Available from: doi:10.1038/nn1788 [Accessed: 24 June 2019].
- Haider, B., Duque, A., Hasenstaub, A.R. & McCormick, D.A. (2006) *Neocortical Network Activity In Vivo Is Generated through a Dynamic Balance of Excitation and Inhibition*. [Online] Available from: doi:10.1523/JNEUROSCI.5297-05.2006 [Accessed: 31 August 2018].
- Hájos, N., Pálhalini, J., Mann, E.O., Németh, B., et al. (2004) Spike timing of distinct types of GABAergic interneuron during hippocampal gamma oscillations in vitro. *Journal of Neuroscience*. [Online] 24 (41), 9127–9137. Available from: doi:10.1523/JNEUROSCI.2113-04.2004 [Accessed: 1 July 2021].

- Hájos, N. & Paulsen, O. (2009) Network mechanisms of gamma oscillations in the CA3 region of the hippocampus. *Neural Networks*. [Online] 22 (8), 1113–1119. Available from: doi:10.1016/j.neunet.2009.07.024.
- Hangya, B., Borhegyi, Z., Szilágyi, N., Freund, T.F., et al. (2009) GABAergic neurons of the medial septum lead the hippocampal network during theta activity. *Journal of Neuroscience*. [Online] 29 (25), 8094–8102. Available from: doi:10.1523/JNEUROSCI.5665-08.2009 [Accessed: 30 June 2021].
- Hara, K. & Harris, R.A. (2002) The anesthetic mechanism of urethane: The effects on neurotransmitter-gated ion channels. *Anesthesia and Analgesia*. [Online] 94 (2), 313–318. Available from: doi:10.1213/00000539-200202000-00015 [Accessed: 2 August 2021].
- Hardy, J. & Selkoe, D.J. (2002) The Amyloid Hypothesis of Alzheimer's Disease: Progress and Problems on the Road to Therapeutics. *Science*. [Online] 297, 353–356. Available from: <http://science.sciencemag.org/content/sci/297/5580/353.full.pdf> [Accessed: 20 November 2017].
- Hardy, J.A. & Higgins, G.A. (1992) Alzheimer's disease: The amyloid cascade hypothesis. *Science*. [Online]. 256 (5054) pp.184–185. Available from: doi:10.1126/science.1566067.
- Harris, J.A., Devidze, N., Halabisky, B., Lo, I., et al. (2010) Many Neuronal and Behavioral Impairments in Transgenic Mouse Models of Alzheimer's Disease Are Independent of Caspase Cleavage of the Amyloid Precursor Protein. *Journal of Neuroscience*. [Online] 30 (1), 372–381. Available from: doi:10.1523/JNEUROSCI.5341-09.2010 [Accessed: 19 July 2021].
- Hartwich, K., Pollak, T. & Klausberger, T. (2009) *Distinct Firing Patterns of Identified Basket and Dendrite-Targeting Interneurons in the Prefrontal Cortex during Hippocampal Theta and Local Spindle Oscillations*. [Online] Available from: doi:10.1523/JNEUROSCI.1397-09.2009 [Accessed: 30 June 2019].
- Hauer, B.E., Pagliardini, S. & Dickson, C.T. (2019) The Reuniens Nucleus of the Thalamus has an Essential Role in Coordinating Slow Wave Activity between Neocortex and Hippocampus. *eneuro*. [Online] ENEURO.0365-19.2019. Available from: doi:10.1523/eneuro.0365-19.2019.
- Hay, Y.A., Deperrois, N., Fuchsberger, T., Quarrell, T.M., et al. (2021) Thalamus mediates neocortical Down state transition via GABAB-receptor-

- targeting interneurons. *Neuron*. [Online] 109 (17), 2682-2690.e5. Available from: doi:10.1016/J.NEURON.2021.06.030.
- He, Z., Guo, J.L., McBride, J.D., Narasimhan, S., et al. (2018) Amyloid- β plaques enhance Alzheimer's brain tau-seeded pathologies by facilitating neuritic plaque tau aggregation. *Nature Medicine*. [Online] 24 (1), 29–38. Available from: doi:10.1038/nm.4443 [Accessed: 15 June 2021].
- Hefter, D., Ludewig, S., Draguhn, A. & Korte, M. (2019) Amyloid, APP, and Electrical Activity of the Brain. *The Neuroscientist : a review journal bringing neurobiology, neurology and psychiatry*. [Online] 1073858419882619. Available from: doi:10.1177/1073858419882619 [Accessed: 7 January 2020].
- Heuer, H., Kohlisch, O. & Klein, W. (2005) The effects of total sleep deprivation on the generation of random sequences of key-presses, numbers and nouns. *Quarterly Journal of Experimental Psychology Section A: Human Experimental Psychology*. [Online]. 58 (2) pp.275–307. Available from: doi:10.1080/02724980343000855 [Accessed: 3 July 2021].
- Hijazi, S., Heistek, T.S., Scheltens, P., Neumann, U., et al. (2019) Early restoration of parvalbumin interneuron activity prevents memory loss and network hyperexcitability in a mouse model of Alzheimer's disease. *Molecular Psychiatry*. [Online] 25 (12), 3380–3398. Available from: <https://www.nature.com/articles/s41380-019-0483-4> [Accessed: 13 August 2021].
- Hillier, D., Fiscella, M., Drinnenberg, A., Trenholm, S., et al. (2017) Causal evidence for retina-dependent and -independent visual motion computations in mouse cortex. *Nature Neuroscience* 2017 20:7. [Online] 20 (7), 960–968. Available from: doi:10.1038/nn.4566 [Accessed: 23 July 2021].
- Hof, P.R., Bouras, C., Perl, D.P., Sparks, D.L., et al. (1995) Age-Related Distribution of Neuropathologic Changes in the Cerebral Cortex of Patients with Down's Syndrome: Quantitative Regional Analysis and Comparison with Alzheimer's Disease. *Archives of Neurology*. [Online] 52 (4), 379–391. Available from: doi:10.1001/archneur.1995.00540280065020 [Accessed: 16 June 2021].
- Hollnagel, J.-O., Elzoheiry, S., Gorgas, K., Kins, S., et al. (2019) Early alterations in hippocampal perisomatic GABAergic synapses and network

- oscillations in a mouse model of Alzheimer's disease amyloidosis. *PLOS ONE*. [Online] 14 (1), e0209228. Available from: <https://journals.plos.org/plosone/article?id=10.1371/journal.pone.0209228> [Accessed: 16 July 2021].
- Holth, J.K., Patel, T.K. & Holtzman, D.M. (2017) Sleep in Alzheimer's Disease—Beyond Amyloid. *Neurobiology of Sleep and Circadian Rhythms*. [Online]. 2 pp.4–14. Available from: doi:10.1016/j.nbscr.2016.08.002 [Accessed: 18 June 2021].
- Hsiao, K., Chapman, P., Nilsen, S., Eckman, C., et al. (1996) Correlative Memory Deficits, A β Elevation, and Amyloid Plaques in Transgenic Mice. *Science*. [Online] 274 (5284), 99–103. Available from: doi:10.1126/SCIENCE.274.5284.99 [Accessed: 26 July 2021].
- Hsieh, H., Boehm, J., Sato, C., Iwatsubo, T., et al. (2006) AMPAR Removal Underlies A β -Induced Synaptic Depression and Dendritic Spine Loss. *Neuron*. [Online] 52 (5), 831–843. Available from: doi:10.1016/j.neuron.2006.10.035.
- Hülsemann, M.J., Naumann, E. & Rasch, B. (2019) Quantification of Phase-Amplitude Coupling in Neuronal Oscillations: Comparison of Phase-Locking Value, Mean Vector Length, Modulation Index, and Generalized-Linear-Modeling-Cross-Frequency-Coupling. *Frontiers in Neuroscience*. [Online] 0 (JUN), 573. Available from: doi:10.3389/FNINS.2019.00573.
- Iaccarino, H.F., Singer, A.C., Martorell, A.J., Rudenko, A., et al. (2016) Gamma frequency entrainment attenuates amyloid load and modifies microglia. *Nature*. [Online] 540 (7632), 230–235. Available from: doi:10.1038/nature20587 [Accessed: 28 June 2021].
- Igarashi, K.M. (2015) Plasticity in oscillatory coupling between hippocampus and cortex. *Current Opinion in Neurobiology*. [Online] 35, 163–168. Available from: doi:10.1016/J.CONB.2015.09.005 [Accessed: 30 June 2019].
- Isomura, Y., Sirota, A., Özen, S., Montgomery, S., et al. (2006) Integration and Segregation of Activity in Entorhinal-Hippocampal Subregions by Neocortical Slow Oscillations. *Neuron*. [Online] 52 (5), 871–882. Available from: doi:10.1016/J.NEURON.2006.10.023 [Accessed: 1 October 2019].
- Ittner, A.A., Gladbach, A., Bertz, J., Suh, L.S., et al. (2014) p38 MAP kinase-mediated NMDA receptor-dependent suppression of hippocampal

- hypersynchronicity in a mouse model of Alzheimer's disease. *Acta Neuropathologica Communications*. [Online] 2 (1). Available from: doi:10.1186/S40478-014-0149-Z [Accessed: 10 September 2021].
- Jacob, S., Davies, G., De Bock, M., Hermans, B., et al. (2019) Neural oscillations during cognitive processes in an App knock-in mouse model of Alzheimer's disease pathology. *Scientific reports*. [Online] 9 (1), 16363. Available from: doi:10.1038/s41598-019-51928-w [Accessed: 14 November 2019].
- Jendryka, M., Palchadhuri, M., Ursu, D., van der Veen, B., et al. (2019) Pharmacokinetic and pharmacodynamic actions of clozapine-N-oxide, clozapine, and compound 21 in DREADD-based chemogenetics in mice. *Scientific reports*. [Online] 9 (1), 4522. Available from: doi:10.1038/s41598-019-41088-2 [Accessed: 4 April 2019].
- Jin, J. & Maren, S. (2015) Prefrontal-Hippocampal Interactions in Memory and Emotion. *Frontiers in Systems Neuroscience*. [Online] 9, 170. Available from: doi:10.3389/fnsys.2015.00170 [Accessed: 7 May 2019].
- Johnson, E.C.B., Ho, K., Yu, G.Q., Das, M., et al. (2020) Behavioral and neural network abnormalities in human APP transgenic mice resemble those of App knock-in mice and are modulated by familial Alzheimer's disease mutations but not by inhibition of BACE1. *Molecular Neurodegeneration*. [Online] 15 (1), 53. Available from: doi:10.1186/s13024-020-00393-5 [Accessed: 18 March 2021].
- Jones, M.W. & Wilson, M.A. (2005) Theta Rhythms Coordinate Hippocampal–Prefrontal Interactions in a Spatial Memory Task Richard Morris (ed.). *PLoS Biology*. [Online] 3 (12), e402. Available from: doi:10.1371/journal.pbio.0030402 [Accessed: 18 February 2020].
- Ju, Y.-E.S., Ooms, S.J., Sutphen, C., Macauley, S.L., et al. (2017) Slow wave sleep disruption increases cerebrospinal fluid amyloid-b levels. *Brain*. [Online] 140, 2104–2111. Available from: doi:10.1093/awx174 [Accessed: 1 June 2020].
- Jun, H., Bramian, A., Soma, S., Saito, T., et al. (2020) Disrupted Place Cell Remapping and Impaired Grid Cells in a Knockin Model of Alzheimer's Disease. *Neuron*. [Online] 107, 1–18. Available from: doi:10.1016/j.neuron.2020.06.023 [Accessed: 4 August 2020].
- Jura, B., Macrez, N., Meyrand, P. & Bem, T. (2019) Deficit in hippocampal

- ripples does not preclude spatial memory formation in APP/PS1 mice. *Scientific Reports*. [Online] 9 (1), 1–12. Available from: doi:10.1038/s41598-019-56582-w [Accessed: 19 July 2021].
- Kabeshita, Y., Adachi, H., Matsushita, M., Kanemoto, H., et al. (2017) Sleep disturbances are key symptoms of very early stage Alzheimer disease with behavioral and psychological symptoms: a Japan multi-center cross-sectional study (J-BIRD). *International Journal of Geriatric Psychiatry*. [Online] 32 (2), 222–230. Available from: doi:10.1002/gps.4470 [Accessed: 18 June 2021].
- Kam, K., Parekh, A., Sharma, R.A., Andrade, A., et al. (2019) Sleep oscillation-specific associations with Alzheimer’s disease CSF biomarkers: Novel roles for sleep spindles and tau. *Molecular Neurodegeneration*. [Online] 14 (1), 1–12. Available from: doi:10.1186/s13024-019-0309-5 [Accessed: 18 June 2021].
- Kametani, F. & Hasegawa, M. (2018) Reconsideration of Amyloid Hypothesis and Tau Hypothesis in Alzheimer’s Disease. *Frontiers in Neuroscience*. [Online] 12, 25. Available from: doi:10.3389/fnins.2018.00025 [Accessed: 2 February 2018].
- Kang, J.E., Lim, M.M., Bateman, R.J., Lee, J.J., et al. (2009) Amyloid- β dynamics are regulated by orexin and the sleep-wake cycle. *Science*. [Online] 326 (5955), 1005–1007. Available from: doi:10.1126/science.1180962 [Accessed: 16 June 2021].
- Kastanenka, K. V, Hou, S.S., Shakerdge, N., Logan, R., et al. (2017) Optogenetic Restoration of Disrupted Slow Oscillations Halts Amyloid Deposition and Restores Calcium Homeostasis in an Animal Model of Alzheimer’s Disease. *PLoS ONE*. [Online] 12, 1–25. Available from: <http://journals.plos.org/plosone/article/file?id=10.1371/journal.pone.0170275&type=printable> [Accessed: 23 January 2018].
- Kemp, N. & Bashir, Z.I. (2001) Long-term depression: A cascade of induction and expression mechanisms. *Progress in Neurobiology*. [Online]. 65 (4) pp.339–365. Available from: doi:10.1016/S0301-0082(01)00013-2.
- Kim, D.Y., Carey, B.W., Wang, H., Ingano, L.A.M., et al. (2007) BACE1 regulates voltage-gated sodium channels and neuronal activity. *Nature Cell Biology* 2007 9:7. [Online] 9 (7), 755–764. Available from: doi:10.1038/ncb1602 [Accessed: 18 September 2021].

- Kim, J., Basak, J.M. & Holtzman, D.M. (2009) The Role of Apolipoprotein E in Alzheimer's Disease. *Neuron*. [Online]. 63 (3) pp.287–303. Available from: doi:10.1016/j.neuron.2009.06.026 [Accessed: 18 June 2021].
- Kim, J., Gulati, T. & Ganguly, K. (2019) Competing Roles of Slow Oscillations and Delta Waves in Memory Consolidation versus Forgetting. *Cell*. [Online] 179 (2), 514–526.e13. Available from: doi:10.1016/j.cell.2019.08.040.
- King, C., Henze, D.A., Leinekugel, X. & Buzsáki, G. (1999) Hebbian modification of a hippocampal population pattern in the rat. *Journal of Physiology*. [Online] 521 (1), 159–167. Available from: doi:10.1111/j.1469-7793.1999.00159.x [Accessed: 14 June 2021].
- King, D.L. & Arendash, G.W. (2002) Behavioral characterization of the Tg2576 transgenic model of Alzheimer's disease through 19 months. *Physiology & Behavior*. [Online] 75 (5), 627–642. Available from: doi:10.1016/S0031-9384(02)00639-X.
- Kitchigina, V.F. (2018) Alterations of Coherent Theta and Gamma Network Oscillations as an Early Biomarker of Temporal Lobe Epilepsy and Alzheimer's Disease. *Frontiers in Integrative Neuroscience*. [Online]. 12 p.36. Available from: doi:10.3389/fnint.2018.00036 [Accessed: 11 May 2021].
- Klauber, M.R., Butters, N., Parker, L. & Kripke, D.F. (1991) Dementia in Institutionalized Elderly: Relation to Sleep Apnea. *Journal of the American Geriatrics Society*. [Online] 39 (3), 258–263. Available from: doi:10.1111/j.1532-5415.1991.tb01647.x [Accessed: 18 June 2021].
- Klausberger, T., Magill, P.J., Márton, L.F., Roberts, J.D.B., et al. (2003) Brain-state- and cell-type-specific firing of hippocampal interneurons in vivo. *Nature*. [Online] 421 (6925), 844–848. Available from: doi:10.1038/nature01374 [Accessed: 7 June 2021].
- Klausberger, T., Márton, L.F., Baude, A., Roberts, J.D.B., et al. (2004) Spike timing of dendrite-targeting bistratified cells during hippocampal network oscillations in vivo. *Nature Neuroscience*. [Online] Available from: doi:10.1038/nn1159.
- Kohto, S., Taguchi, Y., Matsumoto, N., Wada, M., et al. (2008) Algorithm for sleep scoring in experimental animals based on fast Fourier transform power spectrum analysis of the electroencephalogram. *Sleep and Biological Rhythms*. [Online] 6 (3), 163–171. Available from:

- doi:10.1111/J.1479-8425.2008.00355.X [Accessed: 1 September 2021].
- Krishnan, G.P., Chauvette, S., Shamie, I., Soltani, S., et al. (2016) Cellular and neurochemical basis of sleep stages in the thalamocortical network. *eLife*. [Online] 5, e18607. Available from: doi:10.7554/eLife.18607 [Accessed: 19 April 2018].
- Kuchibhotla, K. V., Lattarulo, C.R., Hyman, B.T. & Bacskai, B.J. (2009) Synchronous hyperactivity and intercellular calcium waves in astrocytes in Alzheimer mice. *Science*. [Online] 323 (5918), 1211–1215. Available from: doi:10.1126/science.1169096 [Accessed: 28 June 2021].
- Lanari, A., Amenta, F., Silvestrelli, G., Tomassoni, D., et al. (2006) Neurotransmitter deficits in behavioural and psychological symptoms of Alzheimer's disease. *Mechanisms of Ageing and Development*. [Online] 127 (2), 158–165. Available from: doi:10.1016/J.MAD.2005.09.016.
- Latchoumane, C.-F. V, Ngo, H.-V. V, Born, J. & Shin, H.-S. (2017) Thalamic Spindles Promote Memory Formation during Sleep through Triple Phase-Locking of Cortical, Thalamic, and Hippocampal Rhythms. *Neuron*. [Online] 95 (2), 424-435.e6. Available from: doi:10.1016/j.neuron.2017.06.025 [Accessed: 18 July 2019].
- Latif-Hernandez, A., Shah, D., Craessaerts, K., Saido, T., et al. (2019) Subtle behavioral changes and increased prefrontal-hippocampal network synchronicity in APPNL–G–F mice before prominent plaque deposition. *Behavioural Brain Research*. [Online] 364, 431–441. Available from: doi:10.1016/J.BBR.2017.11.017 [Accessed: 1 October 2019].
- Lee, K., Park, Y., Suh, S.W., Kim, S.-S., et al. (2021) Optimal flickering light stimulation for entraining gamma waves in the human brain. *Scientific Reports 2021 11:1*. [Online] 11 (1), 1–10. Available from: doi:10.1038/s41598-021-95550-1 [Accessed: 27 September 2021].
- Lee, Y.F., Gerashchenko, D., Timofeev, I., Bacskai, B.J., et al. (2020) Slow Wave Sleep Is a Promising Intervention Target for Alzheimer's Disease. *Frontiers in Neuroscience*. [Online]. 14. Available from: doi:10.3389/fnins.2020.00705 [Accessed: 4 August 2020].
- Lemieux, M., Chen, J.-Y., Lonjers, P., Bazhenov, M., et al. (2014) *The Impact of Cortical Deafferentation on the Neocortical Slow Oscillation*. [Online] Available from: doi:10.1523/JNEUROSCI.1156-13.2014 [Accessed: 16 December 2018].

- Lemmens, M.A.M., Sierksma, A.S.R., Rutten, B.P.F., Dennissen, F., et al. (2011) Age-related changes of neuron numbers in the frontal cortex of a transgenic mouse model of Alzheimer's disease. *Brain Structure & Function*. [Online] 216 (3), 227. Available from: doi:10.1007/S00429-011-0305-1 [Accessed: 23 August 2021].
- Lever, C., Kaplan, R., Burgess, N., Lever, C., et al. (2014) The Function of Oscillations in the Hippocampal Formation. In: *Space, Time and Memory in the Hippocampal Formation*. [Online]. pp. 303–350. Available from: doi:10.1007/978-3-7091-1292-2_12.
- Li, H., Guo, Q., Inoue, T., Polito, V.A., et al. (2014) Vascular and parenchymal amyloid pathology in an Alzheimer disease knock-in mouse model: interplay with cerebral blood flow. *Molecular Neurodegeneration*. [Online] 9 (1), 28. Available from: doi:10.1186/1750-1326-9-28 [Accessed: 17 September 2021].
- Li, S., Hong, S., Shepardson, N.E., Walsh, D.M., et al. (2009) Soluble Oligomers of Amyloid β Protein Facilitate Hippocampal Long-Term Depression by Disrupting Neuronal Glutamate Uptake. *Neuron*. [Online] 62 (6), 788–801. Available from: doi:10.1016/j.neuron.2009.05.012 [Accessed: 28 June 2021].
- Li, W., Ma, L., Yang, G. & Gan, W.B. (2017) REM sleep selectively prunes and maintains new synapses in development and learning. *Nature Neuroscience*. [Online] 20 (3), 427–437. Available from: doi:10.1038/nn.4479 [Accessed: 3 September 2020].
- Lisman, J. (2010) Working Memory: The Importance of Theta and Gamma Oscillations. *Current Biology*. [Online] 20 (11), R490–R492. Available from: doi:10.1016/J.CUB.2010.04.011 [Accessed: 10 October 2019].
- Lisman, J.E. & Jensen, O. (2013) The Theta-Gamma Neural Code. *Neuron*. [Online]. 77 (6) pp.1002–1016. Available from: doi:10.1016/j.neuron.2013.03.007.
- Liu, T., Bai, W., Xia, M. & Tian, X. (2018) Directional hippocampal-prefrontal interactions during working memory. *Behavioural Brain Research*. [Online] 338, 1–8. Available from: doi:10.1016/j.bbr.2017.10.003.
- Lloret, M.A., Cervera-Ferri, A., Nepomuceno, M., Monllor, P., et al. (2020) Is sleep disruption a cause or consequence of alzheimer's disease? Reviewing its possible role as a biomarker. *International Journal of*

- Molecular Sciences*. [Online]. 21 (3). Available from:
doi:10.3390/ijms21031168 [Accessed: 18 January 2021].
- Lockmann, A.L. V., Laplagne, D.A., Leão, R.N. & Tort, A.B.L. (2016) A Respiration-Coupled Rhythm in the Rat Hippocampus Independent of Theta and Slow Oscillations. *Journal of Neuroscience*. [Online] 36 (19), 5338–5352. Available from: doi:10.1523/JNEUROSCI.3452-15.2016 [Accessed: 1 September 2021].
- Long, J.M. & Holtzman, D.M. (2019) Alzheimer Disease: An Update on Pathobiology and Treatment Strategies. *Cell*. [Online] 179. Available from: doi:10.1016/j.cell.2019.09.001 [Accessed: 1 October 2019].
- Lopes-dos-Santos, V., van de Ven, G.M., Morley, A., Trouche, S., et al. (2018) Parsing Hippocampal Theta Oscillations by Nested Spectral Components during Spatial Exploration and Memory-Guided Behavior. *Neuron*. [Online] 100 (4), 940-952.e7. Available from: doi:10.1016/j.neuron.2018.09.031.
- Lopes, G., Bonacchi, N., Frazão, J., Neto, J.P., et al. (2015) Bonsai: an event-based framework for processing and controlling data streams. *Frontiers in Neuroinformatics*. [Online] 0 (APR), 7. Available from: doi:10.3389/FNINF.2015.00007.
- López-Madrona, V.J., Pérez-Montoyo, E., Álvarez-Salvado, E., Moratal, D., et al. (2020) Different theta frameworks coexist in the rat hippocampus and are coordinated during memory-guided and novelty tasks. *eLife*. [Online] 9, 1–35. Available from: doi:10.7554/eLife.57313.
- Luczak, A., Barthó, P., Marguet, S.L., Rgy Buzsá Ki, G., et al. (2007) Sequential structure of neocortical spontaneous activity in vivo. *PNAS*. 104 (1), 347–352.
- Lüthi, A. (2014) What Are Sleep Spindle Waves? Sleep Spindles: Where They Come From, What They Do. *The Neuroscientist*. [Online] 20 (3), 243–256. Available from: doi:10.1177/1073858413500854.
- Lüthi, A. & McCormick, D.A. (1999) Modulation of a pacemaker current through Ca²⁺-induced stimulation of cAMP production. *Nature Neuroscience*. [Online] 2 (7), 634–641. Available from: doi:10.1038/10189 [Accessed: 2 June 2021].
- Maezono, S.E.B., Kanuka, M., Tatsuzawa, C., Morita, M., et al. (2020) Progressive changes in sleep and its relations to amyloid- β distribution and learning in single app knock-in mice. *eNeuro*. [Online] 7 (2). Available from:

- /pmc/articles/PMC7196722/ [Accessed: 18 March 2021].
- Maggi, C.A. & Meli, A. (1986) Suitability of urethane anesthesia for physiopharmacological investigations in various systems Part 1: General considerations. *Experientia*. [Online] 42 (2), 109–114. Available from: doi:10.1007/BF01952426 [Accessed: 20 September 2021].
- Mahar, I., Albuquerque, M.S., Mondragon-Rodriguez, S., Cavanagh, C., et al. (2017) Phenotypic Alterations in Hippocampal NPY- and PV-Expressing Interneurons in a Presymptomatic Transgenic Mouse Model of Alzheimer's Disease. *Frontiers in Aging Neuroscience*. [Online] 0 (JAN), 327. Available from: doi:10.3389/FNAGI.2016.00327.
- Maingret, N., Girardeau, G., Todorova, R., Goutierre, M., et al. (2016a) Hippocampo-cortical coupling mediates memory consolidation during sleep. *Nature Neuroscience*. [Online] 19 (7), 959–964. Available from: doi:10.1038/nn.4304.
- Maingret, N., Girardeau, G., Todorova, R., Goutierre, M., et al. (2016b) Hippocampo-cortical coupling mediates memory consolidation during sleep. *Nature Neuroscience*. [Online] 19 (7), 959–964. Available from: doi:10.1038/nn.4304 [Accessed: 30 June 2019].
- Malow, B.A., Carney, P.R., Kushwaha, R. & Bowes, R.J. (1999) Hippocampal sleep spindles revisited: physiologic or epileptic activity? *Clinical Neurophysiology*. [Online] 110 (4), 687–693. Available from: doi:10.1016/S1388-2457(99)00008-5.
- Malthankar-Phatak, G.H., Lin, Y.-G., Giovannone, N. & Siman, R. (2012) Amyloid Deposition and Advanced Age Fails to Induce Alzheimer's Type Progression in a Double Knock-In Mouse Model. *Aging and Disease*. [Online] 3 (2), 141. Available from: /pmc/articles/PMC3377826/ [Accessed: 17 September 2021].
- Mander, B.A., Marks, S.M., Vogel, J.W., Rao, V., et al. (2015a) β -amyloid disrupts human NREM slow waves and related hippocampus-dependent memory consolidation. *Nature Neuroscience*. [Online] 18 (7), 1051–1057. Available from: doi:10.1038/nn.4035.
- Mander, B.A., Marks, S.M., Vogel, J.W., Rao, V., et al. (2015b) β -amyloid disrupts human NREM slow waves and related hippocampus-dependent memory consolidation. *Nature Neuroscience*. [Online] 18 (7), 1051–1057. Available from: doi:10.1038/nn.4035 [Accessed: 28 October 2018].

- Mann, E.O., Kohl, M.M. & Paulsen, O. (2009) Distinct Roles of GABA A and GABA B Receptors in Balancing and Terminating Persistent Cortical Activity. *Journal of Neuroscience*. [Online] 29 (23), 7513–7518. Available from: doi:10.1523/JNEUROSCI.6162-08.2009 [Accessed: 25 October 2017].
- Mann, E.O., Radcliffe, C.A. & Paulsen, O. (2005) Hippocampal gamma-frequency oscillations: From interneurons to pyramidal cells, and back. *Journal of Physiology*. [Online] 562 (1), 55–63. Available from: doi:10.1113/jphysiol.2004.078758 [Accessed: 1 July 2021].
- Manseau, F., Marinelli, S., Méndez, P., Schwaller, B., et al. (2010) Desynchronization of Neocortical Networks by Asynchronous Release of GABA at Autaptic and Synaptic Contacts from Fast-Spiking Interneurons. *PLoS Biology*. [Online] 8 (9), 1000492. Available from: doi:10.1371/JOURNAL.PBIO.1000492 [Accessed: 23 August 2021].
- Marshall, L., Helgadóttir, H., Mölle, M. & Born, J. (2006) Boosting slow oscillations during sleep potentiates memory. *Nature*. [Online] 444 (7119), 610–613. Available from: doi:10.1038/nature05278.
- Martinez-Losa, M., Tracy, T.E., Ma, K., Verret, L., et al. (2018) Nav1.1-Overexpressing Interneuron Transplants Restore Brain Rhythms and Cognition in a Mouse Model of Alzheimer’s Disease. *Neuron*. [Online] 98, 1–15. Available from: <http://www.ncbi.nlm.nih.gov/pubmed/29551491> [Accessed: 27 March 2018].
- Martorell, A.J., Paulson, A.L., Suk, H., Boyden, E.S., et al. (2019) Multi-sensory Gamma Stimulation Ameliorates Alzheimer’s-Associated Pathology and Improves Article Multi-sensory Gamma Stimulation Ameliorates Alzheimer’s-Associated Pathology and Improves Cognition. *Cell*. [Online] 177 (2), 256-271.e22. Available from: doi:10.1016/j.cell.2019.02.014.
- Massey, C.A. & Richerson, G.B. (2017) Isoflurane, ketamine-xylazine, and urethane markedly alter breathing even at subtherapeutic doses. *Pineda and Aghajanian*. [Online] 118, 2389–2401. Available from: doi:10.1152/jn.00350.2017.-Anesthetics [Accessed: 28 July 2021].
- Masuda, A., Kobayashi, Y., Kogo, N., Saito, T., et al. (2016) Cognitive deficits in single App knock-in mouse models. *Neurobiology of learning and memory*. [Online] 135, 73–82. Available from: doi:10.1016/j.nlm.2016.07.001 [Accessed: 13 November 2017].

- Matos, M., Augusto, E., Oliveira, C.R. & Agostinho, P. (2008) Amyloid-beta peptide decreases glutamate uptake in cultured astrocytes: Involvement of oxidative stress and mitogen-activated protein kinase cascades. *Neuroscience*. [Online] 156 (4), 898–910. Available from: doi:10.1016/j.neuroscience.2008.08.022.
- McFarland, W.L., Teitelbaum, H. & Hedges, E.K. (1975) Relationship between hippocampal theta activity and running speed in the rat. *Journal of Comparative and Physiological Psychology*. [Online] 88 (1), 324–328. Available from: doi:10.1037/h0076177 [Accessed: 30 June 2021].
- McGaugh, J.L. (2013) Making lasting memories: Remembering the significant. *PNAS*. [Online] 110 (Suppl 2), 10402. Available from: doi:10.1073/PNAS.1301209110 [Accessed: 19 July 2021].
- Melman, T. & Victor, J.D. (2016) Robust power spectral estimation for EEG data. *Journal of Neuroscience Methods*. [Online] 268, 14–22. Available from: doi:10.1016/J.JNEUMETH.2016.04.015.
- Mikkonen, M., Alafuzoff, I., Tapiola, T., Soininen, H., et al. (1999) Subfield- and layer-specific changes in parvalbumin, calretinin and calbindin-D28k immunoreactivity in the entorhinal cortex in Alzheimer's disease. *Neuroscience*. [Online] 92 (2), 515–532. Available from: doi:10.1016/S0306-4522(99)00047-0.
- Möller, M., Bergmann, T.O., Marshall, L. & Born, J. (2011) Fast and Slow Spindles during the Sleep Slow Oscillation: Disparate Coalescence and Engagement in Memory Processing. *Sleep*. [Online] 34 (10), 1411–1421. Available from: doi:10.5665/sleep.1290.
- Möller, M., Eschenko, O., Gais, S., Sara, S.J., et al. (2009) The influence of learning on sleep slow oscillations and associated spindles and ripples in humans and rats. *European Journal of Neuroscience*. [Online] 29 (5), 1071–1081. Available from: doi:10.1111/j.1460-9568.2009.06654.x.
- Möller, M., Marshall, L., Gais, S. & Born, J. (2002) Grouping of spindle activity during slow oscillations in human non-rapid eye movement sleep. *Journal of Neuroscience*. [Online] 22 (24), 10941–10947. Available from: doi:10.1523/JNEUROSCI.22-24-10941.2002.
- Möller, M., Marshall, L., Gais, S. & Born, J. (2004) Learning increases human electroencephalographic coherence during subsequent slow sleep oscillations. *Proceedings of the National Academy of Sciences of the*

- United States of America*. [Online] 101 (38), 13963–13968. Available from: doi:10.1073/pnas.0402820101.
- Mölle, M., Yeshenko, O., Marshall, L., Sara, S.J., et al. (2006) Hippocampal Sharp Wave-Ripples Linked to Slow Oscillations in Rat Slow-Wave Sleep. *Journal of Neurophysiology*. [Online] 96 (1), 62–70. Available from: doi:10.1152/jn.00014.2006 [Accessed: 7 May 2019].
- Moreno-Gonzalez, I., Baglietto-Vargas, D., Sanchez-Varo, R., Jimenez, S., et al. (2009) Extracellular Amyloid- β and Cytotoxic Glial Activation Induce Significant Entorhinal Neuron Loss in Young PS1 M146L/APP 751SL Mice. *Journal of Alzheimer's Disease*. [Online] 18 (4), 755–776. Available from: doi:10.3233/JAD-2009-1192.
- Mukovski, M., Chauvette, S., Timofeev, I. & Volgushev, M. (2007) Detection of Active and Silent States in Neocortical Neurons from the Field Potential Signal during Slow-Wave Sleep. *Cerebral Cortex*. [Online] 17 (2), 400–414. Available from: doi:10.1093/cercor/bhj157 [Accessed: 20 April 2020].
- Murty, D.V.P.S., Manikandan, K., Kumar, W.S., Ramesh, R.G., et al. (2021) Stimulus-induced gamma rhythms are weaker in human elderly with mild cognitive impairment and Alzheimer's disease. *eLife*. 10.
- Nádasdy, Z., Hirase, H., Czurkó, A., Csicsvari, J., et al. (1999) Replay and time compression of recurring spike sequences in the hippocampus. *Journal of Neuroscience*. [Online] 19 (21), 9497–9507. Available from: doi:10.1523/jneurosci.19-21-09497.1999 [Accessed: 7 June 2021].
- Nakabayashi, T., Uchida, S., Maehara, T., Hirai, N., et al. (2001) Absence of sleep spindles in human medial and basal temporal lobes. *Psychiatry and Clinical Neurosciences*. [Online] 55 (1), 57–65. Available from: doi:10.1046/J.1440-1819.2001.00785.X [Accessed: 21 February 2022].
- Nakashiba, T., Buhl, D.L., McHugh, T.J. & Tonegawa, S. (2009) Hippocampal CA3 Output Is Crucial for Ripple-Associated Reactivation and Consolidation of Memory. *Neuron*. [Online] 62 (6), 781–787. Available from: doi:10.1016/j.neuron.2009.05.013 [Accessed: 3 June 2021].
- Nakazono, T., Lam, T.N., Patel, A.Y., Kitazawa, M., et al. (2017) Impaired In Vivo Gamma Oscillations in the Medial Entorhinal Cortex of Knock-in Alzheimer Model. *Frontiers in systems neuroscience*. [Online] 11, 48. Available from: doi:10.3389/fnsys.2017.00048 [Accessed: 5 June 2019].
- Nalivaeva, N.N. & Turner, A.J. (2013) The amyloid precursor protein: A

- biochemical enigma in brain development, function and disease. *FEBS Letters*. [Online] 587 (13), 2046–2054. Available from: doi:10.1016/J.FEBSLET.2013.05.010 [Accessed: 22 February 2018].
- Neske, G.T., Connelly, W.M., Halassa, M.M. & Lőrincz, M.L. (2016) The Slow Oscillation in Cortical and Thalamic Networks: Mechanisms and Functions. *Frontiers in Neural Circuits*. [Online] 9. Available from: doi:10.3389/fncir.2015.00088.
- Ngo, H.V., Fell, J. & Staresina, B. (2020) Sleep spindles mediate hippocampal-neocortical coupling during long-duration ripples. *eLife*. [Online] 9, 1–18. Available from: doi:10.7554/eLife.57011.
- Nicole, O., Hadzibegovic, S., Gajda, J., Bontempi, B., et al. (2016) Soluble amyloid beta oligomers block the learning-induced increase in hippocampal sharp wave-ripple rate and impair spatial memory formation. *Scientific Reports*. [Online] 6 (1), 22728. Available from: doi:10.1038/srep22728 [Accessed: 29 October 2018].
- Niethard, N., Ngo, H.-V. V, Ehrlich, I., Born, J., et al. (2018) Cortical circuit activity underlying sleep slow oscillations and spindles. *PNAS*. [Online] 115 (39), 9220–9229. Available from: doi:10.1073/pnas.1805517115 [Accessed: 17 December 2018].
- Nilsson, J.P., Söderström, M., Karlsson, A.U., Lekander, M., et al. (2005) Less effective executive functioning after one night's sleep deprivation. *Journal of Sleep Research*. [Online] 14 (1), 1–6. Available from: doi:10.1111/j.1365-2869.2005.00442.x [Accessed: 3 July 2021].
- Nilsson, P., Saito, T. & Saido, T.C. (2014) New Mouse Model of Alzheimer's. *ACS Chemical Neuroscience*. [Online] 5, 499–502. Available from: doi:10.1021/cn500105p [Accessed: 20 November 2017].
- Nir, Y., Staba, R.J., Andrillon, T., Vyazovskiy, V. V., et al. (2011) Regional Slow Waves and Spindles in Human Sleep. *Neuron*. [Online] 70 (1), 153–169. Available from: doi:10.1016/J.NEURON.2011.02.043.
- Nitzan, N., McKenzie, S., Beed, P., English, D.F., et al. (2020) Propagation of hippocampal ripples to the neocortex by way of a subiculum-retrosplenial pathway. *Nature Communications*. [Online] 11 (1). Available from: doi:10.1038/s41467-020-15787-8.
- Nuñez, A. & Buño, W. (2021) The Theta Rhythm of the Hippocampus: From Neuronal and Circuit Mechanisms to Behavior. *Frontiers in Cellular*

- Neuroscience*. [Online]. 15 p.31. Available from:
doi:10.3389/fncel.2021.649262 [Accessed: 1 July 2021].
- O'Brien, J., Hayder, H. & Peng, C. (2016) Automated Quantification and Analysis of Cell Counting Procedures Using ImageJ Plugins. *Journal of Visualized Experiments : JoVE*. [Online] 2016 (117). Available from:
doi:10.3791/54719 [Accessed: 23 August 2021].
- O'Brien, R.J. & Wong, P.C. (2011) Amyloid precursor protein processing and Alzheimer's disease. *Annual review of neuroscience*. [Online] 34, 185–204. Available from: doi:10.1146/annurev-neuro-061010-113613 [Accessed: 22 February 2018].
- O'Neill, P.-K., Gordon, J.A. & Sigurdsson, T. (2013) Theta oscillations in the medial prefrontal cortex are modulated by spatial working memory and synchronize with the hippocampus through its ventral subregion. *The Journal of neuroscience : the official journal of the Society for Neuroscience*. [Online] 33 (35), 14211–14224. Available from:
doi:10.1523/JNEUROSCI.2378-13.2013 [Accessed: 1 October 2019].
- Oblak, A.L., Lin, P.B., Kotredes, K.P., Pandey, R.S., et al. (2021) Comprehensive Evaluation of the 5XFAD Mouse Model for Preclinical Testing Applications: A MODEL-AD Study. *Frontiers in Aging Neuroscience*. [Online] 0, 431. Available from:
doi:10.3389/FNAGI.2021.713726.
- Ognjanovski, N., Schaeffer, S., Wu, J., Mofakham, S., et al. (2017) Parvalbumin-expressing interneurons coordinate hippocampal network dynamics required for memory consolidation. *Nature Communications*. [Online] 8 (1), 15039. Available from: doi:10.1038/ncomms15039 [Accessed: 30 June 2019].
- Ooms, S., Overeem, S., Besse, K., Rikkert, M.O., et al. (2014) Effect of 1 night of total sleep deprivation on cerebrospinal fluid β -amyloid 42 in healthy middle-aged men a randomized clinical trial. *JAMA Neurology*. [Online] 71 (8), 971–977. Available from: doi:10.1001/jamaneurol.2014.1173 [Accessed: 16 June 2021].
- Palop, J., Chin, J., Roberson, E.D., Wang, J., et al. (2007) Aberrant Excitatory Neuronal Activity and Compensatory Remodeling of Inhibitory Hippocampal Circuits in Mouse Models of Alzheimer's Disease. *Neuron*. [Online] 55, 697–711. Available from: doi:10.1016/j.neuron.2007.07.025.

- Palop, J. & Mucke, L. (2016) Network abnormalities and interneuron dysfunction in Alzheimer disease. *Nature reviews. Neuroscience*. [Online] 17 (12), 777–792. Available from: doi:10.1038/nrn.2016.141.
- Palop, J.J. & Mucke, L. (2010) Amyloid-beta-induced neuronal dysfunction in Alzheimer's disease: from synapses toward neural networks. *Nature neuroscience*. [Online] 13 (7), 812–818. Available from: doi:10.1038/nn.2583 [Accessed: 10 October 2017].
- Pangalos, M., Donoso, J.R., Winterer, J., Zivkovic, A.R., et al. (2013) Recruitment of oriens-lacunosum-moleculare interneurons during hippocampal ripples. *Proceedings of the National Academy of Sciences of the United States of America*. [Online] 110 (11), 4398–4403. Available from: doi:10.1073/pnas.1215496110 [Accessed: 10 February 2021].
- Papalambros, N.A., Santostasi, G., Malkani, R.G., Braun, R., et al. (2017) Acoustic Enhancement of Sleep Slow Oscillations and Concomitant Memory Improvement in Older Adults. *Frontiers in Human Neuroscience*. [Online] 0, 109. Available from: doi:10.3389/FNHUM.2017.00109.
- Park, K., Lee, J., Jang, H.J., Richards, B.A., et al. (2020) Optogenetic activation of parvalbumin and somatostatin interneurons selectively restores theta-nested gamma oscillations and oscillation-induced spike timing-dependent long-Term potentiation impaired by amyloid β oligomers. *BMC Biology*. [Online] 18 (1), 1–20. Available from: doi:10.1186/s12915-019-0732-7 [Accessed: 5 July 2021].
- Paxinos, G., Watson, C., Pennisi, M. & Topple, A. (1985) Bregma, lambda and the interaural midpoint in stereotaxic surgery with rats of different sex, strain and weight. *Journal of Neuroscience Methods*. [Online] 13 (2), 139–143. Available from: doi:10.1016/0165-0270(85)90026-3.
- Pelkey, K.A., Chittajallu, R., Craig, M.T., Tricoire, L., et al. (2017) Hippocampal GABAergic inhibitory interneurons. *Physiological Reviews*. [Online] 97 (4), 1619–1747. Available from: doi:10.1152/physrev.00007.2017 [Accessed: 3 June 2021].
- Pervolaraki, E., Hall, S.P., Foresteire, D. & Saito, T. (2019) Insoluble A β overexpression in an App knock-in mouse model alters microstructure and gamma oscillations in the prefrontal cortex, affecting anxiety-related behaviours. *Disease Models and Mechanisms*. 12.
- Peyrache, A., Battaglia, F.P., Destexhe, A. & Sejnowski, T.J. (2011) Inhibition

- recruitment in prefrontal cortex during sleep spindles and gating of hippocampal inputs. *PNAS*. [Online] 108 (41). Available from: doi:10.1073/pnas.1103612108 [Accessed: 21 May 2018].
- Phillips, K.G., Bartsch, U., McCarthy, A.P., Edgar, D.M., et al. (2012) Decoupling of Sleep-Dependent Cortical and Hippocampal Interactions in a Neurodevelopmental Model of Schizophrenia. *Neuron*. [Online] 76 (3), 526. Available from: doi:10.1016/J.NEURON.2012.09.016 [Accessed: 1 September 2021].
- Plihal, W. & Born, J. (1997) Effects of early and late nocturnal sleep on declarative and procedural memory. *Journal of Cognitive Neuroscience*. [Online] 9 (4), 534–547. Available from: doi:10.1162/jocn.1997.9.4.534 [Accessed: 3 July 2021].
- Poskanzer, K.E. & Yuste, R. (2016) Astrocytes regulate cortical state switching in vivo. *PNAS*. [Online] 113 (19), E2675-84. Available from: doi:10.1073/pnas.1520759113 [Accessed: 19 April 2018].
- Price, J.L. (1994) Tangles and plaques in healthy aging and Alzheimer's disease: Independence or interaction. *Seminars in the Neurosciences*. [Online] 6 (6), 395–402. Available from: doi:10.1006/smns.1994.1051.
- Procyk, C.A., Eleftheriou, C.G., Storchi, R., Allen, A.E., et al. (2015) Spatial receptive fields in the retina and dorsal lateral geniculate nucleus of mice lacking rods and cones. *Journal of Neurophysiology*. [Online] 114 (2), 1321. Available from: doi:10.1152/JN.00368.2015 [Accessed: 23 July 2021].
- Rasch, B. & Born, J. (2013) About sleep's role in memory. *Physiological Reviews*. [Online] 93 (2), 681–766. Available from: doi:10.1152/physrev.00032.2012.
- Ribeiro, S., Mello, C. V., Velho, T., Gardner, T.J., et al. (2002) Induction of hippocampal long-term potentiation during waking leads to increased extrahippocampal zif-268 expression during ensuing rapid-eye-movement sleep. *Journal of Neuroscience*. [Online] 22 (24), 10914–10923. Available from: doi:10.1523/jneurosci.22-24-10914.2002 [Accessed: 14 June 2021].
- Ribeiro, S., Shi, X., Engelhard, M., Zhou, Y., et al. (2007) Novel Experience Induces Persistent Sleep-Dependent Plasticity in the Cortex but not in the Hippocampus. *Frontiers in Neuroscience*. [Online] 1 (1), 43–55. Available from: doi:10.3389/neuro.01.1.1.003.2007 [Accessed: 14 June 2021].

- Riga, D., Matos, M.R., Glas, A., Smit, A.B., et al. (2014) Optogenetic dissection of medial prefrontal cortex circuitry. *Frontiers in Systems Neuroscience*. [Online] 8, 230. Available from: doi:10.3389/fnsys.2014.00230 [Accessed: 27 September 2019].
- Rigas, P. & Castro-Alamancos, M.A. (2007) Thalamocortical up states: Differential effects of intrinsic and extrinsic cortical inputs on persistent activity. *Journal of Neuroscience*. [Online] 27 (16), 4261–4272. Available from: doi:10.1523/JNEUROSCI.0003-07.2007 [Accessed: 3 July 2021].
- Roš, H., Sachdev, R.N.S., Yu, Y., Šestan, N., et al. (2009) Neocortical Networks Entrain Neuronal Circuits in Cerebellar Cortex. *Journal of Neuroscience*. [Online] 29 (33), 10309–10320. Available from: doi:10.1523/JNEUROSCI.2327-09.2009 [Accessed: 26 July 2021].
- Rosanova, M. & Ulrich, D. (2005) Pattern-specific associative long-term potentiation induced by a sleep spindle-related spike train. *Journal of Neuroscience*. [Online] 25 (41), 9398–9405. Available from: doi:10.1523/JNEUROSCI.2149-05.2005 [Accessed: 14 June 2021].
- Roth, B.L. (2016) DREADDs for Neuroscientists. *Neuron*. [Online] 89 (4), 683–694. Available from: doi:10.1016/j.neuron.2016.01.040 [Accessed: 22 February 2018].
- Saito, T., Matsuba, Y., Mihira, N., Takano, J., et al. (2014) Single App knock-in mouse models of Alzheimer's disease. *Nature Neuroscience*. [Online] 17 (5), 661–664. Available from: doi:10.1038/nn.3697 [Accessed: 13 November 2017].
- Saiz-Sanchez, D., De la Rosa-Prieto, C., Ubeda-Banon, I. & Martinez-Marcos, A. (2014) Interneurons, tau and amyloid- β in the piriform cortex in Alzheimer's disease. *Brain Structure and Function* 2014 220:4. [Online] 220 (4), 2011–2025. Available from: doi:10.1007/S00429-014-0771-3 [Accessed: 19 August 2021].
- Sakakibara, Y., Sekiya, M., Saito, T., Saido, T.C., et al. (2019) Amyloid- β plaque formation and reactive gliosis are required for induction of cognitive deficits in App knock-in mouse models of Alzheimer's disease. *BMC Neuroscience*. [Online] 20 (1), 13. Available from: doi:10.1186/s12868-019-0496-6 [Accessed: 5 June 2019].
- Sakakibara, Y., Sekiya, M., Saito, T., Saido, T.C., et al. (2018) Cognitive and emotional alterations in App knock-in mouse models of A β amyloidosis.

- BMC neuroscience*. [Online] 19 (1), 46. Available from:
doi:10.1186/s12868-018-0446-8 [Accessed: 5 June 2019].
- Sanchez-Vives, M. & McCormick, D. (2000) Cellular and network mechanisms of rhythmic recurrent activity in neocortex. *Nature neuroscience*. 3 (1027–1034).
- Sanchez-Vives, M. V, Mattia, M., Compte, A., Perez-Zabalza, M., et al. (2010) Inhibitory Modulation of Cortical Up States. *J Neurophysiol*. [Online] 104, 1314–1324. Available from: doi:10.1152/jn.00178.2010 [Accessed: 25 October 2017].
- Sanchez-Mejias, E., Nuñez-Diaz, C., Sanchez-Varo, R., Gomez-Arboledas, A., et al. (2020) Distinct disease-sensitive GABAergic neurons in the perirhinal cortex of Alzheimer's mice and patients. *Brain Pathology (Zurich, Switzerland)*. [Online] 30 (2), 345. Available from: doi:10.1111/BPA.12785 [Accessed: 13 August 2021].
- Saper, C.B., Fuller, P.M., Pedersen, N.P., Lu, J., et al. (2010) Sleep State Switching. *Neuron*. [Online]. 68 (6) pp.1023–1042. Available from: doi:10.1016/j.neuron.2010.11.032.
- Sasaguri, H., Nilsson, P., Hashimoto, S., Nagata, K., et al. (2017) APP mouse models for Alzheimer's disease preclinical studies. *The EMBO journal*. [Online] 36 (17), 2473–2487. Available from: doi:10.15252/embj.201797397 [Accessed: 11 June 2018].
- Sawangjit, A., Oyanedel, C.N., Niethard, N., Salazar, C., et al. (2018) The hippocampus is crucial for forming non-hippocampal long-term memory during sleep. *Nature*. [Online] 564 (7734), 109–113. Available from: doi:10.1038/s41586-018-0716-8.
- Schack, B., Vath, N., Petsche, H., Geissler, H.G., et al. (2002) Phase-coupling of theta-gamma EEG rhythms during short-term memory processing. *International Journal of Psychophysiology*. [Online] 44 (2), 143–163. Available from: doi:10.1016/S0167-8760(01)00199-4.
- Scheffer-Teixeira, R., Belchior, H., Caixeta, F. V., Souza, B.C., et al. (2012) Theta Phase Modulates Multiple Layer-Specific Oscillations in the CA1 Region. *Cerebral Cortex*. [Online] 22 (10), 2404–2414. Available from: doi:10.1093/cercor/bhr319 [Accessed: 14 October 2019].
- Schindelin, J., Arganda-Carreras, I., Frise, E., Kaynig, V., et al. (2012) Fiji: an open-source platform for biological-image analysis. *Nature Methods*.

- [Online] 9 (7), 676–682. Available from: doi:10.1038/nmeth.2019
[Accessed: 26 July 2021].
- Schlingloff, D., Káli, S., Freund, T.F., Hájos, N., et al. (2014) Mechanisms of sharp wave initiation and ripple generation. *The Journal of neuroscience : the official journal of the Society for Neuroscience*. [Online] 34 (34), 11385–11398. Available from: doi:10.1523/JNEUROSCI.0867-14.2014 [Accessed: 30 June 2019].
- Schmid, L.C., Mittag, M., Poll, S., Schwarz, M.K., et al. (2016a) Dysfunction of Somatostatin-Positive Interneurons Associated with Memory Deficits in an Alzheimer's Disease Model. *Neuron*. [Online] 92, 114–125. Available from: doi:10.1016/j.neuron.2016.08.034 [Accessed: 4 March 2019].
- Schmid, L.C., Mittag, M., Poll, S., Steffen, J., et al. (2016b) Dysfunction of Somatostatin-Positive Interneurons Associated with Memory Deficits in an Alzheimer's Disease Model. *Neuron*. [Online] 92 (1), 114–125. Available from: doi:10.1016/J.NEURON.2016.08.034 [Accessed: 11 March 2019].
- Schmitz, C., Eastwood, B.S., Tappan, S.J., Glaser, J.R., et al. (2014) Current automated 3D cell detection methods are not a suitable replacement for manual stereologic cell counting. *Frontiers in Neuroanatomy*. [Online] 0 (MAY), 27. Available from: doi:10.3389/FNANA.2014.00027.
- Schneider, F., Baldauf, K., Wetzel, W. & Reymann, K.G. (2014) Behavioral and EEG changes in male 5xFAD mice. *Physiology & Behavior*. [Online] 135, 25–33. Available from: doi:10.1016/J.PHYSBEH.2014.05.041.
- Seibt, J., Dumoulin, M.C., Aton, S.J., Coleman, T., et al. (2012) Protein synthesis during sleep consolidates cortical plasticity in vivo. *Current Biology*. [Online] 22 (8), 676–682. Available from: doi:10.1016/j.cub.2012.02.016 [Accessed: 3 September 2020].
- Seidenbecher, T., Laxmi, T.R., Stork, O. & Pape, H.C. (2003) Amygdalar and hippocampal theta rhythm synchronization during fear memory retrieval. *Science*. [Online] 301 (5634), 846–850. Available from: doi:10.1126/science.1085818 [Accessed: 30 June 2021].
- Shah, D., Latif-Hernandez, A., De Strooper, B., Saito, T., et al. (2018) Spatial reversal learning defect coincides with hypersynchronous telencephalic BOLD functional connectivity in APPNL-F/NL-F knock-in mice. *Scientific Reports*. [Online] 8 (1), 6264. Available from: doi:10.1038/s41598-018-24657-9 [Accessed: 2 October 2019].

- Shankar, G.M., Bloodgood, B.L., Townsend, M., Walsh, D.M., et al. (2007) Natural oligomers of the Alzheimer amyloid- β protein induce reversible synapse loss by modulating an NMDA-type glutamate receptor-dependent signaling pathway. *Journal of Neuroscience*. [Online] 27 (11), 2866–2875. Available from: doi:10.1523/JNEUROSCI.4970-06.2007 [Accessed: 28 June 2021].
- Sheremet, A., Kennedy, J.P., Qin, Y., Zhou, Y., et al. (2019) Theta-gamma cascades and running speed. *Journal of Neurophysiology*. [Online] 121 (2), 444–458. Available from: doi:10.1152/jn.00636.2018 [Accessed: 11 May 2021].
- Shirvalkar, P.R., Rapp, P.R. & Shapiro, M.L. (2010) Bidirectional changes to hippocampal theta-gamma comodulation predict memory for recent spatial episodes. *Proceedings of the National Academy of Sciences of the United States of America*. [Online] 107 (15), 7054–7059. Available from: doi:10.1073/pnas.0911184107.
- Siapas, A.G., Lubenov, E. V. & Wilson, M.A. (2005) Prefrontal Phase Locking to Hippocampal Theta Oscillations. *Neuron*. [Online] 46 (1), 141–151. Available from: doi:10.1016/J.NEURON.2005.02.028 [Accessed: 7 May 2019].
- Siapas, A.G. & Wilson, M.A. (1998) Coordinated Interactions between Hippocampal Ripples and Cortical Spindles during Slow-Wave Sleep. *Neuron*. [Online] 21 (5), 1123–1128. Available from: doi:10.1016/S0896-6273(00)80629-7 [Accessed: 30 June 2019].
- Sigurdsson, T. & Duvarci, S. (2015) Hippocampal-Prefrontal Interactions in Cognition, Behavior and Psychiatric Disease. *Frontiers in Systems Neuroscience*. [Online] 9, 190. Available from: doi:10.3389/FNSYS.2015.00190 [Accessed: 7 May 2019].
- Simon, A., Oláh, S., Molnár, G., Szabadics, J., et al. (2005) Gap-Junctional Coupling between Neurogliaform Cells and Various Interneuron Types in the Neocortex. *Journal of Neuroscience*. [Online] 25 (27), 6278–6285. Available from: doi:10.1523/JNEUROSCI.1431-05.2005 [Accessed: 10 October 2017].
- Simon, A.P., Poindessous-Jazat, F., Dutar, P., Epelbaum, J., et al. (2006) Firing properties of anatomically identified neurons in the medial septum of anesthetized and unanesthetized restrained rats. *Journal of Neuroscience*.

- [Online] 26 (35), 9038–9046. Available from:
doi:10.1523/JNEUROSCI.1401-06.2006 [Accessed: 30 June 2021].
- Sindi, S., Kåreholt, I., Johansson, L., Skoog, J., et al. (2018) Sleep disturbances and dementia risk: A multicenter study. *Alzheimer's and Dementia*. [Online] 14 (10), 1235–1242. Available from: doi:10.1016/j.jalz.2018.05.012 [Accessed: 18 June 2021].
- Sirota, A., Csicsvari, J., Buhl, D. & Buzsáki, G. (2003) Communication between neocortex and hippocampus during sleep in rodents. *PNAS*. [Online] 100 (4), 2065–2069. Available from: doi:10.1073/pnas.0437938100 [Accessed: 24 June 2019].
- Sirota, A., Montgomery, S., Fujisawa, S., Isomura, Y., et al. (2008) Entrainment of Neocortical Neurons and Gamma Oscillations by the Hippocampal Theta Rhythm. *Neuron*. [Online] 60 (4), 683–697. Available from: doi:10.1016/J.NEURON.2008.09.014 [Accessed: 24 June 2019].
- Sjöström, P.J., Rancz, E.A., Roth, A. & Häusser, M. (2008) Dendritic excitability and synaptic plasticity. *Physiological Reviews*. [Online]. 88 (2) pp.769–840. Available from: doi:10.1152/physrev.00016.2007 [Accessed: 5 July 2021].
- Sohal, V.S., Zhang, F., Yizhar, O. & Deisseroth, K. (2009a) Parvalbumin neurons and gamma rhythms enhance cortical circuit performance. *Nature*. [Online] 459 (7247), 698–702. Available from: doi:10.1038/nature07991 [Accessed: 30 June 2019].
- Sohal, V.S., Zhang, F., Yizhar, O. & Deisseroth, K. (2009b) Parvalbumin neurons and gamma rhythms enhance cortical circuit performance. *Nature*. [Online] 459 (7247), 698–702. Available from: doi:10.1038/nature07991 [Accessed: 1 July 2021].
- Spangenberg, E.E., Lee, R.J., Najafi, A.R., Rice, R.A., et al. (2016) Eliminating microglia in Alzheimer's mice prevents neuronal loss without modulating amyloid- β pathology. *Brain*. [Online] 139 (4), 1265–1281. Available from: doi:10.1093/BRAIN/AWW016 [Accessed: 23 August 2021].
- Sperling, R.A., LaViolette, P.S., O'Keefe, K., O'Brien, J., et al. (2009) Amyloid Deposition Is Associated with Impaired Default Network Function in Older Persons without Dementia. *Neuron*. [Online] 63 (2), 178–188. Available from: doi:10.1016/j.neuron.2009.07.003 [Accessed: 22 March 2021].
- Spires-Jones, T.L. & Hyman, B.T. (2014) The Intersection of Amyloid Beta and Tau at Synapses in Alzheimer's Disease. *Neuron*. [Online] 82 (4), 756–771.

Available from: doi:10.1016/J.NEURON.2014.05.004 [Accessed: 22 February 2018].

- Staresina, B.P., Bergmann, T.O., Bonnefond, M., Van Der Meij, R., et al. (2015) Hierarchical nesting of slow oscillations, spindles and ripples in the human hippocampus during sleep. *Nature Neuroscience*. [Online] 18 (11), 1679–1686. Available from: doi:10.1038/nn.4119 [Accessed: 1 September 2020].
- Stark, E., Roux, L., Eichler, R., Senzai, Y., et al. (2014) Pyramidal cell-interneuron interactions underlie hippocampal ripple oscillations. *Neuron*. [Online] 83 (2), 467–480. Available from: doi:10.1016/j.neuron.2014.06.023.
- Steriade, M. & Amzica, F. (1996) Intracortical and corticothalamic coherency of fast spontaneous oscillations. *PNAS*. [Online] 93 (6), 2533–2538. Available from: doi:10.1073/pnas.93.6.2533 [Accessed: 3 July 2021].
- Steriade, M., Amzica, F. & Nuñez, A. (1993) Cholinergic and Noradrenergic Modulation of the Slow (~0.3 HZ) Oscillation in Neocortical Cells. *Journal of Neurophysiology*. [Online] 70 (4). Available from: <http://www.physiology.org/doi/pdf/10.1152/jn.1993.70.4.1385> [Accessed: 8 January 2018].
- Steriade, M., Contreras, D., Amzica, F. & Timofeev, L. (1996) Synchronization of Fast (30-40 Hz) Spontaneous Oscillations in Intrathalamic and Thalamocortical Networks. *The Journal of Neuroscience*. [Online] 76 (8), 2788–2808. Available from: <http://www.jneurosci.org/content/jneuro/16/8/2788.full.pdf> [Accessed: 13 December 2017].
- Steriade, M., Contreras, D., Dossi, C. & Nuñez, A. (1993) The Slow (<1 Hz) Oscillation in Reticular Thalamic and Thalamocortical Neurons: Scenario of Sleep Rhythm Generation in Interacting Thalamic and Neocortical Networks. *The Journal of Neuroscience*. [Online] 13 (8), 3284–3299. Available from: <https://pdfs.semanticscholar.org/b1ac/63bfa7b67d360179f4a1bd7bbe67e5057701.pdf> [Accessed: 13 June 2018].
- Steriade, M., Deschenes, M., Domich, L. & Mulle, A.C. (1985) Abolition of Spindle Oscillations in Thalamic Neurons Disconnected From Nucleus Reticularis Thalami. *Journal of Neurophysiology*. [Online] 54 (6). Available from: <http://www.physiology.org/doi/pdf/10.1152/jn.1985.54.6.1473>

[Accessed: 5 January 2018].

- Steriade, M., Nunez, A. & Amzica, F. (1993a) A Novel Slow (<1Hz) Oscillation of Neocortical neurons in vivo: Depolarizing and Hyperpolarizing Components. *The Journal of Neuroscience*. [Online] 73 (8), 3252–3285. Available from: <http://www.jneurosci.org/content/jneuro/13/8/3252.full.pdf> [Accessed: 25 October 2017].
- Steriade, M., Nunez, A. & Amzica, F. (1993b) Intracellular analysis of relations between the slow (<1 Hz) neocortical oscillation and other sleep rhythms of the electroencephalogram. *Journal of Neuroscience*. [Online] 13 (8), 3266–3283. Available from: doi:10.1523/jneurosci.13-08-03266.1993 [Accessed: 3 June 2021].
- Stickgold, R. (2005) Sleep-dependent memory consolidation. *Nature*. [Online]. 437 (7063) pp.1272–1278. Available from: doi:10.1038/nature04286.
- De Strooper, B. & Karran, E. (2016) The Cellular Phase of Alzheimer’s Disease. *Cell*. [Online]. 164 (4) pp.603–615. Available from: doi:10.1016/j.cell.2015.12.056.
- Sullivan, D., Mizuseki, K., Sorigi, A. & Buzsáki, G. (2014) Comparison of Sleep Spindles and Theta Oscillations in the Hippocampus. *Journal of Neuroscience*. [Online] 34 (2), 662–674. Available from: doi:10.1523/JNEUROSCI.0552-13.2014 [Accessed: 24 June 2019].
- Taglialetela, G., Hogan, D., Zhang, W.R. & Dineley, K.T. (2009) Intermediate- and long-term recognition memory deficits in Tg2576 mice are reversed with acute calcineurin inhibition. *Behavioural Brain Research*. [Online] 200 (1), 95–99. Available from: doi:10.1016/J.BBR.2008.12.034.
- Tamura, M., Spellman, T.J., Rosen, A.M., Gogos, J.A., et al. (2017) Hippocampal-prefrontal theta-gamma coupling during performance of a spatial working memory task. *Nature Communications*. [Online] 8 (1), 2182. Available from: doi:10.1038/s41467-017-02108-9 [Accessed: 30 June 2019].
- Taxidis, J., Mizuseki, K., Mason, R. & Owen, M.R. (2013) Influence of slow oscillation on hippocampal activity and ripples through cortico-hippocampal synaptic interactions, analyzed by a cortical-CA3-CA1 network model. *Frontiers in Computational Neuroscience*. [Online] 7, 3. Available from: doi:10.3389/fncom.2013.00003 [Accessed: 7 May 2019].
- Tcw, J. & Goate, A.M. (2017) Genetics of β -Amyloid Precursor Protein in

- Alzheimer's Disease. *Cold Spring Harbor perspectives in medicine*. [Online]. 7 (6). Available from: doi:10.1101/cshperspect.a024539 [Accessed: 16 June 2021].
- Teber, I., Köhling, R., Speckmann, E.J., Barnekow, A., et al. (2004) Muscarinic acetylcholine receptor stimulation induces expression of the activity-regulated cytoskeleton-associated gene (ARC). *Molecular Brain Research*. [Online] 121 (1–2), 131–136. Available from: doi:10.1016/j.molbrainres.2003.11.017.
- Thompson, K.J., Khajehali, E., Bradley, S.J., Navarrete, J.S., et al. (2018) DREADD Agonist 21 Is an Effective Agonist for Muscarinic-Based DREADDs in Vitro and in Vivo. *ACS Pharmacology and Translational Science*. [Online] 1 (1), 61–72. Available from: doi:10.1021/acsptsci.8b00012 [Accessed: 15 August 2018].
- Timofeev, I., Bazhenov, M., Seigneur, J. & Sejnowski, T. (2012) Neuronal Synchronization and Thalamocortical Rhythms in Sleep, Wake and Epilepsy. *Jasper's Basic Mechanisms of the Epilepsies*. 4.
- Timofeev, I., Grenier, F., Bazhenov, M., Sejnowski, T.J., et al. (2000) Origin of Slow Cortical Oscillations in Deafferented Cortical Slabs. *Cerebral Cortex*. [Online] 10, 1185–1199. Available from: https://watermark.silverchair.com/1001185.pdf?token=AQECAHi208BE490oan9kkhW_Ercy7Dm3ZL_9Cf3qfKAc485ysgAAAbAwggGsBgkqhkiG9w0B BwagggGdMIIBmQIBADCCAZIGCSqGSIB3DQEHATAeBgIghkgBZQMEAS4wEQQMZS2vxscvBuvU9qpcAgEQgIIBY8VcenutXudLtnG1319iO9CsHDTkDKhaJvbN0e84O9gndjk [Accessed: 8 January 2018].
- Tononi, G. & Cirelli, C. (2006) Sleep function and synaptic homeostasis. *Sleep Medicine Reviews*. [Online]. 10 (1) pp.49–62. Available from: doi:10.1016/j.smrv.2005.05.002.
- Torao-Angosto, M., Manasanch, A., Mattia, M. & Sanchez-Vives, M. V. (2021) Up and Down States During Slow Oscillations in Slow-Wave Sleep and Different Levels of Anesthesia. *Frontiers in Systems Neuroscience*. [Online] 15, 5. Available from: doi:10.3389/fnsys.2021.609645 [Accessed: 22 March 2021].
- Tort, A.B.L., Komorowski, R.W., Manns, J.R., Kopell, N.J., et al. (2009) Theta-gamma coupling increases during the learning of item-context associations. *Proceedings of the National Academy of Sciences of the United States of*

- America*. [Online] 106 (49), 20942–20947. Available from: doi:10.1073/pnas.0911331106 [Accessed: 2 July 2021].
- Tort, A.B.L., Kramer, M.A., Thorn, C., Gibson, D.J., et al. (2008) Dynamic cross-frequency couplings of local field potential oscillations in rat striatum and hippocampus during performance of a T-maze task. *Proceedings of the National Academy of Sciences of the United States of America*. [Online] 105 (51), 20517–20522. Available from: doi:10.1073/pnas.0810524105.
- Tort, A.B.L., Scheffer-Teixeira, R., Souza, B.C., Draguhn, A., et al. (2013) Theta-associated high-frequency oscillations (110-160Hz) in the hippocampus and neocortex. *Progress in Neurobiology*. [Online]. 100 (1) pp.1–14. Available from: doi:10.1016/j.pneurobio.2012.09.002.
- Trujillo-Estrada, L., Dávila, J.C., Sánchez-Mejias, E., Sánchez-Varo, R., et al. (2014) Early Neuronal Loss and Axonal/Presynaptic Damage is Associated with Accelerated Amyloid- β Accumulation in A β PP/PS1 Alzheimer's Disease Mice Subiculum. *Journal of Alzheimer's Disease*. [Online] 42 (2), 521–541. Available from: doi:10.3233/JAD-140495.
- Ts'o, D.Y., Gilbert, C.D. & Wiesel, T.N. (1986) Relationships between horizontal interactions and functional architecture in cat striate cortex as revealed by cross-correlational analysis. *Journal of Neuroscience*. [Online] 6 (4), 1160–1170. Available from: doi:10.1523/jneurosci.06-04-01160.1986 [Accessed: 16 December 2018].
- Tukker, J.J., Beed, P., Schmitz, D., Larkum, M.E., et al. (2020) Up and Down States and Memory Consolidation Across Somatosensory, Entorhinal, and Hippocampal Cortices. *Frontiers in Systems Neuroscience*. [Online]. 14 p.22. Available from: doi:10.3389/fnsys.2020.00022 [Accessed: 13 November 2020].
- Umeda, T., Tomiyama, T., Sakama, N., Tanaka, S., et al. (2011) Intraneuronal amyloid β oligomers cause cell death via endoplasmic reticulum stress, endosomal/lysosomal leakage, and mitochondrial dysfunction in vivo. *Journal of Neuroscience Research*. [Online] 89 (7), 1031–1042. Available from: doi:10.1002/JNR.22640 [Accessed: 23 August 2021].
- Urban-Ciecko, J., Fanselow, E.E. & Barth, A.L. (2015) Neocortical somatostatin neurons reversibly silence excitatory transmission via GABA_B receptors. *Current biology : CB*. [Online] 25 (6), 722–731. Available from: doi:10.1016/j.cub.2015.01.035 [Accessed: 23 November 2018].

- Valderrama, M., Crépon, B., Botella-Soler, V., Martinerie, J., et al. (2012) Human Gamma Oscillations during Slow Wave Sleep Olaf Sporns (ed.). *PLoS ONE*. [Online] 7 (4), e33477. Available from: doi:10.1371/journal.pone.0033477 [Accessed: 23 February 2020].
- Vandecasteele, M., Varga, V., Berényi, A., Papp, E., et al. (2014) Optogenetic activation of septal cholinergic neurons suppresses sharp wave ripples and enhances theta oscillations in the hippocampus. *Proceedings of the National Academy of Sciences of the United States of America*. [Online] 111 (37), 13535–13540. Available from: doi:10.1073/pnas.1411233111.
- Vantomme, G., Osorio-Forero, A., Lüthi, A. & Fernandez, L.M.J. (2019) Regulation of local sleep by the thalamic reticular nucleus. *Frontiers in Neuroscience*. [Online]. 13 (JUN) p.576. Available from: doi:10.3389/fnins.2019.00576 [Accessed: 8 February 2021].
- Varela, C. & Wilson, M.A. (2020) MpfC spindle cycles organize sparse thalamic activation and recently active ca1 cells during non-rem sleep. *eLife*. [Online] 9, 1–34. Available from: doi:10.7554/eLife.48881.
- Varga, A.W., Wohlleber, M.E., Giménez, S., Romero, S., et al. (2016) Reduced Slow-Wave Sleep Is Associated with High Cerebrospinal Fluid A β 42 Levels in Cognitively Normal Elderly. *Sleep*. [Online] 39 (11), 2041–2048. Available from: doi:10.5665/sleep.6240 [Accessed: 1 June 2020].
- Verret, L., Mann, E.O., Hang, G.B., Barth, A.M.I., et al. (2012) Inhibitory Interneuron Deficit Links Altered Network Activity and Cognitive Dysfunction in Alzheimer Model. *CELL*. [Online] 149, 708–721. Available from: doi:10.1016/j.cell.2012.02.046 [Accessed: 2 October 2017].
- Viollet, C., Simon, A., Tolle, V., Labarthe, A., et al. (2017) Somatostatin-IRES-Cre Mice: Between Knockout and Wild-Type? *Frontiers in Endocrinology*. [Online] 8 (JUN), 19. Available from: doi:10.3389/FENDO.2017.00131 [Accessed: 21 September 2021].
- Vitiello, M. V., Prinz, P.N., Williams, D.E., Frommlet, M.S., et al. (1990) Sleep disturbances in patients with mild-stage Alzheimer's disease. *Journals of Gerontology*. [Online] 45 (4). Available from: doi:10.1093/geronj/45.4.M131 [Accessed: 18 June 2021].
- Vogel-Ciernia, A. & Wood, M.A. (2014) Examining Object Location and Object Recognition Memory in Mice. *Current protocols in neuroscience / editorial board, Jacqueline N. Crawley ... [et al.]*. [Online] 69, 8.31.1. Available from:

- doi:10.1002/0471142301.NS0831S69 [Accessed: 1 September 2021].
- Volgushev, M., Chauvette, S., Mukovski, M. & Timofeev, I. (2006) Precise Long-Range Synchronization of Activity and Silence in Neocortical Neurons during Slow-Wave Sleep. *Journal of Neuroscience*. [Online] 26 (21), 5665–5672. Available from: doi:10.1523/JNEUROSCI.0279-06.2006.
- Walker, J.M., Fowler, S.W., Miller, D.K., Sun, A.Y., et al. (2011) Spatial learning and memory impairment and increased locomotion in a transgenic amyloid precursor protein mouse model of Alzheimer's disease. *Behavioural Brain Research*. [Online] 222 (1), 169–175. Available from: doi:10.1016/J.BBR.2011.03.049.
- Walker, L.C. & Jucker, M. (2015) Neurodegenerative Diseases: Expanding the Prion Concept. *Annual Review of Neuroscience*. [Online] 38, 87–103. Available from: doi:10.1146/annurev-neuro-071714-033828 [Accessed: 16 June 2021].
- Walsh, D.A., Brown, J.T. & Randall, A.D. (2020) Neurophysiological alterations in the nucleus reuniens of a mouse model of Alzheimer's disease. *Neurobiology of Aging*. [Online] 88, 1–10. Available from: doi:10.1016/J.NEUROBIOLAGING.2019.12.006.
- Wang, L., Zang, Y., He, Y., Liang, M., et al. (2006) Changes in hippocampal connectivity in the early stages of Alzheimer's disease: Evidence from resting state fMRI. *NeuroImage*. [Online] 31 (2), 496–504. Available from: doi:10.1016/J.NEUROIMAGE.2005.12.033 [Accessed: 1 October 2019].
- Weber, F. & Dan, Y. (2016) Circuit-based interrogation of sleep control. *Nature*. [Online]. 538 (7623) pp.51–59. Available from: doi:10.1038/nature19773 [Accessed: 5 January 2021].
- Weber, F., Hoang Do, J.P., Chung, S., Beier, K.T., et al. (2018) Regulation of REM and Non-REM Sleep by Periaqueductal GABAergic Neurons. *Nature Communications*. [Online] 9 (1). Available from: doi:10.1038/s41467-017-02765-w [Accessed: 5 January 2021].
- Van De Werd, H.J.J.M., Rajkowska, G., Evers, P. & Uylings, H.B.M. (2010) Cytoarchitectonic and chemoarchitectonic characterization of the prefrontal cortical areas in the mouse. *Brain Structure and Function*. [Online] 214 (4), 339–353. Available from: doi:10.1007/s00429-010-0247-z.
- Westerberg, C.E., Florczak, S.M., Weintraub, S., Mesulam, M.M., et al. (2015) Memory improvement via slow-oscillatory stimulation during sleep in older

- adults. *Neurobiology of Aging*. [Online] 36 (9), 2577–2586. Available from: doi:10.1016/j.neurobiolaging.2015.05.014.
- Whittington, M.A., Traub, R.D., Kopell, N., Ermentrout, B., et al. (2000) Inhibition-based rhythms: experimental and mathematical observations on network dynamics. *International Journal of Psychophysiology*. [Online] 38 (3), 315–336. Available from: doi:10.1016/S0167-8760(00)00173-2.
- Whyte, L.S., Hemsley, K.M., Lau, A.A., Hassiotis, S., et al. (2018) Reduction in open field activity in the absence of memory deficits in the App NL–G–F knock-in mouse model of Alzheimer’s disease. *Behavioural Brain Research*. [Online] 336, 177–181. Available from: doi:10.1016/j.bbr.2017.09.006 [Accessed: 24 June 2019].
- Wierzynski, C.M., Lubenov, E. V., Gu, M. & Siapas, A.G. (2009a) State-Dependent Spike-Timing Relationships between Hippocampal and Prefrontal Circuits during Sleep. *Neuron*. [Online] 61 (4), 587–596. Available from: doi:10.1016/j.neuron.2009.01.011 [Accessed: 11 May 2021].
- Wierzynski, C.M., Lubenov, E. V, Gu, M. & Siapas, A.G. (2009b) State-dependent spike timing relationships between hippocampal and prefrontal circuits during sleep. *Neuron*. [Online] 61 (4), 587–596. Available from: doi:10.1016/j.neuron.2009.01.011 [Accessed: 7 May 2019].
- Wildsmith, K.R., Holley, M., Savage, J.C., Skerrett, R., et al. (2013) Evidence for impaired amyloid β clearance in Alzheimer’s disease. *Alzheimer’s Research and Therapy*. [Online]. 5 (4) pp.1–6. Available from: doi:10.1186/alzrt187 [Accessed: 18 June 2021].
- Wilson M, M.B. (1994) Reactivation of Hippocampal Ensemble Memories During Sleep. *Science*. [Online] 265, 676–679. Available from: <http://science.sciencemag.org/> [Accessed: 7 May 2019].
- Witton, J., Staniaszek, L.E., Bartsch, U., Randall, A.D., et al. (2016) Disrupted hippocampal sharp-wave ripple-associated spike dynamics in a transgenic mouse model of dementia. *The Journal of physiology*. [Online] 594 (16), 4615–4630. Available from: doi:10.1113/jphysiol.2014.282889 [Accessed: 29 October 2018].
- Wolansky, T., Clement, E.A., Peters, S.R., Palczak, M.A., et al. (2006) Hippocampal Slow Oscillation: A Novel EEG State and Its Coordination with Ongoing Neocortical Activity. *Journal of Neuroscience*. [Online] 26

- (23), 6213–6229. Available from: doi:10.1523/JNEUROSCI.5594-05.2006 [Accessed: 17 April 2020].
- Wright, A.L., Zinn, R., Hohensinn, B., Konen, L.M., et al. (2013) Neuroinflammation and Neuronal Loss Precede Ab Plaque Deposition in the hAPP-J20 Mouse Model of Alzheimer's Disease. *PLOS ONE*. [Online] 8 (4). Available from: doi:10.1371/journal.pone.0059586 [Accessed: 23 January 2018].
- Xia, F., Richards, B.A., Tran, M.M., Josselyn, S.A., et al. (2017) Parvalbumin-positive interneurons mediate neocortical-hippocampal interactions that are necessary for memory consolidation. *eLife*. [Online] 6. Available from: doi:10.7554/eLife.27868 [Accessed: 10 June 2019].
- Xie, L., Kang, H., Xu, Q., Chen, M.J., et al. (2013) Sleep Drives Metabolite Clearance from the Adult Brain. *Science*. [Online] 342 (6156). Available from: doi:10.1126/science.1241224 [Accessed: 13 November 2017].
- Xu, Y., Wang, L., Liu, Y., zhang, Yang, Y., et al. (2016) GABAergic Interneurons are Required for Generation of Slow CA1 Oscillation in Rat Hippocampus. *Neuroscience Bulletin*. [Online] 32 (4), 363–373. Available from: doi:10.1007/s12264-016-0049-2 [Accessed: 23 February 2020].
- Yamamoto, K., Tanei, Z.-I., Deisseroth, K., Correspondence, T.I., et al. (2015) Chronic Optogenetic Activation Augments Ab Pathology in a Mouse Model of Alzheimer Disease. *Cell Reports*. [Online] 11, 859–865. Available from: doi:10.1016/j.celrep.2015.04.017 [Accessed: 13 November 2017].
- Ylinen, A., Bragin, A., Nádasdy, Z., Jandó, G., et al. (1995) Sharp wave-associated high-frequency oscillation (200 Hz) in the intact hippocampus: network and intracellular mechanisms. *The Journal of neuroscience: the official journal of the Society for Neuroscience*. [Online] 15 (1 Pt 1), 30–46. Available from: doi:10.1523/JNEUROSCI.15-01-00030.1995 [Accessed: 24 June 2019].
- Zanos, P. & Gould, T.D. (2018) Mechanisms of Ketamine Action as an Antidepressant. *Molecular psychiatry*. [Online] 23 (4), 801. Available from: doi:10.1038/MP.2017.255 [Accessed: 2 August 2021].
- Zhang, L., Lee, J., Rozell, C. & Singer, A.C. (2019) Sub-second dynamics of theta-gamma coupling in hippocampal CA1. *eLife*. [Online] 8. Available from: doi:10.7554/eLife.44320.
- Zhong, P., Gu, Z., Wang, X., Jiang, H., et al. (2003) Impaired modulation of

GABAergic transmission by muscarinic receptors in a mouse transgenic model of Alzheimer's disease. *The Journal of biological chemistry*. [Online] 278 (29), 26888–26896. Available from: doi:10.1074/jbc.M302789200 [Accessed: 1 October 2019].

Zhurakovskaya, E., Ishchenko, I., Gureviciene, I., Aliev, R., et al. (2019) Impaired hippocampal-cortical coupling but preserved local synchrony during sleep in APP/PS1 mice modeling Alzheimer's disease. *Scientific Reports*. [Online] 9 (1), 5380. Available from: doi:10.1038/s41598-019-41851-5 [Accessed: 18 July 2019].

Zott, B., Simon, M.M., Hong, W., Unger, F., et al. (2019) A vicious cycle of β amyloid-dependent neuronal hyperactivation. *Science*. [Online] 365 (6453), 559–565. Available from: doi:10.1126/science.aay0198 [Accessed: 28 June 2021].